DYNAMIC ANTIFOULING STRUCTURES AND ACTUATORS USING EAP COMPOSITES

By

CLAYTON CLAVERIE BOHN JR.

A DISSERTATION PRESENTED TO THE GRADUATE SCHOOL
OF THE UNIVERSITY OF FLORIDA IN PARTIAL FULFILLMENT
OF THE REQUIREMENTS FOR THE DEGREE OF
DOCTOR OF PHILOSOPHY

UNIVERSITY OF FLORIDA

2004

Copyright 2004

by

Clayton Claverie Bohn Jr.

This dissertation is dedicated to my loving parents Jack and Kathy Higgins and Clay and Susan Bohn for all there guidance and support throughout my life.

ACKNOWLEDGMENTS

I would like to thank my advisor and committee chair, Dr. Anthony Brennan, for providing me with the opportunity to further develop my understanding of polymers and engineering as a science and an art. He has provided infinite patience, guidance, and support throughout this project. He has continually challenged me as a researcher and a man to grow and find solutions that are not always obvious. I would like to thank the rest of my committee, Dr. Ronald Baney, Dr. Chris Batich, Dr. Amelia Dempere, and Dr. John Reynolds, for their time and valued critique of this dissertation. In addition I would like to further thank Dr. Reynolds for his support, guidance, and extensive knowledge of conducting polymers and electrochemistry during this project. I would also like to thank him for providing me the use of his electrochemical equipment and the knowledge of his graduate students. I would especially like to thank my coworkers on this project, Dr. Said Sadki and Dr. Myoungho Pyo, for being there as friends, coworkers, and teachers. Dr. Sadki provided the critical knowledge of electrochemistry necessary to get this project started. Dr. Pyo provided the exceptional skill and knowledge of the subject necessary to develop the EcAu systems and to get the project to where it is now. To them I owe all my knowledge of conducting polymers and electrochemistry, and without their help and guidance throughout this project none of this would have been possible. I would like to thank Dr. Elisabeth Smela for her continued guidance and support on the development of the EcAu systems. I would also like to thank Dr. Peter Ifju for help on developing the strain sensitive actuator technology. Dr. Ifju provided extensive

knowledge and support on the proper use and application of strain gages and initial strain gage equipment usage.

I would also like to especially thank my past and present group members. They have provided me with invaluable knowledge, assistance, and friendship during my years in the Brennan research group. Jeanne McDonald and Jeremy Mehlem provided exceptional help and guidance during my initial year in the research group. Both of them have been invaluable as coworkers and friends. I would like to thank them and their spouses for providing me with a very enlightening and enjoyable start in this group. I would like to give special thanks to Michelle Carmen, Thomas Estes, Adam Feinberg, Amy Gibson, Brian Hatcher, Nikhil Kothurkar, Chuck Seegert, Jim Schumacher, Leslie Wilson, and Wade Wilkerson who have proven to be exceptional friends and coworkers. I would also like to thank the rest of my research group for their support: Kenneth Williams and Kiran Karve. I would also like to thank the rest of my friends and colleagues in the department that have provided me with support: Brett Almond, Brian Cuevas, Iris Enriquez, Brent Gila, Josh Stopek, Dan Urbaniak, and Amanda York. Out of this group I would especially like to thank Jamie Rhodes and Paul Martin for also providing me with spare parts and expertise needed to help build and keep equipment running. I would also like to especially thank Jennifer Wrighton; with out her this whole place would probable fall apart and no work would ever get done. She had been a good friend and a great secretary to me and the rest of the group for the past 4 years.

I would also like to thank my family and friends for their love and support throughout my life. I would especially like to thank my brother David for always being there and providing a comical and uplifting side to life. I wish him luck in fatherhood

and all that he does. And I would again like to thank him for always being a true brother and friend.

TABLE OF CONTENTS

page

ACKNOWLEDGMENTS iv

LIST OF TABLES xii

LIST OF FIGURES xiii

ABSTRACT xxiv

1 INTRODUCTION 1

2 BACKGROUND 6

2.1 Electroactive Polymer Actuators 6
2.1.1 Introduction to EAPs 6
2.1.1 Conducting Polymers 10
2.1.2 Conducting Polymer Synthesis 11
2.1.3 Conducting Polymer Actuators 13
2.2 Electrical Resistance Strain Gages 16
2.2.1 Strain Gage Theory 18
2.2.2 Strain Gage Materials and Construction 20
2.2.3 Strain Gage Accuracy 23
2.3 Anti-Fouling/Foul-Release Coatings 25
2.4 Electrowetting 30
2.5 Dynamic Surfaces 33
2.5.1 Polypyrrole 34
2.5.2 Poly(3-methylthiophene) 35
2.5.3 Poly(p-phenylene) 36

3 INITIAL *IN SITU* EVALUATION OF CP'S VIA STRAIN GAGE TECHNIQUE 38

3.1 Introduction 38
3.2 Materials and Methods 38
3.2.1 Materials 38
3.2.2 Strain Gages 39
3.2.3 Conducting Polymer Synthesis 39
3.3 Polypyrrole (PPy/TOS) Results 40
3.3.1 Determination of Electropolymerization Conditions for PPy/TOS 40
3.3.2 PPy/TOS Cyclic Voltammetry and Strain Response 41

3.3.3 PPy/TOS Multi-Cycle Strain Response....43
3.3.4 PPy/TOS Square-Wave Potential Experiments....44
3.4 PEDOP Results....46
3.4.1 Electrochemical Analysis of PEDOP....46
3.4.2 PEDOP Multi-Cycle Strain Response....46
3.4.3 Effects of Cyclic Scan Rate on the Strain Response of PEDOP....49
3.4.4 PEDOP Square-Wave Potential Experiments....51
3.5 PBEDOT-Cz Results....52
3.5.1 PBEDOT-Cz Introduction....52
3.5.2 PBEDOT-Cz Electrochemical Conditions....53
3.5.3 PBEDOT-Cz Strain Response (-0.8 V to 0.6 V)....54
3.5.4 PBEDOT-Cz Strain Response (-0.8 V to 1.0 V)....55
3.5.5 PBEDOT-Cz Strain Response (-0.8 V to 1.2 V)....55
3.5.6 Overall Results for PBEDOT-Cz....56
3.6 Overall Comparison of PPy, PEDOP, and PBEDOT-Cz....58
3.7 Effects of Interlayer Adhesion....59
3.8 Conclusions....61

4 *IN SITU* STRAIN MEASURMENTS OF CP'S ON ENHANCED AU SURFACES66

4.1 Introduction....66
4.2 Materials and Methods....66
4.2.1 Materials....66
4.2.2 Electrochemical Gold Deposition Solution....67
4.2.3 Evaporated and Electrochemically Deposited Gold....67
4.2.4 Conducting Polymer Synthesis....68
4.3 Improved Interlayer Adhesion Utilizing Electrochemically Deposited Au Surfaces (EcAu)....68
4.4 Effects of Surface Roughness on EcAu Morphology....70
4.5 Electrochemical Deposition of PPy....77
4.6 Improved PPy Adhesion to EcAu Treated Surfaces....82
4.7 *IN SITU* PPy/EvAu/PI Actuator Results....83
4.7.1 Counter Ion Effects on PPy Strain Response....83
4.7.2 Effects of Potential Limiting on PPy Strain Response....85
4.7.3 Effects of PPy Film Thickness on Strain Response....86
4.7.4 Effects of Polymerization Potential on PPy Strain Response....90
4.8 *IN SITU* PPy/EcAu/EvAu/PI Actuator Results....91
4.8.1 Effects of PPy electropolymerization charge and surface roughness factor92
4.8.1.1 Effects of surface roughness factor....92
4.8.1.2 Effects of PPy electropolymerization charge on strain (PPy film thickness)....95
4.8.1.3 Combined effects of PPy electropolymerization charge and surface roughness factor....97
4.8.2 Counter Ion Effects on PPy Strain Response....98
4.8.3 Frequency response....99
4.8.4 Lifetime....100
4.9 Conclusions....103

5 RAPID ELECTRODE PATTERNING FOR USE IN ADVANCED CONDUCTING POLYER ACTUATORS AND DYNAMIC SURFACES 104

5.1 Introduction 104
5.2 Rapid Electrode Patterning Techniques 105
5.2.1 Rapid Electrode Patterning 105
5.2.2 Line Patterning 106
5.3 Linear Actuators 108
5.3.1 Background 108
5.3.2 Cantilever based linear actuators 109
5.4 Actuator Based Dynamic Surfaces 119
5.5 Conclusions 125

6 PDMSe BASED DYNAMIC NON-TOXIC ANTI-FOULING SURFACE COATINGS 127

6.1 Introduction 127
6.2 Materials and Methods 129
6.2.1 Materials 129
6.2.2 Gelatin Preparation 129
6.2.3 Polydimethylsiloxane Elastomer Preparation 130
6.2.4 Soluble Polypyrrole Preparation 130
6.2.5 Chemical Formation of Conducting Polymer IPN Systems 130
6.2.6 Supercritical CO_2 Solution Formation of Conducting Polymer IPN Systems 131
6.2.7 Electrochemical Formation of Conducting Polymer IPN Systems 132
6.2.8 Mechanical Property Testing of PPy/PDMSe IPN systems 133
6.2.9 ATR-FTIR Analysis 133
6.2.10 Optical Microscopy 134
6.2.11 Electrochemical Analysis 134
6.2.12 EDS Mapping 134
6.3 Background Study 135
6.3.1 Electrochemical formation of Conducting Polymer IPN Systems 136
6.3.2 Chemical formation of Conducting Polymer IPN Systems 138
6.3.3 Conducting Polymer Blend Formation by Solution Blending 140
6.4 Polypyrrole/PDMSe IPN Formation 141
6.4.1 Introduction 141
6.4.2 Supercritical Carbon Dioxide Solution Doping 142
6.4.2.1 Introduction 142
6.4.2.2 EtOH/$scCO_2$ prepared IPNs 143
6.4.2.3 IPA/$scCO_2$ prepared IPNs 147
6.4.3 Tetrahydrofuran Solution Doping 154
6.4.3.1 Effects of hydration of sample conductivity 156
6.4.3.2 Effects of PDMSe surface segregation 158
6.4.3.3 Effects of $FeCl_3$/THF doping on PDMSe mechanical properties 162
6.5 Conclusions 164

7 TP AND TPE BASED DYNAMIC, NON-TOXIC, ANTI-FOULING SURFACE COATINGS 167

7.1 INTRODUCTION 167
7.2 MATERIALS AND METHODS 169
7.2.1 Materials 169
7.2.1.1 General Chemicals 169
7.2.1.2 PPy/Santoprene® Sample Preparation and Mounting 169
7.2.1.3 Polydimethylsiloxane Elastomer Preparation 170
7.2.1.4 ATS Coupling Agent Preparation 170
7.2.2 Sample Preparation Methods 170
7.2.2.1 Sample Mounting 171
7.2.2.6 Micropatterning 173
7.2.2.7 TP Film Formation by Spin Casting and Spraying 173
7.2.2.8 Conductivity Determination 174
7.3 POLYPYRROLE/8281-65 IPN SYSTEMS 175
7.3.1 PPy/Santoprene® 8281-65 Contact Angle Measurements 175
7.3.2 Determination of PPy Content in PPy/8281-65 Samples 176
7.4 POLYPYRROLE/271-55 IPN SYSTEMS 178
7.4.1 Determination of PPy Content in PPy/271-55 Samples 178
7.4.2 Effects of Counter Ion Exchange on PPy/271-55 Conductivity 180
7.4.3 Formation of poly(3-methylthiophene)/271-55 IPN systems 183
7.4.4 Micropatterning of 271-55 185
7.5 EDS and SEM ANALYSIS of SANTOPRENE® TPE's 187
7.6 PPy/POLYSULFONE SYSTEMS 194
7.8 CONCLUSIONS 196

8 DYNAMIC MODULUS MAPPING OF PPY/SANTOPRENE® BLENDS 198

8.1 INTRODUCTION 198
8.2 MATERIALS AND METHODS 199
8.2.1 Materials 199
8.2.2 Sample Preparation Methods 199
8.2.2.1 PPy/TPE (8211-65) Sample Preparation 199
8.2.2.2 Sample Mounting 199
8.2.2.3 Electrochemical Polymerization of Pyrrole 200
8.2.3 Hysitron Nano-DMA 200
8.2.3.1 Hysitron Introduction 200
8.2.3.2 Experimental conditions 202
8.3 HYSITRON NANO-DMA and AFM ANALYSIS 204
8.3.1 Nano-DMA mapping of 271-55 and PPy/271-55 samples 204
8.3.2 Dynamic fluid cell nano-DMA mapping of PPy/8211-65 207
8.4 CONCLUSIONS 215

9 CONCLUSIONS AND FUTURE WORK 216

ABBREVIATIONS 227

LIST OF REFERENCES 229

BIOGRAPHICAL SKETCH 243

LIST OF TABLES

Table page

7.1 Contact angle values obtain for PPy/8281-65 dual element sample in Instant Ocean® artificial sea water versus a Ag/AgCl reference electrode. 175

7.2 Weight and volume change data for the formation of PPy/8281-65 IPN systems using the FeCl3/THF solvent soak process.....177

LIST OF FIGURES

Figure page

2.1 Bipolar unit charge migration as depicted for polythiophene. 10

2.2 Example of one of the possible mechanisms for the oxidative polymerization of polypyrrole. 12

2.3 Examples of basic bending (cantilever) conducting polymer actuators; A) bilayer actuator, B) backbone type actuator, C) shell type actuator. 15

2.4 Diagram of a polyimide based electrical resistance strain gage and EAP actuator setup. 18

2.5 Thermally induced apparent strain for Constantan (Advanced), Isoelastic, and Karma alloys. 22

2.6 Diagram showing the different species breakdown and layering of biofoul film formation. 26

2.7 Design of electrowetting device: (a) no applied electrical potential (hydrophobic surface); (b) with applied electrical potential (hydrophilic surface). Fluid is pumped by continuously cycling the applied electrical potential. 30

2.8 Voltage required to induce a $\Delta\theta$ of 40° (from 120°→80°) versus dielectric layer thickness for Teflon® AF based EWOD device, with $\varepsilon = 2.0$ and $E_{breakdown} = 2x10^{16}$ V/cm. 33

2.9 Relative surface charge of different conducting polymers. 34

2.10 Oxidation (-) and reduction (--) potentials of poly pyrrole (PPy), polyaniline (PA), poly(3-methylthiophene (PMeT), and poly(p-phenylene) (PPP). 36

2.11 Monomer and polymer structures for A) polypyrrole, B) poly(3-methylthiophene), and C) poly(p-phenylene). 37

3.1 SEM micrograph of surface morphology of PPy/TOS film prepared in 1.0 M $LiClO_4$ at a potential of 0.65 V. SEM image taken of an uncoated sample at 1000X and 15 KeV. 41

3.2 (a) PPy/TOS cyclic voltammetry (ν = 10 mV/s) and (b) *in situ* strain response of a 9.6 μm film prepared in aqueous 1.0 M $LiClO_4$.....43

3.3 *In situ* multi-cycle cyclic voltammetry strain response of a 9.6 με film prepared in aqueous 1.0 M $LiClO_4$.....44

3.4 *In situ* square-wave strain response of a 9.6 μm film prepared in aqueous 1.0 M $LiClO_4$. 45

3.5 Cyclic Voltammetry (ν = 100 mV/s) of a PEDOP film produced from aqueous 1.0 M $LiClO_4$ at E = 0.5 V and t = 200 s.....47

3.6 SEM micrograph of a PEDOP film prepared at 0.6 V in 1.0 M LiClO4. SEM image taken of an uncoated sample at 1000X and 15 KeV. 48

3.7 *In situ* multi-cycle cyclic voltammetry (10 mV/s) strain response of a 10.6 μm PEDOP film in aqueous 1.0 M $LiClO_4$. 48

3.8 *In situ* multi-cycle cyclic voltammetry (10 mV/s) strain response of 10.6 μm PEDOP film in aqueous 1.0 M $LiClO_4$. Data from figure 3.7 has been replotted vs. time. 49

3.9 *In situ* multi-cycle cyclic voltammetry (100 mV/s) strain response of a 10.6 μm PEDOP film in aqueous 1.0 M $LiClO_4$. 50

3.10 *In situ* multi-cycle cyclic voltammetry (100 mV/s) strain response of 10.6 μm PEDOP film in aqueous 1.0 M $LiClO_4$ replotted vs. time. 50

3.11 In situ square-wave strain response of a 10.6 με film prepared in aqueous 1.0 M LiClO4. 51

3.12 Cyclic voltammetry (100 mV/s) of PBEDOT-Cz in 0.1 M TBAP/CAN.....53

3.13 Normalized *in situ* cyclic strain response of 9.9 μm PBEDOT-Cz film (-0.8 V to 0.6 V) for the 1st, 2nd, 5th, and 10th scans in 1.0 M $LiClO_4$.....54

3.14 Normalized *in situ* cyclic strain response of 9.9 μm PBEDOT-Cz film (-0.8 V to 1.0 V) for the 1st, 2nd, 5th, and 10th scans in 1.0 M $LiClO_4$.....55

3.15 Normalized *in situ* cyclic strain response of 9.9 μm PBEDOT-Cz film (-0.8 V to 1.2 V) for the 1st, 2nd, 5th, and 10th scans in 1.0 M $LiClO_4$.....56

3.16 Normalized *in situ* cyclic strain response of 9.9 μm PBEDOT-Cz film scanned from -0.8 V to 0.4 V, 1.0 V, and 1.2 V (5th scan) in 1.0 M $LiClO_4$. 57

3.17 Normalized *in situ* cyclic strain response of 9.9 μm PBEDOT-Cz film scanned from -0.8 V to 0.4 V, 1.0 V, and 1.2 V (10th scan) in 1.0 M $LiClO_4$. 58

3.18 Comparison of *in situ* cyclic strain response of PPy, PEDOT, and PBEDOT-Cz in aqueous 1.0 M $LiClO_4$. 59

3.19 SEM micrograph of delamination of PPy resulting from long-term cycling of the actuator; 150X 62

3.20 SEM micrograph of delamination of PPy resulting from exposure to high vacuum; 25X. 62

3.21 Enlarged SEM micrograph of region "A" in Figure 4.20; 1350X 63

3.22 SEM micrograph of porous PPy at PPy-Au interface; 5000X 63

3.23 Enlarged SEM micrograph of region "B" in Figure 4.20; 100X 64

3.24 SEM micrograph of PPy nodules remaining of Au substrate after PPy delamination; 1000X. 64

3.25 SEM micrograph of PPy surface after delamination from Au substrate during long-term repetitive cycling of the actuator; 250X 65

3.26 SEM micrograph of exposed PPy-Au interface exhibiting PPy nodule growth; 1000X. 65

4.1 Correlation between surface roughness factor, nominal EcAu thickness and EcAu deposition charge. EcAu thickness was determined by cross-section SEM. 70

4.2 SEM micrograph of EvAu deposited on smooth polyimide (PI); 4000X 72

4.3 SEM micrograph of 3 minute EcAu deposition on smooth EvAu/PI; 4000X 72

4.4 SEM micrograph of 10 minute EcAu deposition on smooth EvAu/PI; 4000X 73

4.5 SEM micrograph of 30 minute EcAu deposition on smooth EvAu/PI; 4000X 73

4.6 SEM micrograph of 60 minute EcAu deposition on smooth EvAu/PI; 4000X 74

4.7 SEM micrograph of EvAu (r = 2.89) deposited on rough PI strain gage; 4000X 74

4.8 SEM micrograph of EcAu (r = 6.17, 2.5 min.) deposited on rough EvAu/PI strain gage; 4000X 75

4.9 SEM micrograph of EcAu (r = 10.04, 10 min.) deposited on rough EvAu/PI strain gage; 4000X 75

4.10 SEM micrograph of EcAu (r = 18.90, 30 min.) deposited on rough EvAu/PI strain gage; 4000X 76

4.11 SEM micrograph of EcAu (r = 24.50, 60 min.) deposited on rough EvAu/PI strain gage; 4000X 76

4.12 SEM micrograph of PPy (18.9 C/cm^2) deposited on smooth EvAu/PI; 4000X....78

4.13 SEM micrograph of PPy (18.9 C/cm^2) deposited on smooth EvAu/PI treated with EcAu for 10 min.; 4000X....78

4.14 SEM micrograph of PPy (18.9 C/cm^2) deposited on smooth EvAu/PI treated with EcAu for 30 min.; 4000X....79

4.15 SEM micrograph of PPy (18.9 C/cm^2) deposited on smooth EvAu/PI treated with EcAu for 60 min.; 4000X....79

4.16 Cross-section SEM micrograph of EcAu (60 min.) deposited on smooth EvAu/PI; 4000X. 81

4.17 Cross-section SEM micrograph of PPy (18.9 C/cm^2) deposited on smooth EvAu/PI treated with EcAu for 60 min.; 4000X....81

4.18 Surface plot of calculated PPy film thickness as a function of surface roughness factor (r) and electropolymerization charge (C/cm^2) 82

4.19 Strain response of a 2.83 C/cm^2 PPy/EvAu/PI actuator during potential cycling at 5 mV/s in aqueous $NaClO_4$, $LiClO_4$, $CsClO_4$, $NaNO_3$, and NaCl solutions. 84

4.20 Strain response of a 2.83 C/cm^2 PPy/EvAu/PI actuator during potential stepping (100 s/step) in $NaClO_4$ between –0.6 V and (a) 0.1 V, (b) 0.2 V, (c) 0.3 V, (d) 0.4 V, (e) 0.5 V, and (f) 0.6 V 86

4.21 In situ strain response of PPy/EvAu/PI actuators of varying PPy film thickness during potential stepping between –0.6 V and 0.4 V in aqueous NaClO4. Electropolymerization charge densities were 0.79 C/cm2 (2.8 μm, calculated), 1.6 C/cm2 (5.7 μm, cal.), 2.4 C/cm2 (8.6 μm, cal.), 3.2 C/cm2 (11.4 μm, cal.), 4.0 C/cm2 (14.3 μm, cal.), and 4.8 C/cm2 (17.1 μm, cal.). 88

4.22 *In situ* charge response of PPy/EvAu/PI actuators of varying PPy film thickness during potential stepping between –0.6 V and 0.4 V in aqueous $NaClO_4$. Electropolymerization charge densities were 0.79 C/cm^2 (2.8 μm, calculated), 1.6 C/cm^2 (5.7 μm, cal.), 2.4 C/cm^2 (8.6 μm, cal.), 3.2 C/cm^2 (11.4 μm, cal.), 4.0 C/cm^2 (14.3 μm, cal.), and 4.8 C/cm^2 (17.1 μm, cal.)....89

4.23 *In situ* strain response of a 2.83 C/cm^2 PPy/EvAu/PI actuator during potential stepping between –0.6 V and 0.4 V in aqueous $NaClO_4$. PPy was prepared potentiostatically at (a) 0.7 V, (b) 0.8 V, (c) 0.9 V, and (d) 1.0 V. 91

4.24 *In situ* strain response of a 1.18 C/cm^2 PPy/EcAu/EvAu/PI actuator during potential stepping between –0.6 V and 0.4 V in aqueous $NaClO_4$. With surface roughnesses factors of (a) 2.89, (b) 6.17, (c) 7.13, (d) 10.04, (e) 18.90, and (f) 24.50. 93

4.25 Effects of surface roughness factor (r) on the overall change in strain (Δε) of a 1.18 C/cm^2 PPy/EcAu/EvAu/PI actuator during potential stepping between –0.6 V and 0.4 V in aqueous $NaClO_4$. 94

4.26 Effects of surface roughness factor (r) on the strain rate (με/sec) of a 1.18 C/cm2 PPy/EcAu/EvAu/PI actuator during potential stepping between –0.6 V and 0.4 V in aqueous NaClO4. 95

4.27 *In situ* strain response of PPy/EcAu/EvAu/PI actuator during potential stepping between –0.6 V and 0.4 V in aqueous $NaClO_4$. With surface roughnesses factors of 18.90 and PPy electropolymerization charge of (a) 0.79 C/cm^2, (b) 1.6 C/cm^2, (c) 2.4 C/cm^2, (d) 3.2 C/cm^2, (e) 4.0 C/cm^2, and (f) 4.8 C/cm^2. 96

4.28 Maximum change in strain response of PPy/EcAu/EvAu/PI actuators during potential stepping between –0.6 V and 0.4 V in aqueous $NaClO_4$ with increasing electropolymerization charge. Measured on surface roughnesses of (a) r = 2.89 (EvAu), and EcAu samples of r = (b) 6.17, (c) 10.00, (d) 18.90, and (e) 24.50. 97

4.29 Surface plot of the normalized overall strain response of PPy as a function of electropolymerization charge and surface roughness factor (r). 98

4.30 *In* situ Strain response of a 8.0 C/cm^2 PPy/EcAu/EvAu/PI actuator during potential cycling at 5 mV/s in aqueous (a) $LiClO_4$, (b) $NaNO_3$, and (c) NaCl solutions. 99

4.31 *In situ* normalized (relative to 0.01 Hz) strain and charge response of 1.18 C/cm^2 PPy as a function of frequency on (a) r = 2.89 (EvAu) and (b) r = 10.0 (EcAu) surfaces. Inset shows the charge efficiency (με/C) as a function of frequency. ...100

4.32 *In situ* normalized strain and charge response of 1.18 C/cm^2 PPy (inadequate Argon purge) on r = 5.1 (EvAu) and r = 22.1 (EcAu) treated actuators with repeated potential stepping between –0.6 V (10 s) and 0.4 V (20 s). 102

4.33 *In situ* normalized strain and charge response of 1.18 C/cm^2 PPy on r = 3.43 (EvAu), r = 8.26 (EcAu), and r = 18.90 (EcAu) treated actuators with repeated potential stepping between –0.6 V (10 s) and 0.4 V (20 s). 102

5.1 Negative patterns of linear actuator produced using Microsoft Powerpoint (A) and printed on Kapton used to fabricate linear actuators (B) and a negative pattern used for dynamic surfaces (C) 105

5.2 Rapid electrode patterning process for the development of conducting polymer devices. 106

5.3 Diagram of basic linear actuator design and AutoCAD model used to predict the overall developed linear strain for the device. 110

5.4 Initial PPy linear actuator based on 10mm segments deposited on copper foil. Picture of oxidized state enhanced to show placement of PPy. 111

5.5 PPy linear actuator based on 10mm segments deposited on EvAu coated polyimide strip. 112

5.6 PPy linear actuator based on 20mm segments deposited on EvAu coated polyimide strip. 112

5.7 Single sided rapid electrode pattern design and illustration of how it works. The green and blue areas represent the separate electrode patterns (working and counter electrode). 113

5.8 Diagram of linear actuator fabrication process. Initial negative CAD electrode design (A) negative electrode design printed on substrate (B) produced patterned gold electrode from the mask (C) electrochemically deposited conducting polymer on the patterned gold electrode (D). 114

5.9 Pictures of linear actuator fabrication process. CAD design of negative electrode pattern (A) negative pattern printed on substrate (B) gold coated patterned substrate before acetone wash (C) patterned gold electrode after pattern removal (D) electrochemically deposited conducting polymer on the patterned gold electrode (E). 114

5.10 Side view diagram of bilayer (A) and backbone (B) type linear actuator designs. 115

5.11 WLOP image of the polyimide substrate used in the construction of linear actuators before patterning (Magnification = 25X). 117

5.12 WLOP image of the polyimide substrate coated with evaporated gold (Magnification = 25X). 117

5.13 WLOP image of electrochemically deposited gold on top of evaporated gold coated polyimide (Magnification = 25X). 118

5.14 WLOP image of polypyrrole (+0.8V to 2.24 C/cm^2) electrochemically deposited in EcAu/EvAu coated polyimide (Magnification = 25X). 118

5.15 WLOP image of patterned PPy/EcAu/EvAu on polyimide (Magnification = 25X).118

5.16 WLOP image of exposed base polyimide substrate between two patterned PPy/EcAu/EvAu wires (Magnification = 25X). 119

5.17 Schematic of conducting polymer actuator based dynamic surface. 119

5.18 Images of 0.75, 0.50, and 0.25 pt line patterns produced with Xerox Phaser 6200 laser jet, HP Deskjet 6122, and Lexmark i3 inkjet printers (Magnification = 7X).121

5.19 Images of solid printed pattern areas produced with Xerox Paser 6200 laser jet, HP Deskjet 6122, and Lexmark i3 inkjet printers (Magnification = 14X).....121

5.20 Images of 0.75 pt blue photomask (A) and enhanced image of resulting patterned photoresist coated glass slide (B) (Magnification = 7X).....124

5.21 Images of printed field and 0.75 pt brown photomask with black toner cartridge (A) and without black toner cartridge (B) (Magnification = 7X). 124

5.22 Examples of computer designed patterns used to make blue (A) and brown (B) photomasks. 124

6.1 Images of captive air bubble contact angle measurements on PPy/PDMSe oxidizer insertion films. 140

6.2 Captive air bubble contact angle data for PPy/PDMSe oxidizer insertion films conducted at potentials of -0.8, 0.0, and +0.8 V versus Ag/AgCl in distilled H_2O.140

6.3 Phase diagram for carbon dioxide.....143

6.5 Optical images of degraded PDMSe samples after supercritical CO2 doping with 0.1M FeCl3 dopant and 1vol% ethanol cosolvent for 24hrs. 144

6.6 Optical images of untreated PDMSe (A), and PPy/PDMSe IPNs prepared by EtOH (B) and EtOH/$scCO_2$ (C) oxidizer insertion methods. 146

6.7 Changes in PDMSe sample weight during EtOH/$scCO_2$ prepared PPy/PDMSe IPN systems. 147

6.8 Weight change data for IPA/$scCO_2$ prepared PPy/PDMSe prepared samples. 148

6.9 Weight change data for EtOH/$scCO_2$ prepared PPy/PDMSe prepared samples. ...148

6.10 Optical images (Leica G27) of PPy/PDMSe samples prepared by EtOH/$scCO_2$ (A) and IPA/$scCO_2$ (B) oxidizer insertion methods (mag. = 2X). Sample placed on top of printed text to show transparency. 149

6.11 Optical images (Leica G27) of PPy/PDMSe batches prepared by EtOH/$scCO_2$ (A) and IPA/$scCO_2$ (B) oxidizer insertion methods showing the differences in homogeneity of PPy formation between samples. 149

6.12 Optical images (Axioplan II) of PPy/PDMSe samples prepared by EtOH/$scCO_2$ (A) and IPA/$scCO_2$ (B) oxidizer insertion methods (magnification = 100X; scale bar = 200µm). 150

6.13 Optical images (Axioplan II) of PPy/PDMSe samples prepared by EtOH/scCO$_2$ (A) and IPA/scCO$_2$ (B) oxidizer insertion methods (magnification = 200X; scale bar = 100µm). 150

6.14 Weight change of PDMSe samples exposed to different supercritical CO$_2$ treatments. 153

6.15 Average weight change in PDMSe samples exposed to different supercritical CO$_2$ treatments and after an 18 hr degassing period. 153

6.16 Current response of PPy/PDMSe samples prepared by THF solvent soaking and IPA/scCO2 techniques along with untreated PDMSe. Cyclic voltammetry conducted at ±0.8 V at 10 mV/sec versus Ag/AgCl in Instant Ocean® artificial sea water. 156

6.17 Effects of sample hydration on cyclic voltammetry for wet and dry PPy/PDMSe samples. 157

6.18 ATR-FTIR analysis of PPy/PDMSe IPN systems prepared by various solution soaking procedures. Inset box shows location of characteristic pyrrole ring vibrations (1500-1600 cm^{-1}). 159

6.19 EDS spectra of cross sectioned FeCl$_3$/THF doped PDMSe. 160

6.20 EDS mapping of cross sectioned FeCl$_3$/THF doped PDMSe (magnification = 70X).161

6.21 EDS chlorine mapping of cross sectioned FeCl$_3$/THF doped PDMSe showing a ~60-100 µm surface layer of predominantly pure PDMSe (mag. =70X). 161

6.22 Strain at break and peak stress data for the degradation of Silastic® T2 PDMSe with prolonged exposed to a 5 wt% FeCl$_3$/THF solution. 163

6.23 High and low strain modulus data for the degradation of Silastic® T2 PDMSe with prolonged exposed to a 5 wt% FeCl$_3$/THF solution. 164

7.1 Preparation scheme for the formation of PDMSe encapsulated PPy composite samples for contact angle measurement and marine testing. 172

7.2 PDMSe encapsulated PPy composite samples for testing in aqueous/marine environments using a single (A) and dual (B) element designs. 173

7.3 Change in contact angle for a PPy/8281-65 dual element sample in Instant Ocean® artificial sea water versus a Ag/AgCl reference electrode. 176

7.4 Weight loss data for the formation of PPy/271-55 IPN systems. 180

7.5 Volume loss data for the formation of PPy/271-55 IPN systems. 180

7.6 Calculated PPy/271-55 film conductivity based on conductive layer thickness. Value for 0.07 cm is actual conductivity of PPy/271-55 film assuming bulk conductive. 183

7.7 Example of 5µm biomimetic sharklet pattern on PDMSe (A) and patterned silicon wafer used to create the patterned PDMSe. SEM micrographs taken at 1000X (scale bar = 50 µm; WD = 15 mm and EV = 15 KeV, and AuPd coated). 185

7.8 Optical micrograph of 5µm biomimetic sharklet pattern on 271-55 produced at 185°C (A) and patterned silicon wafer used to create the patterned 271-55. Images taken at 1000X. 186

7.9 SEM micrographs of sharklet patterned Santoprene® 271-55 patterned at 185°C; 3300X (A) and 2500X 40° tilt (B). Images taken at 15 KeV with a working distance of 15 mm and a AuPd surface coating. 186

7.10 SEM micrographs of sharklet patterned Santoprene® 271-55 patterned at 200°C; 500X (A) and 1000X (B). Images taken at 15 KeV with a working distance of 15 mm and a AuPd surface coating. 187

7.11 Cross sectional EDS spectrum of $FeCl_3$ doped Santoprene® 271-55 (A) and 8211-65 (B) showing the presence of Fe and Cl. 188

7.12 Cross sectional EDS mapping of $FeCl_3$ doped Santoprene® 271-55 taken at 180X; scale bar = 200 µm. 189

7.13 Cross sectional EDS mapping of $FeCl_3$ doped Santoprene® 8211-65 taken at 85X; scale bar = 500 µm. 190

7.14 Cross sectional EDS mapping for Cl in $FeCl_3$ doped PDMSe (A), 271-55 (B), and 8211-65 (C). Magnification and scale bars equal to 70X, 180X, and 85X and 500 µm, 200 µm, and 500 µm respectively. Images taken at 15 KeV and 15 mm on carbon coated cross section samples. 191

7.15 Cross sectional EDS mapping of $FeCl_3$ doped PPy/271-55 taken at 3000X; scale bar = 10 µm. Images taken at 15 KeV and 15 mm on carbon coated cross section samples. 192

7.16 Cross sectional EDS mapping of $FeCl_3$ doped PPy/8211-65 taken at 3000X; scale bar = 10 µm. Images taken at 15 KeV and 15 mm on carbon coated cross section samples. 193

7.17 Cross sectional SEM secondary (A) and backscatter (B) electron micrographs of PPy/271-55. Images taken at 3000X and scale bar equal to 10 µm. Images taken at 15 KeV and 15 mm on carbon coated cross section samples. 194

7.18 Cross sectional SEM secondary (A) and backscatter (B) electron micrographs of PPy/8211-65. Images taken at 3000X and scale bar equal to 10 µm. Images taken at 15 KeV and 15 mm on carbon coated cross section samples.....194

7.19 Optical micrographs of PSU films sprayed from 5 wt% (A) and 10 wt% (B) PSU/THF solutions. Magnification = 7X.....196

8.1 Diagram of three plate capacitor transducer used in the Hystitron Triboindenter®.201

8.2 Images of cono-spherical (A) and Berkovich (B) Hysitron tips. Images obtained from www.hysitron.com (magnification unknown).....203

8.3 Diagram (A) and optical image (B) of fluid cell setup inside the Hysitron Triboindenter®.....204

8.4 Optical micographs of Santoprene® 271-55 (A) and PPy/271-55 (B) samples obtain by the onboard optical camera of the Hysitron Triboindenter® (magnification = 5X).....205

8.5 3D surface plots of Santoprene® 271-55 (A) and PPy/271-55 (B) surfaces. Scan area is equal to 50 µm x 50 µm square.....205

8.6 Nano-DMA mapping images of Santoprene® 271-55 showing uniform surface phase and modulus morphology. Scan area is 50 µm x 50 µm square. 206

8.7 Nano-DMA mapping images of PPy/271-55 showing uniform surface phase and modulus morphology. Scan area is 50 µm x 50 µm square. 207

8.8 3D surface topography images of PPy/8211-65 at applied potentials of -0.7 V (A), 0.0 V (B), and +0.7 V (C). Scan area is 25 µm x 25 µm square. 208

8.9 AFM optical micrograph (A) of PPy/8211-65 with corresponding surface topography (B) and phase contrast (C) images taken at a 50µm square scan area. Scale bars equal to 15µm. 209

8.10 AFM surface topography, phase imaging, and 3D surface plot of PPy/8211-65 at 50 µm (A), 10 µm (B), 5 µm (C), and 1 µm (D) square scan areas. Scale bars equal to 15 µm, 3 µm, 1.5 µm, and 0.3 µm respectively. 210

r 8.11 Complex modulus maps for PPy/8211-65 at an applied potential of -0.8 V (A), 0.0 V (B), and +0.8 V (C). 212

8.12 Complex modulus line scan data for PPy/8211-65 obtained from the location depicted in figure 7.28.....212

8.13 3D surface plots of PPy/8211-65 under the applied potentials of -0.8 V (A), 0.0 V (B), and +0.8 V (C). 213

8.14 Average surface modulus for PPy and PPy/8211-65 systems as a function of the applied potential. 214

Abstract of Dissertation Presented to the Graduate School
of the University of Florida in Partial Fulfillment of the
Requirements for the Degree of Doctor of Philosophy

DYNAMIC ANTIFOULING STRUCTURES AND ACTUATORS USING EAP COMPOSITES

By

Clayton Claverie Bohn Jr.

August 2004

Chair: Anthony Brennan
Major Department: Materials Science and Engineering

By utilizing strain gage technology it is possible to directly and continuously measure the electrochemically induced strain response of EAP actuators. Strain sensitive actuators were constructed by directly vapor depositing gold (EvAu) on polyimide strain gages which are capable of measuring strain with an accuracy of +/- 1 με. Strain sensitive actuators were used to evaluate the strain response of polypyrrole (PPy), poly(3,4-ethylenedioxypyrrole) (PEDOP) and poly(3,6-bis(2-(3,4-ethylenedioxy)thienyl)-N-carbazole) (PBEDOT-Cz). PPy was shown to produce significantly higher strain when compared to PEDOP and PBEDOT-Cz. The resulting overall strain for the materials was 236, 33, and 35 με respectively. From the initial investigation, adhesion of the EAP to the EvAu layer was identified as a major factor in the resulting lifetime and strain response of these actuators. Therefore an electrochemically deposited Au layer (EcAu) was deposited on top of the EvAu layer to improve the adhesion of the EAP to the working electrode. By changing the surface roughness from r = 3.43 (EvAu) to r = 8.26

and 18.00 (EcAu) the normalized strain response after 2000 cycles increases from 45% to 60% and 68% respectively. Also by changing the surface roughness from r = 5 to r = 23, the resulting strain response increases from ~100 με to 600-800 με for PPy.

By incorporating conducting polymers such as polypyrrole into elastomeric base materials such as PDMSe and Santopene TPEs a tough durable dynamic non-toxic antifouling surface coating was formed. These coatings utilize the dynamic changes in polymer charge, modulus, and swelling that naturally occur during the redox cycling of conducting polymers to dynamically change the surface properties of the resulting films. Dynamic changes in contact angle (surface energy) of 11° and 21° have been measured for PPy/TPE (±0.5V driving potential) and PPy/PDMSe (±1.0V driving potential) IPN systems.

Using a Hysitron Triboindenter® equipped with a electrochemical fluid cell setup; dynamic fluid cell nano-DMA mapping measurements were conducted on PPy/TPE systems. Dynamic surface modulus changes of ~20-40% were measured for the PPy/TPE composite systems when switched between their reduced to oxidized states. All samples showed a decrease in the sample modulus when switched from the reduced to the oxidized state. This is mainly associated with the influx of water and counter ions into the conducting polymer phase during the oxidation process. This in turn increases the free volume of the conducting polymer phase and also acts to plasticize the phase. Changes in the surface topography associated with the redox cycling of the composite structure were also observed during these experiments. This in turn results in a dynamic surface coating that is capable of changing its surface energy, modulus, and topography by changing applied electrical potential.

CHAPTER 1
INTRODUCTION

Smart materials such as electroactive polymers (EAPs) or more specifically conducting polymers (CPs), such as polyaniline and polypyrrole (PPy), have gained a lot of interest as candidates for various actuator applications such as active hinges, anti-vibration systems, micro-catheter steerers, micro-valves and pumps, mechanical shutters, and robotics due to their ability to undergo controllable volumetric changes under a given stimulus.[1-10] More specifically, conducting polymers have been shown to undergo volumetric changes during electrochemical oxidation and reduction due to the electrochemical transport of ions and solvent molecules into and out of the polymeric system.[11-23] Actuators are constructed by directly depositing conducting polymers, electrochemically, onto a metalized flexible substrate, such as polyimide and polyester. By doing this it is possible to directly convert induced volumetric changes into a mechanical (bending) type of actuation.[6, 24-36] The development of actuation in these systems is very similar in nature to the motion developed in bi-metallic strip (i.e., thermostats). One layer changes length with respect to the other inducing a curling motion to develop in the direction away from the expanding layer. During electrochemical switching (oxidation and reduction) the CP layer expands and contracts respectively while the flexible substrate maintains its original dimensions. This induces a bending motion to develop in the direction opposite the expanding CP layer.

The amount of strain ($\varepsilon = \Delta L/Lo$, where ΔL is the overall change in length and Lo is the original length) that is developed by these CP systems during electrochemical

switching is the main physical properties that controls the amount of actuation produced by these devices. Therefore precise measurement of the strain developed by these systems is an essential part in understanding the physical properties and behavior of these materials and devices. A major factor in understanding these materials is that the reported physical properties for CP systems vary from one study to another depending on the characterization techniques utilized and how the sample was prepared (counter ions, potentials, concentrations, etc.). The smallest change in any of these factors can produce dramatic changes in the overall performance (physically and electrochemically) of these materials. Some common characterization techniques used to study the in-plane strain (sample elongation) of these systems are high-speed video capture, laser displacement, and load/stress sensors (Instron/MTS type). With digital video, the motion of the conducting polymer actuator is digitally recorded and imported to a computer for detailed analysis.[11, 37-39] Accurate measurements of deflection and elongation can be obtained however this involves post processing of the recorded data and results can vary depending on what method was used to calculate the strain. Real time laser displacement meters or extensometers have also been utilized to evaluate the degree of motion induced during electrochemical switching.[26, 40, 41] These systems allow for accurate, real time monitoring of tip displacement of the actuator system. Tip displacement can then be converted to strain at a latter time. Use of force/displacement meters or load cells is commonly used in the study of conducting polymers actuators under linear actuation conditions.[13, 42-48] Out-of-plane strain (sample thickening) for PPy has also been measured using atomic force microscopy and has been shown to be significantly higher than the in-plane strain.[49].

A new method has been developed for the *in situ* measurement of the in-plane strain response developed by cantilever (bi-layer) style CP actuators. With this tecnique it is possible to measure very precisely the average strain developed in the system during electrochemical switching. This method employs the utilization of Au coated electrical resistance strain gages as the working electrode (flexible metalized substrate) during electrochemical switching. Strain gages are widely used in many industries (automotive, aeronautical, naval, construction, etc.) for precision *in situ* spot measurements of induced strains in many materials. These devices are capable of measuring strain with a precision of ± 1 με (με = $1 \bullet 10^{-6}$ ε) and have a strain limit of ± 5% (50,000 με). These devices are also utilized as the sensing components of load cells and therefore are capable of measuring stresses when applied in the right configuration.

Strain gages are typically constructed of a constantan foil grid that is encapsulated in a flexible polyimide substrate, but other gages are available utilizing different grid and backing materials. These devices are very flexible in use as well as installation and are capable of measuring strain under various load conditions and environments, including cyclic strains. This ability to conduct *in situ* cyclic strain measurements with high precision is ideal for applications in EAP actuators and sensors due to the relatively low strain produced and cyclic nature of their motion. This technique allows for detailed real-time analysis of the effects of various actuation, electrochemical polymerization, and actuator construction factors such as CP film thickness, working electrode morphology, counter ion type, driving potential, polymerization potential, and scan rate or switch speed.

Another issue associated with the development and use of conducting polymer based actuators is interlayer adhesion. The interface between the flexible Au coated substrate and stiffer conducting polymer is subjected to large amounts of stress during the redox cycling process. The repeated cyclic swelling and deswelling of the conducting polymer layer eventually initiates crack formation at this interface. The cracks then propagate with continued cycling and eventually caused the complete delamination of the conducting polymer layer and the failure of the device.

A new electrochemically deposited Au (EcAu) layer was developed to improve the interlayer adhesion between the conducting polymer and Au electrode layers. The EcAu treatment greatly increased the base electrode surface area by the growth of Au crystals on the preexisting evaporated Au layer. These crystals range in size from sub micron to 10-20μm which can be controlled by the electrodeposition time or current density. These surface treatments have been shown to greatly improve overall actuator performance and lifetime when applied. Performance variable that are improved include properties such as produced strain, strain rate, frequency response, lifetime, and potentially the stress out put from these systems.

By applying the lessons learned from the previous mentioned work a novel dynamic surface coating was developed by the incorporation of conducting polymers such as polypyrrole into elastomeric material such as PDMSe and thermoplastic elastomers (TPEs). These coatings have potential applications as dynamic non-toxic antifouling coatings for marine and industrial applications. Biofouling is estimated to cost the US Navy alone over $1 billion per year by increasing the hydrodynamic drag of

naval vessels [50, 51] thus resulting in decreased range, speed, and maneuverability of naval vessels and increases the fuel consumption by up to 30-40%.[52, 53]

It has been shown that the settlement and adhesion of fouling marine organisms are effected by surface properties such as surface energy, modulus, and topography. Due to genetic diversity of the various fouling marine species the effects of surface properties on settlement and adhesion changes from species to species. Therefore the use of single surface coating with fixed surface properties can not deter the settlement and growth of all marine organisms. In this approach the dynamic changes in polymer charge, modulus, and topography associated with the redox cycling of conducting polymers is used to develop a dynamic surface coating with variable properties. This should in turn provide a wider range of deterrence to settlement and growth than can be obtained from non-dynamic surfaces.

CHAPTER 2
BACKGROUND

2.1 Electroactive Polymer Actuators

2.1.1 Introduction to EAPs

Electroactive polymers (EAP) are a class of polymers that respond to electrical stimuli by changing their properties and shape. As described by Bar-Cohen [54] these materials can be separated into two classes: electronic and ionic electroactive polymers. The electronic EAPs class of materials is driven by an applied electric field or Coulomb forces. The second class of ionic EAPs is driven by the movement of ions and solvent into and out of the polymeric structure.

The electronic EAPs include ferroelectric polymers, dielectric EAPs, electrostrictive graft elastomers, electrostrictive paper, electroviscoelastic elastomers, electrorheological fluids (ERF), and liquid crystal elastomer (LCE) materials. Ionic EAPs consist of ionic polymer gels (IPG), ionomeric polymer-metal composites (IPMC), conducting polymers (CP), and carbon nanotubes (CNT).

Ferroelectric polymers are typically characterized by the piezoelectric materials. The piezoelectric effect was discovered in 1880 by Pierre and Paul-Jacques Curie. They found that by compressing certain crystals such as quartz along the appropriate axes a voltage is produced. The following year they discovered that the opposite was true as well. If a voltage was applied to these crystals they in turn elongated. Ferroelectricity is the phenomenon of piezoelectricity that is observed in nonconducting crystalline or dielectric materials such as poly(vinylidene fluoride) and its copolymers that exhibit

spontaneous polarization under a given electrical stimuli. Piezoelectric materials are characterized as being semi-crystalline with an inactive amorphous phase. These materials are relatively stiff with a Young's modulus between 1-10 GPA. A relatively high driving potential of about 200 MV/m, which is very close to the materials dielectric breakdown point, is required to activate the piezoelectric materials. Piezoelectric materials are capable of producing strains on the order of 2% (5% strain possible at 150 V/μm with specially modified materials) with very rapid speed and are able to be actuated in air, vacuum, and aqueous environment.

Dielectric EAPs are a class of materials that are characterized as having a low modulus with a high dielectric constant. These polymers are capable of inducing large actuation strains with the application of a given electric field. Actuators are typically constructed by placing/laminating electrodes on opposite sides of the elastomeric dielectric material. Once an electric field is applied the electrodes are electrically attracted to each other applying a compressive force on the elastomeric dielectric material causing it to deform and expand in the transverse direction. The dielectric EAP's also require a large driving potential on the order of 100 V/μm, but are capable of producing strains on the order of 10-300%. As with piezoelectric materials this driving voltage is very close to the breakdown point of the material.

Electrostrictive graft elastomers have a flexible amorphous backbone with grafted polar polymer segments that are capable of forming crystalline domains. The crystalline domains react to the applied electrical field. These materials are capable of producing strains on the order of 4% and are readily processable.

Electroviscoelastic elastomers and electrorheological fluids are both characterized as materials that have dielectric particles dispersed throughout the bulk of the material. The most basic example of an ERF is that of dielectric particles (0.1-100 μm) dispersed in insulating base material such as silicone oil. Under an applied electrical field a dipole moment is induced on the particles which then align and form chains increasing the viscosity of the fluid. These fluids take on the consistency of gels under the applied electrical field. Electrovisoelastic elastomers are similar in structure but utilize a crosslinked insulating phase instead of a fluid phase. Under an applied electrical field (<6 V/μm) the particles interact and increase the shear modulus of the material by as much as 50%. Both of these materials have applications as active dampeners.

Ionic EAPs such as ionic polymer gels (IPG) are driven or actuated by the movement counter ions in the material. IPGs are capable of producing strains on the order of 400% under chemical and electrical stimuli. However they suffer from extremely long actuation times on the order of 20 minutes for a 400% increase in size. If these gels are placed in an electrolyte solution and an electrical stimulus is applied the material will expand and in all directions. However if the gel is used in a dry environment and electrodes are placed on opposite sides of the gel it will form a bending actuator. As one side becomes more alkaline (cathode) and the other more acidic (anode) the migration of ions through the material results in an expansion on the cathodic side and a contraction on the anodic side. Besides having relatively long actuation times the large induced strains tend to damage the applied electrodes after only a couple of cycles.

Ionomeric polymer-metal composite actuators operate on the mobility of cations in the composite structure. Upon the application of a low driving voltage (1-10 V) cations

are transported from one side of the actuator to the other through negatively charged channels in the polymer film. Acid functional fluorocarbon polymers such as Nafion® (sulfonate based) and Flemion® (carboxylate based) are two examples of polymers used in these composites. Electrodes are applied chemically from solution by implanting metal ions (gold, platinum, etc.) throughout the hydrophobic regions of the actuators surface. These materials are characterized as producing relatively large strain at frequencies below 1Hz. As with most ionic EAPs, as the switching frequency increases the produced strain decreases.

Carbon nanotubes (CNT) have recently been identified as a class of ionic EAPs. They are very similar to conducting polymers in that they are nearly completely composed of a conjugated carbon-carbon bond network (excluding defects in the structure). However unlike conducting polymers the actuation produced by carbon nanotubes is due to the change in the carbon-carbon bond length as the material is oxidized and reduced. Upon removal (oxidation) of electrons a net positive charge is formed across the conjugated network. This net positive charge on the carbon nuclei causes the carbon nuclei to repel one another resulting in an increase in the overall length of the CNT. Upon injection of electrons (reduction) into the conjugated carbon network an increase in carbon-carbon bond length is also induced. These devices have been shown to produce strains on the order of 1% (along length of nanotube) and are capable of withstanding temperatures in excess of 1000°C. This allows for the development of new high temperature actuators that far exceed the temperature capabilities of current systems.

The main EAP of interest for this research is the conducting polymer. These materials are comprised of polymers that have a completely conjugated backbone such as polypyrrole, polyanaline, and poly(p-phenylene).

2.1.1 Conducting Polymers

Conducting polymers have recently received a lot of attention due to their ability to generate various responses under electrical or chemical stimuli along with the ability to be electrical conductors. Most notable for this application is volumetric changes that occur during chemical or electrochemical oxidation and reduction. The changes in volume are due to development of charge along the polymer backbone.

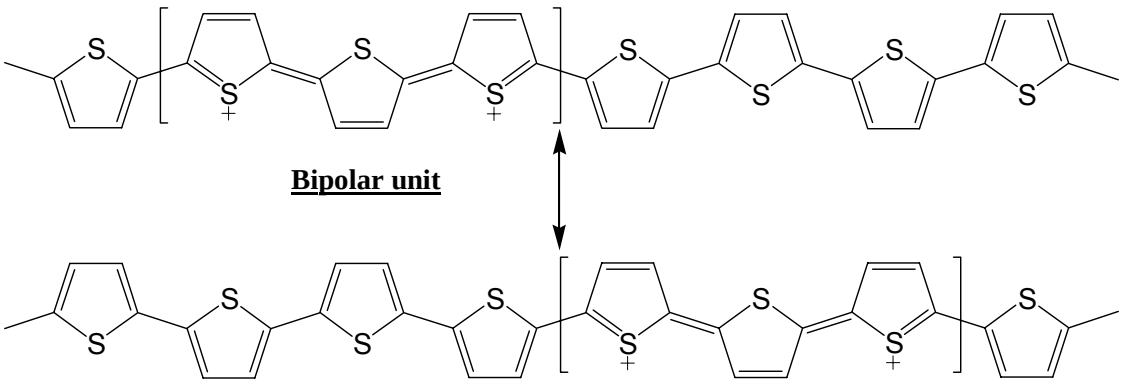

Figure 2.1 Bipolar unit charge migration as depicted for polythiophene.

Conducting polymers are characterized as having a fully conjugated polymer backbone with an extended π-system. This allows for electron and charge delocalization along the polymer backbone as shown in Figure 2.1.[55] The volume change associated with oxidation of conducting polymers in electrolyte solutions (salt solutions, body fluids, etc.) is complex but is mainly induced by the influx of solvent and anions into the conducting polymer matrix to balance the developed increasing charge resulting in a

volume expansion of the material.[11-23] During reduction the material starts to return to its neutral (uncharged) state and anions are expelled from the polymer matrix resulting in a volume contraction. There have been numerous studies examining the developed strain and force associated with the redox swelling and de-swelling of conducting polymers.[23, 29, 33, 56-62]

2.1.2 Conducting Polymer Synthesis

Electrochemical polymerization is generally carried out by the application of an oxidizing potential equal to or greater than the oxidation potential of the monomer.[55, 63] The general mechanism for the polymerization of conducting polymers involves the formation of a radical-cation on the monomer structure. The propagation step involves the subsequent coupling of two oxidized monomers to form a dicationic dimer upon which two hydrogen atoms are expelled and a stable dimer is formed.

Oxidation of the dimer followed by the subsequent coupling with an oxidized monomer, dimer, or oligomer results in the continued propagation of the conjugated polymer chain. The exact mechanism for the oxidative polymerization of conducting polymers is unknown but a series of possible mechanisms is shown by Sadki et al..[64] Figure 2.2 illustrates one of the more accepted polymerization mechanisms for polypyrrole.

The properties of a conducting polymer are dependent upon many variables. The main factors are polymerization/oxidation potential, electrochemical polymerization conditions (potentiostatic, galvanostatic, and variations thereof), dopants (Cl^-, ClO_4^-, etc.), as well as solvents and electrodes that were used during the electropolymerization process.

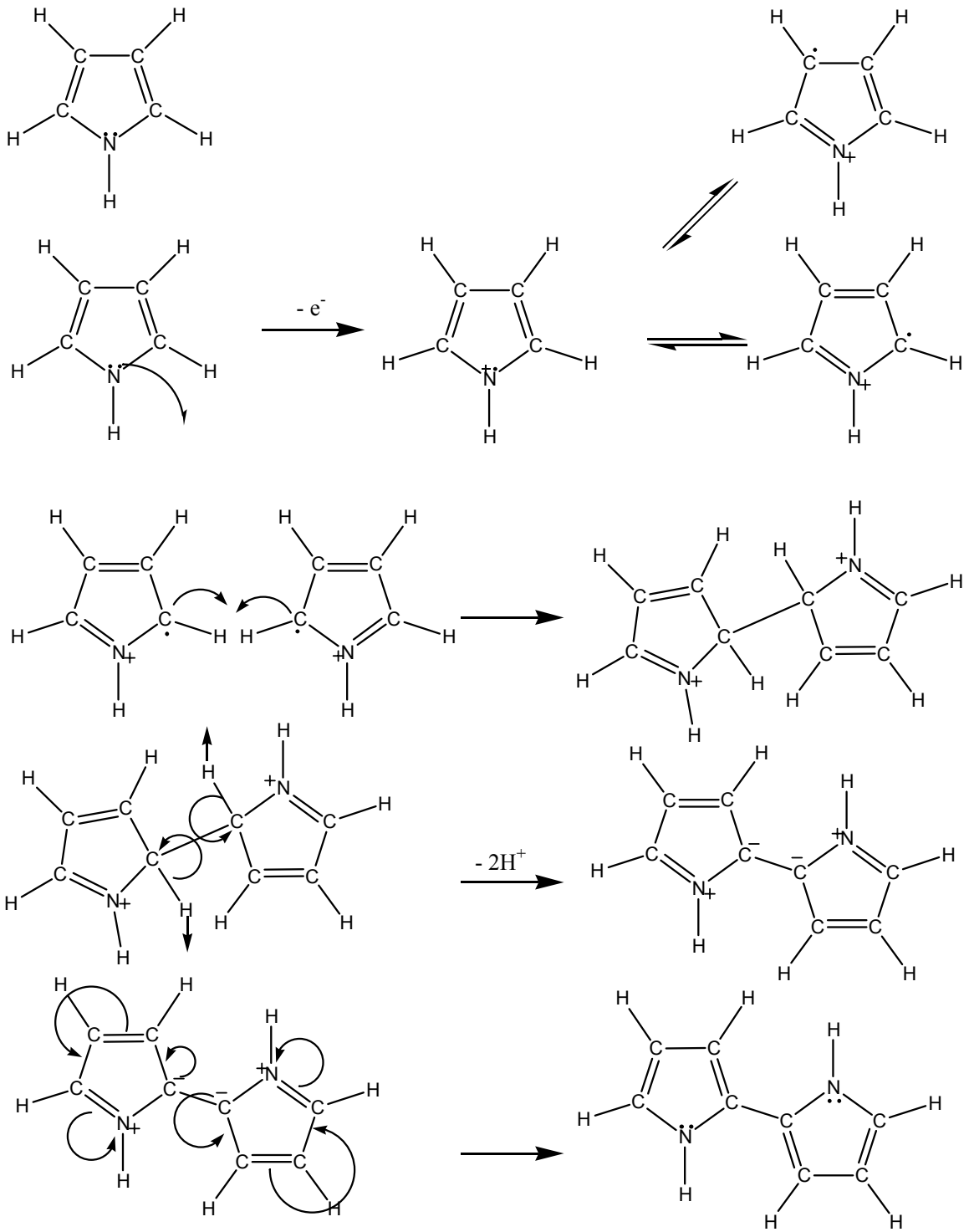

Figure 2.2 Example of one of the possible mechanisms for the oxidative polymerization of polypyrrole. Adapted from Sadki et al..[64]

Conducting polymers can also be formed via chemical polymerization methods such as Lewis acid, ring opening metathesis, and transition metal catalyzed coupling

polymerizations.[55, 63] The most common chemical method utilized to make conducting polymers (due to its simplicity) is the use of Lewis acids such as $FeCl_3$, $FeClO_4$, and ammonium persulfate.

The polymerization mechanism is very similar to that of the electrochemical polymerization; however electron transfer is too oxidizing species instead of an electrode. During polymerization an electron is transferred from the monomer (oxidation) to $Fe(III)Cl_3$ which in turn is reduced to Fe(II) leaving Cl^- (counter ion) to balance the positive charge developed on the monomer during the oxidation process. Chemical polymerization is a bulk polymerization method that is a distinct advantage compared to electrochemical methods. However, chemical synthesis with Lewis acids is not as controllable as the electrochemical methods and is known to produce material with greater defects (disrupted conjugation) densities, thereby decreasing the overall conductivity of the material.

2.1.3 Conducting Polymer Actuators

Conducting polymer actuators are candidates for various actuator applications including robotics, artificial muscles, microvalves, catherter steerers, antivibration systems, and multiple other systems.[1-7, 9, 10, 65, 66]

There are numerous forms of conducting polymer actuators; however all CP actuators are typically based on the idea of a conducting polymer laminated to a flexible conductive substrate. The most basic design involves the deposition of a CP film on one side of a conducting flexible substrate (sputtered Au on polyimide or PET) and utilizes an external counter electrode for operation.

During redox cycling the CP expands (~1-2% in-plane [29, 44, 67]and ~30% out-of-plane[49]) and contracts due to the movement of ions into and out of the CP structure

respectively. This volume change can then be converted into a bending type actuation by deposition of the CP film onto an inactive but flexible substrate such as polyimide or PET. As the CP is oxidized it expands while the flexible substrate maintains its original length. This causes a bending moment in the direction away from the expanding CP layer. This type of actuator is typically referred to as a bilayer actuator and has been studied extensively.[6, 24-36, 45, 65, 66, 68-70]

A modification of the bilayer design is the backbone type design. In the backbone type design a CP layer is deposited on either side of the flexible substrate. One side acts as the anode (working electrode) while the other side acts as the cathode (counter electrode). During redox switching one side expands (anode) while the other side contracts (cathode). When the driving potential is flipped there roles reverse and the bending occurs in the opposite direction. This push-pull technique results in an enhanced bending moment or increased strain performance.

In order for these types of actuators to work they must be run in an electrolyte fluid for ion transport. Another configuration is the shell type design. The shell type actuator is basically a modification of the backbone type design. However in this case, the flexible substrate is replaced with a flexible adhesive polyelectrolyte (source for ion transport) and the whole device is encapsulated to prevent dehydration of the system. These type devices can be actuated in air and do not require an external ion source such as an electrolyte solution.

Figure 2.3 shows some examples of typical CP bending actuators. Linear actuators have also been constructed by wrapping CP fibers around a flexible electrode or vice

versa. In this case the CP fibers expand and contract in length (axial direction) and a linear type actuation is produced.[44, 46, 60, 71]

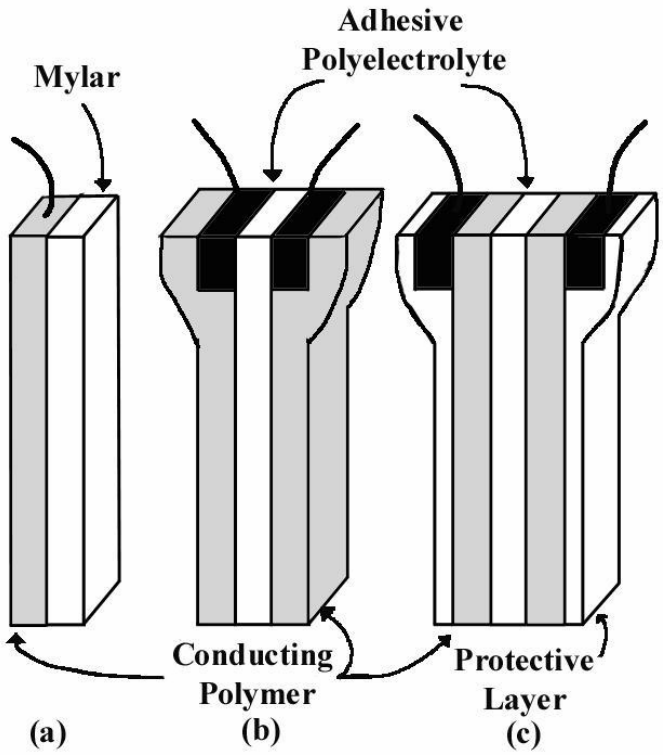

Figure 2.3 Examples of basic bending (cantilever) conducting polymer actuators; A) bilayer actuator, B) backbone type actuator, C) shell type actuator.

These actuating devices are relatively easy to make and due to new lithographic micropatterning techniques they can be fashioned into almost any configuration imaginable making them very versatile. These devices are usually driven with an applied voltage in the range of 1-5 V depending on the polymer used. However there actuation time (strain rate) and performance are very dependent on polymerization and actuation conditions.

One of the main drawbacks to CP actuators is that the whole actuation/swelling process is diffusion limited. Thinner layers have an improved strain rate; however they also produce lower overall stresses and strains than thicker films. Therefore as one increases the CP film thickness to increase the generated stress and strain the overall speed of the system decreases rapidly. These devices are also subject to large amounts of shear at the CP-substrate interface and are prone to interfacial cracking and delamination when cycled for prolonged periods of time.[54, 72, 73]

2.2 Electrical Resistance Strain Gages

The amount of strain developed by the EAP systems during electrochemical switching is one of the main physical properties that controls the amount of actuation produced by the EAP devices. Measurement of the developed strain is an essential part in understanding the physical properties and behavior of these materials and devices. Reported physical properties for EAP's vary from one study to another depending on the characterization technique and sample preparation.

Some common characterization techniques used to study the in-plane strain of these systems are high-speed video capture, laser displacement, and load/stress sensors (Instron/MTS type). With digital video, the motion of the conducting polymer actuator can be recorded and imported to a computer for detailed analysis.[11, 37-39] Accurate measurements of deflection and elongation can be obtained with this technique, but it involves post processing of the data recorded. Another drawback of the video system is as actuation speed increases the speed and resolution of the video capture system also has to increase to record accurate data; therefore the price of the system has to increase as well.

Real time laser displacement meters or laser extensometers have also been used to evaluate the degree of motion induced during redox switching.[26, 40, 41] These systems enable accurate, real time monitoring of tip displacement of the actuator system. Tip displacement can then be converted to strain at a latter time. Force/displacement meters or load cells are also commonly used in the study of conducting polymers actuators under linear actuation conditions.[13, 42-48] Out-of-plane strain has also been measured using atomic force microscopy.[49]

We have developed a new technique for the in-situ measurement of the strain response developed by cantilever (bi-layer) style EAP actuators. This method employs the utilization of gold coated electrical resistance strain gages (Figure 2.4) as the working electrode during electrochemical switching. Strain gages are widely used in many industries (automotive, aeronautical, naval, construction, etc.) for precision in-situ spot measurements of induced strains in many materials. These devices are capable of measuring strain with a precision of ± 1·10-6 ε (=με) and have a strain limit of ± 5% (50,000 με). These devices are also capable of measuring stresses when applied in the right configuration, such as in load cells.

Electrical resistance strain gages are typically constructed of a constantan foil grid that is encapsulated in a flexible polyimide shell, but other gages are available utilizing different grid and backing materials. As the constantan foil grid is deformed (during redox switching) the electrical resistance of the grid changes, this change in electrical resistance is directly related to the strain induced on the grid/system. The strain (ε) is reported as the change in the grid length (ΔL) relative to initial grid length (L_o), $\varepsilon=\Delta L/L_o$.

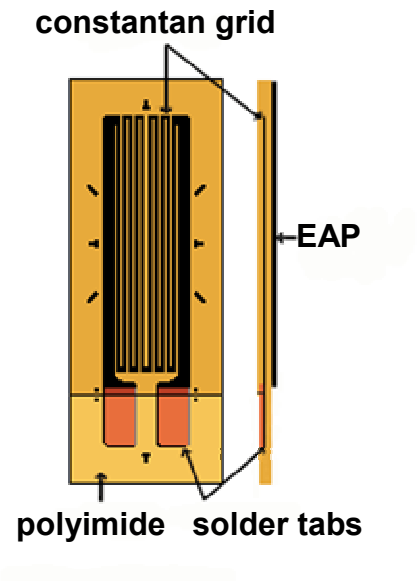

Figure 2.4 Diagram of a polyimide based electrical resistance strain gage and EAP actuator setup. Adapted from www.Vishay.com.

These devices are very flexible in use as well as installation and are capable of measuring strain under various load conditions and environments, including cyclic strains. This ability to measure cyclic strains with high precision is ideal for applications in EAP actuators and sensors due to the relatively low strain produced and cyclic nature of their motion.

2.2.1 Strain Gage Theory

The basic principles allowing for the development of modern electrical resistance strain gages were discovered in 1856 by Lord Kelvin. He observed that under tensile loading of copper and iron wires the resistance of the wires increased for a given amount of strain. He also discovered that the iron wire exhibited a larger change in resistance than copper for a given amount of strain. He finally applied a Wheatstone bridge to accurately measure the resistance changes developed in these systems.

From this it can be said that the resistance of a wire is a function of the strain applied to that wire, different materials produce different resistance changes for a given strain (sensitivity, S_A). Therefore the resistance (R) of a uniform wire can be written as:

$$R = \rho \frac{L}{A} \tag{1.1}$$

where ρ is the specific resistance of the material, L is the wire length, and A is the cross-sectional area of the wire. The sensitivity of the wire can then be describes as the resistance change of the wire per unit of initial resistance divided by the applied strain (ε):

$$S_A = \frac{dR/R_0}{\varepsilon} \tag{1.2}$$

By combining equations 1.1 and 1.2 and rearranging the sensitivity term can be derived to determine the sensitivity as a function of the Poisson's ratio ($\nu, -\varepsilon_x/\varepsilon_z$) of the material and its change in specific resistance due to the applied strain, Eq. 1.3.

$$S_A = 1 + 2\nu + \frac{d\rho/\rho}{\varepsilon} \tag{1.3}$$

Equation 1.3 can be broken down into two parts, the effects of dimensional changes during applied stain (1+2ν) and the effects of specific resistivity (μΩ·m)with applied strain ([dρ/ρ]/ε). Most metallic alloys have an S_A value between 2 to 4 with the value of (1+2ν) varying from 1.4 to 1.7. This gives a range of 0.3 to 2.6 for the change in specific resistance, which can be quite significant compared to the effects of dimensional changes. The change in specific resistance is due to the number of free electrons and the variation of their mobility with the applied strain.

The actual strain is determined from the gage factor (S_g). This factor is experimentally determined for each batch of foil gages by applying a known strain to a series of gages mounted on a specially designed cantilever beam and measuring there resistance response to the applied strain. This is expressed as

$$\frac{\Delta R}{R} = S_g \varepsilon_a \tag{1.4}$$

where ε_a is the applied axial strain.

2.2.2 Strain Gage Materials and Construction

A major factor in choosing an appropriate gage alloy is that the strain sensitivity is linear over a wide range of applied strains. This allows for the use of a single calibration factor and insures that this calibration factor will not change with the various degrees of strain that the gage might see.

Some other factors to consider is that the alloy's S_A should not change significantly as the material enters the plastic regime, the alloy should also have a high specific resistance, thermal stability, and not be significantly affected by temperature change. Temperature compensation can typically be controlled for a particular alloy by the addition of trace impurities and heat treatment. Temperature compensating strain gages reduce the effects of the $\Delta R/R$ induced by temperature changes to less than 10^{-6}/°C.

The most common alloy used is Advanced or Constantan. The Constantan alloy is comprised of 45% nickel and 55% copper and has a specific resistance of 0.49 μΩ·m which allows for the construction of smaller gage patterns with high resistance. Due to electrical circuit requirements the minimum gage resistance needs to be above 100 Ω to prevent overloading of the power supply and to minimize gage self heating (resistive heating). Thus the minimum gage element strand length is on the order of 4" when made

of the finest standard wire. To keep the overall gage length down the sensor elements are typically folded back and forth to form a grid pattern (Figure 2.4). Typical gage resistances are 120 and 350 Ω, but higher resistance gages are available.

Some other common gage alloys are Nichrome V (80 Ni, 20 Cr; $S_A = 2.2$), Isoelastic (36 Ni, 8 Cr, 0.5 Mo, 55.5 Fe; $S_A = 3.6$), Karma (74 Ni, 20 Cr, 3 Al, 3 Fe; $S_A = 2.0$), Armour D (70 Fe, 20 Cr, 10 Al; $S_A = 2.0$), and Alloy 479 (92 Pt, 8 W; $S_A = 4.1$). There are advantages and disadvantages to the use of these alloys when compared to Constantan. For example Isoelastic has a higher sensitivity (3.6) and higher fatigue strength compared to Constantan, allowing for more precise measurements under high cyclic strains exceeding 1500 με. However Isoelastic is extremely sensitive to temperature effects. A change in gage temperature of 1 °C will result in an apparent strain change of 300 – 400 με.

Karma has similar properties compared to Constantan but has a higher fatigue limit and excellent time stability, allowing for extended measurement periods (weeks to months). Karma also has a larger use range (up to 260 °C) than Constantan (up to 204 °C). Karma is difficult to solder, which makes it difficult to attach lead wires. Figure 2.5 shows the thermally induced apparent strain for the Constantan (Advanced), Isoelstic, and Karma alloys.

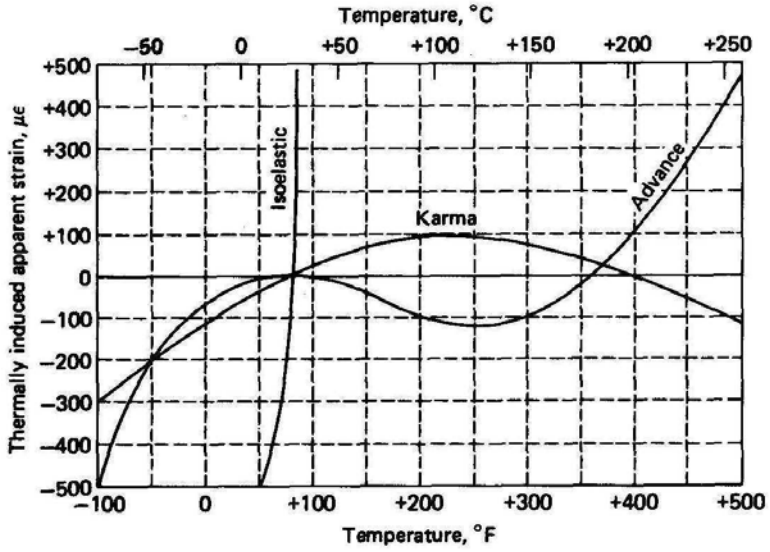

Figure 2.5 Thermally induced apparent strain for Constantan (Advanced), Isoelastic, and Karma alloys. Taken from Dally et al., Figure 6.2.[74]

Current strain gages use metal foil grids produced from a photoetching process. The versatility of this process allows for the production of a variety of gage sizes and shapes. However the patterned metal grid is very thin and fragile. This makes it prone to damage by distortion, wrinkling, and tearing of the grid element.

A solution to this problem is to back the metal film elements with flexible sheets like polyimide (0.025 mm thick). This improves the mechanical stability of the gage and handling. It also improves bonding of the gage to various surfaces including conductive ones (polyimide backing acts as an electrical insulator between the grid element and the substrate). The gage can also be encapsulated with a top layer of polyimide film for use in adverse conditions like under water and in areas prone to high levels of dust/debris. Other substrates like very thin high modulus epoxy (transducer applications) and glass fiber or phenolic reinforced epoxies (high level cyclic strain and high temperature applications) are also used under special conditions. These gages can be affixed to a

variety of surfaces utilizing epoxy cement, cyanoacrylate cement, polyester adhesives, and ceramic cements depending on the testing/application conditions.

2.2.3 Strain Gage Accuracy

Electrical resistance strain gages are considered one of the most accurate methods for determining strain available. These gages are capable of measuring strain with a precision on the order of 1 με. This is due to the ability to produce gages with resistance accuracy of ± 0.3% and with gage factors (calibration constant) certified to ± 0.5%.

However there is some error associated with the transverse sensitivity of the gages. The end loops place a small portion of the gage in the transverse direction. So any transverse strain in the system will increase the resistivety of the gage resulting in a false increase in the measured linear strain. Modern foil gages have enlarged end loops which decrease the sensitivity of the gage to transverse strain in the system. By enlarging the end loops the overall resistance of these segments is very low and therefore any change in the resistance due to the transverse strain will be negligible. The only time error due to transverse strain is not a factor is where the transverse sensitivity factor (K_t) of the gage is zero or when the applied stress field is uniaxial.

The overall change in resistance for a strain gage is a result of the applied strains (axial, transverse, and shear) and the sensitivity of the gage to each of these strains. This is expressed as:

$$\frac{\Delta R}{R} = S_a \varepsilon_a + S_t \varepsilon_t + S_s \gamma_{at} \tag{1.5}$$

where S_a, S_t and S_s are the sensitivities of the gage to the applied axial, transverse and shearing strains and ε_a, ε_t and ε_{at} are the applied axial, transverse, and shearing strains.

The sensitivity of the gage to the shearing stress is negligible and is usually ignored. Thus reducing equation 1.5 down to

$$\frac{\Delta R}{R} = S_a(\varepsilon_a + K_t\varepsilon_t) \tag{1.6}$$

where $K_t = S_t/S_a$ (transverse sensitivity factor; %).

By assuming the effects of K_t and ε_t are negligible; the gage calibration factor or gage factor can be determined. The gage factor as a function of the applied axial strain is expressed as

$$S_g = \frac{\Delta R}{R}\Big/\varepsilon_a \tag{1.7}$$

where S_g is the gage factor. This factor is used to convert the resistance changes observed in the gage to the applied strain seen by the gage.

The amount of error that occurs if only the gage factor is considered in determining the strain is expressed as

$$\xi = \frac{K_t(\varepsilon_t/\varepsilon_a + \nu_o)}{1-\nu_o K_t}\cdot 100 \tag{1.8}$$

where ν_o is the Poisson's ratio of the material being tested. If you assume applied axial and transverse strain are the same ($\varepsilon_t/\varepsilon_a = 1$, usually $\varepsilon_a > \varepsilon_t \therefore \varepsilon_t/\varepsilon_a < 1$), a Poisson's ratio of 0.285 (Poisson's ratio for calibration beam) and a K_t of -0.006 (-0.6%, K_t for strain gages utilized during dissertation work) the error associated with transverse strain is –0.77%.

The strain gages utilized for this work were directly bonded to the conducting polymer being studied (w/ evaporated gold interface). So the Poisson's ratio and the applied strain field are both factors of the conducting polymer being studied. During

electrochemical growth of conducting polymers there is no axial or transverse orientation (to the gage element) of the polymer so during redox cycling the induced strain field would be uniform in both the axial and transverse direction (to grid element). By assuming this both the $\varepsilon_t/\varepsilon_a$ and ν_o terms become one (applied strain field and expansion of CP is biaxial). Assuming this the calculated error associated with the transverse strain would be -1.19%.

2.3 Anti-Fouling/Foul-Release Coatings

Biofouling is the result of marine organisms settling, attaching, and growing on submerged marine surfaces. The biofouling[75] process is initiated within minutes of a surface being submerged in a marine environment by the absorption of dissolved organic materials (conditioning film). Once this conditioning film is deposited, bacteria (unicellular algae) will colonize the surface within hours of submersion. The resulting biofilm produced from the colonization of the bacteria is referred to as microfouling or slime and can reach thicknesses on the order of 500 μm. Macrofouling species may eventually colonize on top of the microfouling or slime layer.

Soft and hard fouling are two different classifications of macrofouling. Soft fouling consists of algae and invertebrates such as anemones, hydroids, soft corals, sponges, and tunicates. Hard fouling consists of invertebrate species like barnacles, muscles, and tubeworms.[50] This results in a multilayer structure with each layer having its own unique properties and adhesion mechanisms.

To further complicate things, the species makeup for each layer is dependent on the geographical location and the makeup of the underlying structure. This issue is further compounded due to the fact that there are 12 well-defined geographical zones in the

world's oceans with varying salinity, clarity, temperature, amount and type of micronutrients, and number and type of fouling organisms.[52]

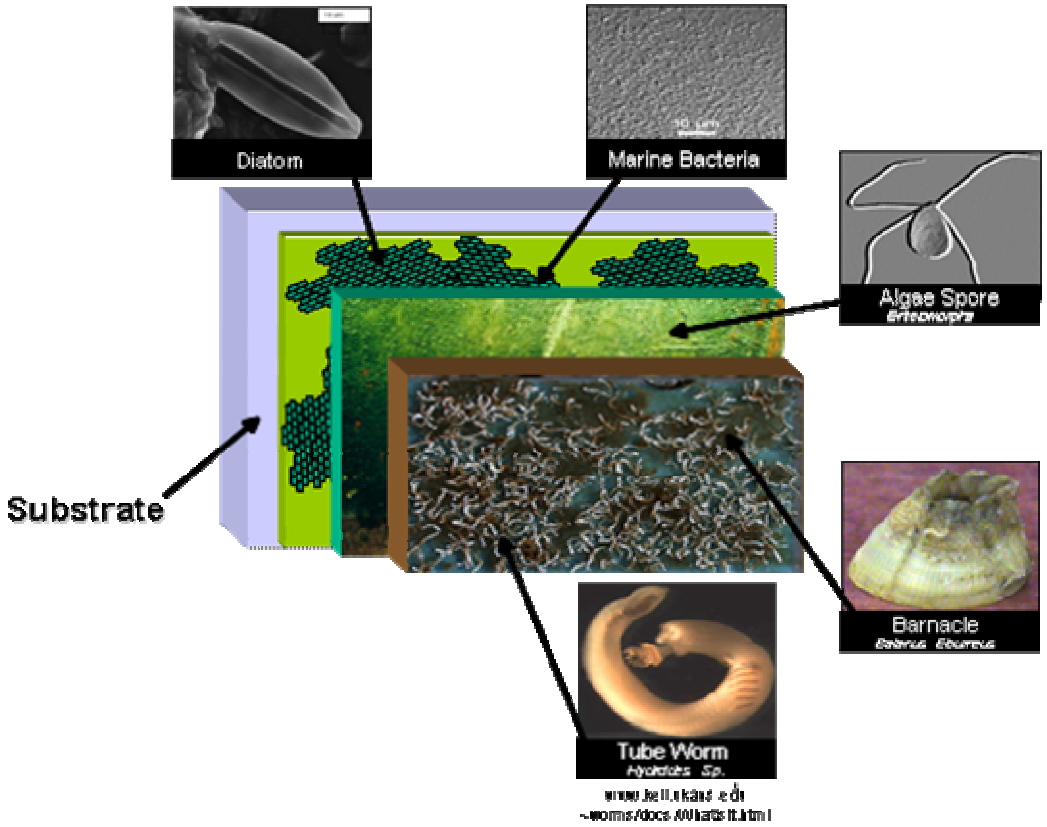

Figure 2.6 Diagram showing the different species breakdown and layering of biofoul film formation.

Biofouling is estimated to cost the US Navy alone over $1 billion per year by increasing the hydrodynamic drag of naval vessels.[50, 51] This in turn decreases range, speed, and maneuverability of naval vessels and increases the fuel consumption by up to 30-40%.[52, 53]

Anti-fouling and foul-release coatings are two main approaches used for combating biofilm formation. Anti-fouling coatings prevent or deter the settling of biofouling organisms on a surface by the use of leached biocides. Foul-release coatings control biofilm formation by modifying surface properties in such a way as to prevent the

formation of strong adherent bond between the biofoulant and the surface. This reduces the work required to remove them.

The first method is typically accomplished through the use of anti-fouling coatings containing heavy metal biocides, such as cuprous oxide or tributyltin (chloride and oxide), which are either tethered to the coated surface or are released from the surface into the surrounding environment. Use of these coatings has caused problems in the marine ecosystem, especially in shallow bays and harbors where the biocides can accumulate. As such the use of tributyltin has been banned in many parts of the world and its use will be completely banned worldwide on all naval vessels by the International Maritime Organization in January 2008.[50, 51]

The second concept for controlling biofouling is the use of foul-release coatings. Foul-release coatings control biofilm formation through the use of engineered surfaces with controlled surface properties such as surface energy, modulus, and roughness to minimize biofoulant adhesion.[50, 52, 76-79] More recently the use of nano and micro-scale topographies has come into interest.[51, 80-82]

The interest in the use of surfaces with controlled/tailored surface energies for foul-release coating is due to the fact that wetting of the surface with biological glue (or any other fluid) is controlled by the surface tension/energy. By controlling the surface energy of a material the wettability of it's surface and therefore bond formation can be controlled.[52] Work done by Pasmore and Bowman [76] has shown that the percent removal of biofilms, Pseudomonas aeruginosa under given conditions, increases with a decreased in contact angle (increase in surface energy) and decreases with an increase in surface roughness. Similar results were produced on smooth glass, electropolished 316 stainless

steel, and PTFE samples which indicated a biofilm accumulation ~35% lower than for rougher surfaces.[77]

Another factor of interest is the modulus of the material being used. Gray and Loeb [78] have shown that the degree of settlement of various organisms decreased with a decrease in modulus of crosslinked PDMS samples. From this it can be said that the force required to remove an adhered biofilm is a factor of the settled surfaces surface energy and surface modulus, this is in agreement with the Kendal theory [52]:

$$P_C = \sqrt{4\pi E w_a a^3 /(1-\nu^2)} \tag{1.9}$$

$$\sigma_C = \sqrt{4E w_a / \pi a(1-\nu^2)} \tag{1.10}$$

which gives the critical pull-off force (P_C) and critical crack propagation stress (σ_C) as a function of elastic modulus (E) and the work of adhesion (w_a; $w_a = 2\cdot\gamma$). The work of adhesion is related to the surface energy by the interfacial tension (γ), where "a" is the contact radius and ν is the Poisson's ratio.

Another current area of interest is the use of micro-topographies in the control of biofoulant spore settlement and adhesion.[51, 80-82] By manipulating surface topography, through the use of micropatterning, the overall surface energy and therefore hydrophilicity or hydrophobicity of a coating material can be manipulated. Many studies have shown the importance of surface roughness on the settling of spores. However the importance of surface feature size and shape has begun to be studied only recently. Work done by Verran and Boyde (2001) has shown that macro-scale surface features (>10 μm) are relatively unimportant in cell settlement since cell dimensions are much smaller than the surface features. It has been suggested that the shape, scale, and periodicity of surface features may influence the settlement of barnacle larvae (Hills & Thomason,

1998; Lapointe & Bourget, 1999; Berntsson et al.,2000), as reviewed by Callow et al..[80] Work by Brennan and coworkers [80, 81] has shown that the settlement of spores can be influenced by the use of ridge and pillar micro-topographies on PDMSe surfaces with feature sizes and spacings on the order of 1.5-20 μm. In this study the minimum spacing between features was 5μm which was similar in size to the diameter of the cells being studied, therefore the cells settled into the valleys between the features. From this work it was determined that the pattern spacing should be reduced to 2-3 μm to increase the work required to settle on the patterned surface. Recently a new biomimiticly engineerd surface topography (B.E.S.T. or sharklet) utilizing 2-3 μm feature sizes has been developed. This pattern has been shown to reduce the settlement of Ulva spore (green algae) by ~85%.

Similar results were found for flocked surfaces by Kim et al..[51] They found that by flocking a smooth PVC surface with a heterogeneous mixture of nylon fibers (90% 1.8 denier and 1.27 mm long; 10% 3.0 denier and 2.54 mm long) that they could influence the settlement and growth of different marine species. However they found that the flocked surface inhibited the growth of some species but had no effect or even enhanced the growth of other species.

From this it can be said that surface features play an important role in the settlement and adhesion of biofouling organisms to a particular surface. However, it has been shown that different factors influence different species in different ways, i.e., what inhibits the growth of one species might enhance the growth of another. This makes it unlikely that a single coating with a fixed set of surface parameters will be effective in preventing biofilm formation for all species. Therefore a surface coating with

dynamically variable surface properties (surface energy, modulus, and roughness) would be more effective in the prevention or retardation of biofilm formation.

2.4 Electrowetting

Electrowetting is the process of changing the surface wetability (surface tension) of a metal electrode by rearrangement and or formation of an electronic double layer (EDL) at the electrode's surface due to an applied electrical potential. The electrowetting (EW) process has been extensively studied for pure metal electrodes with electrolyte solutions.[83-85] EW devices have been limited to uses in polar media due to the nature of the formed EDL.

The EDL is formed from the transfer of electrons from the electrode to redox-active species in the fluid medium. The electrical stability of the EDL limits the use of these devices to low voltages, as low as ~1 V.[86, 87] However the induced change in contact angle ($\Delta\theta$) is proportional to the amount of charge developed at the electrode surface thereby limiting the overall $\Delta\theta$ that can be produced. Two major applications for this technology are in micro-fluidic devices and MEMS type applications. A schematic of an EW capillary pump is depicted in Figure 2.7.[87]

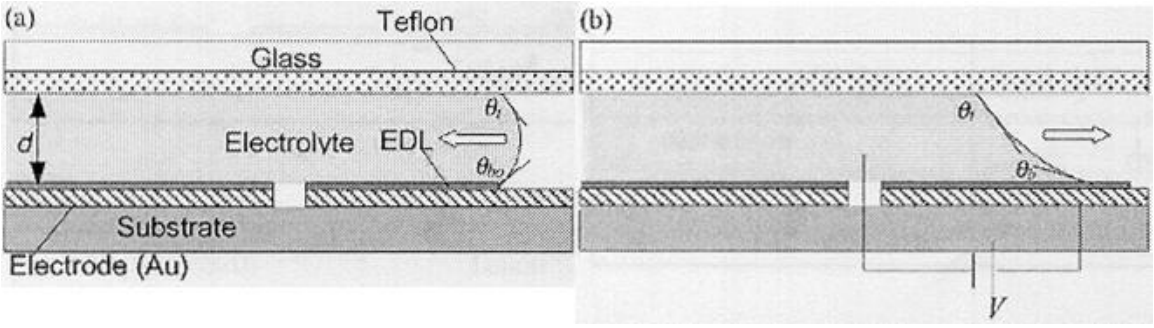

Figure 2.7 Design of electrowetting device: (a) no applied electrical potential (hydrophobic surface); (b) with applied electrical potential (hydrophilic surface). Fluid is pumped by continuously cycling the applied electrical potential.[87]

Recently, it has been shown that the application of a thin dielectric layer (PTFE, SiO_2, etc.) between the electrode and fluid can enhance this EW behavior. This allows the pumping/wetting of virtually any fluid medium. This behavior is referred to as electrowetting-on-dielectric (EWOD). However a higher electrical potential is required to drive these systems.[86-89] Typical operating voltages for EWOD devices typically exceed 100-200 V. Yet, more recently, Moon and coworkers produced EWOD devices operating as low as 15V.[86]

EWOD devices also are resistant to corrosion due to the protection offered to the electrode by the dielectric layer and can produce larger $\Delta\theta$ when a hydrophobic dielectric (higher initial contact angle, lower initial surface energy) is used (i.e., PTFE) when compared to EW based devices. The dielectric layer blocks electron transfer from the electrode to the fluid medium; however it sustains the high electric field at the interface due to charge redistribution when a potential is applied.

The relationship between the applied electrical potential (V) and the resultant surface tension (γ) are expressed in Lippman's equation:

$$\gamma = \gamma_0 - \frac{1}{2} cV^2 \tag{1.11}$$

which when combined with the Young's equation:

$$\gamma_{SL} = \gamma_{SG} - \gamma_{LG} \cos\theta \tag{1.12}$$

can yield the resultant contact angle (θ) according to Lippman-Young's equation:

$$\cos\theta = \cos\theta_0 + \frac{1}{\gamma_{LG}} \frac{1}{2} cV^2 \tag{1.13}$$

Where γ_0 and θ_0 are the surface tension and contact angle of the solid-liquid interface when there is no electrical field across the interface layer (surface tension and

contact angle at point of zero charge), γ_{SL}, γ_{SG}, and γ_{LG} are the solid-liquid, solid-gas, and liquid-gas surface tensions, V is the applied electrical potential, and c is the specific capacitance of the dielectric layer ($c = \varepsilon_0 \varepsilon / t$; F/cm^2) where ε_0 is the permittivity of a vacuum, ε is the dielectric constant of the dielectric layer, and t is the dielectric layer thickness.

The Lippman-Young's equation predicts that the overall $\Delta\theta$ can be increased by increasing the applied electrical potential and the dielectric constant of the material being used and by decreasing the dielectric layer thickness. Therefore the thinner the dielectric layer used the lower the electrical potential required to induce a given $\Delta\theta$.

However the dielectric breakdown voltage is proportional to the thickness of the dielectric layer. Therefore at a certain dielectric thickness the required electrical potential to induce a given $\Delta\theta$ will exceed the dielectric breakdown potential. Thus, there is a thickness limit on the dielectric layer which is dependent on the dielectric material used. An example of this was shown by Moon et al..[86]

Moon and coworkers calculated that the voltage required to induce a 40° $\Delta\theta$ for a Teflon® AF based EWOD device (ε = 2.0 and $E_{breakdown}$ = 2x10^{16} V/cm) as a function of dielectric layer thickness. For dielectric layer thicknesses of less than 0.2 μm the voltage required to induce a 40° change in θ was higher than the dielectric breakdown potential of the Teflon® AF (see Figure 2.8).

In order to prevent the dielectric breakdown of thin film dielectrics Moon and coworkers deposited a 700Å layer of barium strontium titanate between the platinum electrode and the 200Å Teflon® AF outer layer. This resulted in a EWOD device

capable of operating at electrical potentials as low as 15V and generating a $\Delta\theta$ on the order of 40° (from 120°→80°).[86]

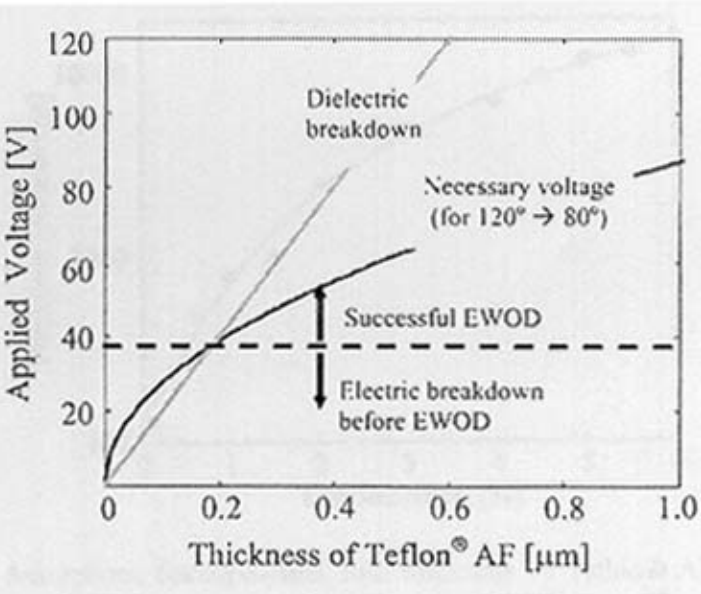

Figure 2.8 Voltage required to induce a $\Delta\theta$ of 40° (from 120°→80°) versus dielectric layer thickness for Teflon® AF based EWOD device, with $\varepsilon = 2.0$ and $E_{breakdown} = 2x10^{16}$ V/cm.[86]

2.5 Dynamic Surfaces

The volume expansion and contraction experienced by conducing polymers during electrochemical switching between there oxidized and reduced states is also associated with other physical property changes in the system. During the oxidation process the developed positive charge induced along the CP backbone will also result in a change in the surface charge or energy of the system. The influx of counter ions and associated solvent that drives the volume expansion during oxidation also results in a drop in the modulus of these materials. By incorporating CPs into other more flexible and durable base materials (such as elastomers, thermoplastic elastomers, thermoplastics, etc.) the dynamic properties of the CP can be utilized to produce coatings with dynamic surface properties.

Changes in surface energy have been studied under both chemical [90, 91] and electrochemically [92, 93] induced redox systems for PPy, polyaniline (PANI), poly(3-(pyrrolyl)-alkanoic acid), poly(3-octylthiophene) (P3OT), and poly(3-hexylthiophene) (P3HT). The results of these studies demonstrate that oxidizing the conducting polymer decreases the Sessile drop contact angle (increase surface energy) of water.

An example of this behavior was reported by Gregory et al..[91] They found that by chemically oxidizing and reducing PANI, PPy, and P3HT contact angle changes of 36.5°, 16.8°, and 31.5° could be induced. However Bartlett et al. [94] stated that by using functionalized thiophenes, i.e., alkanoic acids such as carboxylic, butanoic, and pentanoic, a higher contact angle ($\Delta\theta$= ~ 8°, 20°, 30° respectively) is measured for the oxidized state. This is attributed to the protonation of the alkanoic acids (pKa = 6.5, 5.8, 6.1 respectively) at a low pH (oxidizing environment).

By utilizing various conducting polymer systems it was hypothesized that it should be possible to tailor particular systems to produce desired surface properties changes, compatibilities, and redox switching speeds. The relative differences in oxidation potential of various conducting polymers are shown in Figure 2.9.

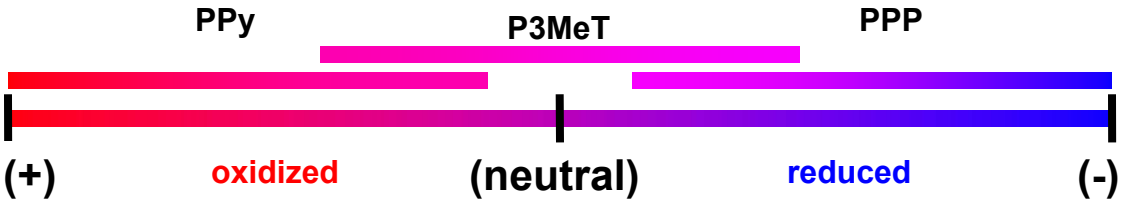

Figure 2.9 Relative surface charge of different conducting polymers.

2.5.1 Polypyrrole

To date a majority of the literature work conducted on conducting polymers has been on polypyrrole (PPy) (Figure 2.11 A). PPy is characterized by high stability in its

oxidized form due to its oxidation potential ~ -0.2 V which is close to the O_2 reduction potential at ~ -0.2-0.3 V.[95] Therefore neutral PPy will be oxidized by O_2 to form its oxidized conducting form when exposed to air. PPy has gained a lot of exposure recently in the field of conducting polymer based artificial muscles due to its ability to produce a large volume expansion (~1-3% longitudinally and ~35% in thickness on a bound surface[49]) when redox cycled between the oxidized and reduced state. This large volume change induced during redox cycling will be beneficial in the modification of the PPy-PDMS surface modulus. PPy can be synthesized chemically or electrochemically in various media. The chemical polymerization can be facilitated in the presence of Lewis Acids such as $FeCl_3$ or ammonium persulfate along with codopants such as $NaClO_4$.[55, 96-101]

2.5.2 Poly(3-methylthiophene)

Polythiophene and its derivatives have received a lot of attention lately due to their stability in the oxidized as well as reduced states.[5, 39, 55, 90, 91, 95, 96, 102-108] They also possess many highly desirable electrical, optical, and redox properties. The thiophene monomer can easily be derivatized using a number of chemistries. It has been shown that by changing the substituents on the thiophene ring the oxidation potential of the resulting monomer and polymer can be varied between 1.20-2.00 V and 0.70-1.45 V respectively.[96] Poly(3-methylthiophene) (PMeT) (Figure 2.11 B) in particular has an oxidation potential of ~0.8 V and reaches a fully reduced state at ~0.2 V vs Ag/AgCl. These values lie well above the O_2 reduction potential and above the H_2O oxidation potentials allowing for good stability in both forms. This can be seen vs. SCE (not Ag/AgCl) along with the oxidation potentials for PPy and PPP in Figure 2.10.[95] PMeT can also be polymerized in a similar fashion as PPy.

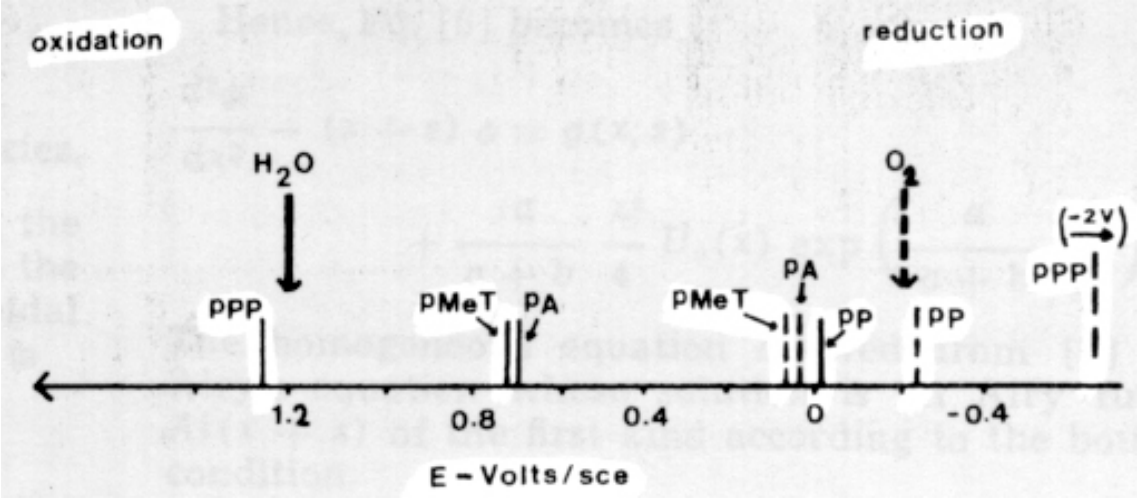

Figure 2.10 Oxidation (-) and reduction (--) potentials of poly pyrrole (PPy), polyaniline (PA), poly(3-methylthiophene (PMeT), and poly(p-phenylene) (PPP).[95]

2.5.3 Poly(p-phenylene)

One of the disadvantages of PPy is its high stability in its oxidized (charged) form. This hinders the return of the PPy-PDMSe surface back to its original (unchargred) surface energy. Poly(p-phenylene) (PPP) (Figure 2.11 C) on the other hand exhibits exceptional stability in its neutral form. The oxidation potential of PPP is around +1.2 V which is very close to the oxidation potential of water, therefore water will reduce the oxidized form of PPP to its more stable neutral form.[95] PPP is also characterized as being highly crystalline, difficult to process, insoluble, and exhibiting high resistance to oxidation, radiation, and thermal degradation.[55, 96] PPP can be synthesized from benzene in the presence of Lewis acid such as $FeCl_3$ (~70 ºC) and $AlCl_3$ (~37 ºC) along with an additional oxidizing agent (codapoant).[55, 96, 109-114]

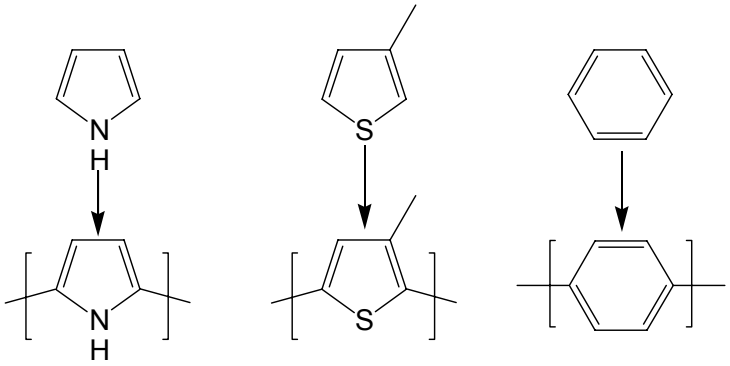

Figure 2.11 Monomer and polymer structures for A) polypyrrole, B) poly(3-methylthiophene), and C) poly(p-phenylene).

CHAPTER 3
INITIAL *IN SITU* EVALUATION OF CP'S VIA STRAIN GAGE TECHNIQUE

3.1 Introduction

Strain sensitive actuators were developed utilizing commercially available strain gage technology. This is the first time sensors of this type have been used in the *in situ* evaluation of conducting polymer based actuators.[56] Strain sensitive actuators were used to evaluate the *in situ* strain response of PPy/TOS based actuator films during redox cycling using cyclic voltammetry and square-wave potential stepping. The strain responses of PEDOP and PBEDOT-Cz were also evaluated and compared to PPy/TOS. It is believed that PPy's high strain response is due to its ability to crosslink through the 3, 4 positions on the monomer structure.[64, 104] By placing substituents in these positions the degree of crosslinking can be controlled. PEDOP was chosen as a candidate for study due to its blocked 3, 4 positions, which should produce a linear polymer structure with a minimal degree of crosslinking. PBEDOT-Cz has been shown to undergo a non-reversible oxidative reaction at about 1.15 V, which has been attributed to a possible crosslinking reaction.[107] This ability to potentially crosslink was the reason that PBEDOT-Cz was chosen for comparison.

3.2 Materials and Methods

3.2.1 Materials

Pyrrole was purchased from Sigma-Aldrich and was filtered through neutral alumina (Brockman activity 1; Fisher Scientific) until colorless before use to remove any impurities. 3,6-bis(2-(3,4-ethylenedioxy)thienyl)-N-carbazole (BEDOT-Cz) and 3,4-

ethylenedioxypyrrole (EDOP) used in this study were synthesized by the Reynolds Research group (University of Florida Chemistry Department).[107, 115, 116] Acetonitrile (ACN), lithium perchlorate ($LiClO_4$), sodium perchlorate ($NaClO_4$), p-toluenesulfonic acid Na salt (NaTOS), and tetrabutylammonium were purchased from Sigma-Aldrich and used as received. Sodium nitrate ($NaNO_3$) was purchased from Mallinckrodt Chemicals and sodium sulfite (Na_2SO_3) was purchased from Fisher Scientific, both were used as received. Deionized water (18 MΩ, Millipore system) was used in all experiments and the solutions were deoxygenated by bubbling argon prior to electropolymerization and redox switching of the CP.

3.2.2 Strain Gages

Electrical resistance strain gages (CEA-06-500UW-120 and EA-06-20BW-120; Figure 2.4) were purchased from Vishay Measurements Group Inc. All strain gages were cleaned prior to Au deposition and use with ethanol to remove any surface oils and debris. These gages were treated with various Au treatments and then coated with the appropriate CP to form strain sensitive actuators. A Vishay Measurements Group Inc. P3500 strain indicator was used to measure the resistance changes in the strain gage and thereby produce the strain measurement. EvAu coated strain gages (no CP) that were exposed to electrolyte solutions and potentiostatically cycled gave a zero strain reading. This was done to verify that the strain gages were unaffected by the potential cycling during redox switching and that all strain measurements acquired were the result of the CP's and not the strain gage.

3.2.3 Conducting Polymer Synthesis

In the initial study EvAu was vapor deposited thermally onto strain gages to a thickness of ca. 700 Å (measured by quartz microbalance). These gages were used as the

working electrode during electropolymerization and redox switching of the CP's. All electrochemical work was carried out utilizing an EG&G Princeton Applied Research 273A potentiostat/galvanostat utilizing the CorrWare software package, a platinum foil counter electrode and an Ag/AgCl (BAS MF2052) reference electrode at room temperature. All potentials given are relative to this reference electrode. Conducting Cu tape (1181, 3M) was utilized to make electrical connections between the EvAu layer and the working electrode lead from the potentiostat. Polypyrrole (PPy) was synthesized potentiostatically (E = 0.65 V, t = 500 s) from an aqueous solution of 0.2 M pyrrole, 0.1 M p-toluenesulfonic acid Na salt (NaTOS), and 1.0 M lithium perchlorate. This resulted in a film thickness of ca. 9.6 μm measured by a Sloan Dektak 3030 profilometer. PEDOP was synthesized potentiostatically (E = 0.6 V, t = 10,000 s) from an aqueous solution of 0.01 M 3,4-ethylenedioxypyrrole, 0.1 M p-toluenesulfonic acid Na salt, and 1.0 M lithium perchlorate. The resulting film thickness was 10.6 μm. PBEDOT-Cz was synthesized potentiostatically (E = 0.8 V, t = 3000 s) from an aqueous solution of 0.01 M Bis-EDOT-Cz, 0.1 M acetonitrile, and 1.0 M tetrabutylammonium. The corresponding film thickness of PBEDOT-Cz was 9.9 μm.

3.3 Polypyrrole (PPy/TOS) Results

3.3.1 Determination of Electropolymerization Conditions for PPy/TOS

In order to obtain the optimal strain response from the strain sensitive actuators the PPy/TOS electropolymerization conditions were first evaluated on a gold-button working electrode (MF-2014 Au electrode (AUE), Bioanalytical Systems, Inc.). PPy/TOS films were prepared by cyclic voltammetry (–0.8 V to 1.0 V) in an aqueous solution of 0.2 M pyrrole, 0.1 M NaTOS and 1.0 M $LiClO_4$. The pyrrole oxidation peak was observed at 0.65 V, which corresponds to the optimal electropolymerization voltage for these

electrochemical conditions. The adhesion of the PPy/TOS film to the gold-button working electrode was tested using a tape (810, 3M) peel off method. PPy/TOS films electropolymerized at a constant potential of 0.65 V produced the most adherent films, while films polymerized at voltages exceeding 0.8 V exhibited very poor adhesion to the electrode.

3.3.2 PPy/TOS Cyclic Voltammetry and Strain Response

Utilizing these electropolymerization conditions (E = 0.65 V) a PPy/TOS film was deposited on a Au coated strain gage (CEA-06-500UW-120) for 500 seconds and resulted in a film thickness of 9.6 μm (Sloan Dektak 3030). PPy/TOS films have been shown to produce films of high conductivity (150 S/cm) and tensile strength (73.4 MPa).[61, 117] A representative SEM micrograph of PPy/TOS is shown in Figure 3.1.

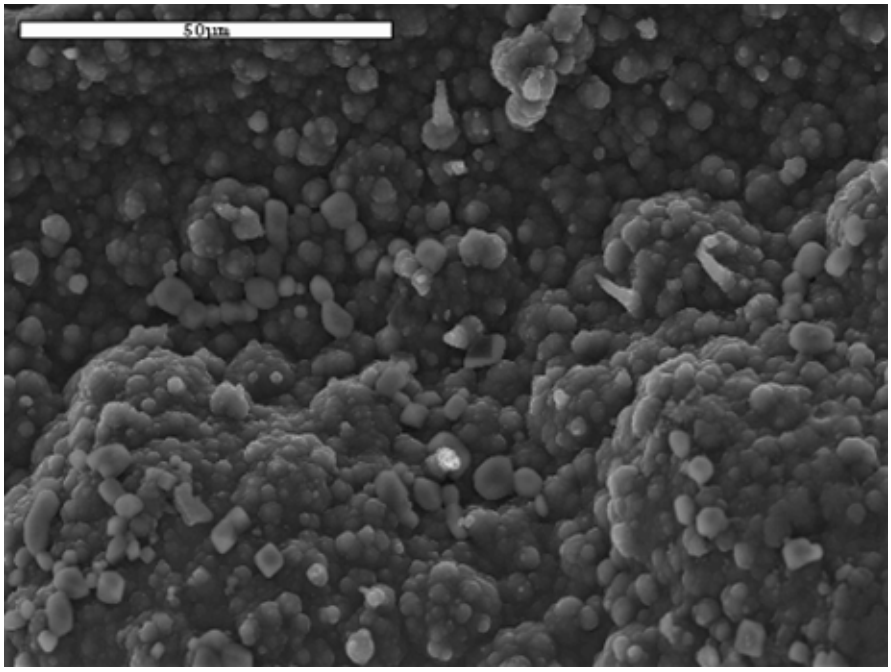

Figure 3.1 SEM micrograph of surface morphology of PPy/TOS film prepared in 1.0 M $LiClO_4$ at a potential of 0.65 V. SEM image taken of an uncoated sample at 1000X and 15 KeV.

PPy/TOS samples were scanned from -0.8 V to 0.4 V at 10 mV/s in 1.0 M aqueous $LiClO_4$. The resulting strain response measured by the strain sensitive actuator followed

the cyclic voltammetry data (Figure 3.2). These results were obtained during the 5th potential cycle to attain reproducible cyclic voltammetry and strain data. The strain response was collected manually at 0.2 V intervals while the cyclic voltammogram was acquired directly from the potentiostat. The PPy/TOS cyclic voltammetry (Figure 3.2a), on the strain gage, is relatively broad due to the high surface area of the working electrode (ca. 100 mm^2) and large film thickness (9.6 μm). The PPy reduction peak is centered at -0.2 V. The overall change in strain (Δε) for the PPy/TOS systems was on the order of 236 με.

Upon further examination (Figure 3.2b) it is evident that a small initial decrease in the strain response (contraction) is present, starting at –0.8 V, and is followed by a much larger increases (expansion) in strain as the oxidation potential is reached. This is similar to results previously published in literature [37] and is evident in all samples of PPy/TOS, PEDOP, and PBEDOT-Cz under cyclic voltammetry. It is also evident that there is hysteresis in the strain response. It is believed to be due to ion and solvent concentrations, in the CP, never reaching equilibrium under these scan conditions (10 mV/s).[44] This also causes the strain response to initially continue to rise on the reverse scan, resulting in the maximum strain response to be observed at 0.2 V instead of 0.4 V. Similar results have been obtained during electrochemical quartz crystal microbalance (EQCM) experiments conducted with PPy. These results are attributed to the diffusion of the dopant ions and the corresponding solvent molecules into and out of the polymer structure during redox cycling.

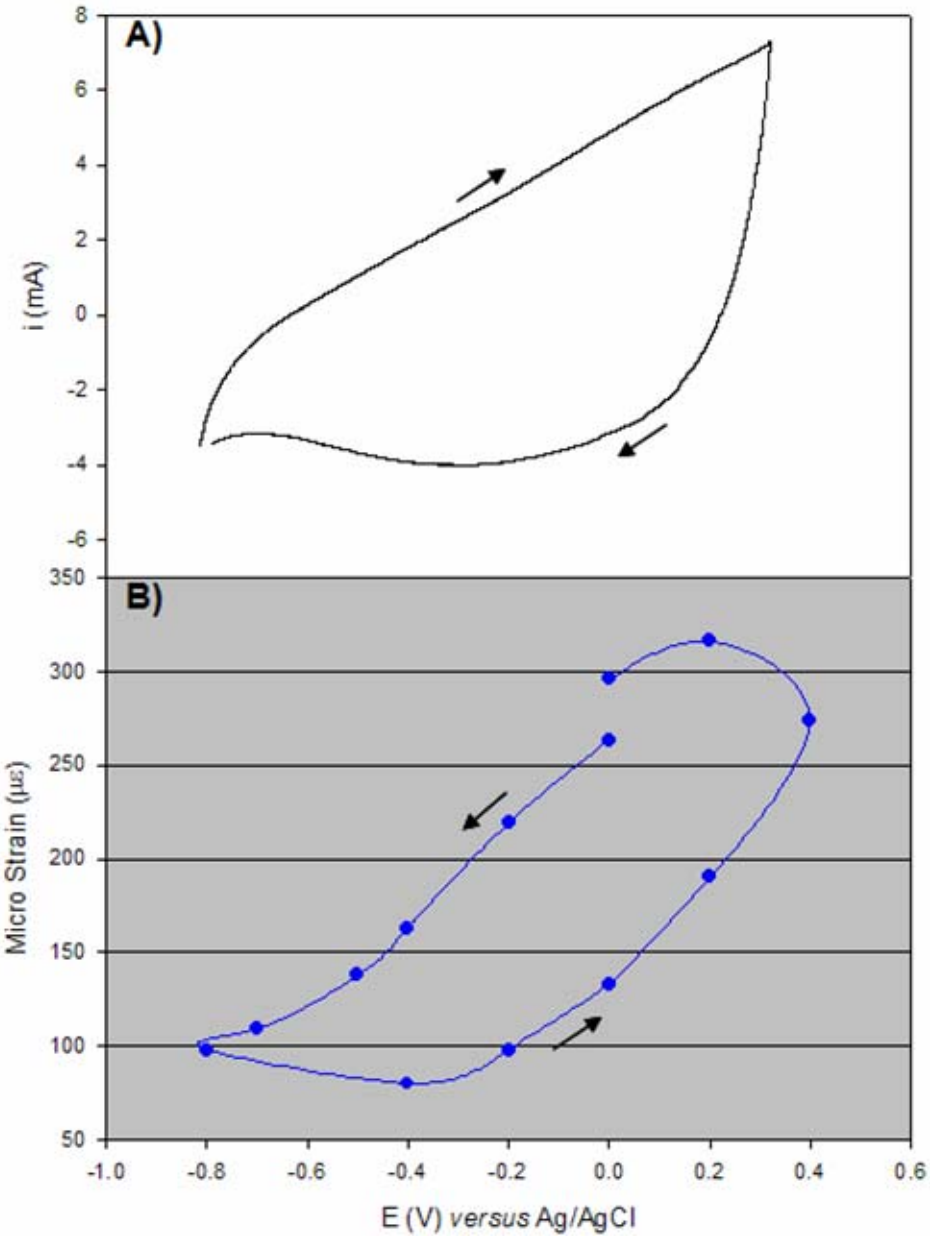

Figure 3.2 (a) PPy/TOS cyclic voltammetry (ν = 10 mV/s) and (b) *in situ* strain response of a 9.6 μm film prepared in aqueous 1.0 M $LiClO_4$.

3.3.3 PPy/TOS Multi-Cycle Strain Response

Strain sensitive actuators were also used to acquire multi-cycle strain data as shown in Figure 3.3. It is evident from the multi-cycle data that the strain response does not return to its initial starting value, but has a positive drift. The difference in the initial starting points for the 2nd and 5th cycle is on the order of 100 με and decreases with each

cycle. However the overall change in strain for each cycle is reproducible on the order of 200 με. The drift in cycle measurements is attributed to the film possibly not returning to the same state of solvation from cycle to cycle. It has also been suggested that the drift could be part of the break-in process for these materials (i.e., the film remembers it is bent and there is some molecular rearrangement). This break-in process is evident during the 1st cycle (Figure 3.3) by the very erratic strain response, which starts to normalize after a couple of scans.

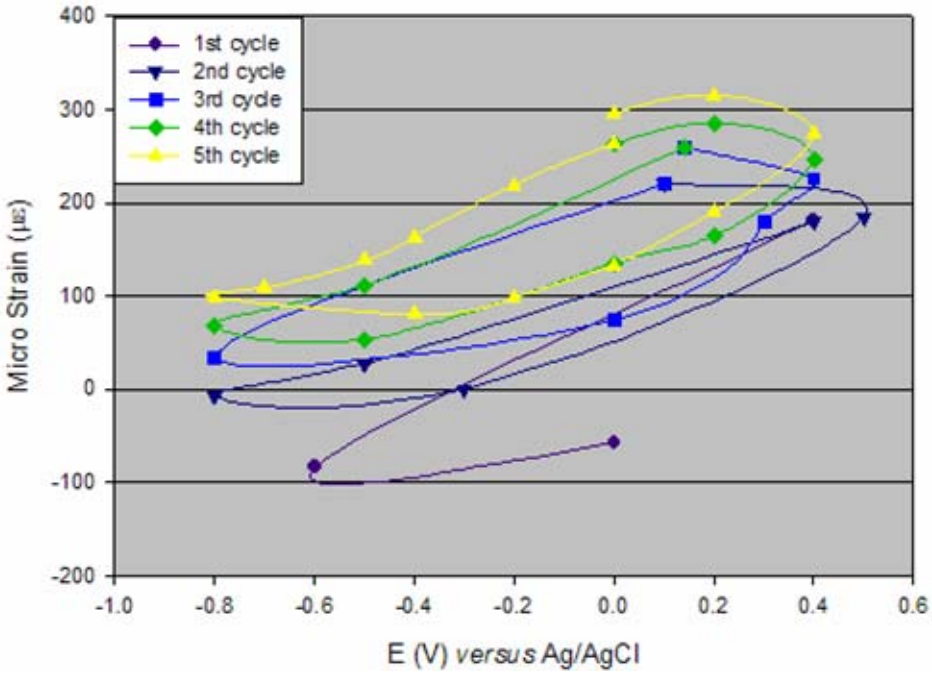

Figure 3.3 *In situ* multi-cycle cyclic voltammetry strain response of a 9.6 με film prepared in aqueous 1.0 M $LiClO_4$.

3.3.4 PPy/TOS Square-Wave Potential Experiments

Square-wave potential experiments were also utilized to evaluate the strain response of PPy/TOS. PPy/TOS films were stepped from –0.8 V to 0.4 V and then back to –0.8 V five times with a 50 s hold time at each potential (Figure 3.4). These stepping

experiments resulted in a reproducible Δε of 70 με. The minimum and maximum strain values were collected manually at –0.8 V and 0.4 V respectfully.

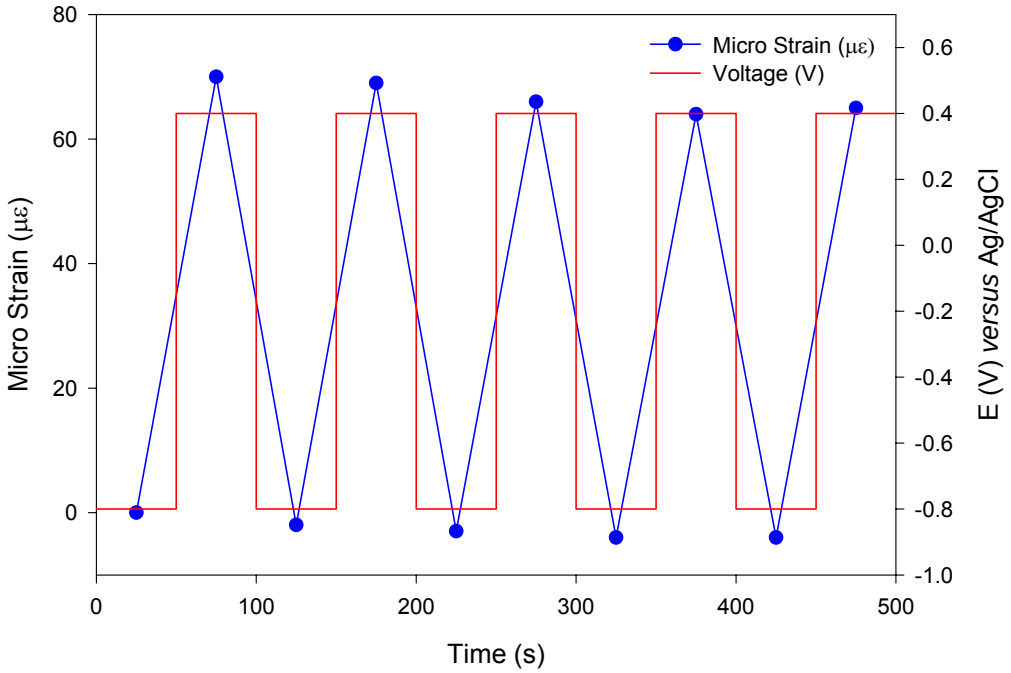

Figure 3.4 *In situ* square-wave strain response of a 9.6 μm film prepared in aqueous 1.0 M $LiClO_4$.

The overall change in the strain response obtained by square-wave voltammetry is less than that obtained by cyclic voltammetry; however the time required to complete one cycle from each experiment is different. The time required to complete one cycle is 240 s for cyclic voltammetry while the time required to complete one cycle by square-wave stepping is 100 s. The strain produced by oxidative doping of these devices is diffusion limited. Therefore longer cycle times allows more ion and solvent molecules to diffuse into and out of these films (i.e., higher degree of oxidative doping), which produces a higher overall degree of strain.

3.4 PEDOP Results

3.4.1 Electrochemical Analysis of PEDOP

Poly(3,4-ethylenedioxypyrrole) (PEDOP) was recently introduced as a conducting polymer with a very low redox switching potential and a high stability to repeated redox switching in aqueous electrolytes.[115, 118] Initial electrochemical evaluations were conducted on a gold-button electrode as with PPy/TOS. PEDOP electropolymerized potentiostatically from aqueous solutions of 0.01 M EDOP, 0.1 M NaTOS, and 1.0 M $LiClO_4$ at 0.5 V produced nicely adherent and electroactive films. As with PPy/TOS, PEDOP electropolymerized at potentials greater than or equal to 0.8 V produced film with poor adhesion, these films spontaneously delaminated from the gold-button electrode. PEDOP films produced at 0.5 V were electrochemically characterized by cyclic voltammetry, scanned at 100 mV/s from 0.0 V to –1.2 V, in aqueous 1.0 M $LiClO_4$. The resulting cyclic voltammetry is shown in Figure 3.5.

From the cyclic voltammetry it is evident that PEDOP's redox switching potential is much lower than that of PPy/TOS. PEDOP has a measured half-wave potential ($E_{1/2}$) of –0.6 V. This low redox switching potential is attributed to the electron donating alkoxy substituents producing a highly electron-rich polyhetrocycle backbone. This electron-rich nature produces high stability to air and aqueous electrolytes in the doped and conducting form. This allows PEDOP to be held in the oxidized (conducting) form for extended periods of time without degradation and also leads to the high cyclic stability of this material.

3.4.2 PEDOP Multi-Cycle Strain Response

EDOP was electropolymerized potentiostatically at E = 0.60 V for 10,000 s from a aqueous solution of 0.01 M EDOP, 0.1 M NaTOS, and 1.0 M $LiClO_4$ to produce a

PEDOP film of 10.6 μm on a Au coated strain gage. A representative SEM micrograph of the surface morphology of PEDOP is shown in Figure 3.6. As can be seen the surface morphology of PEDOP films is comparable to that of PPy. The strain response of PEDOP during cyclic voltammetry was evaluated at a scan rate of 10 mV/s from –0.8 V to 0.0 V in an aqueous solution of 1.0 M $LiClO_4$. The resulting strain response (Figure 3.7) is considerably less than that attained from PPy/TOS with a Δε that ranged from 36 με to 47 με with an average Δε of 42.6 με for the 2nd through 10th cycles. The same data has been replotted against a time axis, in Figure 3.8, to improve resolution of the strain response from cycle to cycle.

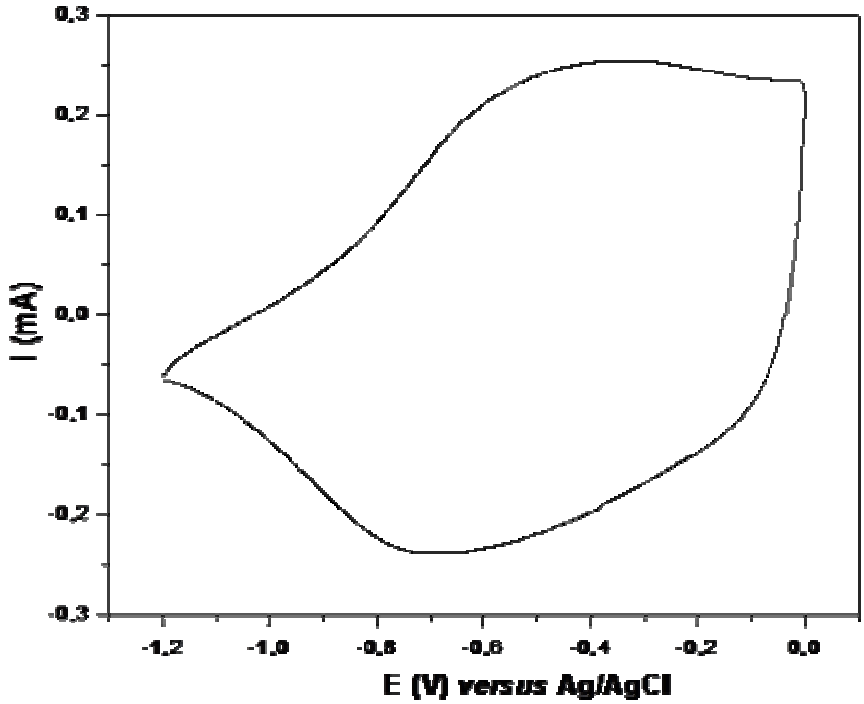

Figure 3.5 Cyclic Voltammetry (ν = 100 mV/s) of a PEDOP film produced from aqueous 1.0 M $LiClO_4$ at E = 0.5 V and t = 200 s.

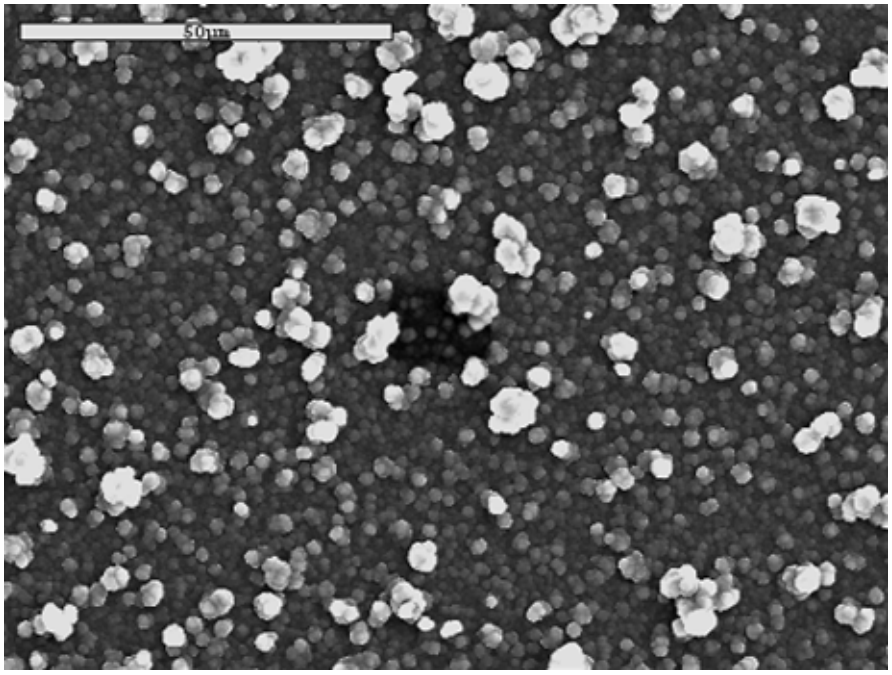

Figure 3.6 SEM micrograph of a PEDOP film prepared at 0.6 V in 1.0 M LiClO4. SEM image taken of an uncoated sample at 1000X and 15 KeV.

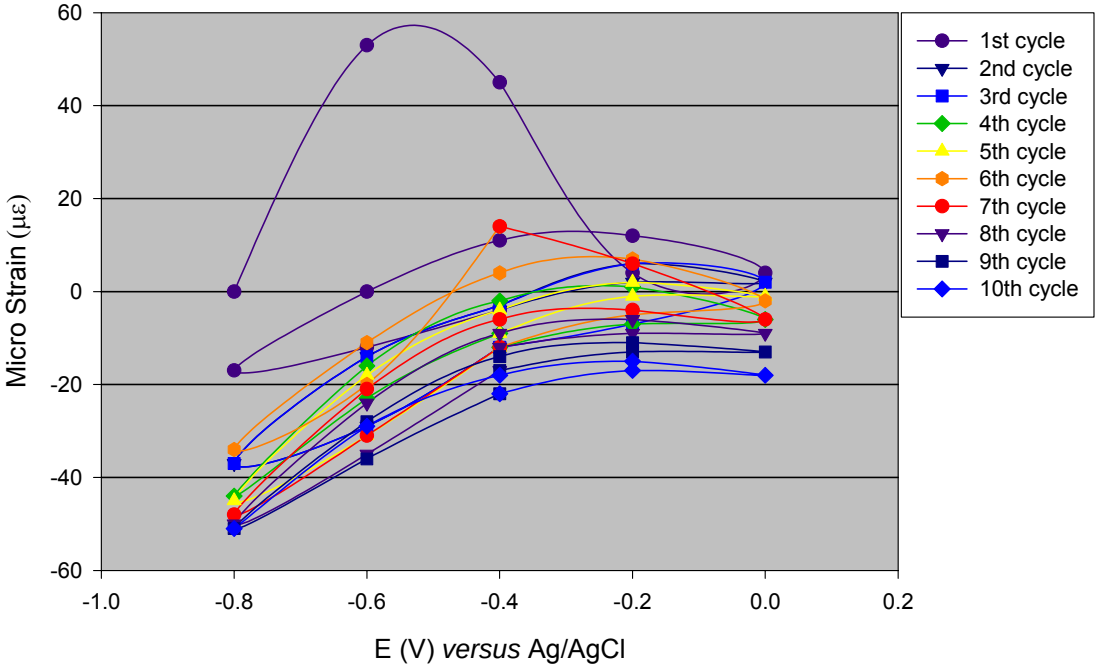

Figure 3.7 *In situ* multi-cycle cyclic voltammetry (10 mV/s) strain response of a 10.6 µm PEDOP film in aqueous 1.0 M $LiClO_4$.

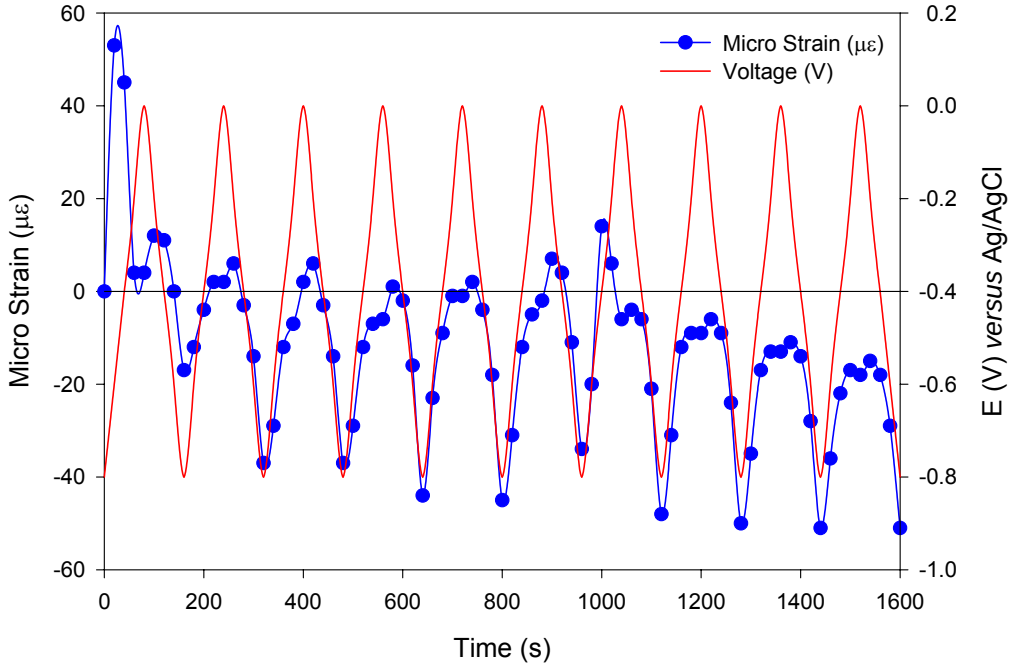

Figure 3.8 *In situ* multi-cycle cyclic voltammetry (10 mV/s) strain response of 10.6 μm PEDOP film in aqueous 1.0 M $LiClO_4$. Data from Figure 3.7 has been replotted vs. time.

3.4.3 Effects of Cyclic Scan Rate on the Strain Response of PEDOP

The effects of scan rate were also evaluated. PEDOP films were electropolymerized as previously stated and then scanned at 100 mV/s by cyclic voltammetry from 0.0 V to –0.8 V in aqueous $LiClO_4$. The resulting strain response was significantly less than that obtained at 10 mV/s. Due to the speed of the redox switching, data was only collected at each end of the potential scan (i.e., 0.0 V and –0.8 V). The average Δε was 6.6 με for the first 10 cycles (Figures 3.9 and 3.10). However iot should be noted that the 1st and 6^{th} cycle both produced a Δε of –1 με while the rest of the cycles all had Δε values between 7 με and 9 με. This dramatic decrease in the strain response is expected due to the diffusion limited swelling nature of this and other conducting polymers. The scan rate of this experiment was conducted 10 times faster than the previous experiment, thus not allowing for full oxidative doping of the polymer network.

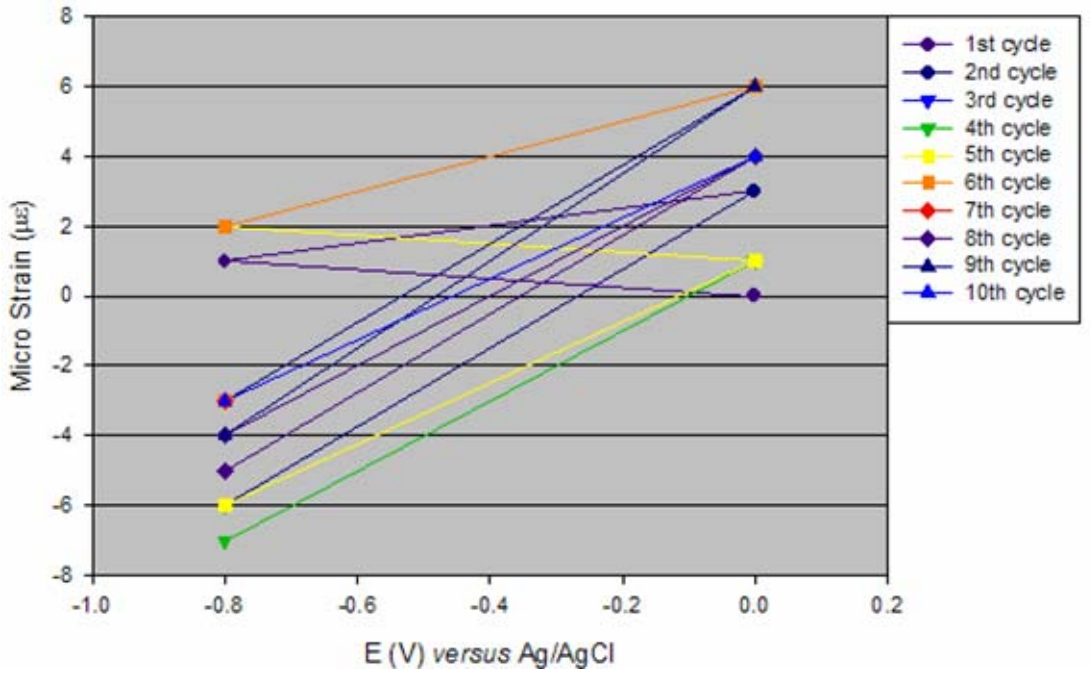

Figure 3.9 *In situ* multi-cycle cyclic voltammetry (100 mV/s) strain response of a 10.6 μm PEDOP film in aqueous 1.0 M $LiClO_4$.

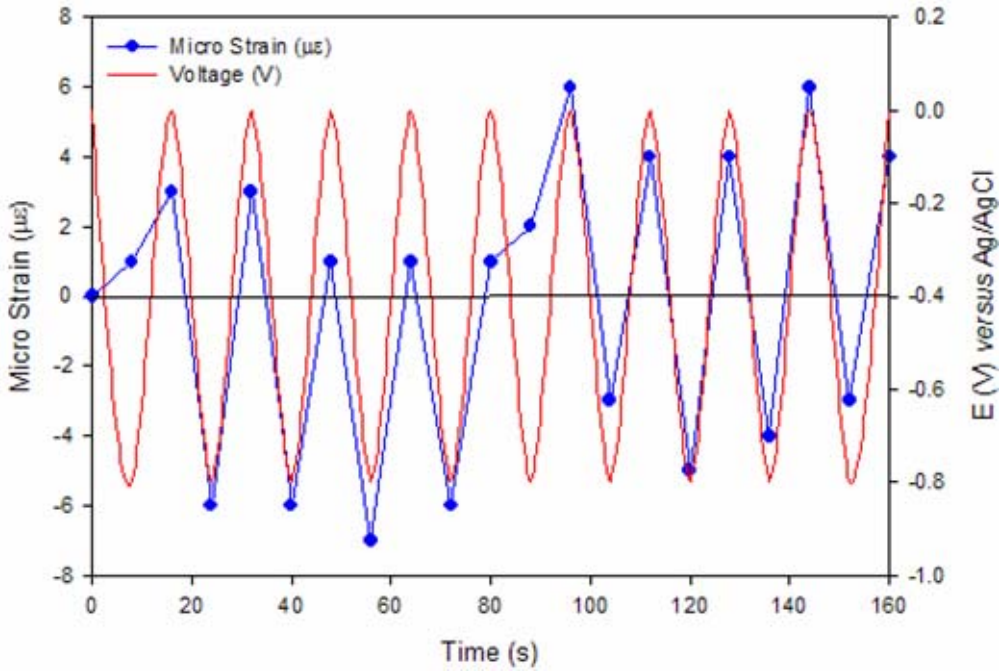

Figure 3.10 *In situ* multi-cycle cyclic voltammetry (100 mV/s) strain response of 10.6 μm PEDOP film in aqueous 1.0 M $LiClO_4$ replotted vs. time.

3.4.4 PEDOP Square-Wave Potential Experiments

Square-wave potential experiments were also conducted on PEDOP. Using the electropolymerization conditions stated above a 10.6 μm film was stepped from –0.8 V to 0.0 V with a 50 s equilibrium hold at each voltage. The resulting square-wave strain response exhibited a Δε that varied from 11 με to 33 με with an average value of 21 με. The strain response with the corresponding potential sweep is plotted versus time in Figure 3.11.

As stated earlier, it is believed that a cross-linked structure, like PPy, will develop a higher degree of strain/swelling than a non cross-linked structure. The cross-links act to tie the whole polymer network together; therefore a small change (strain due to swelling) in one section of the network will exert an affect (strain) on the rest of the networked structure.

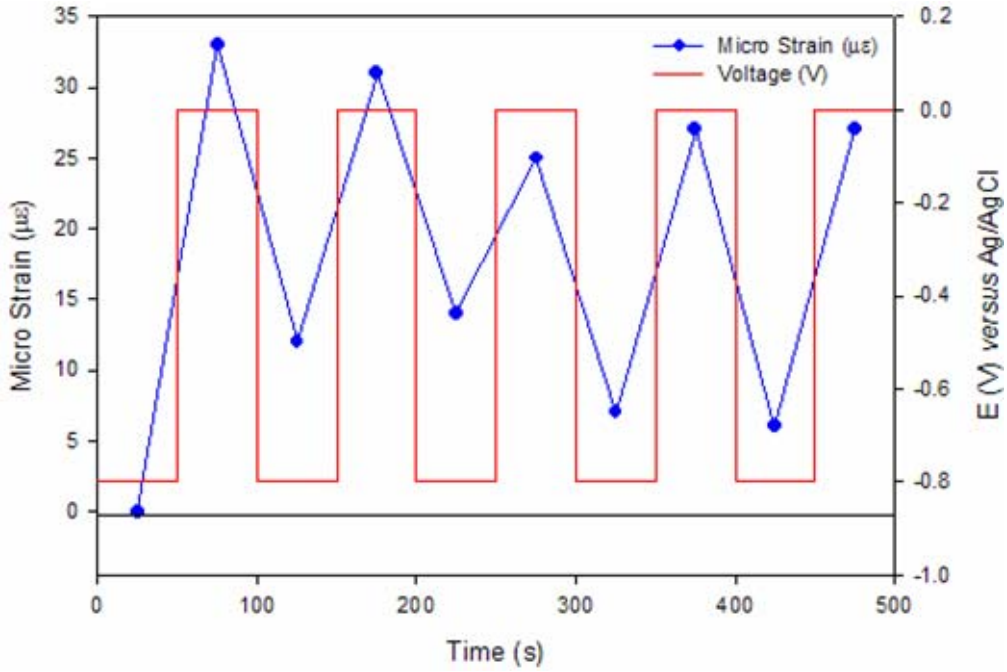

Figure 3.11 In situ square-wave strain response of a 10.6 με film prepared in aqueous 1.0 M LiClO4.

During anion insertion (oxidation) the cross-linked polymer network would be highly strained due to inability of the polymer chains to separate/relax through simple chain motion. By blocking the 3- and 4- positions on the pyrrole ring PEDOP cannot form cross-links and forms a linear structure through the 2- and 5- positions. This lack of cross-linking would allow the polymer network to relax through simple chain motions during ion transport into and out of the structure (during redox switching). Therefore anion insertion into the polymer network would result in a much lower degree of overall strain than in a cross-linked network. However with most things, this can be overdone. As the cross-link density of the network increases the stiffness of the network also increases. Thus requiring an increased amount of force (potential driving force) to develop the same amount of strain in the system. As the cross-link density of the polymer network increases the diffusion rate of counter ions in the system will decrease. Also as the cross-link density increases the modulus increases and the film can become too rigid to deflect/strain resulting in zero strain development and therefore no actuation.

3.5 PBEDOT-Cz Results

3.5.1 PBEDOT-Cz Introduction

Poly [3,6-2(2-(3,4-ethylenedioxythienyl)-carbazole] (PBEDOT-Cz) and other bis-EDOT derivitized carbazoles were found to be of interest, by Reynolds et al., for there ability to form three distinct redox states (neutral, cation-radical, and di-cation forms) at low potentials and to be stable to thousands of redox switches.[107] These low switching potentials are attributed to the electron-rich biEDOT structure in the PBEDOT-Cz polymer repeat structure. Its was found during electrochemical analysis that a irreversible higher potential redox process at 1.15 V (Figure 3.12) was present during the first cyclic voltammetry scan but was absent for all subsequent scans. This process could

not be attributed to over oxidation (breakdown) of the polymer backbone. This was theorized by Reynolds et al. to be a possible cross-linking reaction, however no spectroscopic evidence of cross-linking has been reported to date.

PBEDOT-Cz was chosen as a candidate for evaluation due to this possible cross-linking reaction. It was theorized that the cross-linking of PBEDOT-Cz would lead to an improved strain response in the material when compared to non-cross-linked materials. This was based on the observation that PPy's strain response is related to its crosslinked structure.[64, 104]

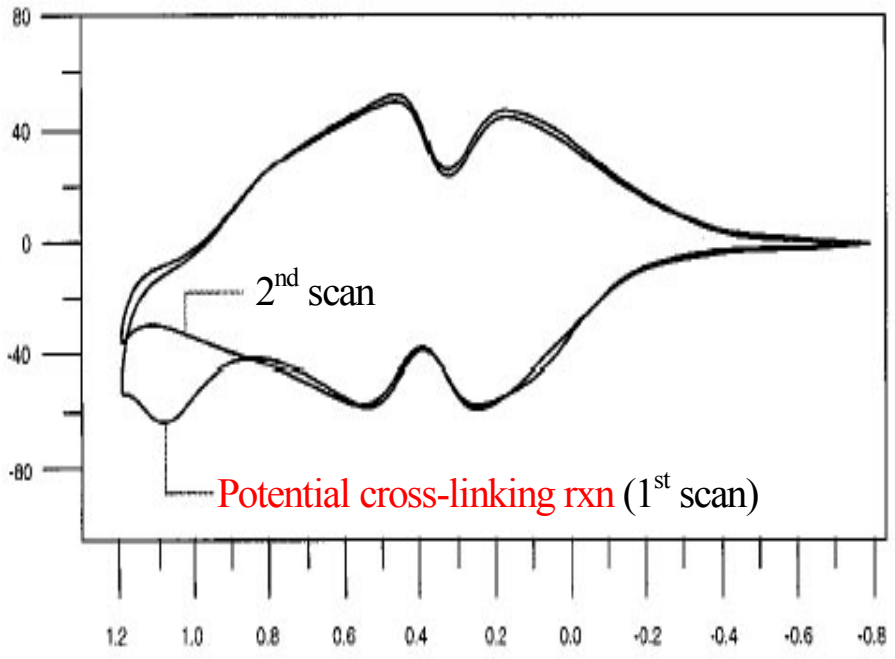

Figure 3.12 Cyclic voltammetry (100 mV/s) of PBEDOT-Cz in 0.1 M TBAP/CAN. Adapted from Figure 8 of Reynolds et al..[107]

3.5.2 PBEDOT-Cz Electrochemical Conditions

The effects of possible cross-linking at 1.15 V [107] in PBEDOT-Cz was evaluated in samples that were electropolymerized from a solution of 0.01 M BEDOT-Cz and 0.1 M tetrabutlyammonium perchlorate in acetonitrile. Samples were cycled from -0.8 V to 0.6,

1.0, and 1.2 V at 10 mV/s in 1.0 M aqueous $LiClO_4$ successively. Data was collected for the 1st, 2nd, 5th, and 10th scans at 0.2 V intervals.

3.5.3 PBEDOT-Cz Strain Response (-0.8 V to 0.6 V)

The cyclic strain response acquired from –0.8 V to 0.6 V exhibited a very irregular shape for the first four scans but then normalized after the 5th scan. This is due to the normal break in period for these materials, as discussed earlier for PPy and PEDOP. The normalized cyclic strain data for the 1st, 2nd, 5th, and 10th cycles (Figure 3.13) exhibits a Δε range from 15 με to 21 με. The average change in strain was 17με.

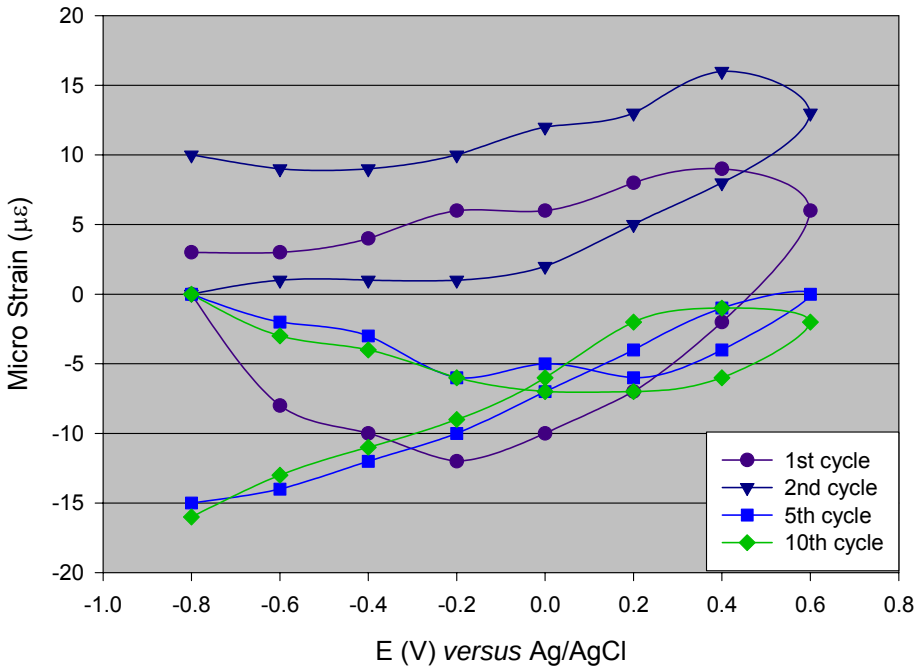

Figure 3.13 Normalized *in situ* cyclic strain response of 9.9 μm PBEDOT-Cz film (-0.8 V to 0.6 V) for the 1st, 2nd, 5th, and 10th scans in 1.0 M $LiClO_4$.

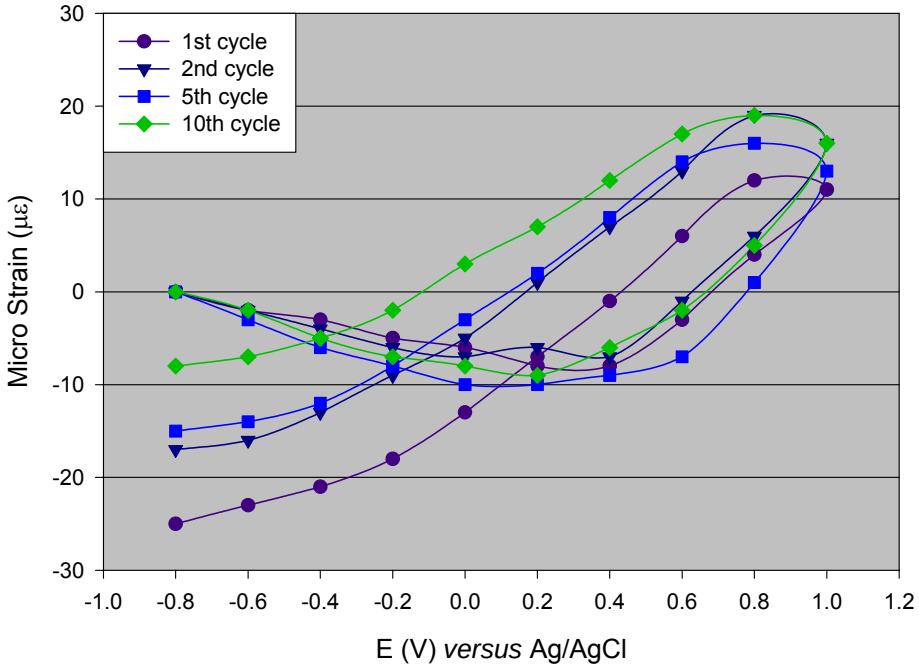

Figure 3.14 Normalized *in situ* cyclic strain response of 9.9 μm PBEDOT-Cz film (-0.8 V to 1.0 V) for the 1st, 2nd, 5th, and 10th scans in 1.0 M $LiClO_4$.

3.5.4 PBEDOT-Cz Strain Response (-0.8 V to 1.0 V)

The cyclic strain data acquired from –0.8 V to 1.0 V was very regular in shape and exhibited its max strain at –0.2 V on the reverse scan as shown in Figure 3.14. The Δε measured for this set of scans ranged from 28 με to 37 με with an average value of 33 με. This is a change of 16 με and 0.6 V between the average Δε measured for the –0.8 V to 0.4 V and –0.8 V to 1.0 V scans.

3.5.5 PBEDOT-Cz Strain Response (-0.8 V to 1.2 V)

The strain data acquired from –0.8 V to 1.2 V is also very regular in shape when compared to the scans obtained from –0.8 V to 0.4 V. This set of data was obtained above the potential cross-linking potential of 1.15 V for PBEDOT-Cz, however there are no significant visual differences in the shape or measured values of the strain data from above and below this potential cross-linking voltage. The Δε ranged from 34 με to 35 με

with an average value of 34.75 με for the 1st, 2nd, 5th, and 10th scans. These scans are shown in Figure 3.15. This is a change of 1.75 με and 0.2 V between the average Δε measured for the –0.8 V to 1.0 V and –0.8 V to 1.2 V scans. This data does not support the argument of potential crosslinking of PBEDOT-Cz at potentials above 1.15 V.

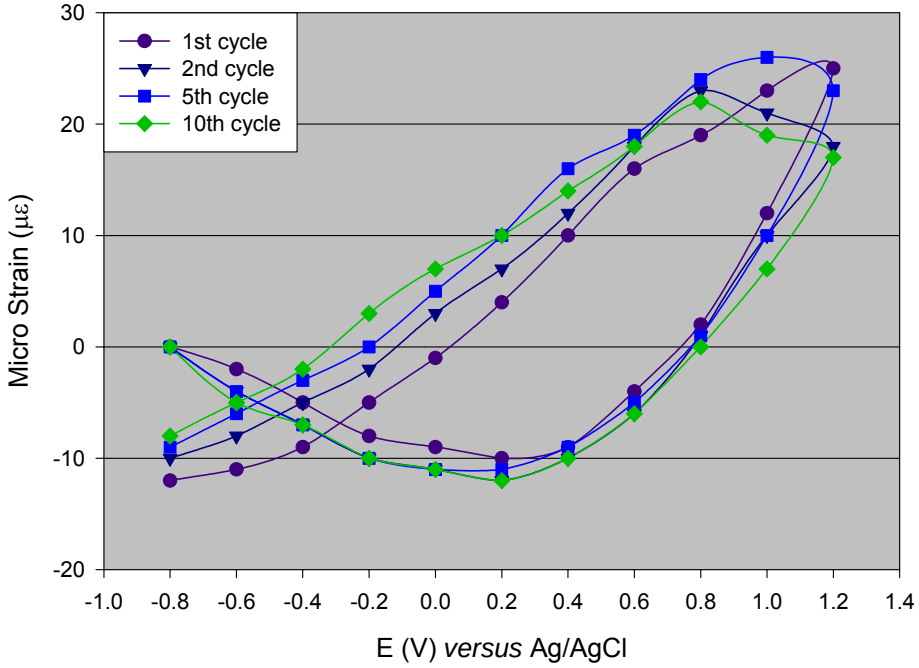

Figure 3.15 Normalized *in situ* cyclic strain response of 9.9 μm PBEDOT-Cz film (-0.8 V to 1.2 V) for the 1st, 2nd, 5th, and 10th scans in 1.0 M $LiClO_4$.

3.5.6 Overall Results for PBEDOT-Cz

The overall change in strain for the 0.6, 1.0, and 1.2 V scans ranged from 15-21, 28-37, and 34-35 με with average values of 17, 33, and 34.75 με respectively. These values are significantly lower than those obtained from PPy. However there is no significant difference in the data obtained from the –0.8 V to 1.0 V and –0.8 V to 1.2 V scans (below and above potential cross-linking voltage). The normalized strain response of the 5th and 10th cycles for all three potential ranges is shown in Figures 3.16 and 3.17 respectfully.

The slight increase in the strain response between the scans from –0.8 V to 1.0 V and 1.2 V is most likely due to the increased driving potential of 0.2 V. This combined with the fact that no spectroscopic evidence of cross-linking for PBEDOT-Cz could be found by Reynolds et al.,[107] leads to the conclusion that the PBEDOT-Cz cross-linking reaction is non-existent or so minimal that no enhancement in the strain production is evident. However the overall strain response of PBEDOT-Cz is comparable to that of PEDOP. This is due to the inability of PBEDOT-Cz to crosslink as with PEDOP. This low strain response combined with the cost to produce the BEDOT-Cz monomer makes PBEDOT-Cz a poor candidate for actuator construction.

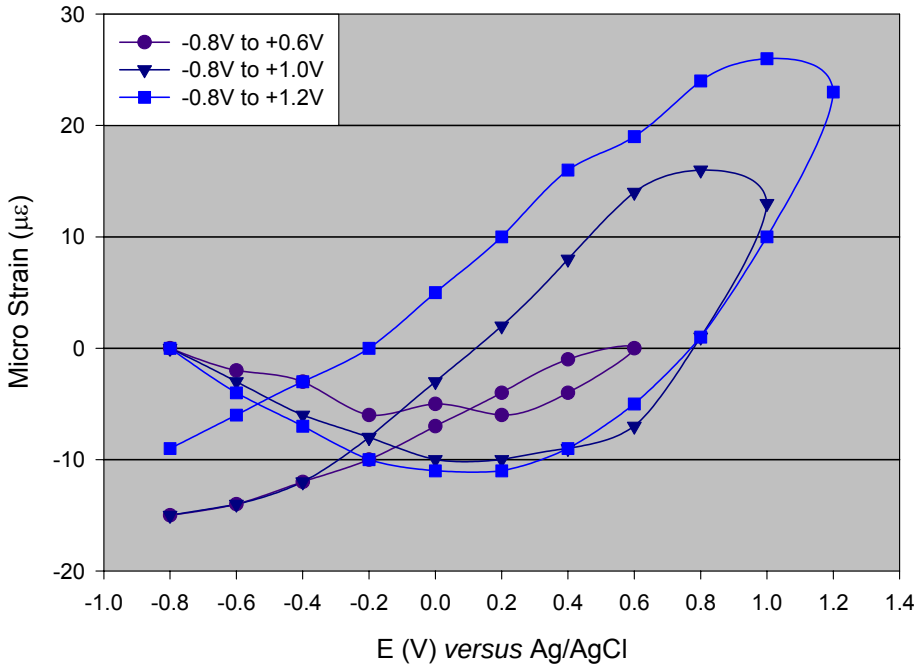

Figure 3.16 Normalized *in situ* cyclic strain response of 9.9 μm PBEDOT-Cz film scanned from -0.8 V to 0.4 V, 1.0 V, and 1.2 V (5^{th} scan) in 1.0 M $LiClO_4$.

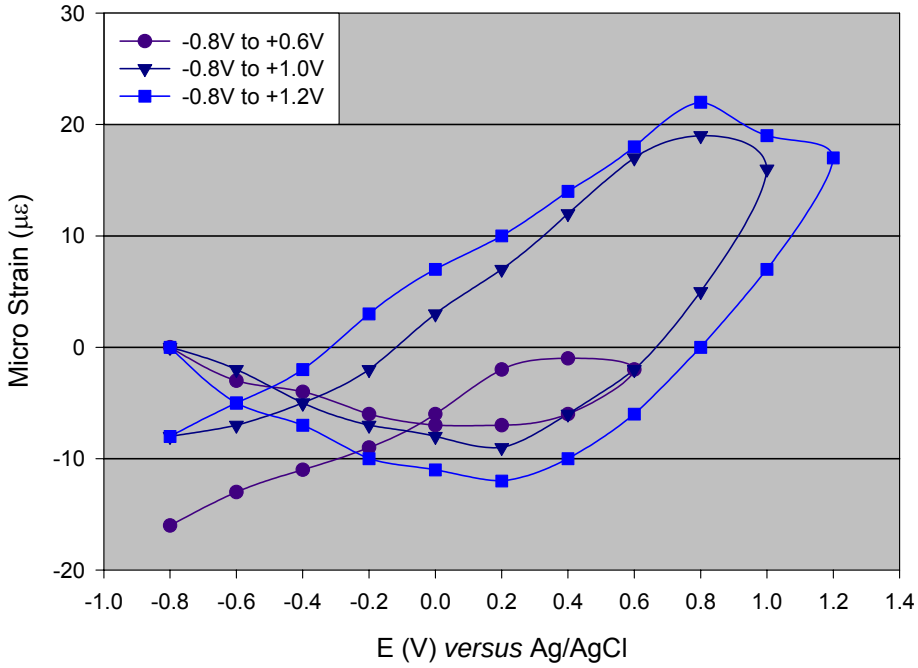

Figure 3.17 Normalized *in situ* cyclic strain response of 9.9 μm PBEDOT-Cz film scanned from -0.8 V to 0.4 V, 1.0 V, and 1.2 V (10^{th} scan) in 1.0 M $LiClO_4$.

3.6 Overall Comparison of PPy, PEDOP, and PBEDOT-Cz

If the strain data for PPy/TOS, PEDOP, and PBEDOT-Cz is normalized and plotted on the same graph it is easy to see that PPy/TOS produced significantly more strain than PEDOP and PBEDOT-Cz (Figure 3.18). It is believed that the higher strain response of PPy/TOS over PEDOP and PBEDOT-Cz is due to its ability to crosslink during electropolymerization.[64, 104]

The possible ability of PBEDOT-Cz to cross-link at a potential of 1.15 V has been shown to be non-existent or at least so minimal that it is not significant in the strain production of this system.

From this study it was shown that it is possible to obtain a detailed strain response measurement of various CP's directly and precisely utilizing standard strain gages technology to construct strain sensitive actuators. These gages determine strain by

directly measuring the strain induced on the embedded constantan grid (inside the actuator) not the overall deflection of the actuator tip like most measurement techniques. This provides a detailed measurement of the actual strain produced internally in the system.

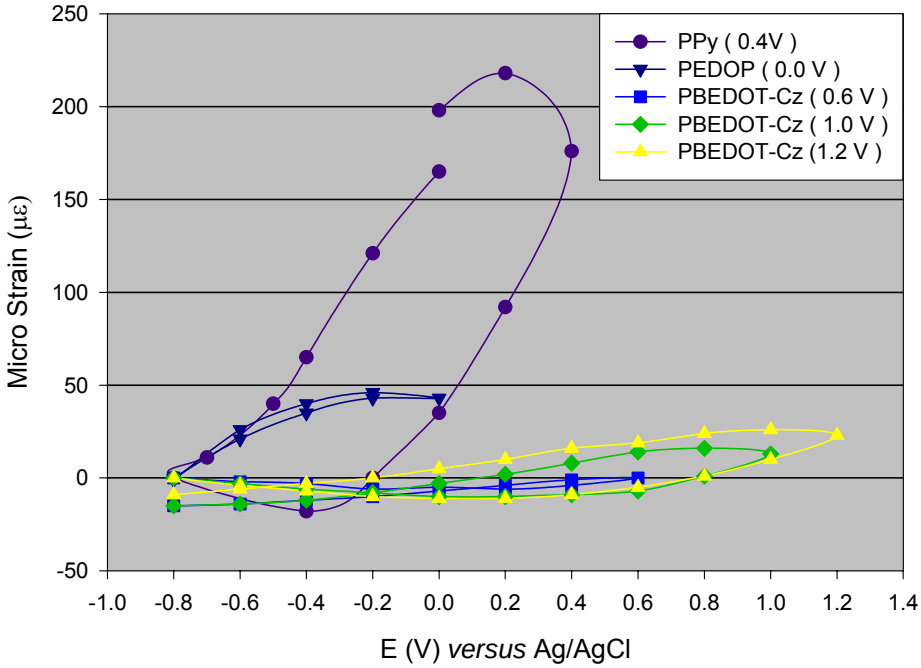

Figure 3.18 Comparison of *in situ* cyclic strain response of PPy, PEDOT, and PBEDOT-Cz in aqueous 1.0 M $LiClO_4$.

3.7 Effects of Interlayer Adhesion

Adhesion of the CP to the EvAu coated substrate was found to be a potential problem during long term repeated redox switching. In our study PPy, PEDOP, and PBEDOT-Cz were all found to have poor adhesion to a gold-button working electrode when electropolymerized at potentials ≥ 0.8 V. However large-scale (>70%) delamination of PPy was seen after long term cycling (>500 cycles) of actuators (Figure 3.19) and one film completely delaminated from a Au coated polyimide sample when exposed to a high vacuum (~ $1 \cdot 10^{-5}$ Torr) during SEM examined (Figure 3.20).

Examination of the image of the sample that delaminated in the SEM, it is obvious that the PPy surface in contact with the Au layer is porous and irregular in texture (Figures 3.21 and 3.22), which leads to poor interlayer adhesion between the PPy and the Au substrate. Also regions of small nodules or nucleation sites of PPy were left behind on the Au substrate during the delamination process (Figures 3.23 and 3.24). The same features are also evident in SEM's of the underside of a PPy film that cracked and delaminated during repeated redox switching.

The partially delaminated PPy film was rolled back to expose the surface that was in contact with the Au substrate for further examination by SEM (Figure 3.25). The adhesion of the PPy nodules to the Au substrate was non-homogenous upon delamination. From closer examination it can be seen that these nodules grow at the surface of the PPy film, and either lie directly on the surface or in some of the many pores present at PPy-Au interface (Figure 3.26).

Delamination of the CP film most likely initiates in isolated regions with high stress concentrations that eventually propagate into total delamination. As delamination of the CP film from the substrate propagates a loss of electrical and physical contact between the CP and the working electrode develops. This decreases the ability to redox switch the CP film, thus retarding swelling/oxidation of the CP and therefore the development of strain in these systems. This combined with a decreasing amount of physical contact between the CP and the substrate reduces the overall movement and the total lifetime of actuators made from these systems. Once total delamination of the CP from the working electrode occurs no strain can be developed by the system and the actuator will totally stop functioning.

3.8 Conclusions

From this study it was shown that strain gage technology can readily be utilized as an inexpensive and highly accurate method of evaluating the resultant physical properties of different electrochemical polymerization and actuation conditions on a given conducting polymer structure. And due to the vast array of different strain gage designs it is possible to incorporate this technology into almost any actuator design.

It has also been shown that PPy produced significantly higher strains than PEDOP and PBEDOT-Cz under the given electrochemical conditions. PBEDOT-Cz also produced higher strain responses around and above the potential crosslinking potential of ~1.15 V than at lower potentials. However it is believe that the increased strain response is due to higher applied driving potentials than the possible crosslinking reaction due to the lack of any electrochemical, spectroscopic, or strain/performance evidence.

It has also been determined that the interfacial adhesion of the conducting polymer to the EvAu coated surface is a potential problem for long term actuator lifetimes. During repeated electrochemical cycling the induced cyclic strains initiate micro-crack formation between the CP and EvAu layers which then grow and eventually result in device failure. All utilized conducting polymers (PPy, PEDOP, and PBEDOT-Cz) were found to exhibit poor adhesion to EvAu when electropolymerized at potentials of 0.8 V and greater. The most obvious case of this was for PPy which was shown to undergo large-scale delamination from the EvAu substrate when subjected to long term redox switching (Figure 3.19) and upon exposure to high vacuum during SEM examination (Figure 3.20). It is important to improve interlayer adhesion to increase CP actuator performance and overall lifetime.

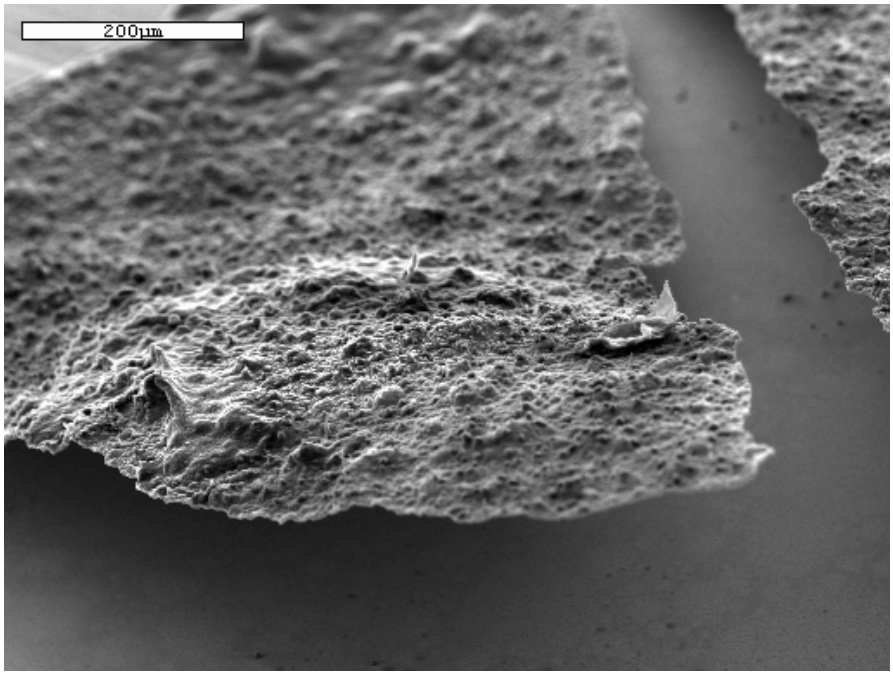

Figure 3.19 SEM micrograph of delamination of PPy resulting from long-term cycling of the actuator; 150X

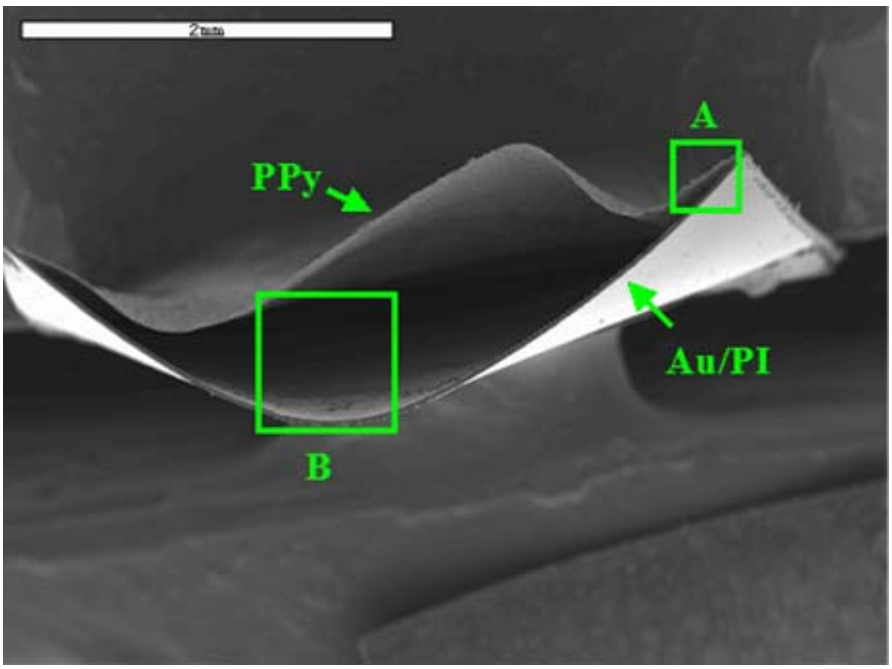

Figure 3.20 SEM micrograph of delamination of PPy resulting from exposure to high vacuum; 25X

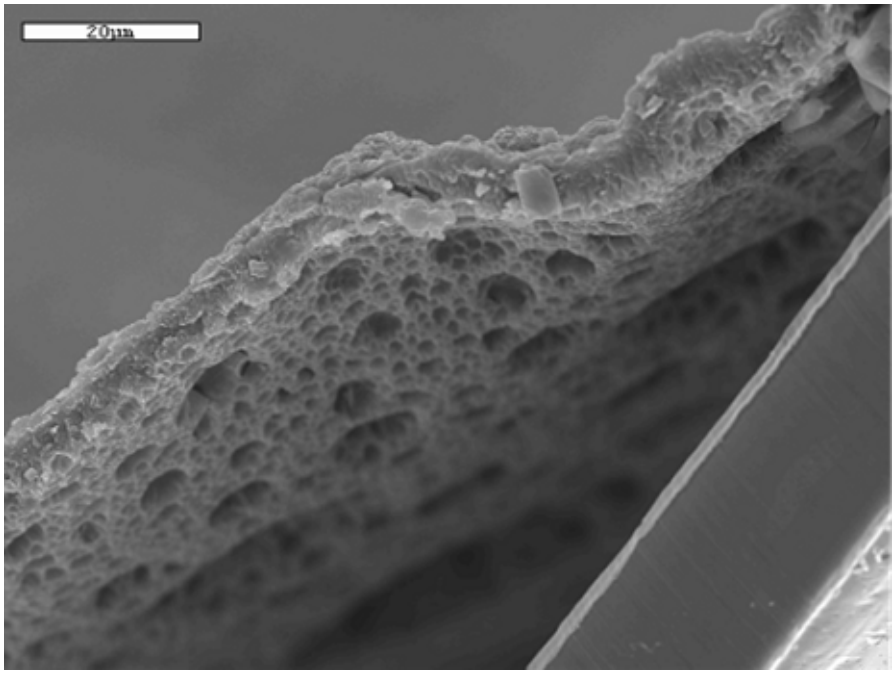

Figure 3.21 Enlarged SEM micrograph of region “A” in Figure 4.20; 1350X

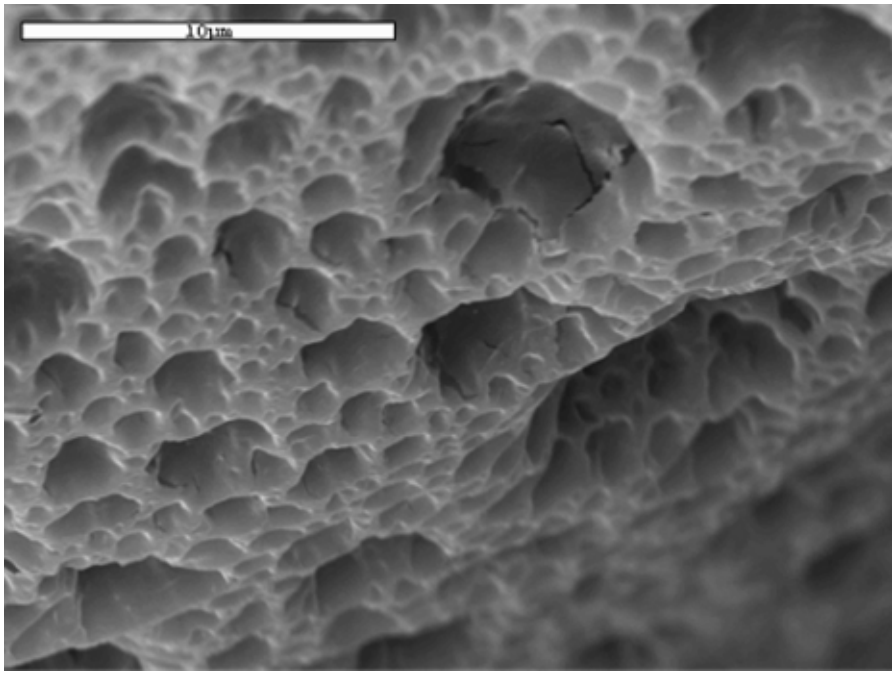

Figure 3.22 SEM micrograph of porous PPy at PPy-Au interface; 5000X

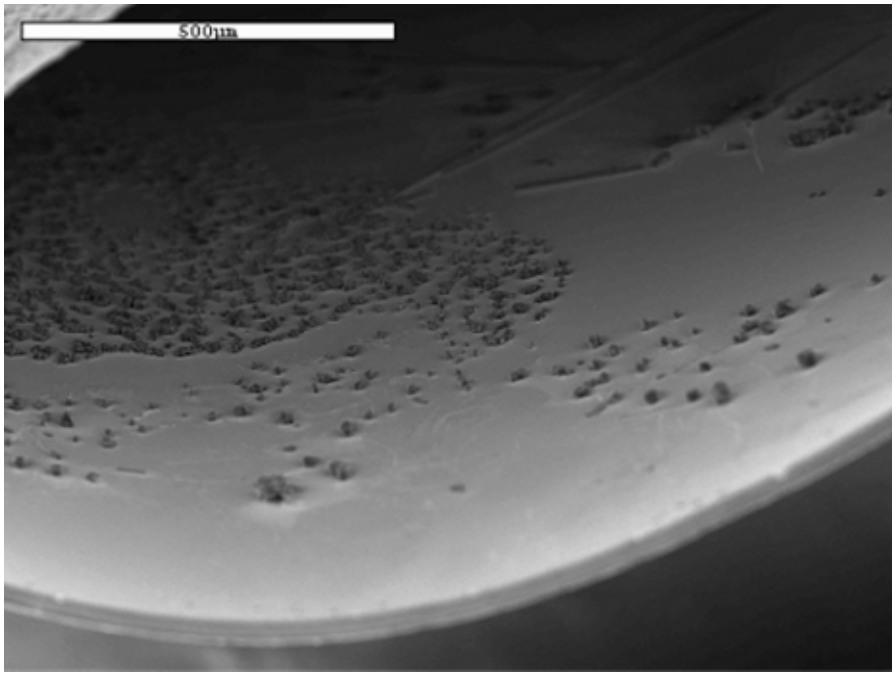

Figure 3.23 Enlarged SEM micrograph of region “B” in Figure 4.20; 100X

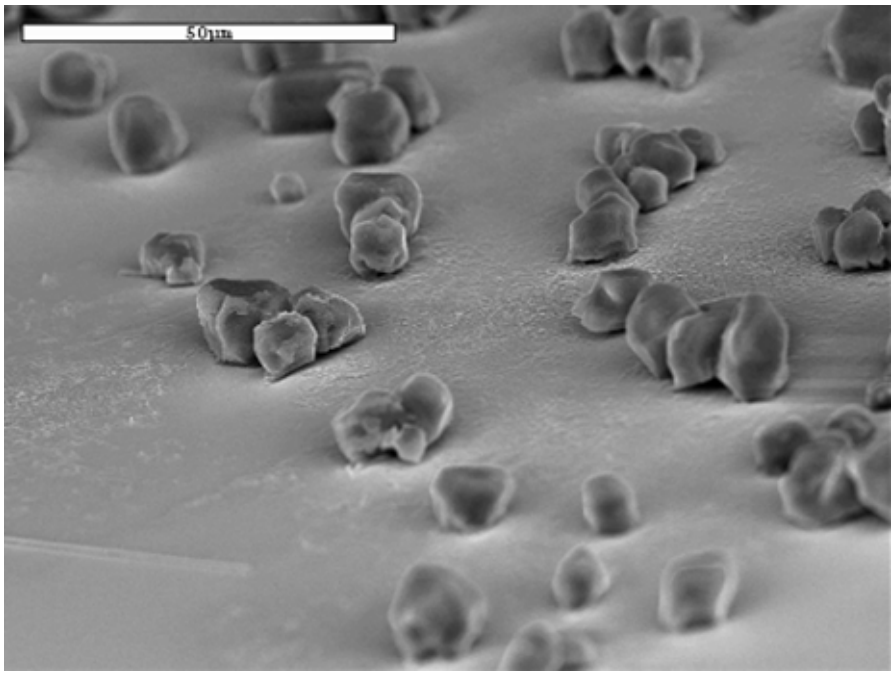

Figure 3.24 SEM micrograph of PPy nodules remaining of Au substrate after PPy delamination; 1000X

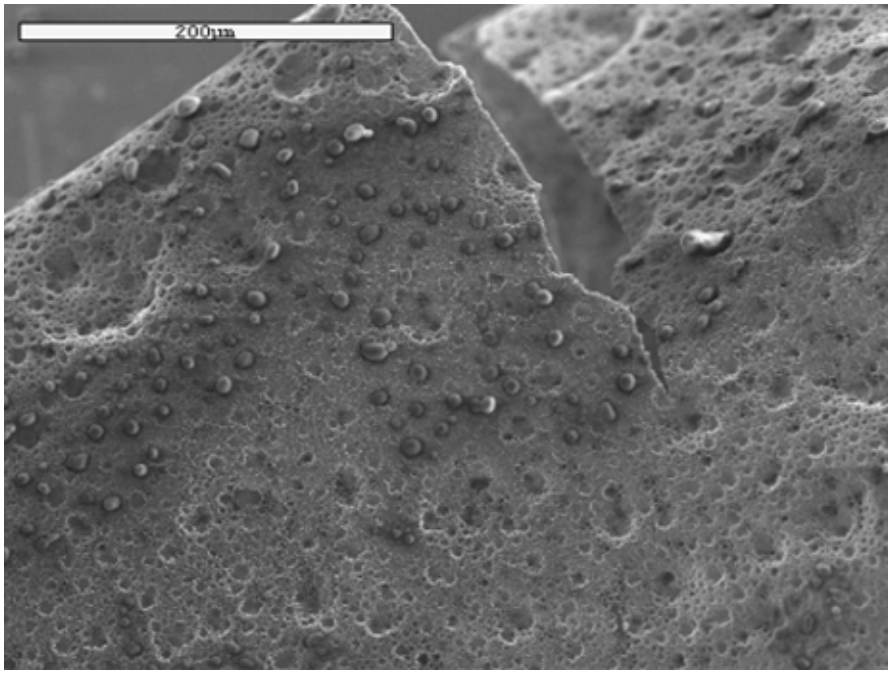

Figure 3.25 SEM micrograph of PPy surface after delamination from Au substrate during long-term repetitive cycling of the actuator; 250X

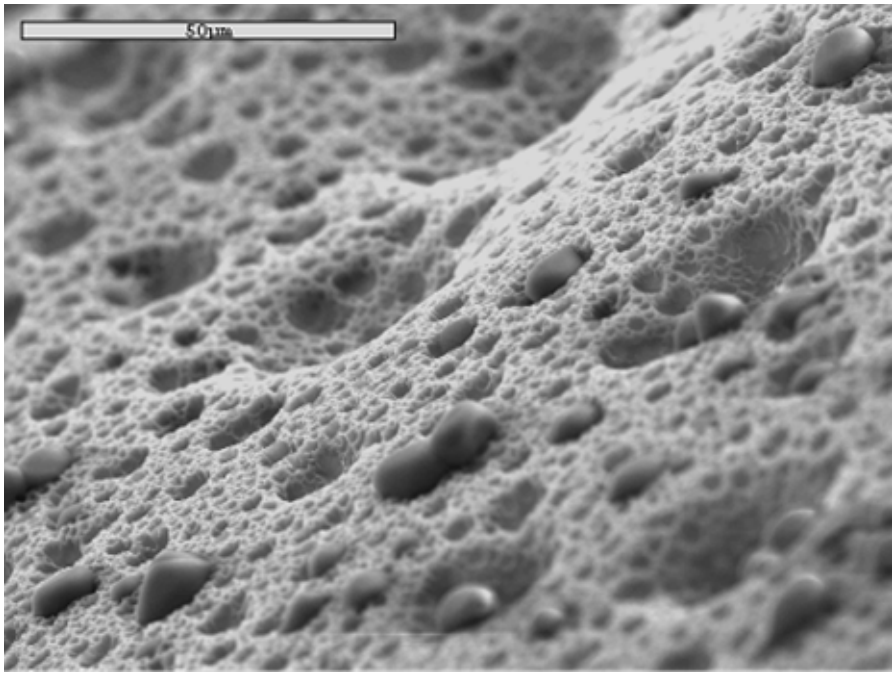

Figure 3.26 SEM micrograph of exposed PPy-Au interface exhibiting PPy nodule growth; 1000X

CHAPTER 4
IN SITU STRAIN MEASURMENTS OF CP'S ON ENHANCED AU SURFACES

4.1 Introduction

Adhesion of CP's to EvAu coated substrates was identified as a potential problem during the previous study. Poor adhesion of the CP to the substrate will lead to low or no strain development and will greatly reduce the working lifetime for these actuators due to eventual delamination of the CP from the substrate. PPy, PEDOP, and PBEDOT-Cz were found to exhibit poor adhesion to Au when electropolymerized on Au-button electrodes at potentials of 0.8 V and greater. PPy was also shown to undergo large-scale delamination when subjected to long term redox switching (Figure 3.19) and upon exposure to high vacuum during SEM examination (Figure 3.20). The purpose of this study was to improve the interfacial adhesion between the conducting polymers and the substrate. Further characterization of the effects of various polymerization and actuation conditions on these systems was conducted on both standard and enhanced interfacial surfaces using the strain sensitive actuator technology.

4.2 Materials and Methods

4.2.1 Materials

Pyrrole was (Sigma-Aldrich) was filtered through neutral alumina (Brockman activity 1; Fisher Scientific) until colorless before use to remove any impurities. Acetonitrile (ACN), lithium perchlorate ($LiClO_4$), sodium perchlorate ($NaClO_4$), p-toluenesulfonic acid Na salt (NaTOS), and tetrabutylammonium were all used as received from Sigma-Aldrich. Sodium nitrate ($NaNO_3$) was purchased from Mallinckrodt

Chemicals and sodium sulfite (Na_2SO_3) was purchased from Fisher Scientific, both were used as received. Deionized water (18 MΩ, Millipore system) was used in all experiments and the solutions were deoxygenated for 15 minutes by bubbling argon prior to electropolymerization and redox switching of the CP.

4.2.2 Electrochemical Gold Deposition Solution

Electrochemical deposition of Au (EcAu) on thermally evaporated Au (EvAu) coated polyimide substrates utilized a solution of Oromerse SO Part B "replenisher" ($Na_3Au(SO_3)_2$), a commercially available gold plating solution purchased from Technic Inc. EcAu deposition was carried out in a solution of 25% (10 mL) $Na_3Au(SO_3)_2$ and 75% (30 mL) of aqueous 1.7 M Na_2SO_3 as reported for electroless Au deposition.[119]

4.2.3 Evaporated and Electrochemically Deposited Gold

Thermally evaporated Au (EvAu) was vacuum deposited on the bottom side of the strain gages to the desired thickness. All electrochemical work was carried out utilizing an EG&G Princeton Applied Research 273A potentiostat/galvanostat utilizing the CorrWare software package, a platinum foil counter electrode and an Ag/AgCl (BAS MF2052) reference electrode at room temperature. All potentials given are relative to this reference electrode.

Conducting Cu tape (1181, 3M) was utilized to make electrical connections between the EvAu layer and the working electrode lead from the potentiostat. Electrochemically deposited Au (EcAu) samples were then prepared on EvAu samples potentiostatically from a diluted solution of $Na_3Au(SO_3)_2$ (mentioned above) at –0.9 V. EcAu layer thickness (and therefore surface roughness) was controlled by varying the cathodic charge during electrochemical deposition.

The surface roughness factor (r) of the Au layer was determined by taking the ratio of the electrochemical area, determined from the charge required to reduce the surface oxide layer (potential cycling between 0.0 V and 1.5 V in aqueous 50 mM H_2SO_4),[120] to the geometric area. The surface roughness factor varied from r = 2.89 for EvAu to r = 6.17 to r = 24.5 for the EcAu samples. Surface morphology was examined by utilizing a scanning electron microscope (JEOL 6400) and white light optical profilometry (Wyko/Veeko NT1000).

4.2.4 Conducting Polymer Synthesis

In this study EvAu was thermally vapor deposited to a thickness of ca. 1.0 μm (measured by cross-section SEM), some EvAu samples when subsequently treated with EcAu of varying thicknesses (~1-10 μm) as described above. PPy films of varying thicknesses were prepared potentiostatically on EvAu and EcAu samples from a solution of 0.1 M pyrrole in 0.1 M aqueous sodium perchlorate at E = 0.9 V unless otherwise mentioned.

The high surface roughness of EcAu samples made it difficult to determine PPy film thickness directly; therefore polymerization charge density (C/cm2) was utilized to compare PPy film thicknesses in this study. The polymerization charges ranged from 0.35 to 5.42 C/cm2. By assuming a 100% efficiency for the PPy deposition reaction and a charge thickness ratio of 0.28 C/(μm - cm^2) [121] this correlates to a PPy film thickness of ~1.25-19.40 μm on a smooth surfaces.

4.3 Improved Interlayer Adhesion Utilizing Electrochemically Deposited Au Surfaces (EcAu)

Interlayer adhesion between PPy and the EvAu coated substrate has been enhanced by the electrochemical deposition of Au (EcAu) onto the EvAu surface. The EcAu

treatment increases the surface area of the working electrode via the growth of Au crystals on the EvAu surface. EcAu films were deposited on EvAu coated PI substrates (EcAu/EvAu/PI samples) potentiostatically at –0.9 V from a solution consisting of 25% $Na_3Au(SO_3)_2$ (Oromerse SO Part B "replenisher") and 75% aqueous 1.7 M Na_2SO_3.

The EcAu layer thickness (Au crystal height), and therefore surface roughness (r), was initially controlled by limiting the deposition time on smooth PI samples and then was later controlled by monitoring the total charge passed during the electrochemical deposition process for all strain gage samples. The surface roughness factor (r), of the Au surfaces, was determined by taking the ratio of the surface area measured electrochemically, obtained from the charge required to reduce the surface oxide layer,[120] to the geometric surface area of the working electrode. The electrochemical surface area was measured by potential cycling the Au surface between 0.0 V and 1.5 V in an aqueous 50 mM H_2SO_4 solution. The charge passed during re-oxidation of the Au oxide monolayer was converted to the surface area using a factor of 0.43 mC/cm^2.

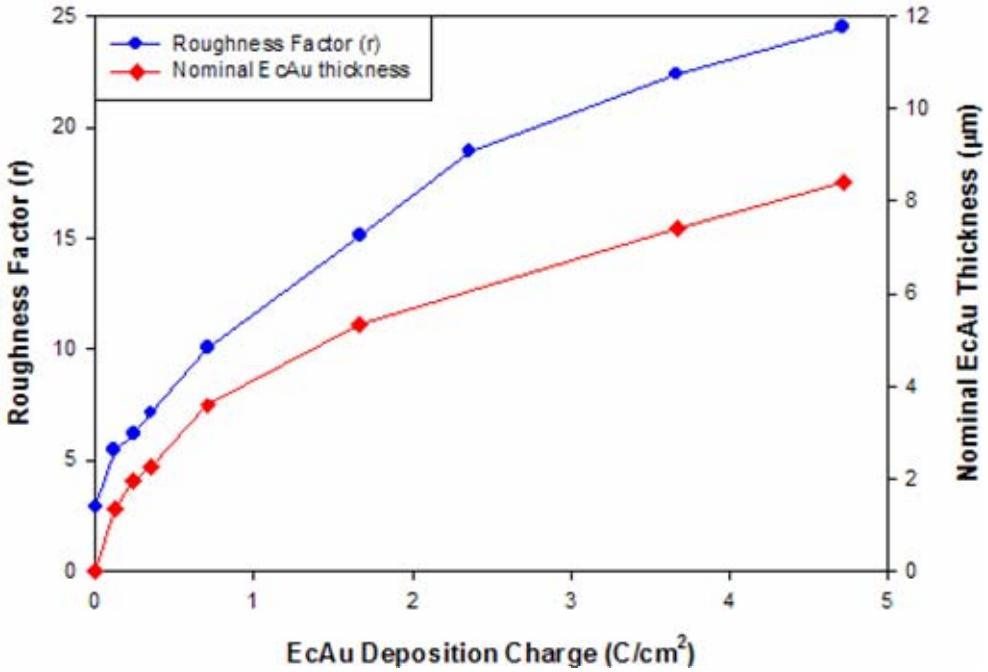

Figure 4.1 Correlation between surface roughness factor, nominal EcAu thickness and EcAu deposition charge. EcAu thickness was determined by cross-section SEM.

Figure 4.1 illustrates the relationship between the surface roughness factor (r) and EcAu deposition charge. The EcAu layer thicknesses were measured by cross-section SEM.

4.4 Effects of Surface Roughness on EcAu Morphology

Many factors such as electrolyte type, pH, deposition potentials, additives, and substrate structure (surface texture) have all been shown to affect the resulting surface morphology of electrochemically deposited Au surfaces.[122-126] The effects of substrate structure on EcAu morphology can easily be seen from SEM micrographs of the EcAu deposited on smooth EvAu/PI substrates versus the rough EvAu/PI surface of the strain gages. EcAu growth on smooth EvAu/PI surfaces results in the formation of large 5-point start structures. The Au crystals grow about normal to the EvAu/PI surface on the smooth samples. Crystal growth starts at many small nucleation sites. As the crystals continue to grow they coalesce to form fewer but larger crystal structures.

However the application side (backside) of the PI strain gages is roughened (sanded) to help promote adhesion of the strain gage to the sample it is being applied to. This roughened surface (surface roughness factor (r) = 2.89) produces very irregularly shaped Au crystal structures when grown to high charge densities (3.67 C/cm^2, r = 18.90 and 4.72 C/cm^2, r = 24.50). At lower charge densities (0.24 C/cm^2, r = 6.17 and 0.71 C/cm^2, r = 10.04) the Au crystal structures are very regular and resemble these obtained on the smooth EvAu/PI samples.

However, the irregular surface of the strain gages causes the Au crystals to grow off the normal axis causing the crystals to collide at random angles and coalesce to form spiky tree-like structures when grown to high deposition charges. SEM micrographs (4000X) of the different Au substrate surface roughness generated by varying the EcAu deposition time between 0 and 60 minutes on smooth EvAu/PI samples are shown in Figures 4.2 – 4.6. The corresponding SEM micrographs of Au surfaces deposited on roughened EvAu/PI strain gages are shown in Figures 4.7 – 4.11. The topographies are very different from those obtained by chemical deposition of Au from a similar solutions on glass and polycarbonate substrates.[127, 128]

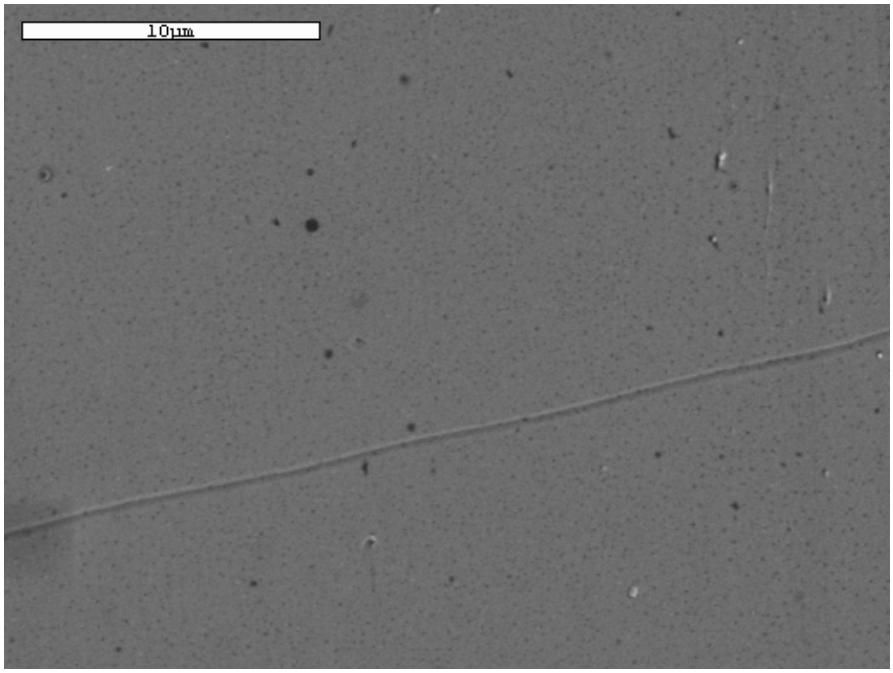

Figure 4.2 SEM micrograph of EvAu deposited on smooth polyimide (PI); 4000X

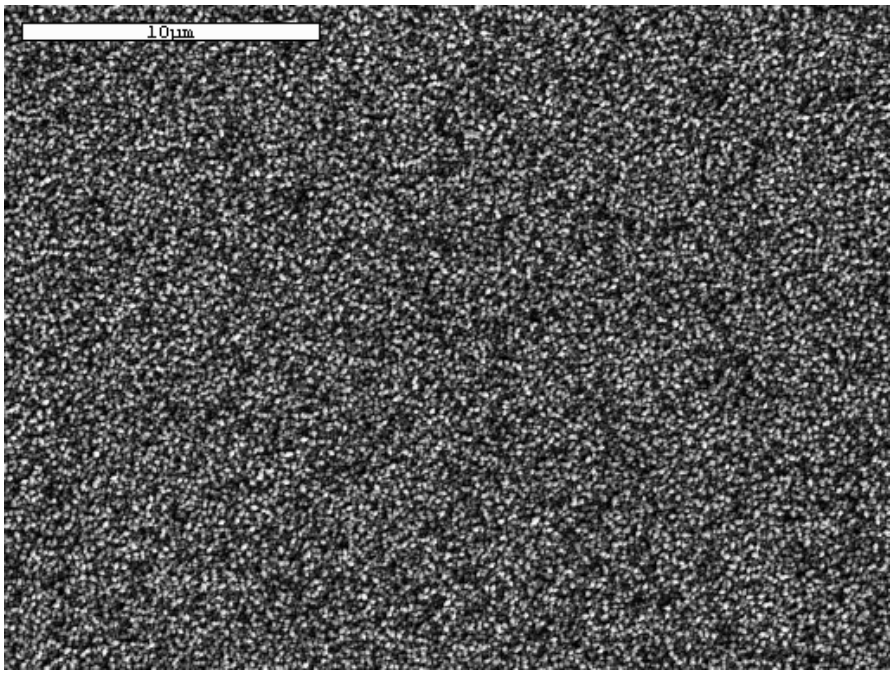

Figure 4.3 SEM micrograph of 3 minute EcAu deposition on smooth EvAu/PI; 4000X

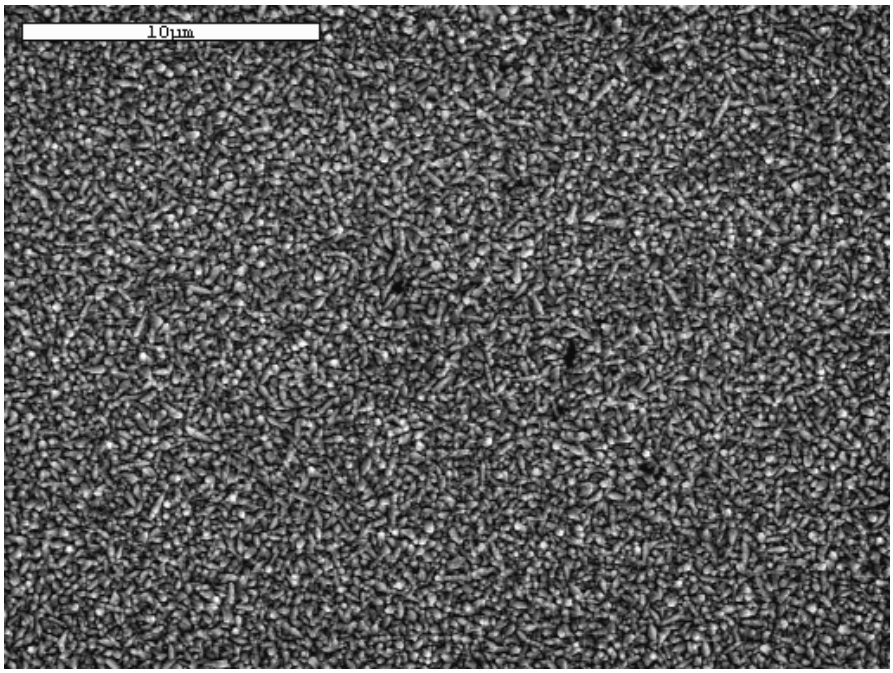

Figure 4.4 SEM micrograph of 10 minute EcAu deposition on smooth EvAu/PI; 4000X

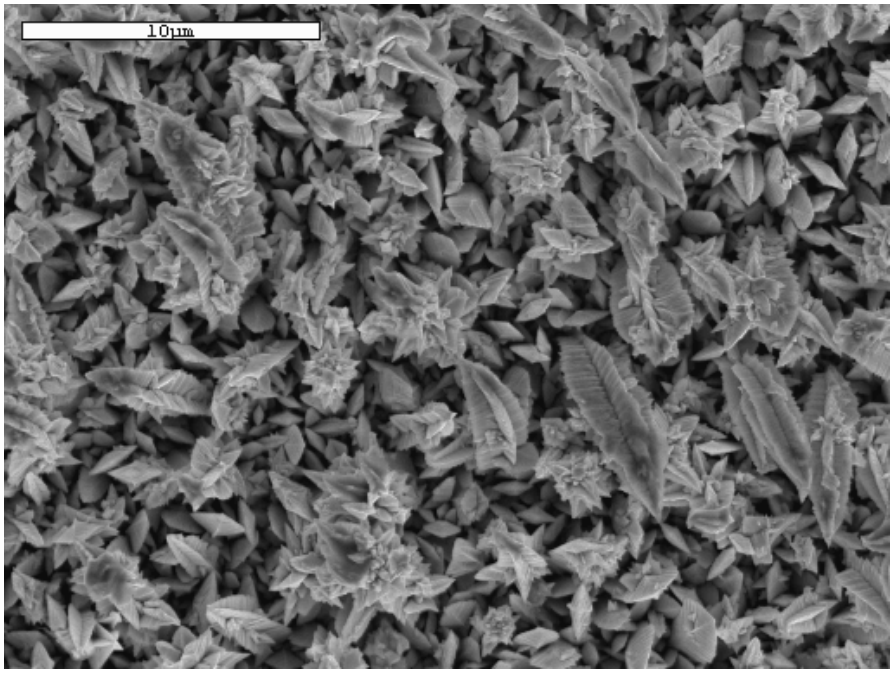

Figure 4.5 SEM micrograph of 30 minute EcAu deposition on smooth EvAu/PI; 4000X

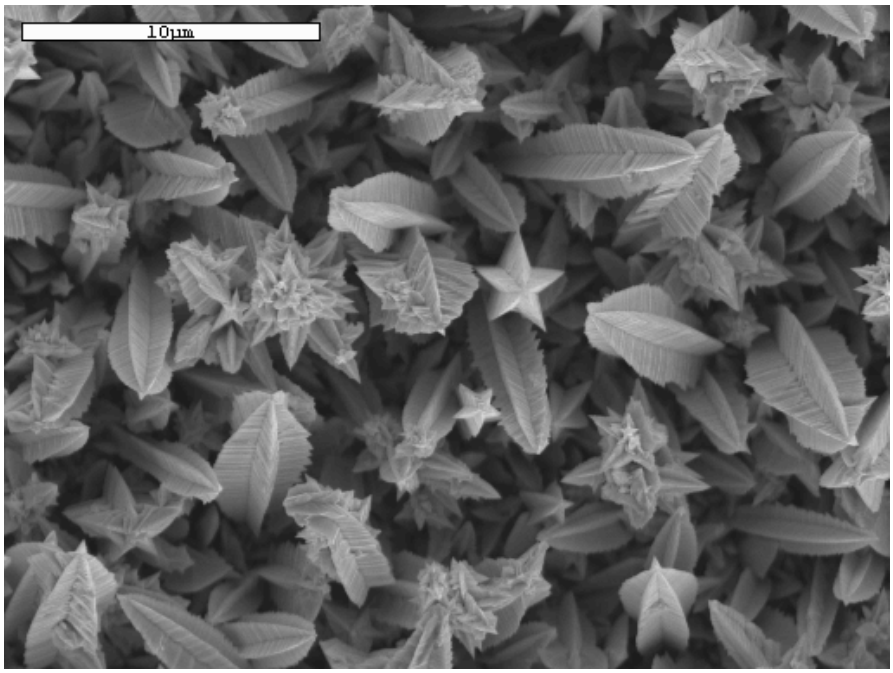

Figure 4.6 SEM micrograph of 60 minute EcAu deposition on smooth EvAu/PI; 4000X

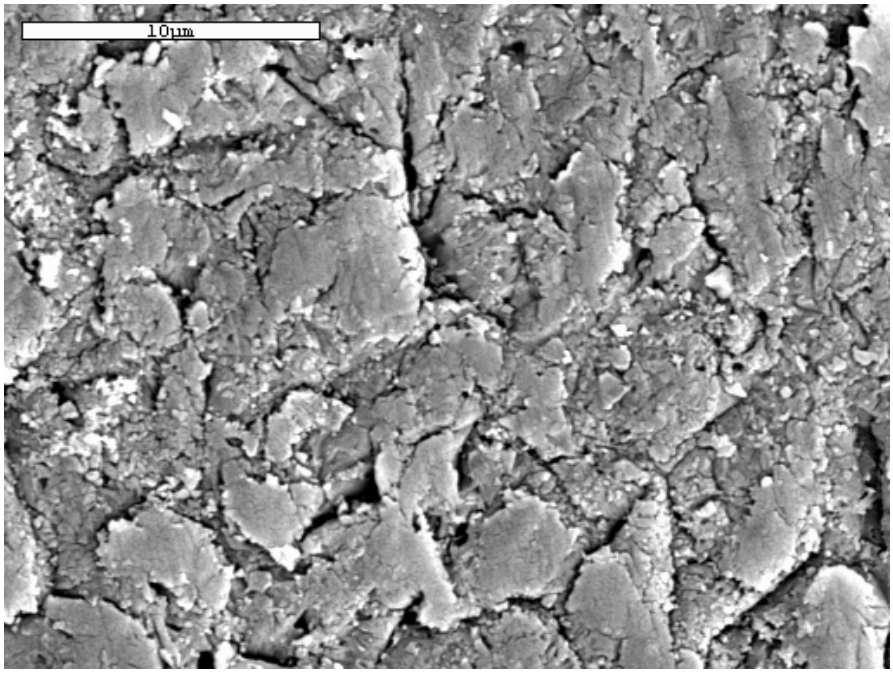

Figure 4.7 SEM micrograph of EvAu (r = 2.89) deposited on rough PI strain gage; 4000X

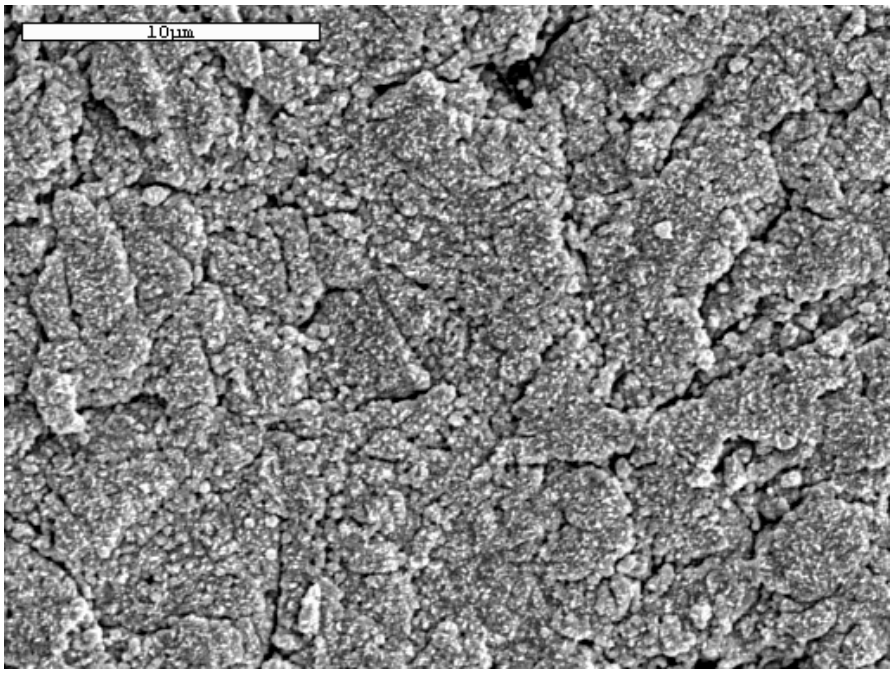

Figure 4.8 SEM micrograph of EcAu (r = 6.17, 2.5 min.) deposited on rough EvAu/PI strain gage; 4000X

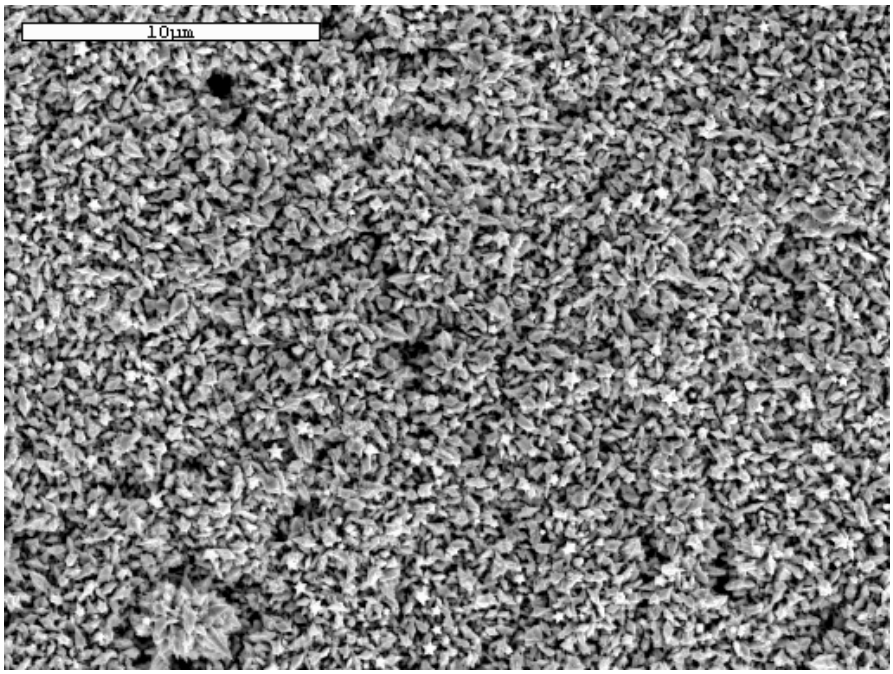

Figure 4.9 SEM micrograph of EcAu (r = 10.04, 10 min.) deposited on rough EvAu/PI strain gage; 4000X

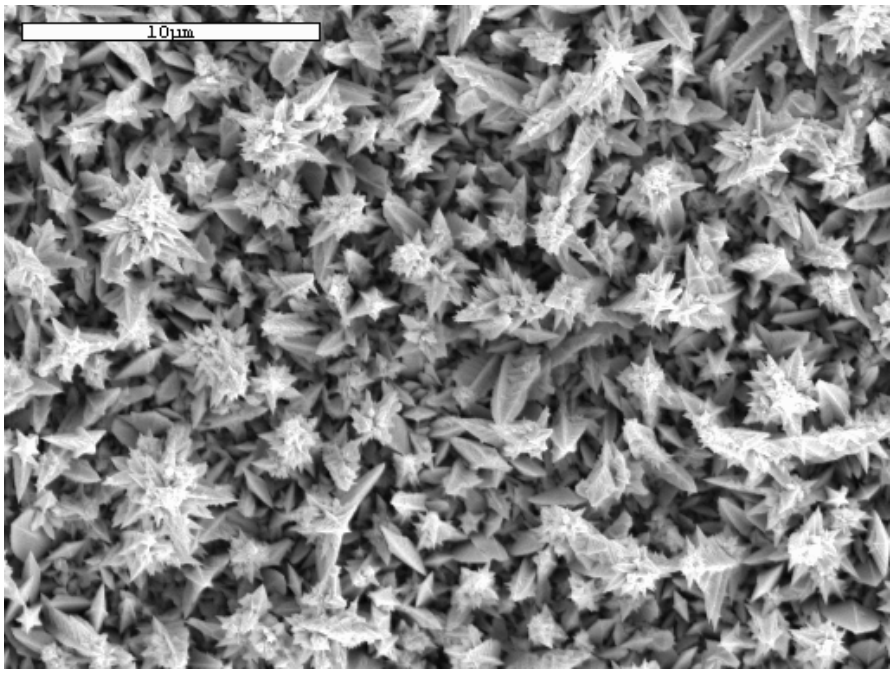

Figure 4.10 SEM micrograph of EcAu (r = 18.90, 30 min.) deposited on rough EvAu/PI strain gage; 4000X

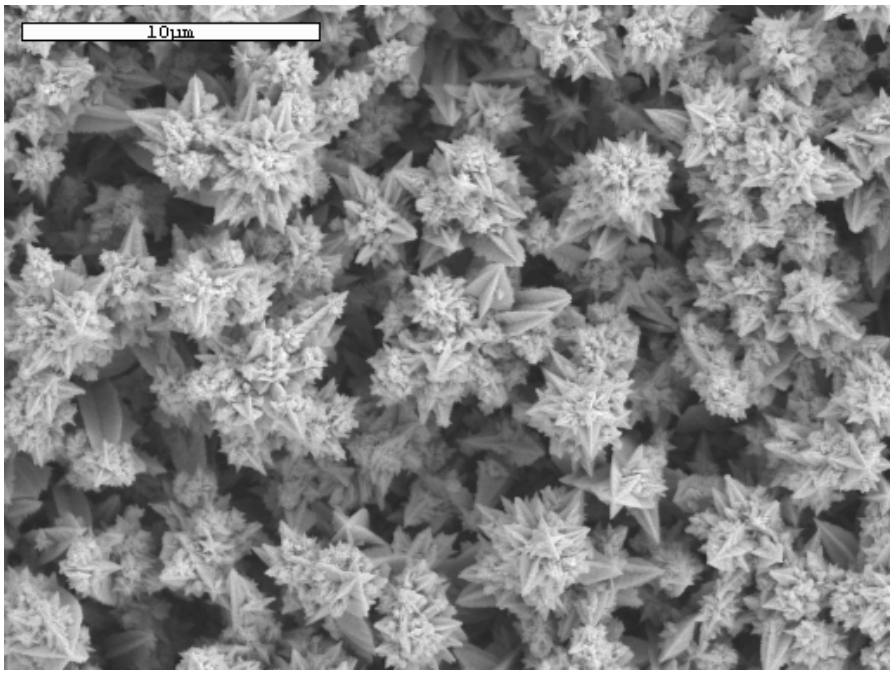

Figure 4.11 SEM micrograph of EcAu (r = 24.50, 60 min.) deposited on rough EvAu/PI strain gage; 4000X

4.5 Electrochemical Deposition of PPy

PPy films were electropolymerized potentiostatically on EvAu/PI and EcAu/EvAu/PI surfaces from a solution of 0.1 M pyrrole in aqueous 0.1 M $NaClO_4$ at 0.9 V, unless otherwise mentioned.

Figures 4.12 (EvAu), 4.13 (10 min. EcAu), 4.14 (30 min. EcAu), and 4.15 (60 min. EcAu) are SEM micrographs (4000X) which show the changes in PPy (18.9 C/cm^2) surface morphology with increased EcAu deposition time (increased surface roughness factor) on smooth PI samples. The typical nodular growth (for thick PPy films on EvAu/PI) of PPy becomes relatively flat and conforms nicely to the crystal structures as the surface roughness increases for EcAu/EvAu/PI samples (Figures 4.12 and 4.15). This reduces the overall PPy film thickness and increases the overall surface area for a given electropolymerization charge. By reducing the cross-sectional area of the PPy film and increasing the surface area the diffusion properties of the film can be improved, i.e., ions and corresponding solvent molecules can diffuse into and out of the film faster. This results in enhanced strain properties (developed strain and strain rate) of the PPy actuators as measured during redox switching of the strain sensitive actuators.

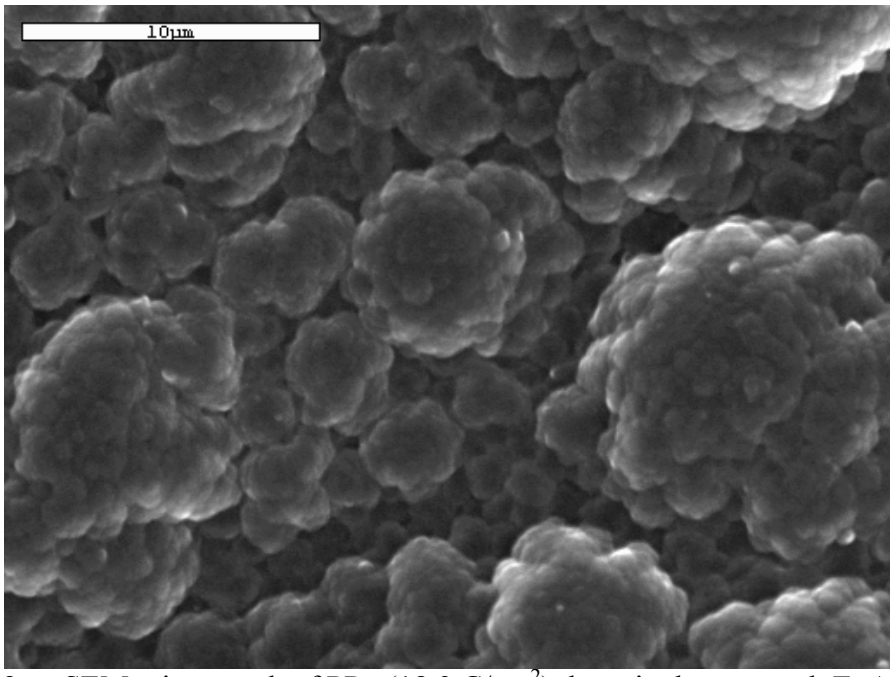

Figure 4.12 SEM micrograph of PPy (18.9 C/cm^2) deposited on smooth EvAu/PI; 4000X

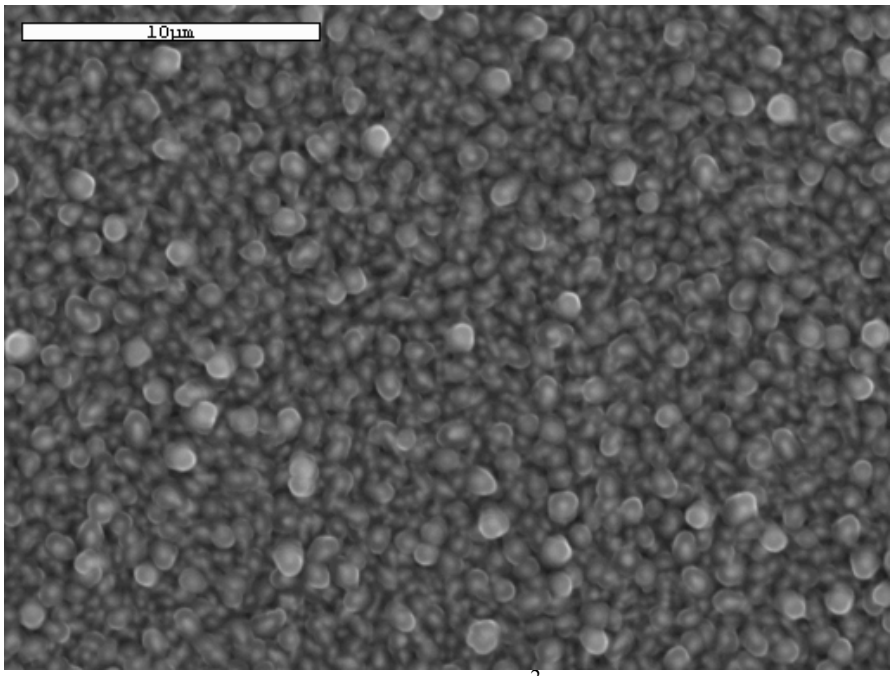

Figure 4.13 SEM micrograph of PPy (18.9 C/cm^2) deposited on smooth EvAu/PI treated with EcAu for 10 min.; 4000X

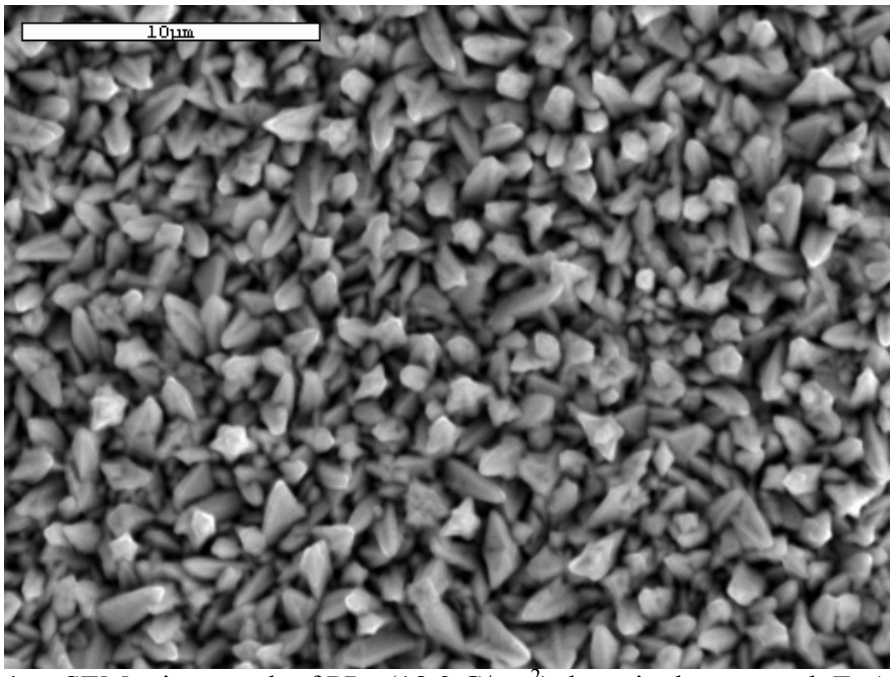

Figure 4.14 SEM micrograph of PPy (18.9 C/cm^2) deposited on smooth EvAu/PI treated with EcAu for 30 min.; 4000X

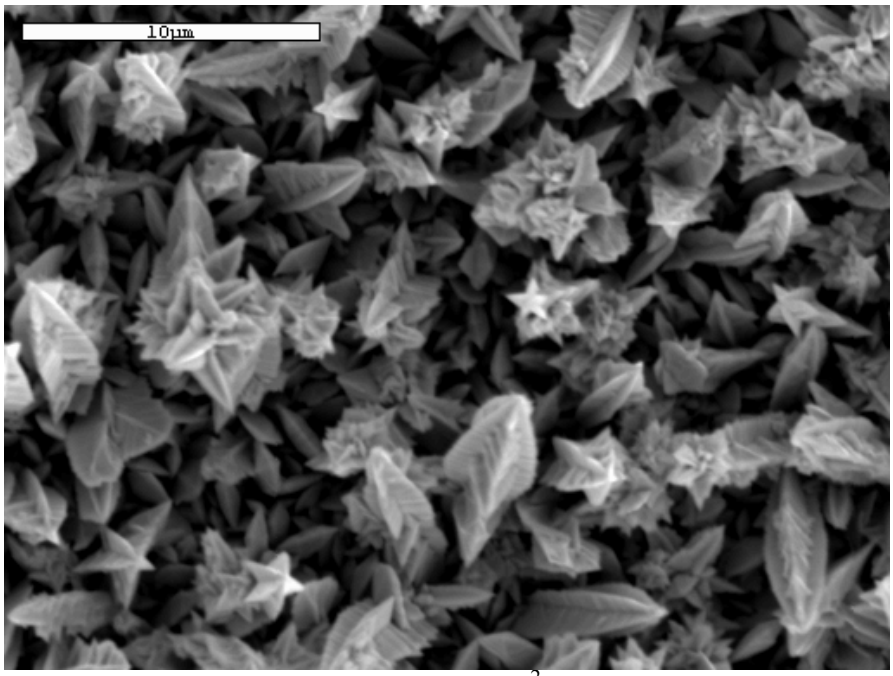

Figure 4.15 SEM micrograph of PPy (18.9 C/cm^2) deposited on smooth EvAu/PI treated with EcAu for 60 min.; 4000X

Direct determination of the PPy film thickness was difficult due to the high surface roughness of some EcAu/EvAu/PI samples (Figures 4.16 and 4.17, EcAu/EvAu/PI and PPy/EcAu/EvAu/PI samples respectively, 60 min EcAu treatment time, 4000X).

Therefore the total charge (C/cm^2) passed during electropolymerization was utilized to compare the effects of the amount of PPy on the strain response. The charge passed during electropolymerization can be directly related to the number of moles of monomer polymerized, therefore by monitoring the charge passed we can accurately deposit the same amount of PPy on each sample independent of surface roughness. This is the same technique used to control the EcAu surface roughness.

The PPy polymerization charge ranged from 0.35 C/cm^2 to 5.42 C/cm^2. Assuming 100% efficiency for the anodic deposition reaction and a charge thickness ration of 0.28 $C/\mu m \cdot cm^2$,[121] this correlates to PPy film thicknesses of 1.25 μm to 19.4 μm on smooth EvAu/PI samples. Using this information it is possible to calculate the PPy thickness as a function of electropolymerization charge and surface roughness. Assuming the same number of moles of pyrrole monomer are polymerized on all surfaces independent of surface roughness for a given polymerization charge, we can assume that the total volume of PPy is also the same for all film for a given polymerization charge. Therefore as the working electrode surface area increases the PPy thickness has to decrease to maintain the same total volume of PPy.

The equations used for this calculation are given below:

$$\text{Given:} \quad T_2 = \frac{A_1}{A_2} \cdot T_1 \qquad r = \frac{A_2}{A_1} \qquad T_1 = \frac{EPC}{0.28 \cdot C \cdot cm^{-2} \cdot \mu m^{-1}} \tag{4.1}$$

$$\text{Therefore:} \quad T_2 = \frac{1}{r} \cdot T_1 \quad \Rightarrow \quad T_2 = \frac{1}{r} \cdot \frac{EPC}{0.28 \cdot C \cdot cm^{-2} \cdot \mu m^{-1}} \tag{4.2}$$

where r is the surface roughness factor, EPC is the electropolymerization charge (C/cm^2), and $A_{1,2}$ and $T_{1,2}$ are the surface areas and PPy film thicknesses on surfaces 1 and 2

respectfully. A surface plot of the calculated PPy film thickness as a function of electropolymerization charge and surface roughness is shown in Figure 4.18.

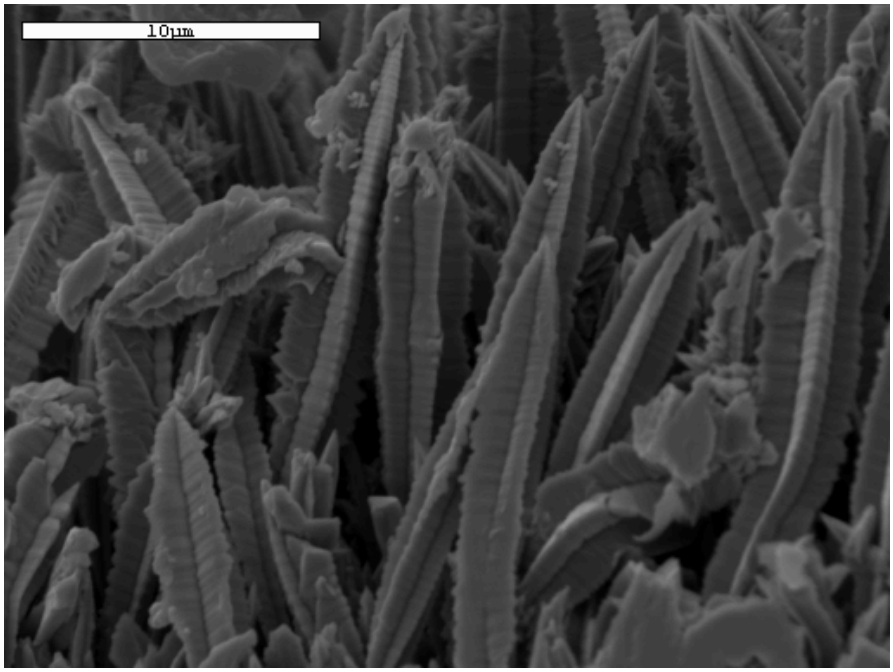

Figure 4.16 Cross-section SEM micrograph of EcAu (60 min.) deposited on smooth EvAu/PI; 4000X

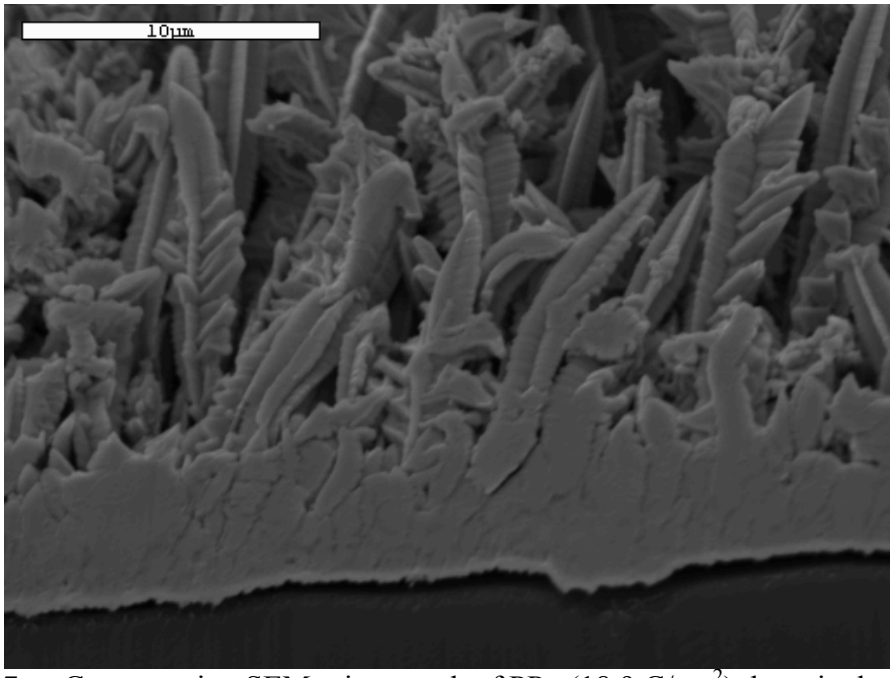

Figure 4.17 Cross-section SEM micrograph of PPy (18.9 C/cm^2) deposited on smooth EvAu/PI treated with EcAu for 60 min.; 4000X

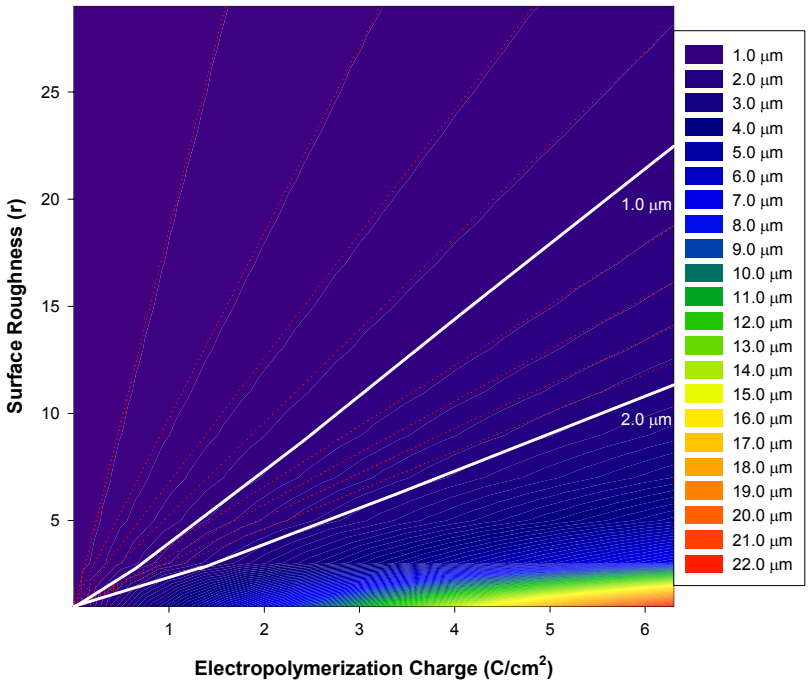

Figure 4.18 Surface plot of calculated PPy film thickness as a function of surface roughness factor (r) and electropolymerization charge (C/cm^2)

4.6 Improved PPy Adhesion to EcAu Treated Surfaces

Interlayer adhesion of PPy to EvAu/PI and EcAu/EvAu/PI was tested by a tape (810, 3M) peel-off test. PPy (0.30 C/cm2) was electrochemically deposited on EvAu (r = 2.89) and EcAu/EvAu ($r \geq 10$) coated strain gage samples. The PPy films were washed in double distilled water and dried in air for at least 24 hrs before testing. Tests were conducted with a 90° pull-of angle. PPy films were readily removed from all EvAu/PI surfaces while no delamination was noticed for films deposited on the EcAu/EvAu/PI surfaces (11 samples). This is attributed to the larger surface area of the EcAu/EvAu/PI samples providing more area for PPy bonding to Au and also physical/mechanical bonding provided by the “nooks and crannies” present on the EcAu surface.

4.7 *IN SITU* PPy/EvAu/PI Actuator Results

Initial studies were conducted utilized a 2.28 C/cm^2 PPy film (~ 10 μm) to investigate the effects of counter ion type (anion), potential limiting during redox switching, PPy film thickness, and electropolymerization potential on the overall strain response of PPy/EvAu/PI-strain gage actuators.

4.7.1 Counter Ion Effects on PPy Strain Response

It has been well documented that the actuation response of CP actuators is dependent many factors including the specific counter ion and solvent species utilized during redox switching.[9, 12, 36, 129, 130] It is also believed that the swelling behavior of these films is anion dominant.

The strain response of ClO_4^- doped (polymerized in $NaClO_4$) PPy/EvAu/PI actuators was evaluated during redox switching by potential cycling in 0.1 M aqueous $Na^+ClO_4^-$, $Na^+NO_3^-$, and Na^+Cl^- electrolyte solutions. The PPy films were fully reduced at –0.6 V for 60 s and then cycled between -0.6 V to 0.4 V at 5 mV/s. The films were cycled five times in each electrolyte to obtain a reproducible strain response. After cycling in the ClO_4^- solution the films were thoroughly washed with double distilled water and then cycled in NO_3^- and Cl^- solutions respectively. These experiments were conducted on three ClO_4^- doped samples and one NO_3^- doped (polymerized in $NaNO_3$) sample to verify the results. There was no significant difference in the ClO_4^- doped and NO_3^- doped samples. PPy films were also cycled in aqueous Li^+ ClO_4^- and Cs^+ ClO_4^- solutions to verify the performance of the ClO_4^- anion. Figure 4.19 shows the resultant normalized strain responses for these materials.

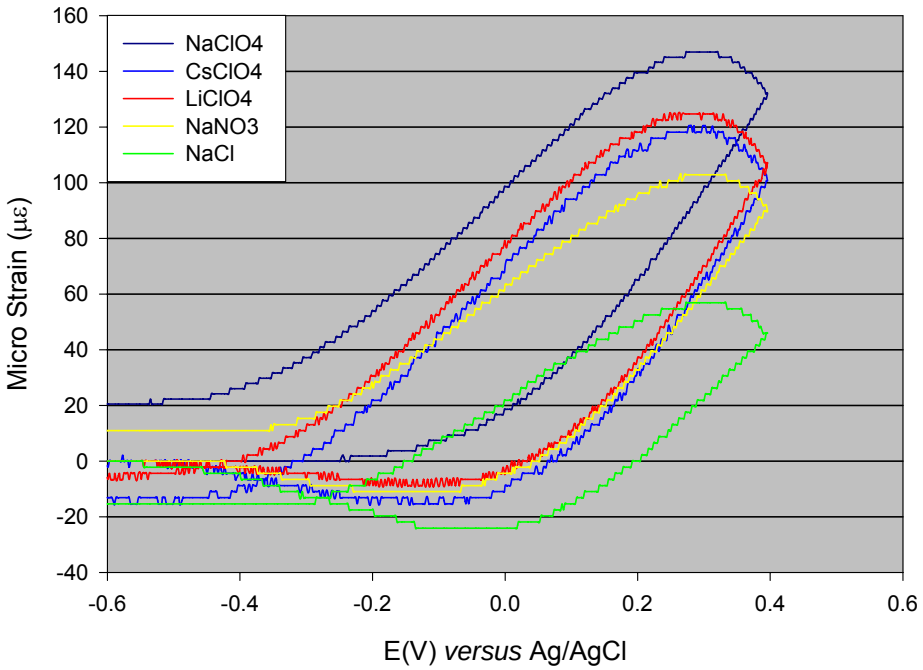

Figure 4.19 Strain response of a 2.83 C/cm^2 PPy/EvAu/PI actuator during potential cycling at 5 mV/s in aqueous $NaClO_4$, $LiClO_4$, $CsClO_4$, $NaNO_3$, and NaCl solutions.

PPy films cycled in aqueous ClO_4^- solutions exhibited Δε values of 147 με, 134 με, and 136 με for $NaClO_4$, $LiClO_4$, and $CsClO_4$ respectfully with an average Δε of 139 με between the three samples. The maximum strain was obtained at 0.3 V on the reverse scan for all three tests. This is due to the slow diffusion process of the ion migration into and out off the PPy film. Both the $LiClO_4$ and $CsClO_4$ samples exhibited an initial slight decrease in strain between –0.4 V and –0.1 V on the forward scan which was then followed by a large increase in strain, however the $NaClO_4$ samples did not exhibit this initial decrease in strain. This is indicative of cation influx during the initial reduction process.[11-13, 19, 20, 22] This process has also been shown by De Rossi et al..[44] PPy oxidizes at about –0.2 V therefore the film is reduced during the initial part of the scan. PPy films cycled in $NaNO_3$ again showed an initial decrease in strain followed by a large increase

in strain with the maximum strain value obtained at 0.3 V on the reverse scan. However the overall change in strain was smaller for $NaNO_3$ samples compared to $NaClO_4$, with a $\Delta\varepsilon$ of 114 με. This is a $\Delta\varepsilon$ difference of 33 με between the two. Similar results were obtained for samples cycled in NaCl. But NaCl produced an even lower $\Delta\varepsilon$ of 81 με. This is a difference of 66 με between NaCl and $NaClO_4$ and a difference of 33 με between NaCl and $NaNO_3$.

In review $NaClO_4$ exhibited a strain response 1.3 times higher than $NaNO_3$ and 1.8 times higher than NaCl. While $NaNO_3$ exhibited a 1.4 times higher strain response that NaCl. Similar results have been observed by Kaneto et al. for poly(styrene sulfonate) doped PPy.[131] They found that swelling during oxidation due to anion incorporation into the film was linearly proportional to the solvated anion volume. The solvated ionic volumes of Cl^- and ClO_4^- are 25 $Å^3$ and 56 $Å^3$ respectively. ClO_4^- has about a 2.2 times larger solvated ionic volume than Cl^-, which resulted in a 1.8 times increase in strain between the two counter ions for these systems. This suggests that anion exchange during redox switching is the dominant factor controlling swelling and therefore strain production.

4.7.2 Effects of Potential Limiting on PPy Strain Response

The effects of potential limiting on the PPy strain response during redox switching was also investigated utilizing strain sensitive actuators. This was also done to verify that the consumed charge followed the strain response. A square-wave potential was used to step the films between their oxidized and reduced (-0.6 V) forms. The oxidation potential was varied between 0.1 V and 0.6 V at 0.1 V increments. The films were held at each potential for 100 s starting in the reduced state. Figure 4.20 shows the square-wave strain response as a function of oxidation potential. The strain responses were normalized for

comparative purposes. From the inset of Figure 4.20 it can be seen that the normalized strain response and consumed charge have an almost linear dependency on the oxidation potential and follow each other nicely. This also supports that the number of anions in the film, determined from the consumed charge and controlled by the doping level/oxidation potential, is a dominant factor in the production of strain in these systems.[69] It can also be seen that the reduction/contraction process was faster than the oxidation process, especially at the lower oxidation potentials.

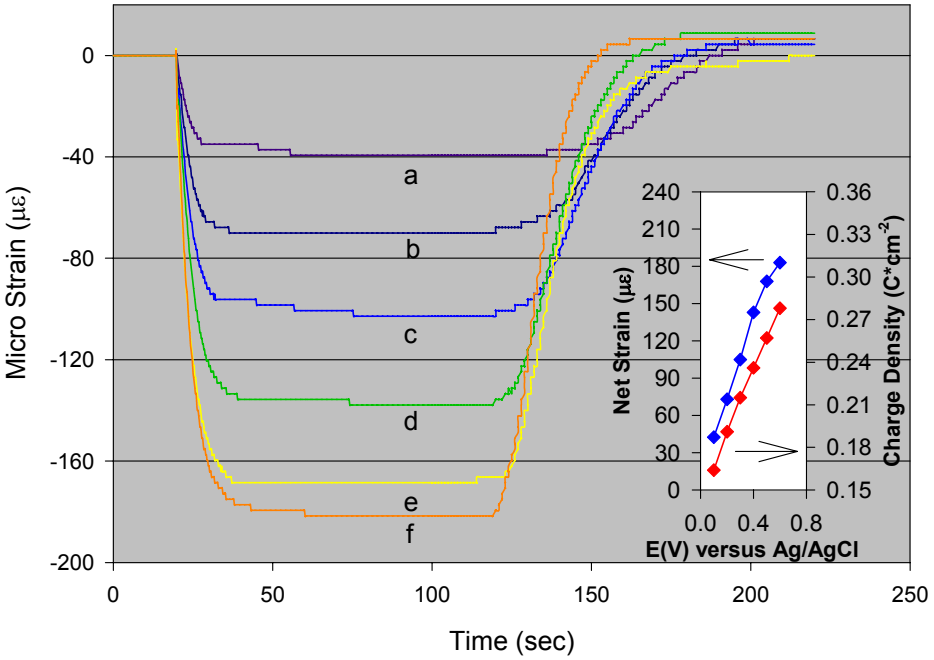

Figure 4.20 Strain response of a 2.83 C/cm^2 PPy/EvAu/PI actuator during potential stepping (100 s/step) in $NaClO_4$ between –0.6 V and (a) 0.1 V, (b) 0.2 V, (c) 0.3 V, (d) 0.4 V, (e) 0.5 V, and (f) 0.6 V

4.7.3 Effects of PPy Film Thickness on Strain Response

The effects of PPy film thickness on the overall strain performance of PPy/EvAu/PI actuators were evaluated utilizing the strain sensitive actuator technology. PPy films were electropolymerized on a EvAu/PI strain gage to six different charge densities: 0.79

C/cm2, 1.6 C/cm2, 2.4 C/cm2, 3.2 C/cm2, 4.0 C/cm2, and 4.8 C/cm2. The film were fully oxidized at 0.4 V and then potentiostatically stepped to –0.6 V and held for 100 s to allow the strain response to equilibrate and then stepped back to 0.4 V and held for an additional 100 s. This was done five times to obtain reproducible results. As can be seen from Figure 4.21 as the electropolymerization charge density was increased the overall strain response of the actuator also increased. However the given amount of change in strain for a given increase in film thickness decreased with increasing charge densities. The same trend can be seen in the charge data (Figure 4.22). PPy films electropolymerized to 0.79 C/cm2 (2.8 μm, calculated) produced a Δε of 59 με. Where a 4.8 C/cm2 PPy films (17.1 μm, cal.) produced a Δε of 236 με, this is a 4 times increase in strain for a 6.1 times increase in PPy film thickness. The rest of the data is as follows: 1.6 C/cm2 (5.7 μm, cal.) PPy Δε = 113 με, 2.4 C/cm2 (8.6 μm, cal.) PPy Δε = 162 με, 3.2 C/cm2 (11.4 μm, cal.) PPy Δε = 186 με, and 4.0 C/cm2 (14.3 μm, cal.) PPy Δε = 212 με. An interesting trend is that the 1.6 C/cm2 and 2.4 C/cm2 PPy films produced a 1.9 and 2.8 times increase in strain for a calculated 2.0 and 3.1 times increase in the PPy film thickness respectively (same for electropolymerization charge) when compared to the 0.79 C/cm2 PPy films. There is almost a direct relationship between PPy film thickness and the produced strain response of these films. However, 3.2 C/cm2, 4.0 C/cm2, and 4.8 C/cm2 PPy films produced a 3.2, 3.6, and 4 times increase in strain for a 4.1, 5.1, and 6.1 times increase in PPy film thickness respectfully when compared to 0.79 C/cm2 PPy films. A simpler way of looking at this is to normalize the overall change in strain (Δε) to the PPy film thickness by dividing by the calculated PPy thickness (T_{PPy}). The resulting $\Delta\varepsilon/T_{PPy}$ ratio gives the strain (με) produced per unit thickness (μm) of PPy. The

resulting $\Delta\varepsilon/T_{PPy}$ ($\mu\varepsilon/\mu m$) ratios for the above PPy/EvAu/PI strain gage samples are 21.07, 19.82, 18.84, 16.32, and 13.80 for 2.8 μm, 5.7 μm, 8.6 μm, 11.4 μm, and 17.1 μm PPy films respectfully. As can be seen, the amount of strain produced for a given thickness of PPy decreases as PPy film thickness increases.

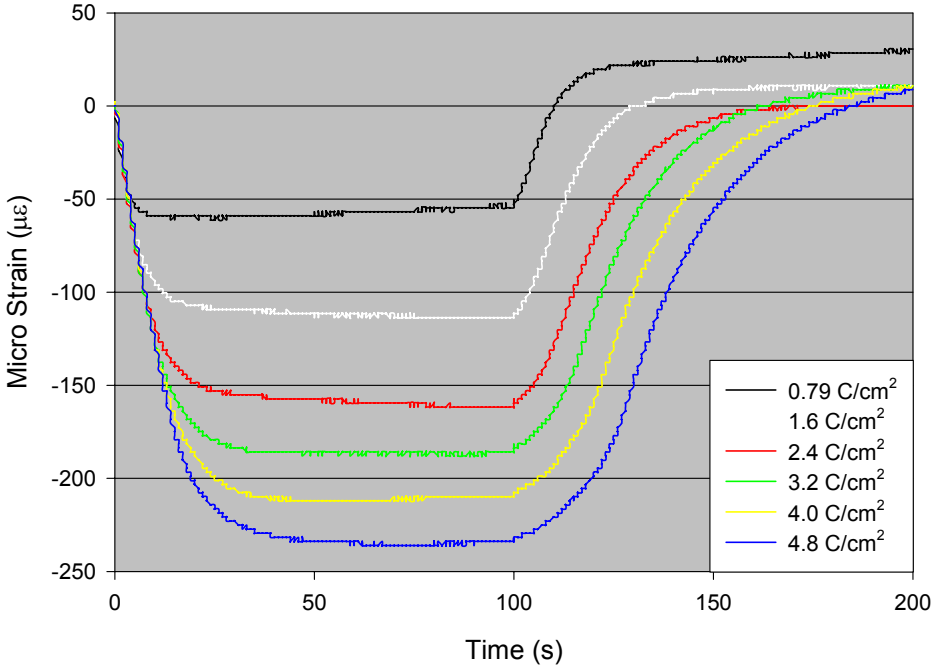

Figure 4.21 In situ strain response of PPy/EvAu/PI actuators of varying PPy film thickness during potential stepping between –0.6 V and 0.4 V in aqueous NaClO4. Electropolymerization charge densities were 0.79 C/cm2 (2.8 μm, calculated), 1.6 C/cm2 (5.7 μm, cal.), 2.4 C/cm2 (8.6 μm, cal.), 3.2 C/cm2 (11.4 μm, cal.), 4.0 C/cm2 (14.3 μm, cal.), and 4.8 C/cm2 (17.1 μm, cal.).

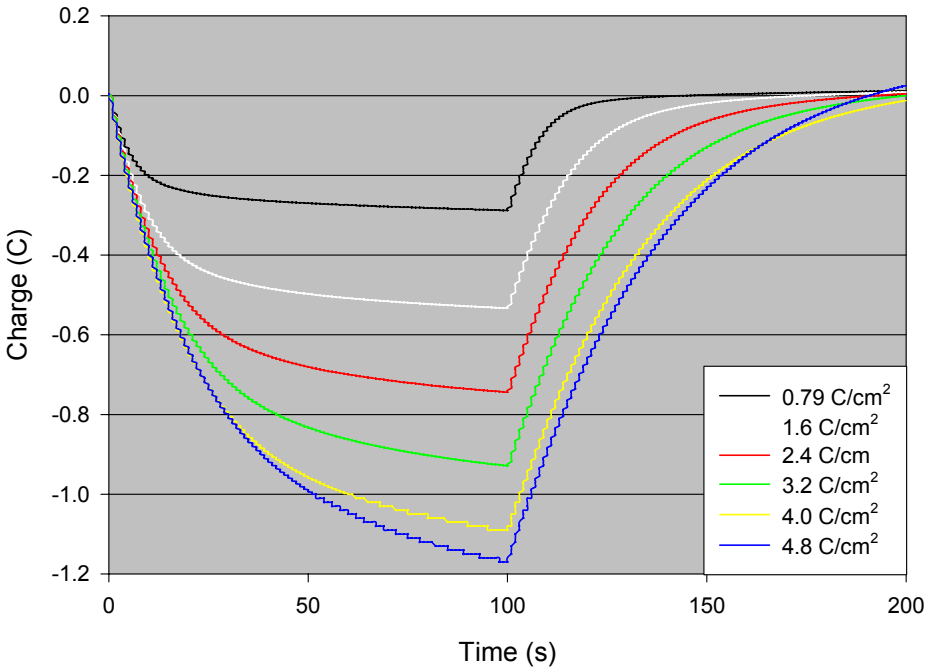

Figure 4.22 *In situ* charge response of PPy/EvAu/PI actuators of varying PPy film thickness during potential stepping between –0.6 V and 0.4 V in aqueous $NaClO_4$. Electropolymerization charge densities were 0.79 C/cm^2 (2.8 μm, calculated), 1.6 C/cm^2 (5.7 μm, cal.), 2.4 C/cm^2 (8.6 μm, cal.), 3.2 C/cm^2 (11.4 μm, cal.), 4.0 C/cm^2 (14.3 μm, cal.), and 4.8 C/cm^2 (17.1 μm, cal.).

PPy film thickness is an important factor in the overall strain performance of PPy based actuators. The thicker the film the more material there is to swell and therefore more strain is produced. However as the film thickness increases the diffusion-limited nature of these materials becomes a greater influence on the overall mechanical properties. As the film thickness increases the diffusion of ions into the film is slowed and therefore the deeper regions of the film (closer to the electrode) do not swell as much as the surface regions. Therefore a strain gradient or swelling gradient is developed in the film and the given increase in strain for a given increase in film thickness decreases as film thickness increases. Also as the film thickness increases the effects of Ohmic drop [48] (film resistance) becomes more significant. As the film thickness increases the resistance

of the film causes a potential gradient through the cross section of the film. In result different regions of the film are exposed to different oxidation potentials and as shown previously lower oxidation potentials produce lower strains.

4.7.4 Effects of Polymerization Potential on PPy Strain Response

The effects of electropolymerization potential on the strain response of PPy were also investigated utilizing strain sensitive actuators. This was also done to determine the optimal electropolymerization potential to produce the maximum strain for these systems. It is believed that by controlling the electropolymerization potential the cross-link density of the resultant PPy film can also be controlled. Higher cross-linking densities should produce systems yielding higher degree of strain, however if the cross-link density becomes to high the film will become too rigid and this will decrease the overall strain response of the actuator. Recently, Maw et al. [132] demonstrated that bending deformation for PPy(dodecylbenzenesulfonate)/Au/PI laminates prepared galvanostatically was greater at low deposition current densities (0.4 mA/cm^2) when compared to higher deposition current densities (40 mA/cm^2).

PPy films (2.83 C/cm^2) were prepared potentiostatically at 0.7 V, 0.8 V, 0.9 V, and 1.0 V and then subsequently were switched between –0.6 V and 0.4 V by square-wave potentials, with 100 s steps. The resultant strain response (shown in Figure 4.23) was found to be inversely proportional to the polymerization potential at potentials greater than 0.7 V. Films prepared at potentials of 0.9 V and 1.0 V had an overall strain response on the order of ~20 % less than films prepared at 0.7 V. This trend was also later confirmed on EcAu samples; however it was also shown on EcAu samples that the strain response increased linearly with the electropolymerization potential at potentials ≤ 0.7 V. The switching charge density, during PPy oxidation, (inset Figure 4.23) for all

films were found to be similar indicating that the decrease in the strain response is not due to a decrease in the electroactivity of the PPy films. It can be inferred that at electropolymerization potentials above 0.7 V the increasing cross-link density of the PPy film start to hamper strain development in these systems.

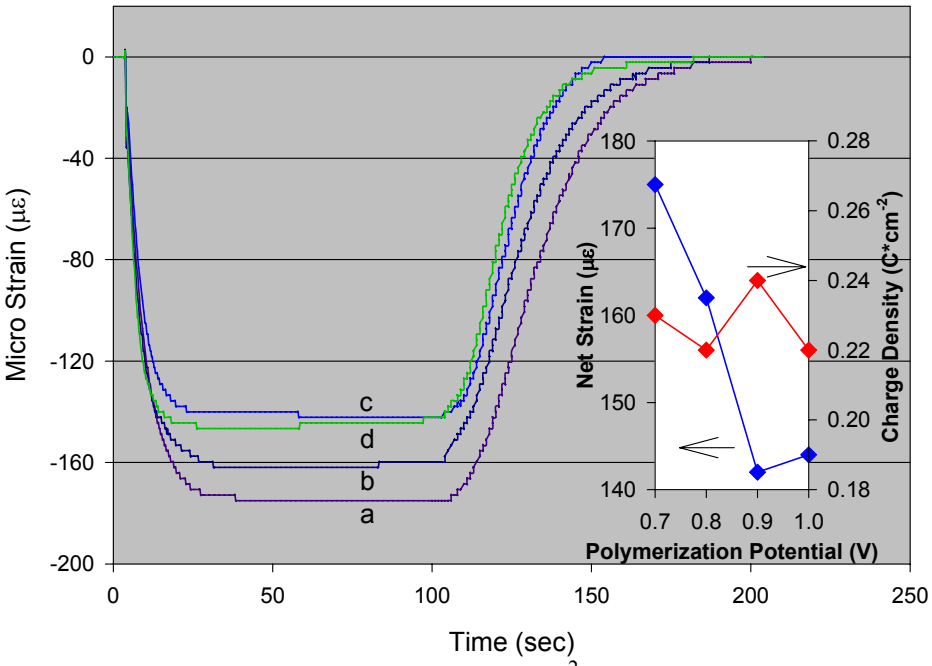

Figure 4.23 *In situ* strain response of a 2.83 C/cm^2 PPy/EvAu/PI actuator during potential stepping between –0.6 V and 0.4 V in aqueous $NaClO_4$. PPy was prepared potentiostatically at (a) 0.7 V, (b) 0.8 V, (c) 0.9 V, and (d) 1.0 V.

4.8 *IN SITU* PPy/EcAu/EvAu/PI Actuator Results

As stated earlier, by electrochemically depositing Au (EcAu) on EvAu coated substrates adhesion of CP's can be dramatically improved due to the increased surface roughness of the EcAu layer. By increasing the adhesion of the CP to the substrate the overall strain response of the actuator should be increased. Also be utilizing the EcAu surface modification the overall CP film thickness is reduced improving diffusion and reducing the effects of Ohmic drop in the film. Studies were conducted on EcAu treated EvAu/PI strain gages to investigate these effects. The effects of surface roughness (EcAu

film thickness), PPy electropolymerization charge (PPy film thickness), counter-ion type, frequency response, and overall actuator lifetime were evaluated on EcAu/EvAu/PI stain gages actuators. These results were also compared to the results obtained on EvAu/Pi strain gages.

4.8.1 Effects of PPy electropolymerization charge and surface roughness factor

The two main factors of interest in these experiments are the effects of PPy film thickness and EcAu film thickness or surface roughness factor. Both of these factors are controlled by the electrochemical charge passed during the deposition of these materials. However the PPy film thickness is also dependent on the surface roughness factor. As stated earlier, as the surface roughness factor increases, for a given PPy electropolymerization charge, the resulting PPy film thickness decreases. The total amount of PPy present on the working electrode remains the same; however the working electrode surface area is increased. Resulting in the distribution of the same amount of PPy over a larger surface area and thereby decreasing the overall PPy film thickness.

4.8.1.1 Effects of surface roughness factor

The effects of Au surface roughness were tested for surface roughnesses of r = 2.89 for EvAu and r = 6.17, 7.13, 10.04, 18.90, and 24.50 for EcAu. Three 1.18 C/cm^2 PPy films were tested on each surface roughness by potentially stepping between -0.6 V to 0.4 V in 0.1 M aqueous NaClO4. It was shown that for a given PPy film thickness (specific polymerization charge) the strain response increases up to an optimal surface roughness factor and then decreased when this optimal point was passed. The square-wave strain response is shown in Figure 4.24. The resulting $\Delta\varepsilon$ for each surface roughness is plotted in Figure 4.25, from this it can be seen that the overall change in strain increases from 80 $\mu\varepsilon$ for r = 2.89 (EvAu, PPy = 1.46 μm cal.) up to 166 $\mu\varepsilon$ for r = 10.04 (0.42 μm cal.) and

then falls back off to 150 με for r = 18.90 (0.22 μm cal.) and 107 με for r = 24.50 (0.17 μm cal.).

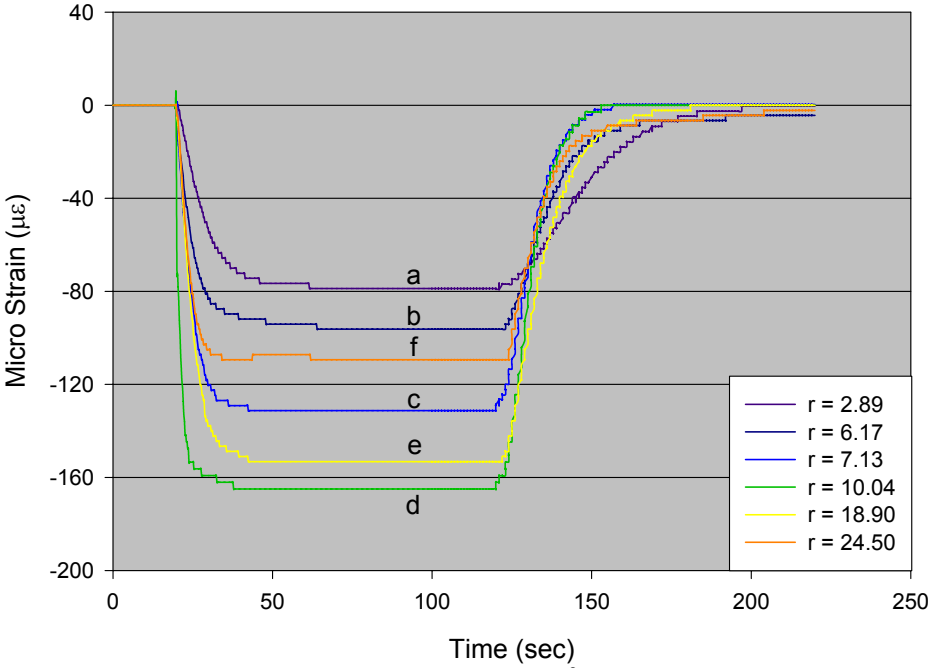

Figure 4.24 *In situ* strain response of a 1.18 C/cm^2 PPy/EcAu/EvAu/PI actuator during potential stepping between –0.6 V and 0.4 V in aqueous $NaClO_4$. With surface roughnesses factors of (a) 2.89, (b) 6.17, (c) 7.13, (d) 10.04, (e) 18.90, and (f) 24.50.

The same trend can be seen in the strain rate (με/sec) response (Figure 4.26). The strain rate increases from 5.69 με/sec during expansion (1.75 με/sec during contraction) for r = 2.89 up to 30.68 με/sec (8.68 με/sec) for r = 10.04 and then falls back off to 18.38 με/sec (7.00 με/sec) for r = 18.90 and 16.19 με/sec (5.25 με/sec) for r = 24.50. This is due to the overall decrease in PPy film thickness. For a given PPy polymerization charge, as the surface roughness factor increases and the PPy film thickness decreases. There is an optimal point whereby the PPy film thickness becomes insufficient to deflect/strain the strain gage based actuator. This point is dependent on the PPy polymerization charge and will be shown later. However as the film thickness decreases

the diffusion rate of ions in the film increases producing a higher strain rate. This is true until the overall strain response of the actuator is hindered by the EcAu film thickness.

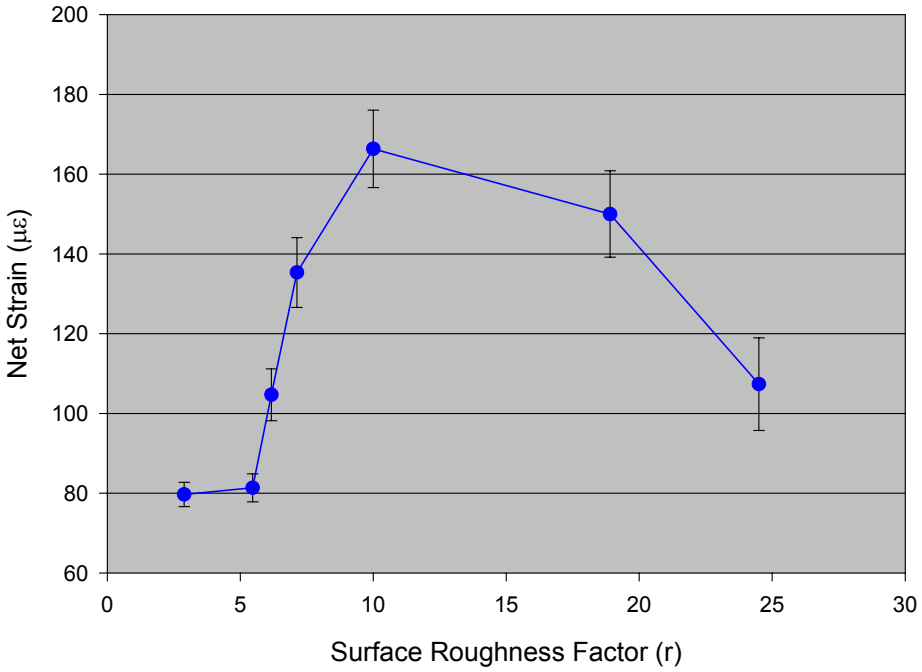

Figure 4.25 Effects of surface roughness factor (r) on the overall change in strain (Δε) of a 1.18 C/cm^2 PPy/EcAu/EvAu/PI actuator during potential stepping between –0.6 V and 0.4 V in aqueous $NaClO_4$.

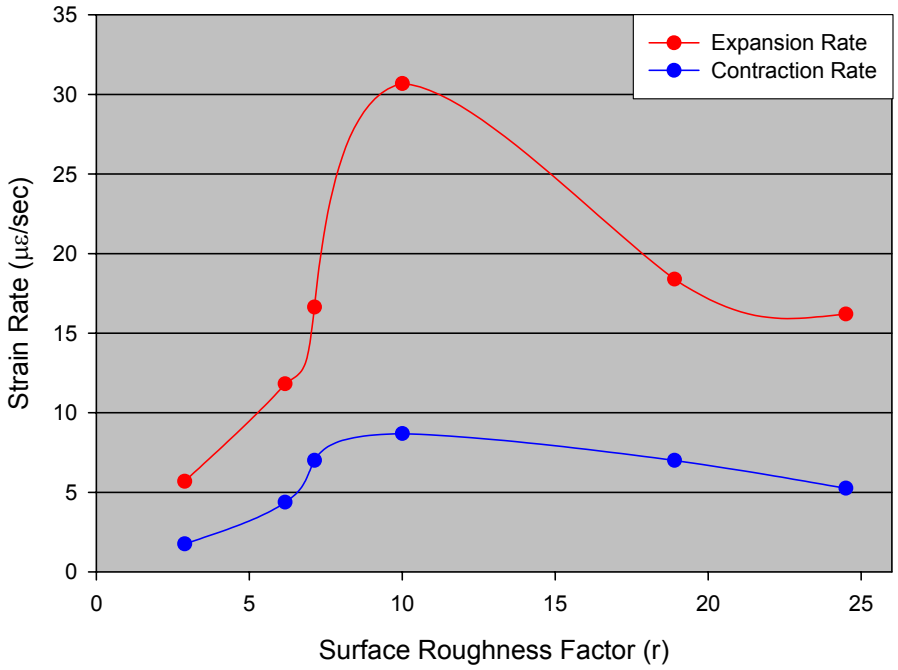

Figure 4.26 Effects of surface roughness factor (r) on the strain rate (με/sec) of a 1.18 C/cm2 PPy/EcAu/EvAu/PI actuator during potential stepping between –0.6 V and 0.4 V in aqueous NaClO4.

4.8.1.2 Effects of PPy electropolymerization charge on strain (PPy film thickness)

The effects of PPy electropolymerization charge were also evaluated on a number of surface roughnesses. PPy samples were electropolymerized at 0.79 C/cm^2, 1.6 C/cm^2, 2.4 C/cm^2, 3.2 C/cm^2, 4.0 C/cm^2, and 4.8 C/cm^2 and then potentially stepped between –0.6 V and 0.4 V (100 s steps) in 0.1 M $NaClO_4$. An example is shown in Figure 4.27 for a surface roughness factor of 18.9. Unlike the surface roughness effects, the strain response was shown to increase with increasing PPy electropolymerization charge for all samples. The resulting Δε for PPy of 0.79 C/cm^2 (0.15 μm cal.), 1.6 C/cm^2 (0.30 μm cal.), 2.4 C/cm^2 (0.45 μm cal.), 3.2 C/cm^2 (0.60 μm cal.), 4.0 C/cm^2 (0.76 μm cal.), and 4.8 C/cm^2 (0.91 μm cal.) is 162 με, 270 με, 339 με, 389 με, 450 με, and 498 με respectively on a surface roughness of 18.90 (~30 min EcAu treatment). The same effects of PPy film thickness can be seen here as was seen for the PPy/EvAu/PI samples. As the PPy thickness increases the increase in strain for a given increase in PPy film

thickness decreases. The resulting strain to thickness ratios ($\Delta\varepsilon/T_{PPy}$) are 1080, 900, 753, 648, 592, and 547 for the PPy samples mentioned above respectfully. The effects of PPy electropolymerization charge for different surface roughness values of 2.89, 6.17, 10.00, 18.90, and 24.50 are shown in Figure 4.28.

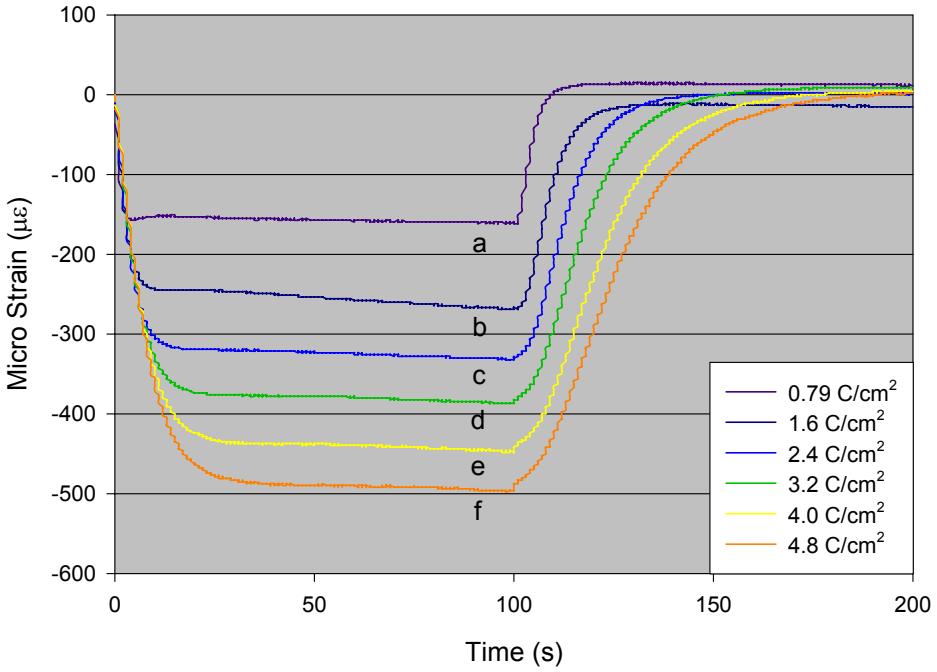

Figure 4.27 *In situ* strain response of PPy/EcAu/EvAu/PI actuator during potential stepping between –0.6 V and 0.4 V in aqueous $NaClO_4$. With surface roughnesses factors of 18.90 and PPy electropolymerization charge of (a) 0.79 C/cm^2, (b) 1.6 C/cm^2, (c) 2.4 C/cm^2, (d) 3.2 C/cm^2, (e) 4.0 C/cm^2, and (f) 4.8 C/cm^2.

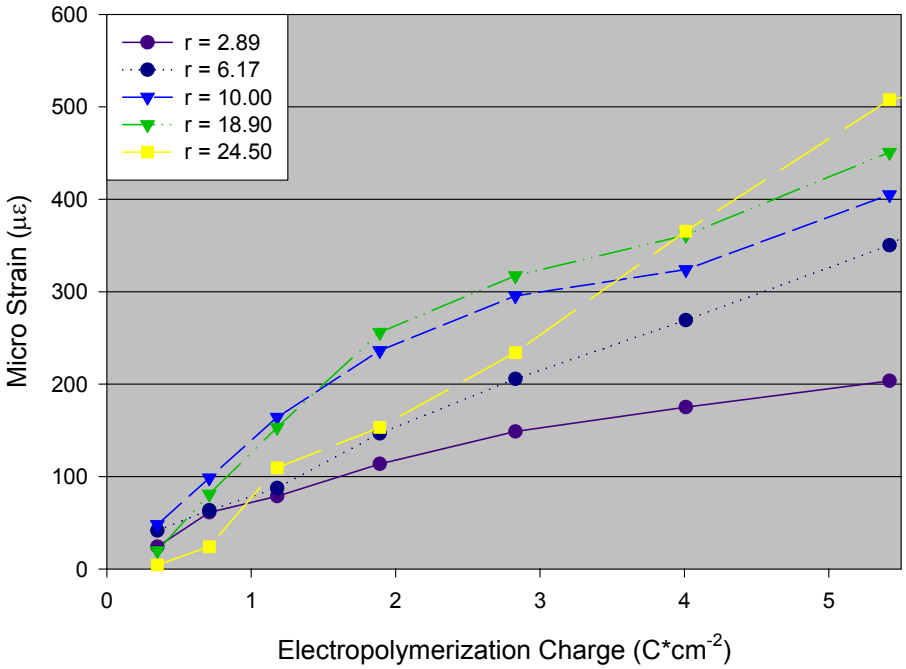

Figure 4.28 Maximum change in strain response of PPy/EcAu/EvAu/PI actuators during potential stepping between –0.6 V and 0.4 V in aqueous $NaClO_4$ with increasing electropolymerization charge. Measured on surface roughnesses of (a) r = 2.89 (EvAu), and EcAu samples of r = (b) 6.17, (c) 10.00, (d) 18.90, and (e) 24.50.

4.8.1.3 Combined effects of PPy electropolymerization charge and surface roughness factor

The overall combined effects of PPy electropolymerization charge and surface roughness factor (r) on strain response are tied together nicely in the surface plot shown in Figure 4.29. From the surface plot it is evident that the effects of electropolymerization charge and surface roughness decrease as the value of these factors increase. If you look at the effects of electropolymerization charge and surface roughness separately it is evident that the slope of the strain versus factor plot is greatest initially and then decreases with increased factor level. It is evident that the increased strain response from both of these factors will eventually reach a plateau at an optimal value.

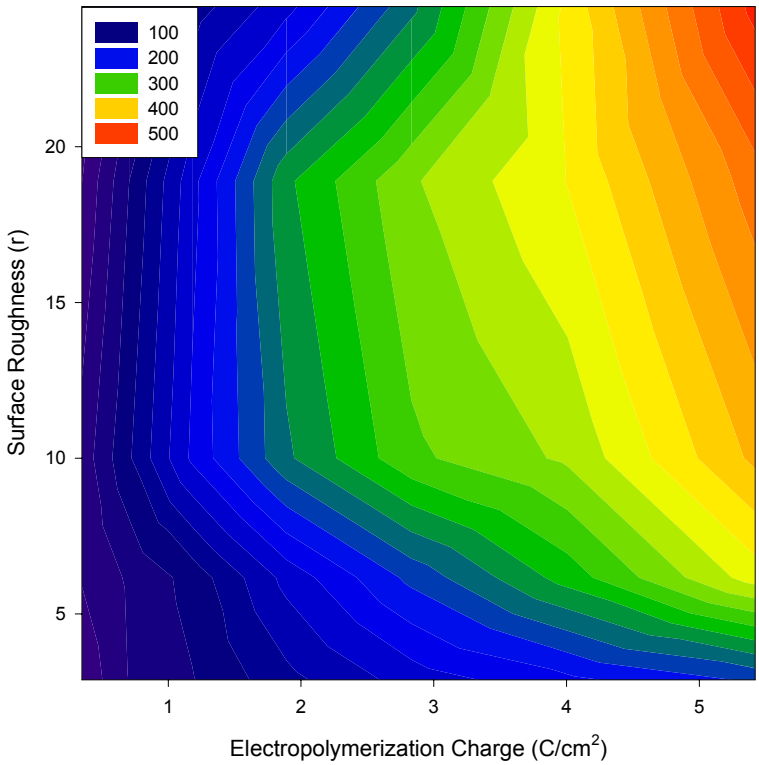

Figure 4.29 Surface plot of the normalized overall strain response of PPy as a function of electropolymerization charge and surface roughness factor (r).

4.8.2 Counter Ion Effects on PPy Strain Response

Counter ion effects were also evaluated on EcAu/EvAu/PI strain gage actuators and the results were found to similar to those found on EvAu/PI strain gage actuators. However the overall $\Delta\varepsilon$ was much higher for the EcAu samples when compared to EvAu samples. PPy/EcAu/EvAu/PI strain gages (PPy = 8 C/cm^2, r = 18.9) were cycled between –0.6 V and 0.4 V at 5 mM/s in aqueous $LiClO_4$, $NaNO_3$, and NaCl. Samples cycled in $LiClO_4$ produced a $\Delta\varepsilon$ of 457$\mu\varepsilon$. While samples cycled in $NaNO_3$ and NaCl produced $\Delta\varepsilon$ of 278 $\mu\varepsilon$ and 219 $\mu\varepsilon$ respectfully. The $\Delta\varepsilon$ results for the EvAu samples were 147 $\mu\varepsilon$, 133 $\mu\varepsilon$, 136 $\mu\varepsilon$, 114 $\mu\varepsilon$, and 81 $\mu\varepsilon$ for $NaClO_4$, $LiClO_4$, $CsClO_4$, $NaNO_3$, and NaCl respectfully. It should be noted that the PPy electropolymerization charge for the EvAu samples was 2.28 C/cm^2 (~10 μm) while the electropolymerization charge for

the EcAu samples was 8 C/cm^2 (1.5 μm). However, the $LiClO_4$ produced a 2.1 times grater strain response than NaCl and as stated before the solvated ion size for ClO_4^- ~2.2 times larger than Cl^-. This is a much closer correlation between the strain response and solvated ionic size than in EvAu samples. The cyclic voltammetry strain response is shown in Figure 4.30.

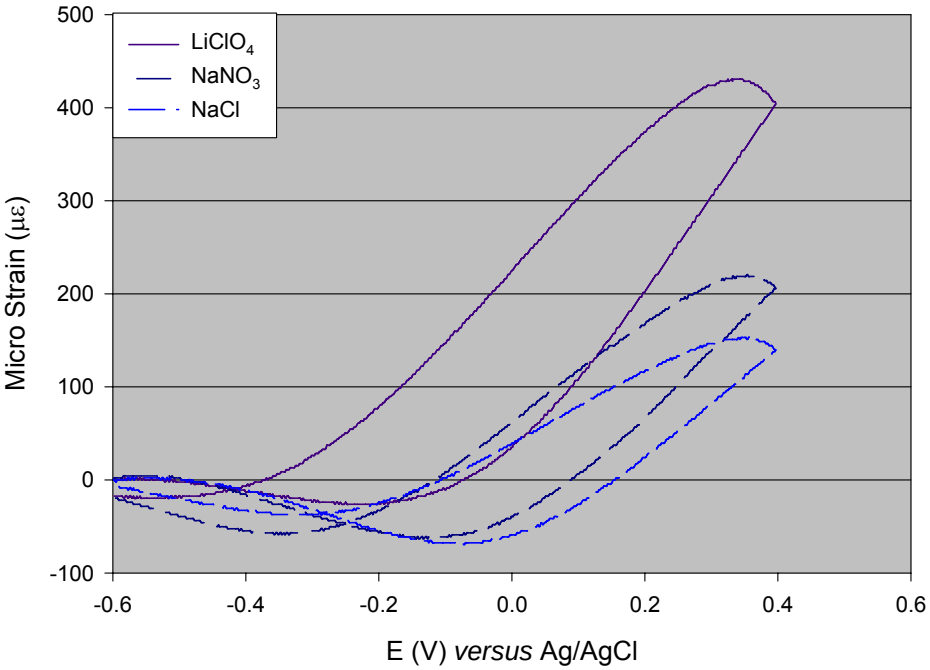

Figure 4.30 *In* situ Strain response of a 8.0 C/cm^2 PPy/EcAu/EvAu/PI actuator during potential cycling at 5 mV/s in aqueous (a) $LiClO_4$, (b) $NaNO_3$, and (c) NaCl solutions.

4.8.3 Frequency response

The frequency response of these systems was also evaluated using the strain sensitive actuators. PPy (1.18 C/cm2) on EvAu (r = 2.89) and EcAu (r = 10.00) was stepped between -0.6 V and 0.4 V in aqueous 0.1 M $NaClO_4$ at increasing frequencies from 0.01 to 0.5 Hz. Strain decreased as a function of frequency for both systems; however the strain response for the EcAu systems remained consistently higher than for EvAu systems at all frequencies (Figure 4.31). The charge response exhibited a similar

response to frequency as the strain response. The charge efficiency (με/C) was also evaluated and is shown in the inset of Figure 4.31. The charge efficiency of PPy on EcAu was significantly higher than on EvAu surfaces. The greater efficiency of the EcAu systems can be a result of improved adhesion of the PPy to the electrode and smaller Ohmic drop in the system due to the thinner PPy layer.

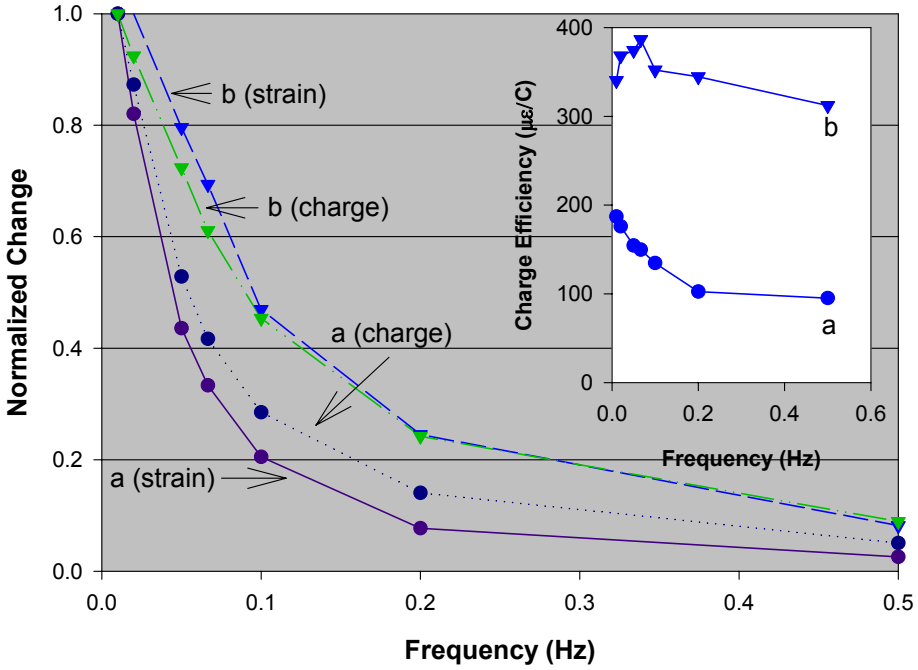

Figure 4.31 *In situ* normalized (relative to 0.01 Hz) strain and charge response of 1.18 C/cm^2 PPy as a function of frequency on (a) r = 2.89 (EvAu) and (b) r = 10.0 (EcAu) surfaces. Inset shows the charge efficiency (με/C) as a function of frequency.

4.8.4 Lifetime

The effects of EcAu treatments on actuator lifetime were also initially investigated by potentially stepping of 1.13 C/cm^2 PPy films on EvAu (r = 5.1) and EcAu (r = 22.1) surfaces. One cycle consisted of stepping from -0.6 V (10 sec) to 0.4 V (20 sec) and then back to -0.6 V (10 sec). EvAu samples only exhibited 11.5% and 35% of their initial strain and charge responses respectively after 900 cycles. Consequently EcAu samples

only exhibited 25% and 46% (after 900 cycles) and 12% and 41% (after 1200 cycles) of their initials strain and charge responses respectively. Both of these systems exhibited poor overall lifetimes for both their strain and charge responses, Figure 4.32.

It was later determined that the electropolymerization solutions were not purged with argon adequately prior to electropolymerization. The presence of oxygen can interfere with the electropolymerization process yielding poor PPy films. A second set of experiments was conducted with 1.18 C/cm^2 PPy films on EvAu (r = 3.43) and EcAu (r = 8.26 and 18.90) surfaces for 2000 cycles. The electropolymerization solutions were purged with argon for 15 min prior to electropolymerization. Both systems (EvAu and EcAu) exhibited a decrease in the normalized strain response; however the EcAu systems stabilized after 1000 cycles while the EvAu systems continued to decrease. The EcAu systems retained about 60% of their initial strain response after 2000 cycles while the EvAu systems retained only 40%. The change in the normalized consumed charge was smaller than the change in strain. All three samples exhibited a normalized consumed charge of ~75%. This improved strain response after 2000 cycles is attributed to improved interlayer adhesion between PPy and EcAu. Figure 4.33 shows the normalized strain response of the EvAu and EcAu systems tested.

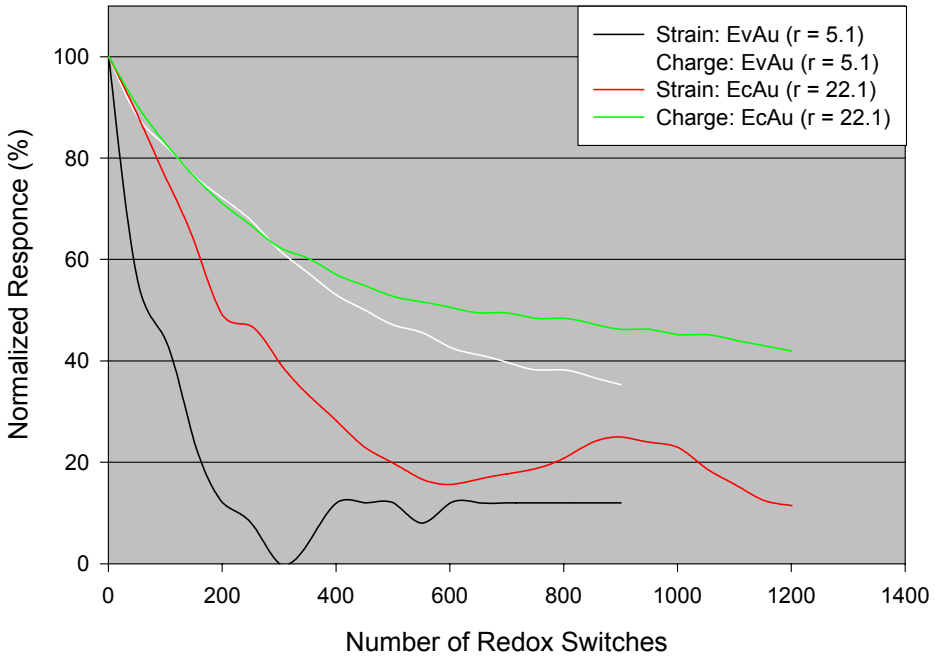

Figure 4.32 *In situ* normalized strain and charge response of 1.18 C/cm^2 PPy (inadequate Argon purge) on r = 5.1 (EvAu) and r = 22.1 (EcAu) treated actuators with repeated potential stepping between –0.6 V (10 s) and 0.4 V (20 s).

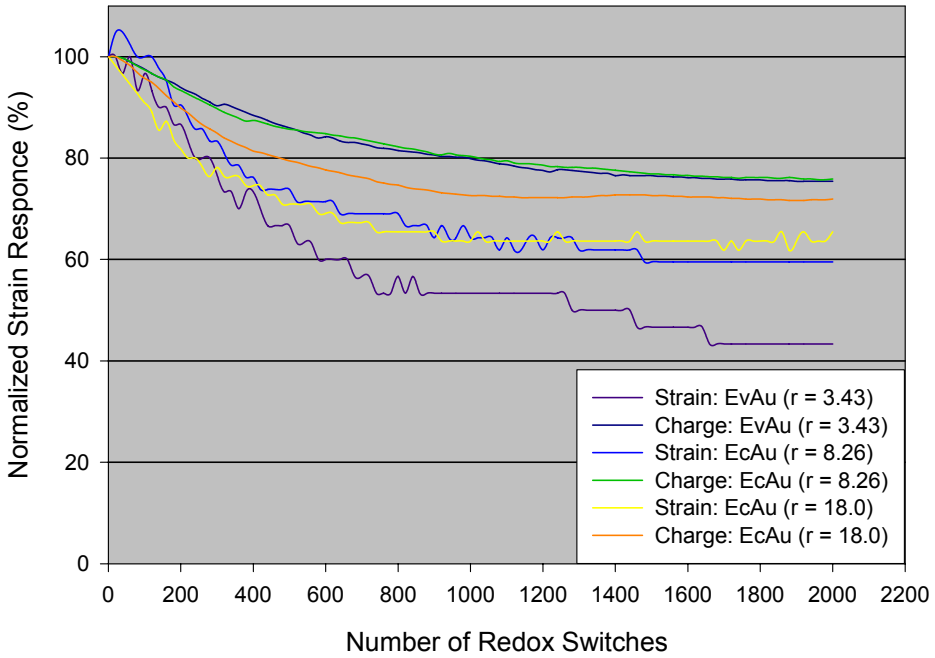

Figure 4.33 *In situ* normalized strain and charge response of 1.18 C/cm^2 PPy on r = 3.43 (EvAu), r = 8.26 (EcAu), and r = 18.90 (EcAu) treated actuators with repeated potential stepping between –0.6 V (10 s) and 0.4 V (20 s).

4.9 Conclusions

The strain of PPy/Au/PI bending actuators during redox switching of PPy was directly and quantitatively monitored using an in-situ strain gage, a sensitive and reliable method. The results support previously reported trends for the effect of deposition potentials and redox switching of PPy.

The roughness of the substrate significantly affects the maximum strain attainable. When the surface roughness and the amount of PPy are judiciously chosen, the actuator exhibits 3 times higher strain than PPy actuators prepared with a thermally evaporated Au surface. It is also important that long-term stability is significantly improved by good adhesion between PPy and the EcAu. These effects are probably a result of better adhesion and electrical contact due to mechanical interlocking of the PPy and the metal electrode.

CHAPTER 5
RAPID ELECTRODE PATTERNING FOR USE IN ADVANCED CONDUCTING POLYER ACTUATORS AND DYNAMIC SURFACES

5.1 Introduction

A critical step in the advancement of conducting polymer actuators and devices is the ability to develop new electrode patterns rapidly and accurately at a low production cost. Conducting polymers although inherently susceptible to polymerization conditions are easily applied to any electrode surface in any configuration. Therefore the design/form and capabilities of these devices are only limited to the designers imagination and their ability to fabricate the desired electrode pattern.

Here we describe the development and use of a new rapid patterning technique very similar to but developed separately from the line patterning technique developed by MacDiarmid and coworkers.[133-136] With these techniques it is possible to rapidly design and fabricate virtually any electrode pattern desired within a matter of hours and at a very low cost compared to standard electrode fabrication.

The initial use of this technique was to produce linear conducting polymer actuators based on the basic cantilever/bimorph design but capable of producing linear strains of up to 24% depending on the CP segment length (in-plane strain (linear stain) on standard CP bimorph actuators is typically ~1% max). The design of these linear actuators is based on altered bimorph and shell type (CP on both sides of flexible substrate) configurations with staggered CP segments that have independent oxidation/reduction control.

The aforementioned rapid patterning technique was also used to develop the base electrode structure for a new actuator design which results in a thin film surfaces with dynamic surface properties.

5.2 Rapid Electrode Patterning Techniques

5.2.1 Rapid Electrode Patterning

The rapid patterning technique developed in our lab utilizes standard laser jet or ink jet printers and a desktop computer to produce the patterns. A negative image of the desired pattern is first electronically designed on the computer using any number of drawing or drafting software programs, such as AutoCAD, PowerPoint, and Adobe Illustrator , which can be used to produce detailed and accurate patterns. However the fidelity of the final printed pattern is directly dependent on the resolution of the printer. For simple pattern designs and for ease of use Microsoft PowerPoint's drawing features are more than adequate. Once the desired negative pattern is created it is then printed onto the desired substrate utilizing standard office laser jets or ink jet printers.

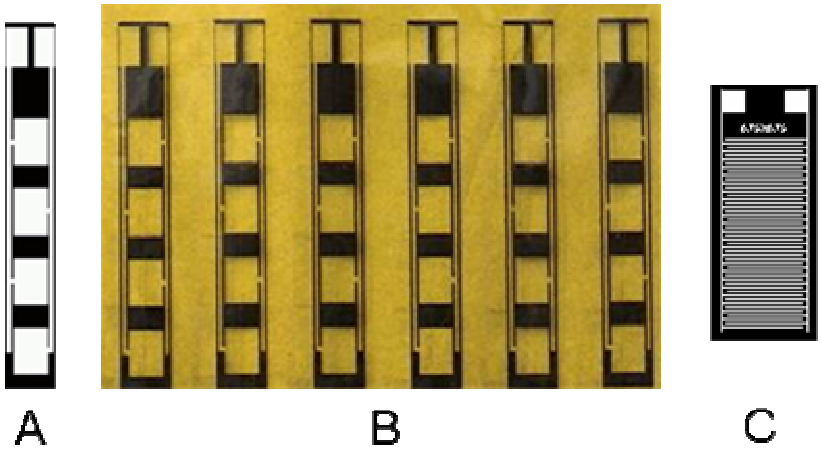

Figure 5.1 Negative patterns of linear actuator produced using Microsoft Powerpoint (A) and printed on Kapton used to fabricate linear actuators (B) and a negative pattern used for dynamic surfaces (C)

Kapton® polyimide and PET (standard laser jet transparencies) were used as the substrate materials in this research. Figure 5.1 shows two examples of different patterns designed using Powerpoint. Once the negative pattern is printed on the substrate the whole device is coated with gold (or any other desired material) using standard sputter or thermal coating techniques. Electroless [127, 128]gold (or other metal) depositing techniques can also be used to form the electrode layer. After the gold coating process the device is rinsed/stripped with acetone and ethanol to remove the printed ink pattern and the gold on top of the pattern. This stripping process leaves only the gold that was directly deposited on the substrate. This is the final step in forming the electrode layer. After this step standard electropolymerization techniques are used to deposit the desired conducting polymer yielding the final CP device. Figure 5.2 depicts the rapid electrode patterning technique.

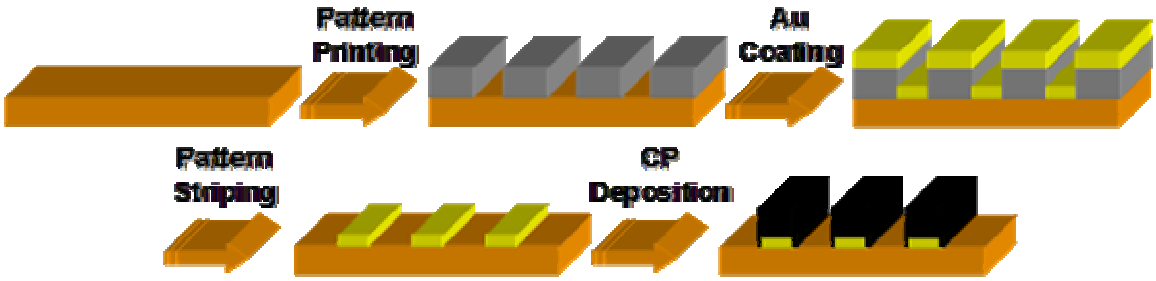

Figure 5.2 Rapid electrode patterning process for the development of conducting polymer devices.

5.2.2 Line Patterning

The method of line patterning developed by MacDiarmid [133-135] and coworkers is very similar to the method described above. The difference in the two techniques is the application of the conducting polymer and/or metal layer. The previous method utilizes standard metallization techniques followed by electropolymerization of the conducting

polymer. Line patterning uses selective chemical absorption to form the conducting polymer and/or metal layers. The substrate, after it is patterned, is exposed to a solution or vapor containing the material (conducting polymer or metal solution) to be deposited. Due to the chemical and/or physical differences between the substrate and the pattern lines the material will deposit selectively either on the substrate, the printed lines, or both. MacDiarmid [133] showed that by exposing a patterned substrate (PET transparency) to an aqueous polypyrrole solution for 20 minutes and by changing the polypyrrole dopant ion from toluenesulfonate to chloride he could get the PPy to preferentially deposit on the printed lines or both the printed lines and the bare substrate respectively. By ultrasonicating the film in toluene the printed lines are removed and only the PPy deposited directly on the substrate remains. It has also shown that by exposing standard PET transparencies to a commercial dispersion of poly(3,4-ethylenedioxythiophene) (PEDOT, "Baytron P" Bayer Corp.) that the PEDOT preferentially wets the transparencies and not the printed, patterned lines. By repeatedly exposing the patterned transparency to the PEDOT solution and then drying a patterned PEDOT film was be produced on the transparency. These CP patterned substrates were then used to produce simple push button type switches, field effect transistors, and as the electrode layers for liquid crystal displays.[134-136] Work currently being conducted in the Reynolds research group (Univ. Florida Department of Chemistry) utilizes a modified line patterning technique for use in photochromic devices and polymer light emitting diodes. Their electrode formation technique uses electroless gold deposition to deposit gold onto the patterned substrate instead of a conducting polymer. The pattern is then removed and standard electopolymerization techniques are used to form the final CP device.

5.3 Linear Actuators

5.3.1 Background

As stated earlier there has been a lot of work put into the development of polymer based actuators. One of the most promising polymers of choice is the class of conducting polymers. However most of the research that has been conducted in this area has been on the development of bending/cantilever type actuators. Currently there is a drive to develop polymeric actuators capable of producing linear strain. The two main forms of linear actuators being developed are free standing conducting polymer films[44, 71, 137, 138] and fibers.[46, 139, 140]

Conducting polymers typically are capable of producing an in-plane strain (linear strain) of only ~1%. This was also the case of CP linear actuators developed by Della Santa[44] and Madden[71] et al. Della Santa showed that polypyrrole linear actuators made from free standing films are capable of producing strains of 1%. Madden and coworkers have produced encapsulated PPy linear actuators capable of producing linear strains of 2%. However these designs have been improved on by Bay and Hara. Bay et al. [138] have produced linear actuators capable of producing strains on the order of 12% from free standing films of PPy doped with alkylbenzene sulfonate electropolymerized on gold foil. Hara et al. [137] formed highly flexible PPy (free standing film) linear actuators by electropolymerizing PPy from a methyl and butyl benzoate solutions of tetra-n-butyl-ammonium tetrafluoroborate ($TBABF_4$) and pyrrole on different electrode materials. Films produced from methyl benzoate/$TBABF_4$ solutions on titanium electrodes and redox cycled in $NaPF_6$ aqueous solutions produced linear stains of 12.4%. While films produced from butyl benzoate/$TBABF_4$ solutions on nickel electrodes produced linear strains of 15.1%. By using other common organic solvents such as propylene carbonate

and acetonitrile during electropolymerization actuators capable of producing strains of 8-10% can be formed. When aqueous solutions of $NaBF_4$ were employed during electropolymerization brittle films capable of producing strains of only 0.3% were formed.

Qi et al. [139] have produced polyaniline (PANi) fibers capable of producing linear strains of 0.51-1.18% in aqueous solutions. They showed that by changing the counter ion used during redox cycling. As the counter ion size increased from fluorine (F^-, 10.3 Å) to chlorine (Cl^-, 31.0 Å) and bromine (Br^-, 31.0 Å) the produced linear strain increased from 0.76% to 1.05% and 1.18% respectively. However as the anion size is increased beyond bromine to BF_4^- (31.0 Å), ClO_4^- (52.9 Å), and $CF_2SO_3^-$ (70.4 Å), the produced linear strain decreases from 0.57, to 0.51, and to 0.40%, respectively.

Lu et al. have produced dry PANi solid-in-hollow fiber actuators (solid fiber inside a hollow fiber filled with a solid polymer electrolyte (SPE) gel) capable of producing linear strain on the order of 0.90%. These values are comparable to those obtained by Mazzoldi and coworkers of 0.55% for dry perchlorate (ClO_4^-) doped PANi/SPE fiber actuators.

5.3.2 Cantilever based linear actuators

The linear actuator design developed in our lab is based on the standard cantilever design used in typical bimorph actuators. The basic design consists of placing alternating conducting polymer segments on adjacent sides of a flexible conductive substrate. This has the same effect as placing multiple cantilever actuators end to end so the final actuated device forms an “S” shape.

The pattern is formed by masking off sections of the substrate with tape to prevent the electrochemical deposition of the conducting polymer. After the CP deposition

process the tape is removed and the device is ready to be used. An example of this design and an AutoCAD model of this device is depicted in Figure 5.3.

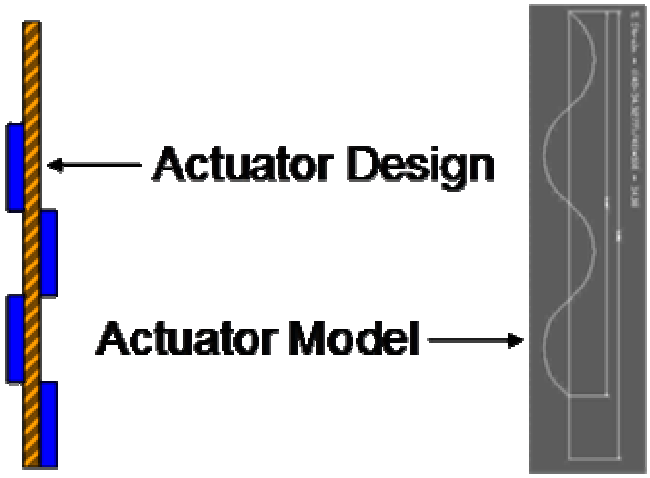

Figure 5.3 Diagram of basic linear actuator design and AutoCAD model used to predict the overall developed linear strain for the device.

The initial design consisted of alternating 10mm strips of PPy placed on adjacent sides of a thin copper foil. This device produces a linear strain of -9.75% during oxidation (contraction) as depicted in Figure 5.4. Subsequent revisions of this design employed a gold coated (EvAu) flexible polyimide substrate instead of a solid copper foil. Utilizing this design the PPy segment lengths was produced in 5, 10, and 20 mm segments with an overall dimension of 2mm X 50mm.

We can adjust the overall strain produced by the device by controlling the length of the PPy segment length. The overall strain produced by the device also increases with longer segments. The resulting strains produced by actuators with 5, 10, 20 mm PPy segment lengths are: -2.44, -12.41, and -23.84% respectively. The deflection of the actuators was also modeled in AutoCAD 2000 and the calculated strains were -3.67, -14.18, and -49.62% respectively. This is higher than the actual experimental values.

The model is based on a uniform 1% (max reported strain for PPy switching) strain produced in the PPy layer resulting in a perfect "S" or sine wave shape in the device (as shown in the model shown in Figure 5.3). However the actual strain produced in this layer is probably much less the 1%, which would account for the lower experimental strain. By back calculating it was determined that the strain required to produce the experimental strain values was 0.66, 0.93, and 0.81% respectively.

However as stated above this model assumes a completely uniform curvature in each of the PPy segments and that the actuator is completely straight in the reduced state which is not the case in the actual devices. Figures 5.3, 5.4, and 5.6 show images of the actual devices in action. From this it can be said that linear actuators can be fabricated by alternating the placement of conducting polymer segments on opposite sides of a flexible conductive substrate. However better control over the placement and alignment of the conducting polymer segments is needed to improve the linearity of the actuation.

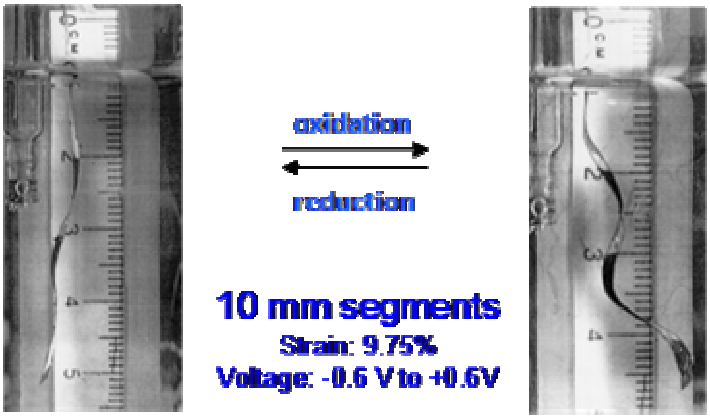

Figure 5.4 Initial PPy linear actuator based on 10mm segments deposited on copper foil. Picture of oxidized state enhanced to show placement of PPy.

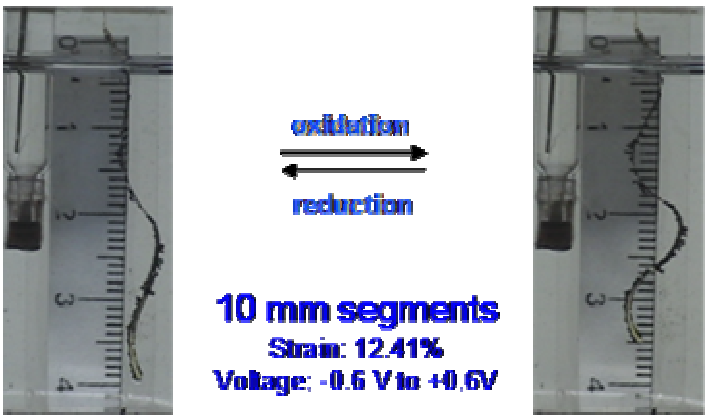

Figure 5.5 PPy linear actuator based on 10mm segments deposited on EvAu coated polyimide strip.

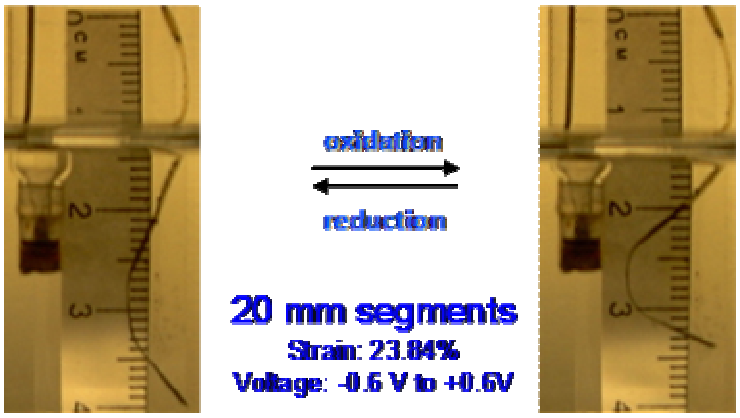

Figure 5.6 PPy linear actuator based on 20mm segments deposited on EvAu coated polyimide strip.

This first generation device was crude and simplistic but effective in producing linear strain. A new method of rapid electrode patterning was developed for the fabrication of these actuators to improve reliability and linearity. More accurate control over conducting polymer placement is accomplished by designing and patterning the electrode pattern electronically. Utilizing this technique, a new electrode design was created utilizing two separate electrodes patterns on a single actuator. This technique places both the working and counter electrode on the actuator itself (Figure 5.7)

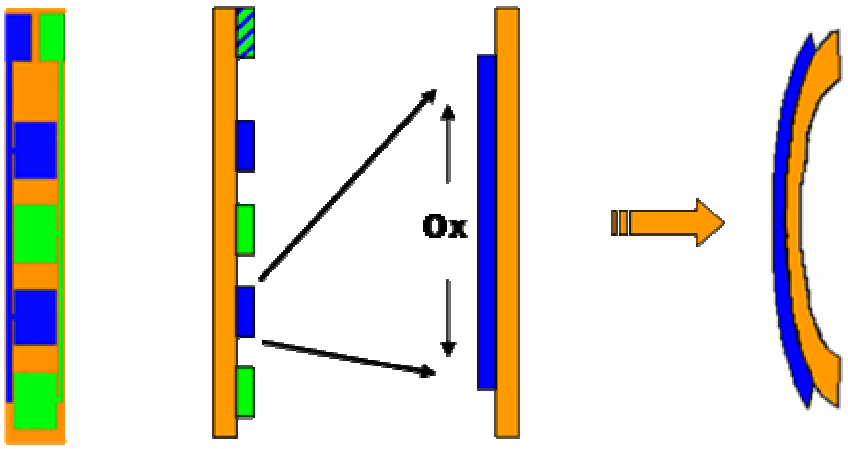

Figure 5.7 Single sided rapid electrode pattern design and illustration of how it works. The green and blue areas represent the separate electrode patterns (working and counter electrode).

As stated above, the electrode pattern is created by first designing the negative of the pattern utilizing computer aided design or other computer drawing programs. After the electrode design is created it is then printed onto the desired substrate using either a standard laser or ink jet printer. After the substrate is patterned it is then coated with conductive material (typically gold) using standard metallization techniques. The coated substrate is subsequently washed in acetone and ethanol to strip off the printed pattern. This leaves only the gold that is deposited directly on the substrate and not the printed pattern. After this step, the desired conducting polymer can be electrochemically deposited on the gold electrode creating the finished linear actuator (Figures 5.8 and 5.9).

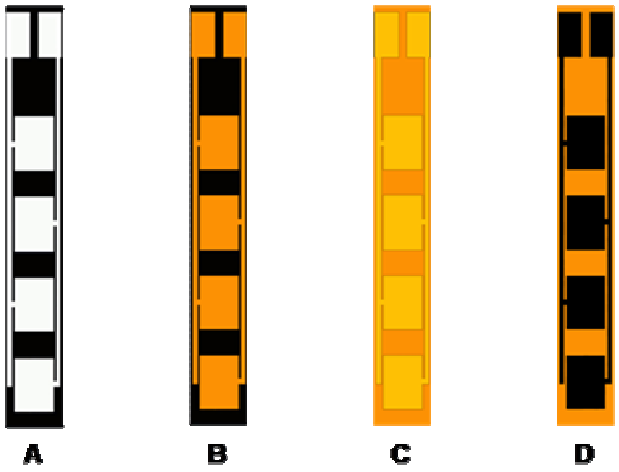

Figure 5.8 Diagram of linear actuator fabrication process. Initial negative CAD electrode design (A) negative electrode design printed on substrate (B) produced patterned gold electrode from the mask (C) electrochemically deposited conducting polymer on the patterned gold electrode (D).

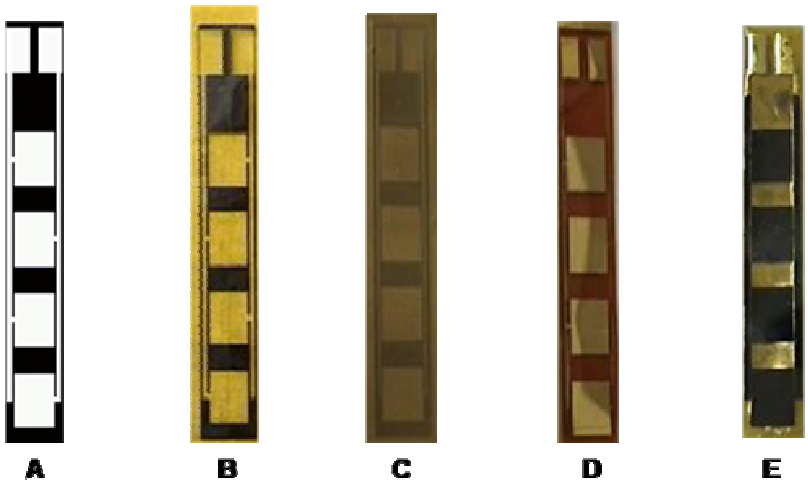

Figure 5.9 Pictures of linear actuator fabrication process. CAD design of negative electrode pattern (A) negative pattern printed on substrate (B) gold coated patterned substrate before acetone wash (C) patterned gold electrode after pattern removal (D) electrochemically deposited conducting polymer on the patterned gold electrode (E).

Even though this design shows promise, a more advanced design was fabricated utilizing the backbone type actuator concept. As described earlier, the backbone design employs two conducting polymer layers placed adjacently to each other on opposite sides of the flexible substrate. In this design one side acts as the working electrode while the other side serves as the counter electrode. Therefore as one side is oxidized and expands

the other side is reduced and contracts. This simultaneous push-pull process increases the strain and force produced by the device. In this advanced linear actuator design the negative electrode pattern is printed on both sides of the flexible substrate and then processed. Side views of both of these designs are depicted in Figure 5.10.

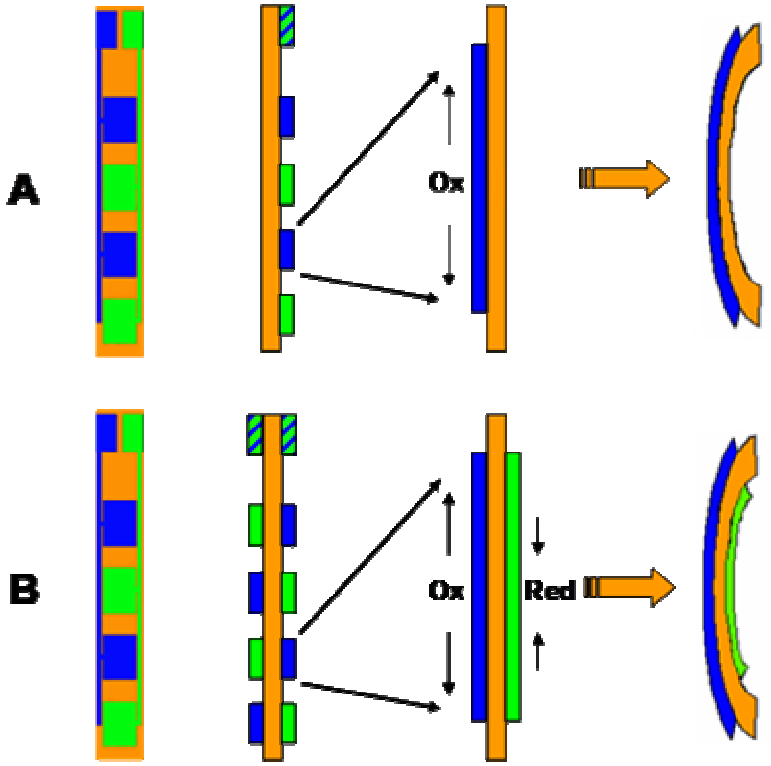

Figure5.10 Side view diagram of bilayer (A) and backbone (B) type linear actuator designs.

One problem with the backbone type linear actuators is the alignment or registration of the electrode patterns on opposite sides of the substrate. To print the double sided pattern the electrode pattern is printed on one side of the substrate and then the substrate is simply turned over and the pattern is printed again. However if the pattern registration is off it will cause misalignment of the printed electrodes pattern. This will cause twisting and other erratic movement in the linear actuator. Due to this problem care must be taken to balance the designed grid of patterned electrodes in the

computer software (see Figure 5.10 B) and that the substrate is aligned and centered properly in the printer.

Another issue is the interlayer adhesion of these devices. Failure at either the conducting polymer/Au interface or the Au/substrate interface is detrimental to the performance and lifetime of the device. The effects of the conducting polymer/Au interlayer adhesion were discussed in the previous chapter. Previously, it was shown that the overall performance of the device was enhanced by applying an electrochemically deposited gold surface onto the preexisting evaporated gold surface.

However a new problem arises with this patterning technique. Due to the printing process some residual debris and oils can contaminate the substrate surface prior to Au deposition. The substrate should be cleaned with acetone and ethanol prior to Au deposition process. The application of a short (~1 minute) plasma treatment process can also be used to thoroughly clean the substrate surface and will roughen the surface as well improving the adhesion of the deposited Au layer. If the substrate is not properly cleaned prior to Au deposition then it is likely that the deposited Au will not adhere well to the substrate and will eventually delaminate from the surface rendering the device inoperable. If residual debris is not removed from the substrate prior to Au deposition or if the toner particles overspray the unmasked areas wholes/defects can be produced in the evaporated gold electrode.

White light optical profilometry (Wyko NT1000) was used to evaluate the surface roughness and printed line fidelity for polyimide, EvAu polyimide, EcAu polyimide, and PPy/EcAu polyimide substrates (Figures 5.11-16, magnification = 25X). The NT1000 is capable of surface height measurements from 0.1 nm to 1 mm and is non-contact

therefore the surface is not altered during measurements. The EcAu treatment was conducted at -0.9 V for 10 minutes on EvAu coated polyimide and PPy was electrochemically deposited at +0.8 V to 2.24 C/cm^2.

The root mean squared surface roughness (RMS or R_q) of these surfaces changes from ~1.05 µm for Pi to ~315 nm for EvAu/Pi, ~631 nm EcAu/EvAu/Pi, and ~7 µm PPy/EcAu/EvAu/Pi. Some surface defects are also present in these deposited films. Figure 5.13 shows a defect in the EcAu/EvAu/Pi electrode structure caused by a stray toner particle (over spray) from the pattern printing process.

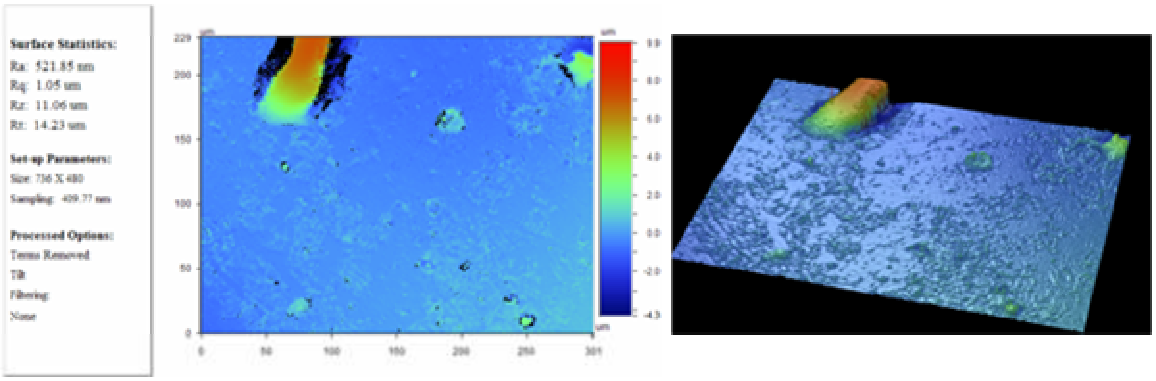

Figure 5.11 WLOP image of the polyimide substrate used in the construction of linear actuators before patterning (Magnification = 25X).

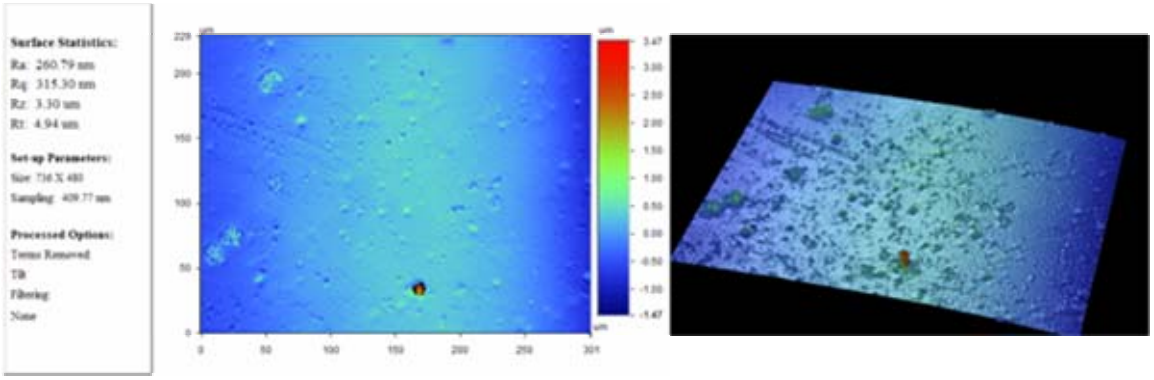

Figure 5.12 WLOP image of the polyimide substrate coated with evaporated gold (Magnification = 25X).

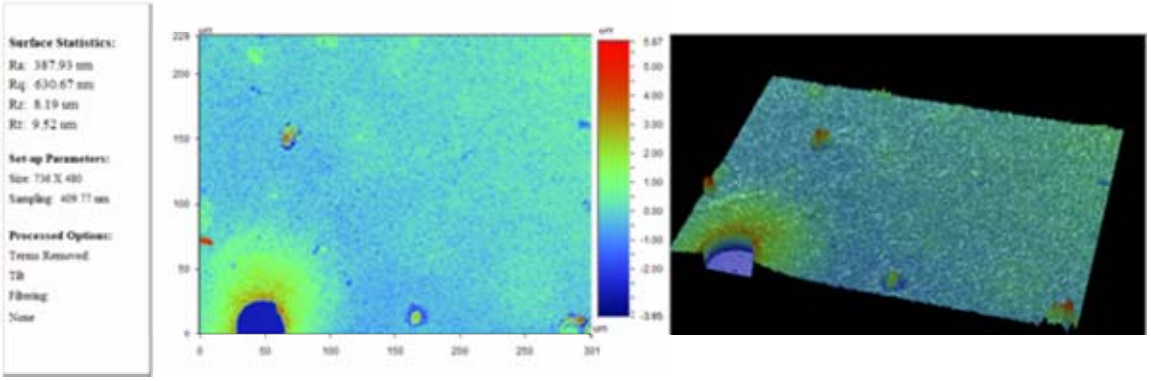

Figure 5.13 WLOP image of electrochemically deposited gold on top of evaporated gold coated polyimide (Magnification = 25X).

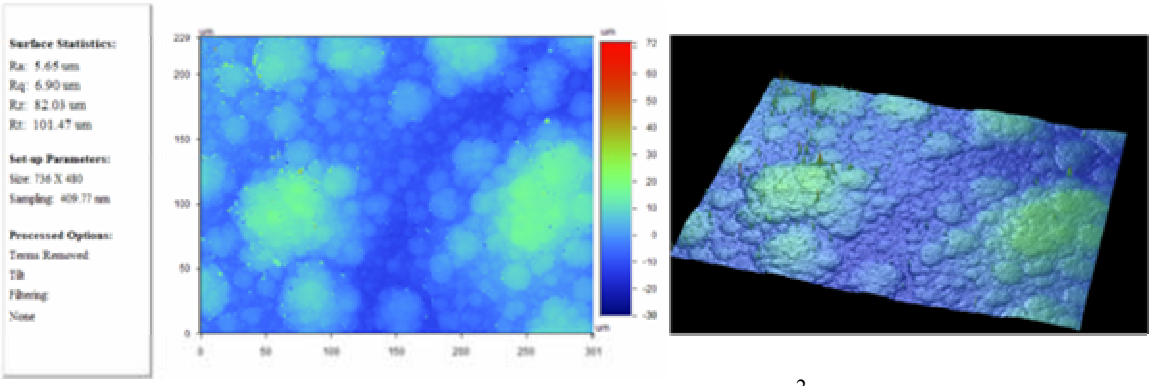

Figure 5.14 WLOP image of polypyrrole (+0.8V to 2.24 C/cm^2) electrochemically deposited in EcAu/EvAu coated polyimide (Magnification = 25X).

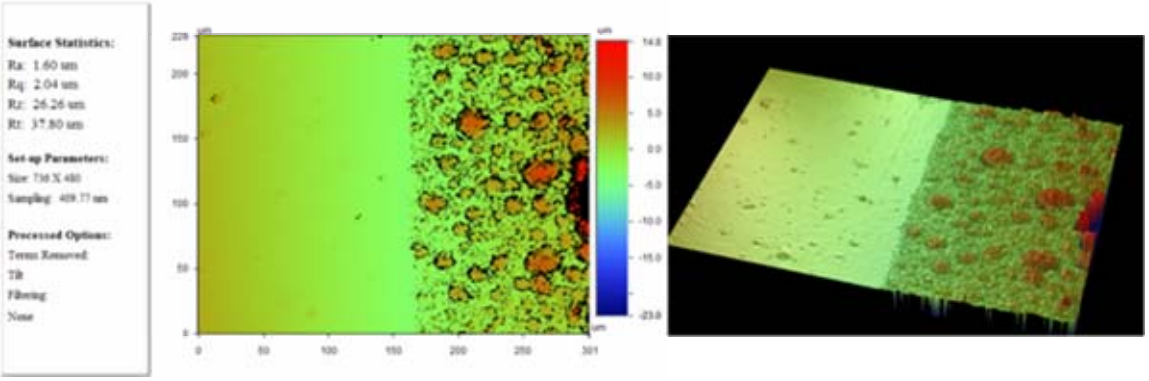

Figure 5.15 WLOP image of patterned PPy/EcAu/EvAu on polyimide (Magnification = 25X).

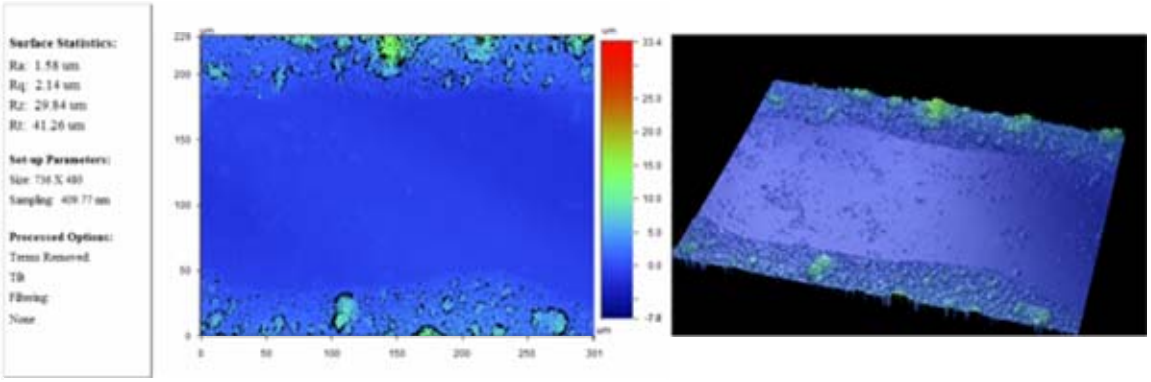

Figure 5.16 WLOP image of exposed base polyimide substrate between two patterned PPy/EcAu/EvAu wires (Magnification = 25X).

5.4 Actuator Based Dynamic Surfaces

Another application for this technology is in the development of conducting polymer actuator based dynamic surfaces. In this project a patterned conducting polymer electrode/actuator is deposited beneath a flexible surface coating. Therefore as the conducting polymer expands and contracts during redox cycling it will replicate its pattern in the flexible top coating (Figure 5.17).

Figure 5.17 Schematic of conducting polymer actuator based dynamic surface.

Initially, the desired pattern with three different line thicknesses, i.e., 0.75, 0.50, and 0.25 pt, was printed on standard PET transparencies. The patterned line thicknesses correspond to line widths of 264 µm, 176 µm, and 88 µm respectively. The patterns were tested on thrree different printers, i.e., Xerox Phaser 6200 laser jet printer, HP Deskjet 6122, and Lexmark i3 Inkjet.

The Xerox Phaser 6200 is capable of printing at 2400 X 600 dpi in color and 1200 X 1200 dpi in black and white (BW). The HP Deskjet 6122 is capable of printing at 4800 X 1200 dpi (optimized) in color and 1200 X 1200 dpi BW. And the Lexmark i3 has a print resolution of 2400 X 1200 dpi in color. The patterns produced on the Xerox Phaser 6200 in black and white at a resolution of 1200 X 1200 dpi exhibited too much overspray in the unpatterned areas and small dispersed holes in the solid patterned areas. This caused defects in the final Au electrode. The Au electrodes produced on the Xerox Phaser were not completely conductive due to multiple large defects in the electrode structure.

Similar effects were produced from other laser jet printers at this resolution. The HP Deskjet 6122, which has a higher printing resolution in black and white, produced less overspray compared to the Phaser. However, the solid patterned area had fewer holes that were larger compared to those printed on the Phaser printer.

The next set of tests utilized color printing due to higher resolution. The Deskjet is capable of printing at 4800 X 1200 dpi in color using computer software enhanced mode, which does not translate to a real line image resolution. The Lexmark i3 produces a true color line printing resolution of 2400 X 1200 dpi. The i3 produced patterns were similar in resolution to the Deskjet generated lines, but have less overspray and more uniform density in the solid patterned areas, i.e., no holes in the printed pattern(Figures 5.18 and 5.19).

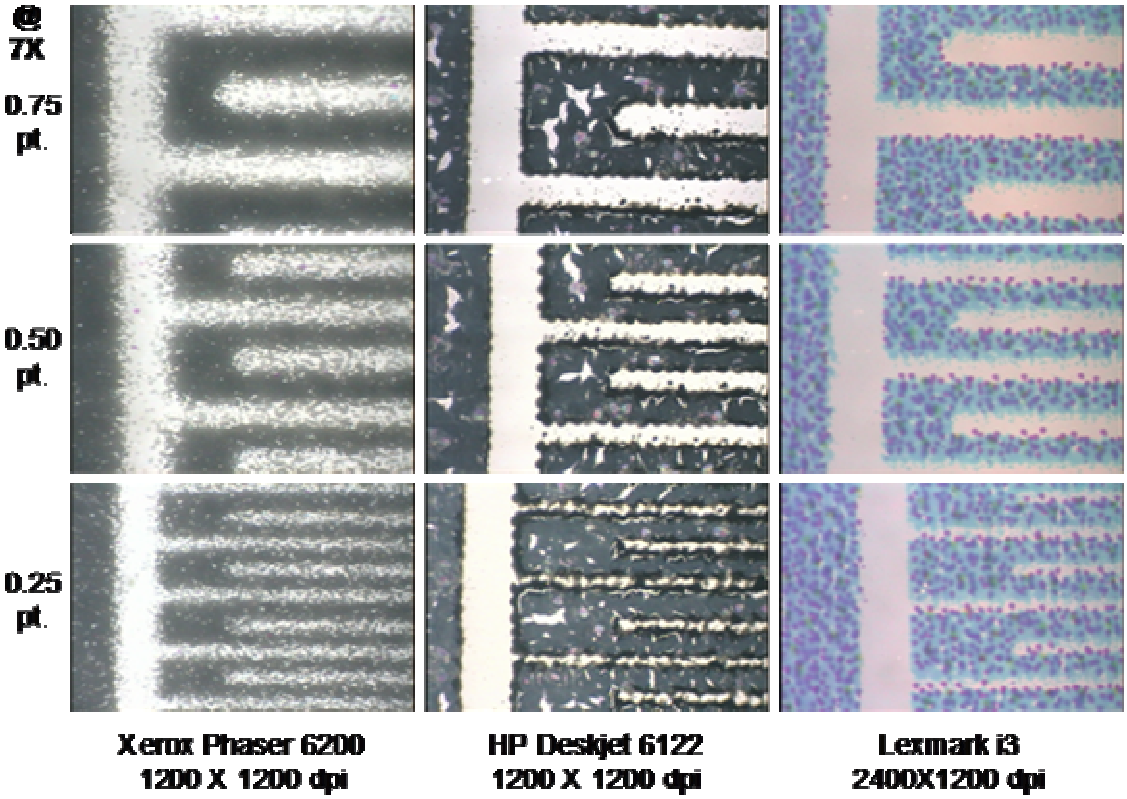

Figure 5.18 Images of 0.75, 0.50, and 0.25 pt line patterns produced with Xerox Phaser 6200 laser jet, HP Deskjet 6122, and Lexmark i3 inkjet printers (Magnification = 7X).

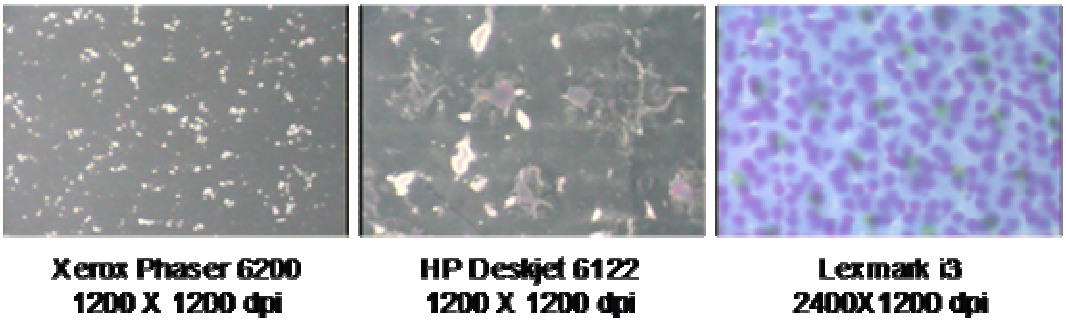

Figure 5.19 Images of solid printed pattern areas produced with Xerox Paser 6200 laser jet, HP Deskjet 6122, and Lexmark i3 inkjet printers (Magnification = 14X).

The Lexmark i3 produced the best overall patterns in blue ink compared to the Xerox Phaser 6200 and HP Deskjet 6122 printers, which are black and white. However direct gold coating of the patterned inkjet transparencies is ineffective. Standard inkjet

transparencies are coated with a hydrophilic surface coating to improve the wetting and drying characteristics of the ink on the transparency. This in turn prevents smearing of the printed ink on the transparency surface. If this coating is left intact the deposited gold will be deposited on this coating and not the base PET substrate. Once the substrate is washed to remove the printed pattern the Au that was deposited on the nonpatterned areas will also be removed. Removal of this this surface coating is removed then the ink will not wet or dry correctly on the PET substrate. This results in the ink beading up smearing and thus rendering the pattern useless.

Another alternative to printing and forming the electrode surface directly on the PET transparency is to use the printed PET transparency as an inexpensive photomask for use in photolithographic processing. Utilizing this technique PET photomasks can be produced rapidly and inexpensively with various pattern features. However the resolution of the mask is still limited by the printing resolution of the printer. Also the PET photomask can be used in the patterning of almost any substrate. This is advantageous in the case of the actuator based dynamic surfaces. A stiff substrate is required in this application to direct all the produced strain in the system toward the surface of the flexible top coating.

Photolithography is carried out by spin coating a photoresist onto the surface that is being patterned. The photoresist is then exposed to UV light through the patterned photomask to develop it. If a positive photoresist is used the areas that are exposed to the UV light degrades and are subsequently removed during a rinsing process. This leaves only the photoresist that was masked (unexposed) from the UV light by the photomask. The sample is then gold coated in a similar process to that described previously for the

rapid patterning process. The remaining patterned photoresist is then removed leaving only an Au pattern.

Initially, the blue pattern produced on the Lexmark i3 printer was evaluated as a photomask. However during the photolithographic processing some of the UV light penetrated through the blue photomask. The partial exposure of the underlying photoresist can result in a random speckled pattern to develop in the photoresist. This can caused random holes and other defects to be form in the patterned photoresist resulting in random Au spots to be produced on the patterned electrode surface were the holes were. Figure 5.20 shows 7X optical images of the 0.75 pt blue photomask and the resultant patterned photoresist (computer enhanced/colored) on a glass slide developed from this photomask. The random holes are shown in image B and appear as white spots in the patterned brown photoresist. To overcome this problem the ink color was changed to brown. However the black toner cartridge had to be removed from the printer to maintain good pattern resolution. When the black cartridge is installed the printer also applies black ink which has a much lower dpi than the color ink. This produced random large black ink spots which degraded the overall resolution of the pattern (Figure 5.21). The final printed photomask was much darker and less transparent than a similar mask produced from blue ink. This in turn prevented the UV light from penetrating the photomask and exposing the underlying photoresist. This eliminated the partial exposure of the photoresist without any loss in pattern resolution. Examples of the blue and brown photomask used to pattern glass slides are presented in Figure 5.22.

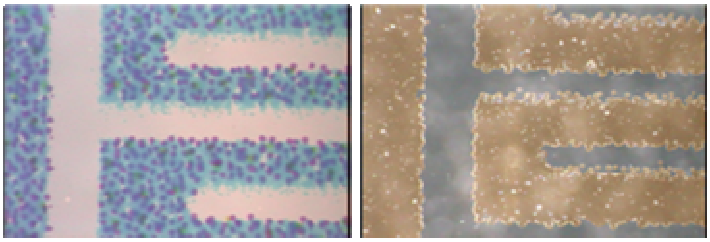

A B

Figure 5.20 Images of 0.75 pt blue photomask (A) and enhanced image of resulting patterned photoresist coated glass slide (B) (Magnification = 7X).

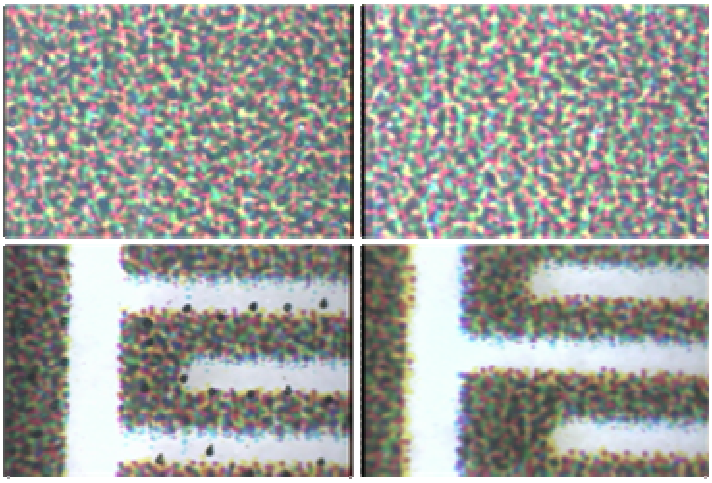

A B

Figure 5.21 Images of printed field and 0.75 pt brown photomask with black toner cartridge (A) and without black toner cartridge (B) (Magnification = 7X).

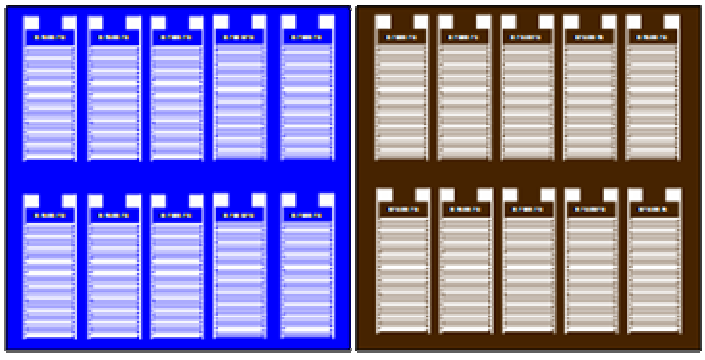

A B

Figure 5.22 Examples of computer designed patterns used to make blue (A) and brown (B) photomasks.

5.5 Conclusions

A new patterning technique for the rapid development of various electrode patterns has been described in this chapter. The patterning technique was used to develop conducting polymer based linear actuators. Standard office equipment such as desktop computers and printers were utilized in conjunction with photolithographic methods to produce various electrode patterns. The patterns facilitated the rapid generation of linear actuators at a minimal cost.

Initial linear actuator designs were basic in construction and were shown to be capable of producing linear strain of 2.44, 12.41, 23.84% for 5, 10, 20 mm PPy segment lengths respectively. The new rapid patterning technique was used to develop new advanced linear actuator designs. Both a single sided and double sided design was developed utilizing this technique. These designs place both the working and counter electrodes on the same surface. This eliminates the need for an external counter electrode in the system. The double sided design utilizes the same push-pull type technique used in the back bone type devices. In these devices conducting polymer layers are placed on opposite sides of the flexible substrate and as one layer is used as the working electrode while the opposite layer s used as the counter electrode. This causes one layer to expand while the other contracts increasing the overall developed stress and strain produced by the device. It was shown that the final device fidelity or pattern fidelity is directly dependent on the resolution of the printer used. Ink jet printers were shown to produce patterns of higher quality compared to laser jet printers due to there higher printing resolution and lower degree of over spray. This in turn produces patterns and final devices with higher fidelity and accuracy. However the ink jet printers suffer from one major set back. The transparencies used during ink jet printing are coated with a

hydrophilic coating used to improve the wetting and drying of the ink. This coating prevents the deposition of the gold electrode layer directly on the transparency. This prevents the gold from sticking to the transparency substrate rendering the pattern useless. If this coating is removed the ink from the printer will not stick and dry to the transparency also rendering the pattern useless. This makes the use of ink jet printers inadequate for the production of electrode designs. However these patterns have been shown to be suitable as inexpensive photomasks. Utilizing these photomasks glass slides coated with standard photoresist and developed with standard photolithography techniques were patterned and used to produce the base electrode for conducting polymer actuator based dynamic surfaces. The only problem experienced with the use of ink jet printed photomasks was with the partial exposure of the photoresist under the masked areas. This was found to be due to the color used to produce the photomask. Blue ink was found to produce patterns of high fidelity however the blue ink allows some of the UV light used to develop the photoresist to penetrate through the mask creating small holes in the final electrode pattern. It was found that by changing the mask color from blue to brown the partial exposure of the photoresist could be eliminated.

CHAPTER 6
PDMSE BASED DYNAMIC NON-TOXIC ANTI-FOULING SURFACE COATINGS

6.1 Introduction

As mentioned earlier biofouling is the result of marine organisms settling, attaching, and growing on submerged marine surfaces and is a very expensive and complex problem facing military, commercial, and private naval vessels and structures. This process is initiated within minutes of expose of the surface to the marine environment and is initiated by the absorption of dissolved organic materials onto the submerged surface forming a conditioning film. Once this film is formed various marine organisms settle and then grow on this surface and on top of other organisms already growing on this surface. This is further complicated by to the fact that there are 12 well-defined geographical zones in the world's oceans with varying salinity, clarity, temperature, amount and type of micronutrients, and number and type of fouling organisms.[52] Due to the vast number and diversity of marine fouling organisms each having its own unique properties and adhesion mechanisms it is difficult to produce a single coating that prevents the settlement of all fouling marine species.

It has been shown that the three major surface properties that control the settlement and growth of fouling marine species are surface energy, surface modulus, and surface topography.[50-52, 76-82] It has also been shown that different marine species react differently to each of these properties. Therefore while one set of surface properties might prevent one marine species from settling and growing on a given surface the same set of properties might increase the settlement and growth of other marine species.[141, 142]

This makes it very difficult to produce a single marine coating that can prevent the settlement and growth of all fouling marine species.

For example, Rittschof and coworkers [141] determined that barnacles prefer to settle on surfaces with higher initial wettability while bryozoans prefer to settle on surfaces with lower initial wettability. This was determined by conducting settlement assays on bryozoans and barnacles on surfaces with varying surface energies (through silanization of glass surfaces).

The approach of this research is to utilize the electrochemically induced changes in the bulk properties of conducting polymers (CP) during redox cycling to develop a surface coating with dynamic surface properties. During electrochemical switching (redox cycling) of conducting polymers in an electrolyte medium (salt solution) counter ions and solvent are drawn into and expelled from the CP matrix due to changes in the induced charge on CP backbone charge. This influx and expulsion of counter ions and solvent is due to a charge neutralization process which results in a swelling and contraction of the CP matrix.

The swelling process also induces a decrease in the overall modulus of the CP material.[94, 143-147] By incorporating conducting polymers into traditional polymeric surface coating (paint or appliqué/tile coatings) thus combining the effects of the electrochemically induced CP charge and swelling with these materials it is possible to produce a single durable surface coating with variable surface energy, modulus, and topography.

Dynamic composite films based on PPy and PDMSe have been produced that are capable of generating a 21° change in contact angle under an electrical stimuli. It is felt

that this dynamic change in contact angle might be sufficient to perturb the settlement and growth of marine organisms.

6.2 Materials and Methods

6.2.1 Materials

Pyrrole was purchased from Sigma-Aldrich and was filtered through a neutral alumina (Brockman activity 1; Fisher Scientific) column until colorless before use to remove any impurities. Lithium perchlorate ($LiClO_4$), sodium perchlorate ($NaClO_4$), and gelatin Type B ~255 bloom (Mn = 100,000) were purchased from Sigma-Aldrich and used as received. Ammonium persulfate (APS), dodecylbenzene sulfonic acid (DBSA), or alkylbenzene sulfonic acid), iron (III) chloride ($FeCl_3$), ethanol, methanol, and tetrahydrofuran were purchased from Fisher Scientific and used as received. All deionized (ultrapure) water was produced using an 18 MΩ Millipore system. Artificial sea water was made using Instant Ocean® (obtained from Fisher Scientific) synthetic sea salt and deionized water.

6.2.2 Gelatin Preparation

Gelatin films (yellow/orange in color) were prepared by mixing 10wt% gelatin (thermally denatured bovine collagen) in ultrapure water. NaN_3 was added (~200 ppm) as an anti-microbial. Gelatin films were allowed to gel and dry for 3hr at 25°C. Crosslinked gelatin films were prepared by adding 50 vol% crosslinker solution (4.5 wt% glutaraldehyde solution in ultrapure water) after the gelatin films is dried. The dried gelatin film and the crosslinker solution are then heated to ~38-40°C in an oven for 1hr. The gelatin films un-gel at 40°C allowing the crosslinker to mix and react with the gelatin.

6.2.3 Polydimethylsiloxane Elastomer Preparation

PDMSe films were prepared using Silastic® T2 resin (Dow Corning). The resin and curing agent are mixed in a 10:1 weight ratio. The resin is then thoroughly mixed and degassed under vacuum until most of the bubbles are removed. The resin is then poured into sheets and cured between glass or PET cover glass plates using spacers to achieve the desired thickness. The cast films can then be cured at room temp (25°C) for 24 hrs or at 50, 60, 65, or 80°C for 5, 4, 2-3, or 1.5 hrs respectively.

6.2.4 Soluble Polypyrrole Preparation

Soluble polypyrrole was prepared from a technique reported by Song et al..[98] Pyrrole (0.3 mol) and dodecylbenzene sulfonic acid (0.15 mol) are dissolved in 400 ml ultrapure water. The solution is cooled to 0°C in an ice bath and allowed to mix for 1.5 hrs while being degassed by bubbling N_2. After mixing a aqueous solution of ammonium persulfate (0.045 mol in 200 ml ultrapure H_2O) is added drop wise under N_2 using an addition funnel.

The reaction was allowed to run for ~36 hrs and then terminated by adding excess methanol. The solution is then filtered and washed with ultrapure water and methanol to remove unreacted pyrrole, APS, and DBSA. After filtering the resulting PPy powder is dried at 25°C for 12 hrs under vacuum. The dried PPy powder plus an additional 1-2 wt% DBSA are then dissolved (dispersed) in chloroform using ultrasonication.

6.2.5 Chemical Formation of Conducting Polymer IPN Systems

Conducting polymer/base material IPN systems were prepared using an oxidizer insertion method. The general process scheme is described as follows. Samples films of the base material were soaked for 24 hrs in a solvent oxidizer (FeCl3) solution. The oxidizer solution consisted of either 0.1 M or 1 M FeCl3 in EtOH, IPA, H_2O, scCO2, or

THF. Initially a perchlorate codopant (0.1 M or 1 M LiClO4 or NaClO4) was added to insert the –ClO4 anion instead of –Cl.

After soaking the doped films were dried under vacuum for 1 hr to remove any residual solvent. The films were then placed in a sealed container containing pyrrole monomer vapor for 24 hrs. After exposure to the pyrrole monomer the films were dried under vacuum for 1 hrs to remove any residual pyrrole monomer.

Initial THF solution soaking experiments were conducted using a saturated FeCl3/THF solution. This solution was dark brown-orange/black in color. The color of the solution indicates the degree of hydration the FeCl3 has undergone. Hydrated FeCl3 (FeCl3 hexahydrate) is yellowish/orange in color while dry FeCl3 is dark black in color; the same is true for FeCl3 in solution. The same effect was observed in FeCl3/IPA solutions. It was found that if regular (~95% pure) IPA was used to make FeCl3 solutions the solutions turned orange in color while if ultra pure IPA (~+99%) was used the resulting solution was black in color. The dark brown-orange color of the solution indicates that the THF was slightly wet and that the some of the FeCl3 had gone to its hydrated form which is less reactive and potentially less soluble in the PDMSe than the dry form.

6.2.6 Supercritical CO_2 Solution Formation of Conducting Polymer IPN Systems

Supercritical CO_2 solution doping of base materials was conducted using a Tousimis Samdri 780A critical point dryer. The Samdri 780A is semi-automatic scCO_2 critical point dryer equipped with a 1.25” diameter by 1.25” height reaction chamber (volume ≈ 26 ml). The operating pressure and temperature are ~82.7 bar ± 5-7% (~1200 psi ± 5-7%) and 33-39°C. The basic construction of this unit does not allow pressure, temperature control or for the recovery of the CO_2 after the reaction process.

Base material samples (on a rack), cosolvent, and oxidants are placed in the reaction chamber and then the chamber is sealed and cooled to ~ 0°C. The chamber is then filled with liquid CO_2 while maintaining the chamber temperature at ~ 0°C. This is increases the CO_2 charge in the system. Once the chamber is filled it is then heated to ~33-39°C thus increasing the chamber pressure to above the critical pressure of ~82.7 bar. The pressure is maintained by an automatic pressure relief valve set to a pressure a little above 82.7 bar. If the pressure exceeds this set point the CO_2 is automatically vented to the room. After the samples are soaked in $scCO_2$ for the desired amount of time the chamber is slowly vented at a rate of ~100 psi/min until the chamber is returned to room pressure. Care must be taken not too vented or decompressed the chamber too quickly the $scCO_2$ that is still dissolved inside the sample will return to the gas state and potentially destroy/explode the samples.

In order to determine the actual solvent ($scCO_2$) volume of the $scCO_2$ chamber the chamber volume was measured and the volumes of the samples and sample rack were subtracted from the chamber volume. This was used to calculate the volume percent cosolvent and molar concentrations of the oxidizers.

The changes in sample weight were monitored throughout the process to determine the extent of the $FeCl_3$ and PPy incorporation into the PDMSe base material.

6.2.7 Electrochemical Formation of Conducting Polymer IPN Systems

The electropolymerization of PPy inside various base materials is conducted using the following technique. Base material films are solution cast on one side of the working electrode (either EvAu coated polyimide or stainless steel electrode (other side coated with polyurethane)). The coated working electrode was allowed to soak in the monomer/salt solution for 20 minutes to allow for sample hydration. Pyrrole

electropolymerization was conducted in side the base material at +0.7 V for 130 minutes in an aqueous 0.1 M pyrrole, 0.1M $NaClO_4$ solution.

6.2.8 Mechanical Property Testing of PPy/PDMSe IPN systems

An Instron 1122 load frame updated with an MTS ReNew/E upgrade package and TestWorks 4 software was used to evaluate the tensile strength, stain at break, and modulus of PDMSe dog bones samples. An Interface SMT1-22 (22lb capacity) load cell was used for these measurements. PDMSe samples were prepared by casting uncured PDMSe between PET cover glass plates with 1.2 mm spacers and cured at 80°C for 1.5 hrs. Samples were then punched from the PDMSe sheets with an ASTM D 1822-68 Type L bog bone die with 3/8" tabs. Tests were conducted at a cross head speed of 2 inches per minute and displacement was measured with an MTS LX1500 laser extensometer. Data values are reported as the average of five samples.

6.2.9 ATR-FTIR Analysis

ATR-FTIR analysis was conducted on a Nicolet 20SXB FTIR equipped with an ATR stage and Omnic ESP 4.1 software. A KRs-5 (Thallium Bromide-Iodide) 45° SPP (surface plasmon polariton) ATR crystal was used. The crystal geometry was 50 mm X 10 mm X 2 mm. This technique has a average penetration/sampling depth of 0.6 to 6μm depending on the refractive index of the sample and ATR crystal used along with the sampling wavelength.

Scans were conducted from 400-4000 cm^{-1} with a resolution of 4 cm^{-1} (data spacing = 1.928 cm^{-1}) in absorbance mode; scan number = 32. Measurements were acquired using a DTGS KBr detector and KBr beam splitter and mirror velocity of 1.5825 cm/sec; gain = 2.

6.2.10 Optical Microscopy

Optical microscopy was used to monitor the phase size and distribution of PPy in the PPy/PDMSe materials. For this a Leica G27 dissecting microscope (2X objective) equipped with a Sony CCD-IRIS color CCD camera and Canopus DV Raptor image captures software and a Zeiss Axioplan II microscope (high magnification images) were used to capture optical images of the PPy/PDMSe systems. A standard green filter was used with the Axioplan II microscope analysis to improve contrast between the PPy and bulk PDMSe.

6.2.11 Electrochemical Analysis

In order to investigate the electrochemical properties of the materials sample were subjected to cyclic voltammetry measurements. These measurements were conducted in I.O. at ±0.8 V with a sweep rate of 10 mV/sec vs. an Ag/AgCl reference electrode and an Au wire working electrode. The CV current-voltage response of the material was monitored to determine electroactivity and conductivity of the samples.

A Omega HHM57 digital multimeter was used to conduct quick conductivity measurements on these materials. Conductivity measurements were taken on each side from corner to corner (diagonal). This results in four measurement locations for each sample. These measurements were repeated three times in random order.

6.2.12 EDS Mapping

EDS mapping measurements were conducted on a JEOL SEM 6400 at 15 KeV and a 15 mm working distance. PDMSe samples were doped with a 5 wt% $FeCl_3$/THF solution for 24 hrs and then dried overnight under vacuum. After drying the samples were carbon coated for three minutes prior to EDS mapping.

6.3 Background Study

Three possible routes for the direct incorporation of conducting polymers into base materials have been proposed. The three methods include electrochemical, chemical, and solution or bulk blending. Both electrochemical and chemical routes to the formation PPy/PDMSe were used in this study.

In the electrochemical method the working electrode is coated with an aqueous or organic compatible material depending on the type of electrochemical electrolyte medium/system being used. As the base material swells in the monomer and electrolyte solution an oxidizing potential is applied inducing the electrochemical polymerization of the conducting polymer inside the base material. This results in the formation of interpenetrating polymer network (IPN) of conducting polymer inside the base material which initiates at the electrode surface and grows out towards the films surface. The degree of interpenetration of the conducting polymer can be controlled by the electropolymerization potential and deposition time.

Another method for the formation of conducting polymer IPN systems is through the utilization of chemical oxidants such as $FeCl_3$. Two different methods can be used in the formation of these networks. The first method is referred to as oxidizer insertion. In this method a given concentration of the chemical oxidizer is dissolved in an appropriate solvent capable of swelling the base material (EtOH, IPA, $scCO_2$, THF, etc.). The base material is then soaked in this solution for a predetermined time resulting in the deposition of the oxidizer inside the base material. The soak time determines the degree of oxidant insertion into the base material and also the dispersion of the oxidant into the material.

Shorter exposure times tend to deposit more oxidant in the surface layer than in the bulk resulting in materials with higher surface conductivities due to the higher concentration of the resulting conducting polymer on the surface of the material. However the resultant material is not bulk conductive and is subject to electrode damage due to surface contact. Longer soak times result in more uniform bulk deposition of the oxidant leading to more bulk like conductivity but with lower surface conductivities. After the soaking process the doped base material is exposed to the conducting polymer monomer or monomer vapor resulting in the formation of a conducting polymer IPN inside the base material. The doped base material is soaked in either pure monomer (if liquid) or a solvent monomer solution. Vapor phase polymerization is conducted in a sealed chamber containing a small amount of volatile monomer; the doped base material is suspended above the monomer.

The second chemical polymerization method is similar to the previous method except the oxidizer and monomer soak steps are reversed. This method is referred to as monomer insertion due to the monomer soak step being done first instead of oxidizer soaking. In this process the penetration of the CP IPN can be altered by the oxidizer solvent used. If an aqueous oxidizer solution is used and the base material is not water swellable then the CP formation will be limited the surface layer of the base material. If the base material is swellable in the oxidizer solvent then a deeper CP IPN formation will occur.

6.3.1 Electrochemical formation of Conducting Polymer IPN Systems

In the initial tests electrochemically prepared CP/gelatin IPN systems were investigated. All electrochemistry was done utilizing an Ag/AgCl reference electrode unless otherwise noted. Crosslinked gelatin films were cast on EcAu (T=1 hr, I=100 ma)

treated EvAu coated polyimide films (in a mold) using the previous described method and allowed to dry over night. The crosslinked gelatin films tended to delaminate the corner of the EcAu/EvAu coating from the polyimide substrate when dried due to the contraction of the gelatin.

Polypyrrole was electrochemically polymerized inside the crosslinked gelatin film (t = 50 minutes). The gelatin film was allowed to presoak in the monomer/salt solution for ~ 20 minutes prior to the electropolymerization process. This was done to allow the gelatin film to completely hydrate. After 50 minutes the gelatin film visually turned a uniform light grey/black color and had a non-conductive surface.

Due to the nonconductive surface PPy formation was continued for an additional 50 minutes. The film turned completely black after 15 minutes. However after 50 minutes the PPy/gelatin film surface still looked like gelatin (shiny black). The PPy/gelatin EcAu/EvAu film completely delaminated from the polyimide substrate after the electropolymerization process. The surface was completely (uniform) black in color and nonconductive.

This experiment was repeated on a stainless steel electrode (other side coated with polyurethane). Pyrrole electropolymerization was conducted at +0.7 V for 130 minutes in an aqueous 0.1 M pyrrole, 0.1M $NaClO_4$ solution. The gelatin films were not allowed to presoak in the monomer/salt solution prior to electropolymerization. Polypyrrole started to form in spots randomly dispersed across the electrode surface inside the gelatin film after 1hr. The PPy spots continued to grow but did not totally cover the gelatin film. The resulting PPy/gelatin film was easily delaminated from the stainless steel working

electrode after it was dried. The side of the film that was in contact with the working electrode was conductive while the outer surface was nonconductive.

In both cases the electropolymerization process was too short to allow for the complete formation of polypyrrole throughout the bulk of the material resulting in a nonconductive sample surface. The polymerization process begins at the working electrode and propagates out toward the film surface. Longer electropolymerization times (>130 min.) should result in the formation of a more completely bulk conductive PPy/gelatin film. However once the PPy reaches the surface it would most likely form a complete PPy layer on top of the PPy/gelatin film thus negating the surface effects of the base material. In this research a film surface comprising of a composite or IPN structure is desired not a completely PPy surface. Also from the first experiment by presoaking the gelatin film in the monomer solution prior to electropolymerization a more uniform pyrrole polymerization occurs instead of the spotty growth described above.

6.3.2 Chemical formation of Conducting Polymer IPN Systems

The oxidizer insertion method was also used to form PPy/gelatin films. Crosslinked gelatin films were soaked for 4hrs in the oxidizer solution (1 M FeCl3/LiClO4; aqueous). These samples were prepared using pyrrole vapor and a pyrrole solution (1M; aqueous). The samples were stored in an aqueous LiClO4 solution (0.1 M; aqueous) until tested. All samples had a shiny black nonconductive surface. This suggests that the surface was mainly gelatin and not PPy.

Another set of experiments was carried out using gelatin where the gelatin films were predoped with oxidizer prior to gelation. Gelatin films were prepared as previously described however 1 M and 3 M of FeCl3 were added in with the gelatin powder. Both mixtures did not gel and the experiments were terminated at this point. The gelation of

gelatin is an ionic process; it is believed that the gelation process was interrupted due to charge screening from the FeCl3 salt.

The oxidizer insertion method was also tried using Silastic® T2 resin (PDMSe). The choice of solvent is very important in this process. A solvent that is capable of dissolving the oxidizer (polar) used and swelling the base material (PDMSe, nonpolar) is required. The degree that the solvent is capable of swelling the base material dictates how deep the oxidizer will penetrate into and deposit inside the base material. In this experiment ethanol was used because it is a good solvent for the oxidizer FeCl3, but a poor solvent for PDMSe. This caused surface swelling of the PDMSe. The deposition of the oxidizer was limited to the surface layer of the film. Thus PPy modification of the PDMSe films was also localized to the surface.

PDMSe films were prepared as previously described (0.1 M FeCl3/NaClO4 ethanol solution; 70 Hrs). The doped PDMSe films were then exposed to pyrrole monomer vapor for 48.

Captive air bubble contact angle measurements were conducted on these samples in ultrapure water. A reproducible contact angle change of 21° was measured when the potential was switched between ±1V (Figure 6.1). The contact angles for this experiment were 23 ±5, 31 ±6, 40 ±7, and 44 ±3 degrees for potentials of +1.0, 0.0, -0.6, and -1.0 V respectively (Figures 6.2).

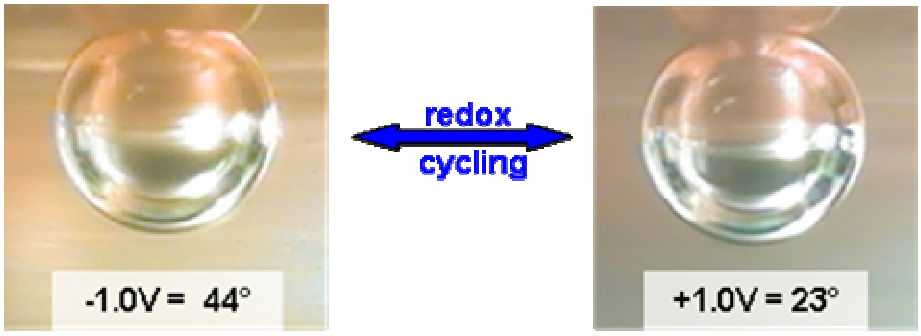

Figure 6.1 Images of captive air bubble contact angle measurements on PPy/PDMSe oxidizer insertion films.

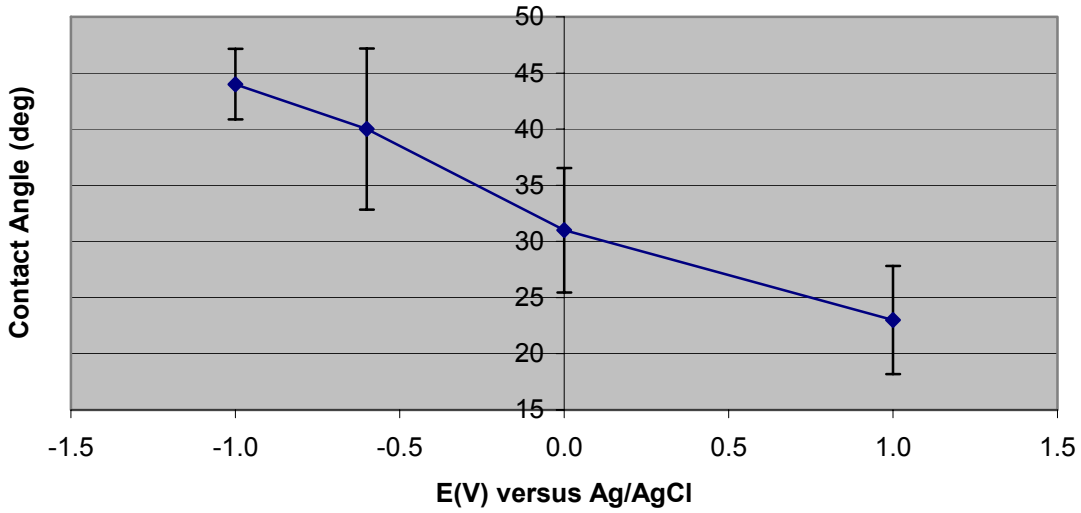

Figure 6.2 Captive air bubble contact angle data for PPy/PDMSe oxidizer insertion films conducted at potentials of -0.8, 0.0, and +0.8 V versus Ag/AgCl in distilled H_2O.

6.3.3 Conducting Polymer Blend Formation by Solution Blending

A solution blending process was also tried to form PPy/PDMSe blends. In this experiment soluble polypyrrole/DBSA was prepared as previously described. Two PDMSe films were placed in a 1wt% PPy, 2wt% DBSA chloroform solution and allowed to soak for ~20hrs. This resulted in the complete degradation of the PDMSe samples

To determine what caused the degradation of the PDMSe films two new PDMSe films were placed in chloroform and allowed to soak for 24hrs. After 24hrs both films

were completely intact with no signs of degradation. The films were left sealed in the chloroform for over 4 weeks with no signs of degradation.

It is believed that the sulfonic acid group of the excess DBSA caused the degradation of the PDMSe network. And it has now been determined that DBSA is the major component in some commercial silicone solvents and removers for both cured and uncured silicone. Dynaloy Engineered Chemistries (http://www.dynaloy.com/silicone_products.html) produces a commercial grade series of silicone solvents/removers under the tradename Dynasolve. Dynasolve consists of either methylene chloride or naptha (60-100%) and 10-30% DBSA which are capable of removing silicone coating in under 24hrs. The methylene chloride containing product is the fastest acting of the series but can also attack other materials present such as metals, epoxies, and polyurethanes. By replacing the methylene chloride with different grades of naptha the side reactions are limited unless the system is contaminated with water. From this it was determined that the solution blending process previously described is not suitable for use with PDMSe.

6.4 Polypyrrole/PDMSe IPN Formation

6.4.1 Introduction

As stated above solvent soaking is a viable method for the preparation of polypyrrole/PDMSe IPN systems. However solvents like ethanol are not the best choice for this base material. Ethanol is a good solvent in the sense that oxidizers such as $FeCl_3$ are readily soluble in it; but ethanol is not a good solvent for the swelling of PDMSe. Ethanol is a poor solvent for PDMSe and is only capable of solvating/swelling a very limited surface layer of the PDMSe sample. This results in PPy/PDMSe IPN formation only in a very thin surface layer, thus limiting the conductivity of the resultant film and

the overall durability of this conductive layer. Due to the very thin layer of PPy/PDMSe any surface damage can potentially destroy the electrical properties of the film and therefore the dynamic properties of the film.

In order to prevent loss of electrical properties a more bulk conductive material is needed. In order to form a more bulk conductive system deeper IPN formation is needed. The use of better solvents that are capable of swelling the base material to greater degree (solubility parameter closer to that of the base material) should result in the formation of IPN systems that penetrates deeper into the bulk of the sample. However the solvent must also be able to adequately solvate the desired oxidizer/dopant in order to deposit the oxidant into the base material.

6.4.2 Supercritical Carbon Dioxide Solution Doping

6.4.2.1 Introduction

Supercritical carbon dioxide ($scCO_2$) has gained a lot of attention lately as being an environmentally friendly replacement for organic solvents due to its non-toxic, non-flammable nature, ease of recycling, and low cost. Supercritical CO_2 is formed when CO_2 is compressed and heated above its critical point. The critical temperature and pressure for CO_2 is about 73.8bar (1070psi) and 31.1°C so most $scCO_2$ processes run at temperatures between 32-49°C and pressures between 73.8-241.3bar (1070-3500psi). A phase diagram for CO_2 is depicted in Figure 6.3. Once in the supercritical phase CO_2 exhibits the properties of both a liquid and a gas.

The lower surface tension of $scCO_2$ compared to liquid CO_2 enhances the ability to wet and penetrate various materials. However by maintaining some of its liquid properties, $scCO_2$ is also able to solvate mixtures. The organic nature of supercritical CO_2 allows it to swell and penetrate organic materials very easily. Inorganic compounds

such as inorganic oxidizers are relatively insoluble in $scCO_2$ however the solubility of $scCO_2$ can be tuned by varying the process temperature and pressure. Also small amounts of co-solvents such as ethanol and methanol can also be added to the system to increase the solubility of inorganic species.

One nice feature of $scCO_2$ is the ability to ease of removal of any contaminates/additives such as co-solvents, oxidizers, and oils from the system by lowering the pressure and/or temperature below the supercritical point. When this is done the CO_2 returns to the gas phase and can easily be bled off and recycled leaving any contaminated in the bottom of the reaction chamber.

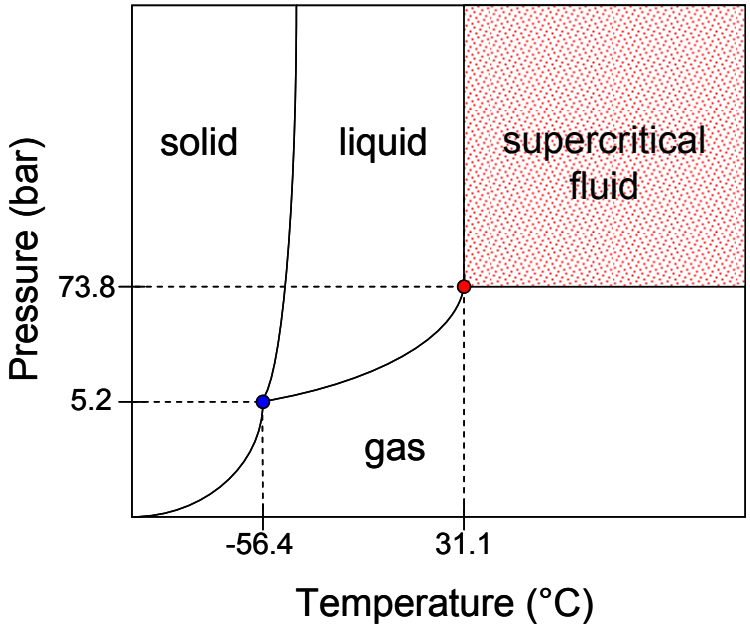

Figure 6.3 Phase diagram for carbon dioxide. Adapted from Figure 1 on http://www.pprc.org/pprc/p2tech/co2/co2intro.html

6.4.2.2 EtOH/$scCO_2$ prepared IPNs

An initial study was conducted to compare the effectiveness of the $scCO_2$ treatment versus the ethanol soak treatment. For this study ethanol (EtOH) was added to the $scCO_2$ system as a cosolvent to improve the solubility of $FeCl_3$ in $scCO_2$. Iron chloride is not

very soluble in $scCO_2$ but by adding co-solvents such as ethanol the solubility can be greatly improved. For this first study a 0.1M $FeCl_3/NaClO_4$ solution was made in $EtOH/scCO_2$ (1vol% EtOH) and pure EtOH. Two PDMSe samples (cylinders; ~24.75mm X 9.5mm v ≈ 1.75ml) were placed in the $scCO_2$ chamber with $FeCl_3/NaClO_4$ and EtOH cosolvent. The sample chamber was then sealed and the $scCO_2$ treatment was conducted for 24hrs as described previously. The experiment was duplicated in pure EtOH and was conducted in a 50ml polypropylene centrifuge tube with 14ml of a 0.1M $FeCl_3/NaClO_4$ solution in EtOH. After 6 hrs the $scCO_2$ system was visually checked and the oxidizer was not visible through the sight glass (gone into solution) and the PDMSe samples appeared swollen and puffy white in appearance. At this point the chamber temperature had reached 42°C. After 24hrs the $scCO_2$ chamber was slowly vented and the samples removed. The PDMSe samples were completely destroyed and only a degraded yellow resin remained in the chamber (Figure 6.5). However after 24hrs in the oxidizer EtOH solution the EtOH soak samples were completely intact and relatively unchanged except for a slight color change due to oxidizer insertion into the PDMSe sample.

Figure 6.5 Optical images of degraded PDMSe samples after supercritical CO2 doping with 0.1M FeCl3 dopant and 1vol% ethanol cosolvent for 24hrs.

In order to determine the cause of the degradation of the EtOH/$scCO_2$ PDMSe samples a $scCO_2$ experiment was conducted with 2vol% EtOH and oxidizer. After 24hrs the two PDMSe samples were intact but swollen and white in appearance. The swollen whitish appearance slowly disappeared over about a 1 hr period and the samples returned to there original condition. This is believed to be due to the EtOH dispersed inside the PDMSe sample. From this it is believed that the degradation of EtOH/$scCO_2$ PDMSe samples was primarily due to the oxidizer concentration.

In order to prevent sample degradation the $scCO_2$ oxidizer insertion method was repeated but at different oxidizer and co-solvent concentrations. The oxidizer concentration as dropped from 0.1M to 0.01M and the EtOH concentration were increased to 2vol% from 1vol%. After a 24hr treatment, the two samples were completely intact prior to the decompression of the sample chamber (chamber venting). After decompression the samples split and fractured slightly due to the inability of the CO_2 to diffuse out of the center of PDMSe samples fast enough. From this it was determined that a slower decompression rate is needed to prevent the destruction of the samples.

After the doping treatments both the EtOH/$scCO_2$ and EtOH prepared samples were placed in a 50ml PP centrifuge tube with 2ml of pyrrole monomer and allowed to soak for 24hrs. After 24hrs the samples were removed and allowed to dry (evaporate residual pyrrole monomer) at room temperature and pressure. The EtOH treated samples exhibited a slight color change turning light transparent brown in appearance while the EtOH/$scCO_2$ prepared samples turned completely opaque black in color. Both sets of samples exhibited a shiny surface texture similar in appearance to pure PDMSe. Optical

images of untreated PDMSe and EtOH doped and EtOH/$scCO_2$ doped PPy/PDMSe samples are shown in Figure 6.6.

Figure 6.6 Optical images of untreated PDMSe (A), and PPy/PDMSe IPNs prepared by EtOH (B) and EtOH/$scCO_2$ (C) oxidizer insertion methods.

This result shows that the EtOH/$scCO_2$ treatment is a much more effective method for the doping (oxidizer insertion) used for the subsequent vapor phase polymerization of PPy than EtOH solvent soaking techniques.

The sample weight varied during processing of PPy/PDMSe IPNs on PDMSe films (18 mm X 18 mm X 2 mm) using 0.01M $FeCl_3/NaClO_4$ and 2vol% EtOH in $scCO_2$. The weight increases with EtOH/$scCO_2$ oxidant insertion (24 hrs) and pyrrole monomer exposure (48 hrs). But then the weight decreases below the initial sample weight after being dried in vacuum for 1 hr. These weight changes (Figure 6.7) are attributed to the $scCO_2$ process extracting uncured resin and oils from the PDMSe samples. In addition, residual solvent and monomer present in the films were removed during the vacuum drying process. The PPy/PDMSe films were inhomogeneous visually. This is most likely an indication of the PPy distribution inside the PDMSe. ATR-FTIR analysis (Figure 6.18) of these films, which were also nonconductive, reveals pure PDMSe on the surface identical to an untreated Silastic® T2 PDMSe.

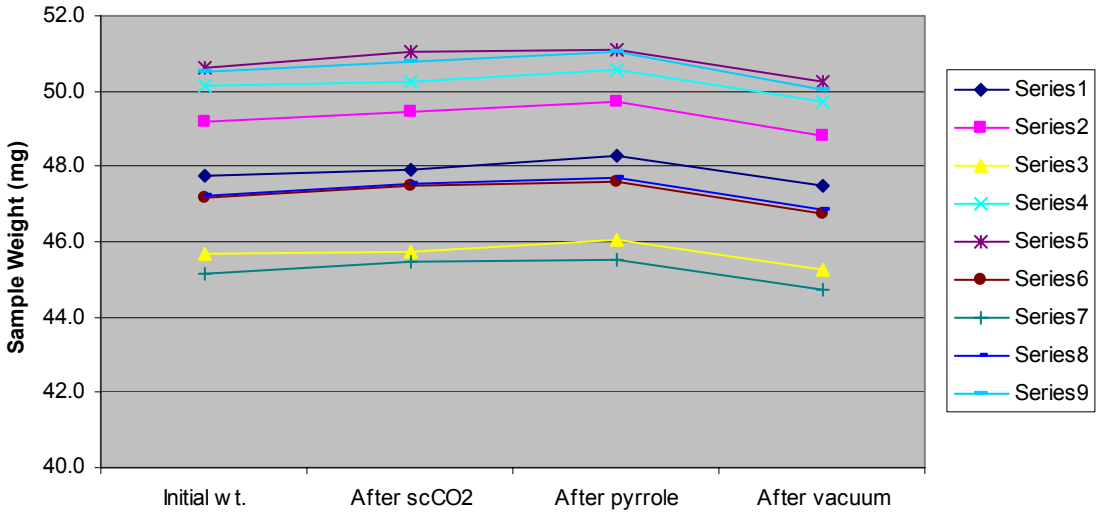

Figure 6.7 Changes in PDMSe sample weight during EtOH/$scCO_2$ prepared PPy/PDMSe IPN systems.

6.4.2.3 IPA/$scCO_2$ prepared IPNs

Isopropyl alcohol (IPA) is a better solvent for PDMSe than EtOH and is still capable of solvating $FeCl_3$. The use of IPA was evaluated in an attempt to improve the dispersion and formation of PPy inside PDMSe films. Additional oxidizer was also tested. The IPA was used in conjunction with $scCO_2$ and the results are compared to the EtOH/$scCO_2$ system.

Seven PDMSe samples (18 mm X 18 mm X 2 mm) were treated in both 2 vol% IPA/$scCO_2$ and EtOH/$scCO_2$ solutions containing 0.02 M $FeCl_3$ and 0.02 M $NaClO_4$. Samples were allowed to soak in the cosolvent/$scCO_2$ solutions for 24 hrs and then were soaked in pyrrole monomer vapor for 24 hrs. Sample weights were measured before oxidizer insertion (solvent soaking), between oxidizer insertion and pyrrole monomer exposure, and after pyrrole monomer exposure.

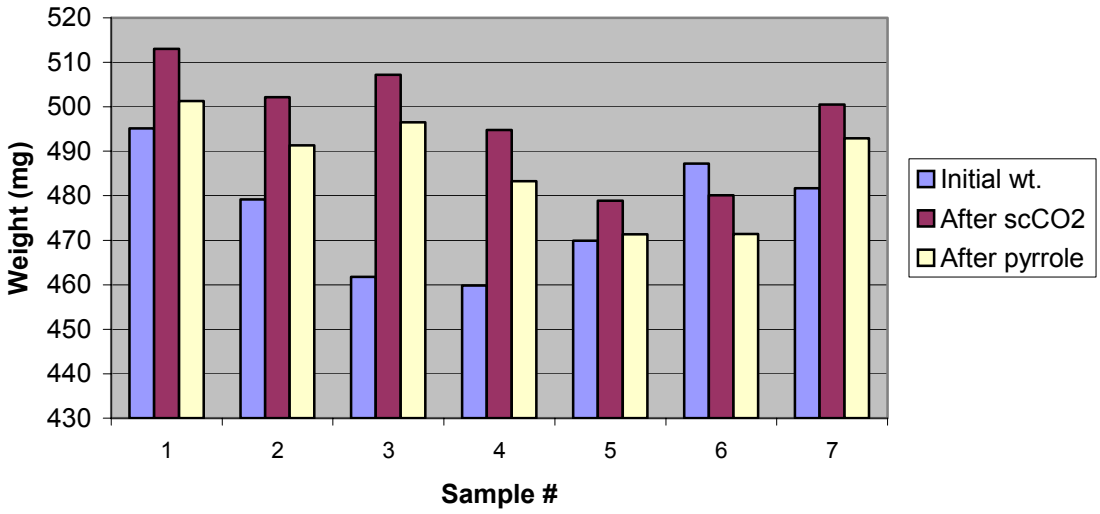

Figure 6.8 Weight change data for IPA/scCO$_2$ prepared PPy/PDMSe prepared samples.

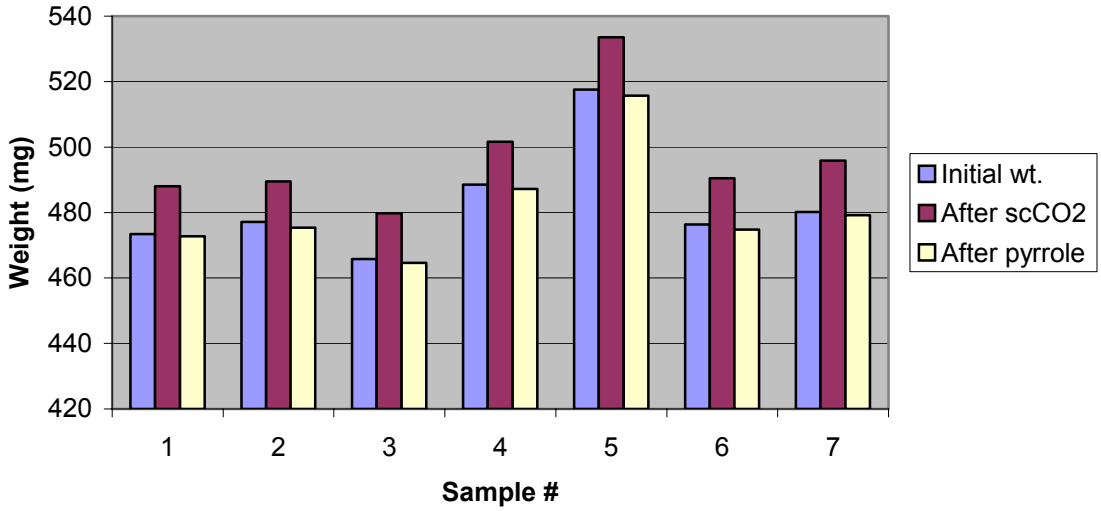

Figure 6.9 Weight change data for EtOH/scCO$_2$ prepared PPy/PDMSe prepared samples.

The samples prepared using the IPA/scCO$_2$ oxidizer insertion method resulted in a slight overall increase in sample weight while the IPA/scCO$_2$ preparation method resulted in a slight overall decrease in sample weight (Figures 6.8 and 6.9). The weight change is probably due to a combination between the effects of oxidizer insertion and subsequent PPy formation and the extraction of soluble components from the PDMSe films during the scCO$_2$ treatment. The effects of this are clearly visible in the optical images. Optical

images of IPA/$scCO_2$ and EtOH/$scCO_2$ prepared PPy/PDMSe samples are shown in Figures 6.10 - 6.13.

Figure 6.10 Optical images (Leica G27) of PPy/PDMSe samples prepared by EtOH/$scCO_2$ (A) and IPA/$scCO_2$ (B) oxidizer insertion methods (mag. = 2X). Sample placed on top of printed text to show transparency.

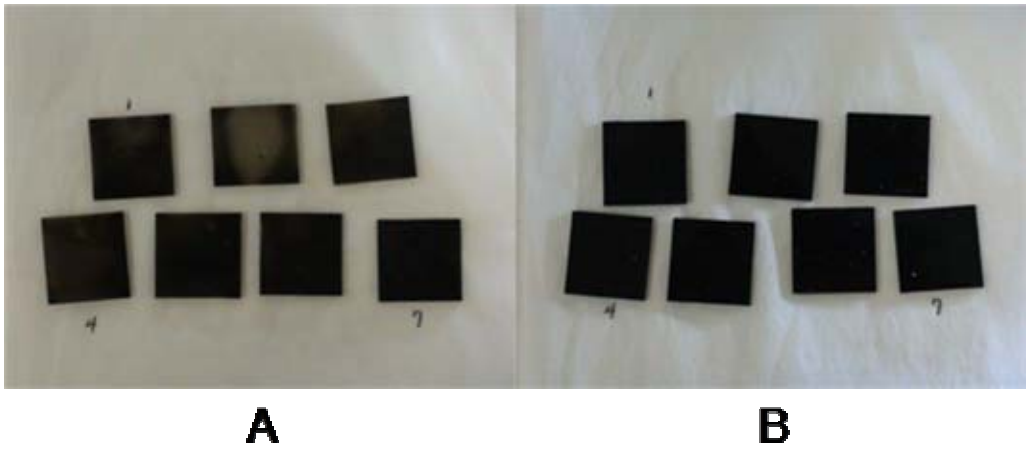

Figure 6.11 Optical images (Leica G27) of PPy/PDMSe batches prepared by EtOH/$scCO_2$ (A) and IPA/$scCO_2$ (B) oxidizer insertion methods showing the differences in homogeneity of PPy formation between samples.

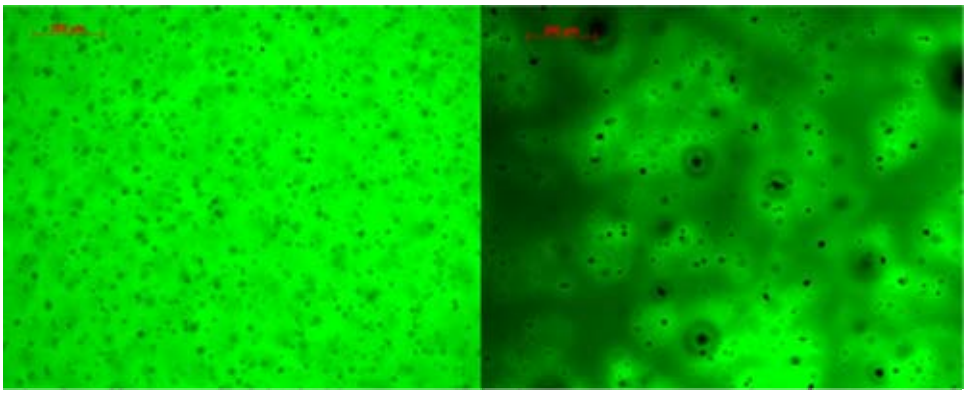

Figure 6.12 Optical images (Axioplan II) of PPy/PDMSe samples prepared by EtOH/$scCO_2$ (A) and IPA/$scCO_2$ (B) oxidizer insertion methods (magnification = 100X; scale bar = 200μm).

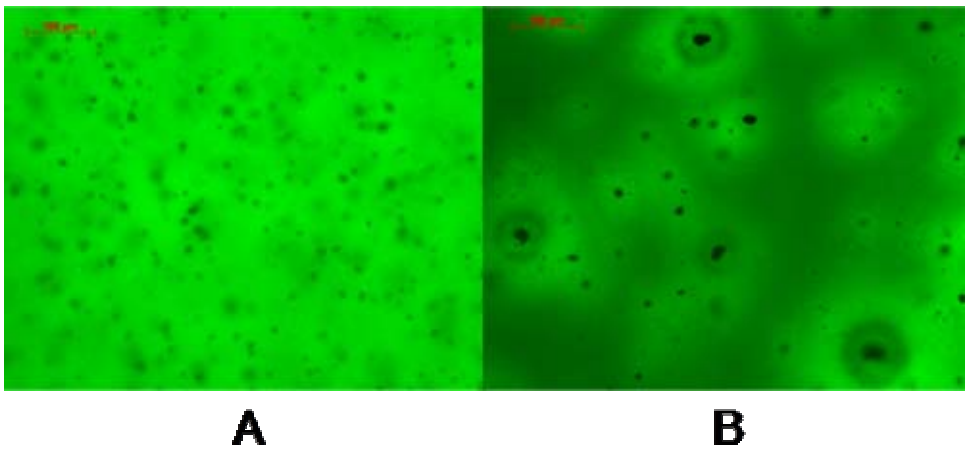

Figure6.13 Optical images (Axioplan II) of PPy/PDMSe samples prepared by EtOH/$scCO_2$ (A) and IPA/$scCO_2$ (B) oxidizer insertion methods (magnification = 200X; scale bar = 100μm).

From the optical images it is evident that the dispersion and PPy phase size produced from the EtOH and IPA $scCO_2$ treatments is different. The samples prepared by EtOH/$scCO_2$ have a relatively uniform particle size on the order of ~9-22 μm. However the samples prepared by the IPA/$scCO_2$ method have relatively large particles on the order of ~20-100 μm with a much finer dispersed particle phase with particles on the order of ≤1-2 μm.

This is believed to be mainly due to the improved solubility of IPA and the resulting $FeCl_3$/IPA solution in the PDMSe material. Both sets of samples are visually dark black in color but have different degrees of opacity. Samples prepared by EtOH/$scCO_2$ have a splotchy non-uniform appearance while the IPA/$scCO_2$ samples have a more uniform appearance when viewed with the naked eye. From the images above (Figures 6.10) the letters "PPy" are clearly visible in the EtOH/$scCO_2$ samples while they are not visible in the IPA/$scCO_2$ sample. The reason for this is apparent from Figures 6.12 and 6.13. The EtOH/$scCO_2$ samples have finely dispersed and locally uniform PPy phases (black speck in the optical image, Figure 6.12 and 6.13). While the samples prepared by IPA/$scCO_2$ exhibit much larger PPy phases with a finely dispersed and uniform secondary PPy phase which appears as the dark smoky regions in the optical micrograph.

In order to investigate the weight change effects of extraction of soluble components from the PDMSe films a series of tests were conducted on four sample systems (n=7). The sample sets consisted of controls (no treatment) and samples exposed to $scCO_2$, scCO2 with 1vol% EtOH, and $scCO_2$ with 1 vol% IPA for 24 hrs. The initial sample weight was recorded and then the samples weights were rerecorded after the 24 hr treatment and then again at 1hr and 18 hrs (air dry) after the 24 hr $scCO_2$ treatments to allow for complete offgassing of CO_2 and solvent evaporate from inside the samples.

The weight changes between each step and overall weight changes were then calculated. The control samples exhibited an average weight change (Δwt_{avg}) of -0.76 mg after the $scCO_2$ treatment. After 1hr they exhibited an additional Δwt_{avg} of -0.09 mg and after 18 hrs they exhibited an additional Δwt_{avg} of -0.02 mg, for an overall Δwt_{avg} of -0.86

mg compared to the initial sample weights. For samples treated with $scCO_2$ the Δwt_{avg} $scCO_2$ treatment, Δwt_{avg} 1 hr, and Δwt_{avg} 18 hrs were: -3.02 mg, -0.49 mg, and -0.34 mg. This resulted in an overall Δwt_{avg} of -3.85 mg. For samples treated with $scCO_2$ and 1 vol% EtOH the Δwt_{avg} $scCO_2$, Δwt_{avg} 1 hr, and Δwt_{avg} 18 hrs were: +12.59 mg, -17.57 mg, and -6.47 mg resulting in an overall Δwt_{avg} of -11.45 mg.

The samples treated with $scCO_2$ and 1 vol% IPA showed the largest initial swelling/weight change when compared to $scCO_2$ and EtOH/$scCO_2$ samples. However the overall changes in weight were not much higher than that for the EtOH/$scCO_2$ samples. The Δwt_{avg} $scCO_2$, Δwt_{avg} 1 hr, and Δwt_{avg} 18 hrs were: +23.69 mg, -27.13 mg, and -9.23 mg resulting in an overall Δwt_{avg} of -12.67 mg. Due to differences in initial sample weight the % weight changes were calculated for the initial $scCO_2$ treatment and the overall process ($scCO_2$ treatment and 18 hrs degassing).

The %Δwt for just the $scCO_2$ process is -0.17%, -0.66%, +2.56%, and 5.19% for the controls, $scCO_2$, $scCO_2$-EtOH, and $scCO_2$-IPA respectively. While the overall %Δwt for the samples were -0.19%, -0.84%, -2.36%, -2.78% respectively. This data is displayed in Figures 6.14 and 6.15. Due to the fact that the samples prepared by the IPA/$scCO_2$ method had an average weight change of about twice that obtained for the EtOH/$scCO_2$ samples after the $scCO_2$ treatment, but only exhibited an extra -0.42% decrease in final sample weight compared to the EtOH/$scCO_2$ samples, it can be said that the IPA/$scCO_2$ method is more efficient at swelling the PDMSe material but that both systems extract about the same amount of soluble material from the PDMSe films or that both systems extracted out all the soluble material from the system.

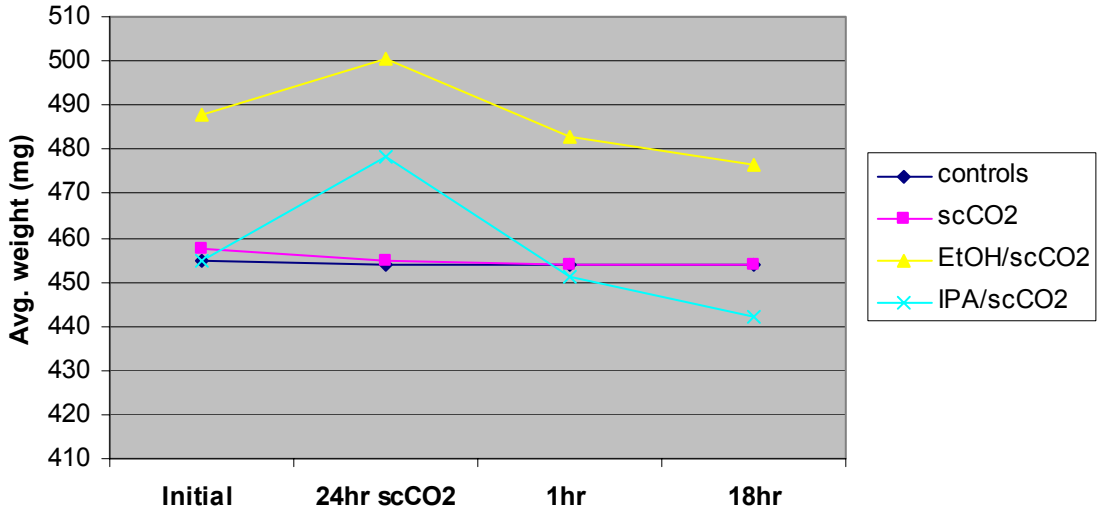

Figure 6.14 Weight change of PDMSe samples exposed to different supercritical CO_2 treatments.

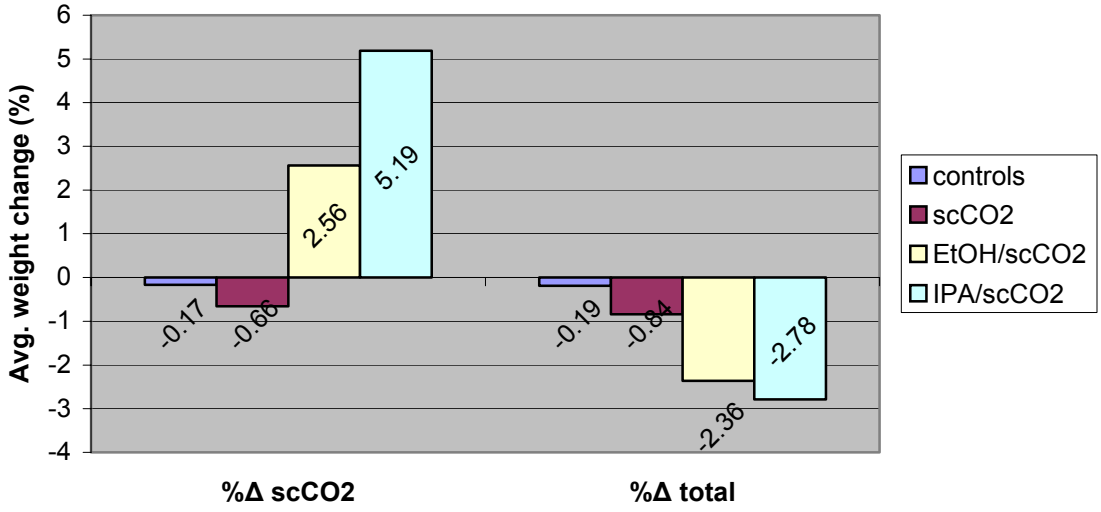

Figure 6.15 Average weight change in PDMSe samples exposed to different supercritical CO_2 treatments and after an 18 hr degassing period.

From this it can be said that on average ~2-3% of the samples weight is extracted from the samples during scCO2 treatments with EtOH and IPA. This complicated the determination of how much oxidizer and polypyrrole are incorporated into the PDMSe matrix during scCO2 processing. When this is accounted for in the previous IPA/$scCO_2$

and EtOH/scCO$_2$ PPy/PDMSe samples it equates to ~4.1-5.1 wt% and ~1.7-2.7 wt% PPy for the IPA and EtOH samples.

6.4.3 Tetrahydrofuran Solution Doping

As previously shown scCO2 treatment is an effective way to incorporate oxidant into PDMSe for the polymerization of pyrrole and other conducting polymers. However due to the limited sample compartment size only a limited number of samples (currently 7) can be prepared per cycle (24 hrs per cycle). A solvent soak system is more advantageous due to the ability to prepare large number of samples per cycle. However it is difficult to find a solvent that is a good solvent for both PDMSe (for swelling) and inorganic oxidizers ($FeCl_3$, $NaClO_4$, etc.).

In a paper by Zoppi and De Paoli,[148] THF was found to be a good solvent for $FeCl_3$. It was also shown to swell EPDM rubber (ethylene-propylene-5-ethylidene-2-norborene) used to form PPy/EPDM conductive blends. From their work, it is known that ~15-30% PPy is needed to produce conductive blends. The solubility parameter (δ) for THF is 18.5 $(MPA)^{1/2}$ while the δ for PDMSe is 14.9-15.59 $(MPA)^{1/2}$. So from this information, THF should be a good choice as a solvent for the $FeCl_3$ and the PDMSe system that we are currently using.

An initial test was conducted with a saturated solution of $FeCl_3$ in THF. PDMSe samples were soaked in a saturated solution for 41hrs. When removed, the samples were bright orange in color and very swollen. The samples were then degassed in a hood for 7 hrs at which time they were placed in a centrifuge tube filled with pyrrole vapor. The samples immediately (15 sec) started to turn black around the edges and slightly on the sample face.

The resulting PPy/PDMSe samples were jet black in color and completely opaque when viewed with the naked eye or under the Zeiss microscope as previously done therefore no transmission optical images could be taken for these samples.

Another set of experiments was conducted with a 10wt% $FeCl_3$ solution in THF. The PDMSe samples were soaked in the $FeCl_3$/THF solution for 24hrs and then dried under vacuum for 1hr to remove the residual THF. The samples turned cloudy opaque yellow in color from a clear transparent color. Once dried the samples were exposed to pyrrole monomer vapor for 96 hrs to ensure full PPy formation for the given $FeCl_3$ doping. After pyrrole monomer exposure the samples were again dried under vacuum for 2 hrs to remove any residual pyrrole monomer and THF. These PPy/PDMSe samples appeared to have no bulk conductivity when tested with an Omega HHM57 digital multimeter.

Two samples each of IPA/$scCO_2$ and THF/$scCO_2$ were placed in a 50 ml PP centrifuge tube containing 15 ml Instant Ocean® artificial sea water (I.O.) to determine if sample hydration influenced the conductivity of the samples two THF prepared. The THF prepared samples had a rough flat black surface while the IPA/$scCO_2$ samples had a smooth shiny black surface.

The samples were allowed to soak in I.O. for ~64 hrs to fully hydrate prior to electrochemical analysis. The THF prepared samples turned the I.O. light brown in color. This is probably due to residual Fe(III) and Fe(II) leaching from the samples. However the IPA/$scCO_2$ samples produced no color change in the I.O. salt solution.

The samples were patted dry with Kimwipes® and then suspended in the solution from alligator clips making sure the clips did not come near the waters surface. Both the

untreated PDMSe and the IPA/scCO$_2$ prepared PPy/PDMSe samples exhibited no electrochemical response. However the PPy/PDMSe sample prepared by THF soaking showed a low electrochemical response (0.27 mA/cm^2) during the cyclic voltammetry experiment. The electrochemical response of the PDMSe and two PPy/PDMSe samples is shown in Figure 6.16.

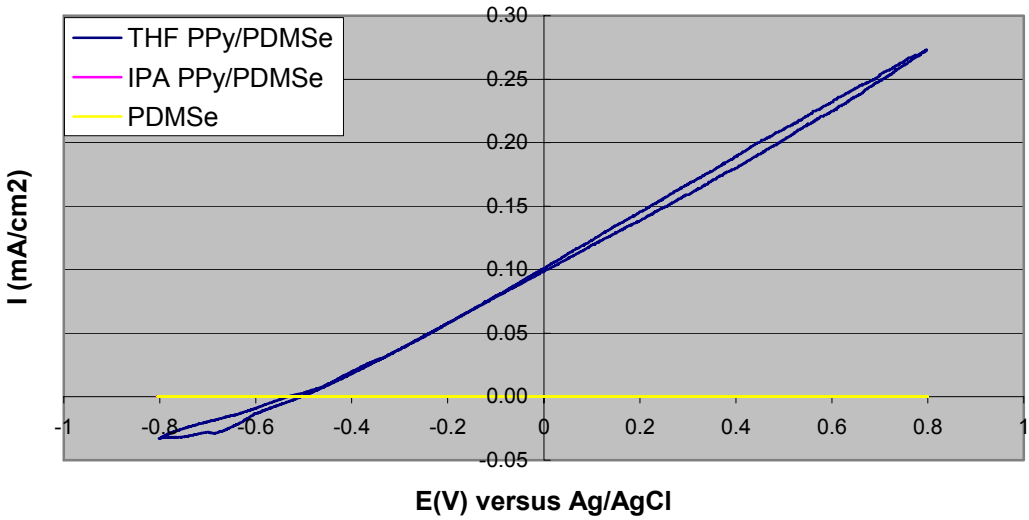

Figure 6.16 Current response of PPy/PDMSe samples prepared by THF solvent soaking and IPA/scCO2 techniques along with untreated PDMSe. Cyclic voltammetry conducted at ±0.8 V at 10 mV/sec versus Ag/AgCl in Instant Ocean® artificial sea water.

Visual inspection of the samples after the cyclic voltammetry experiment showed that the THF PPy/PDMSe sample had increased in size by ~10% during the 64 hr I.O. soak when compared to the other samples. This increase in volume suggests that the PPy/PDMSe samples are uptaking water and swelling during the I.O. soak.

6.4.3.1 Effects of hydration of sample conductivity

The effects of sample hydration were investigated by conducting cyclic voltammetry experiments in I.O. on dry PPy/PDMSe samples prepared by the THF method. Cyclic voltammetry was conducted at ±1.0 V with a rate of 10 mV/sec vs.

Ag/AgCl. A dry sample was suspended in the I.O. solution and cycled five times; the experiment lasted approximately 34 minutes. After the first five cycles the samples was allowed to soak for ~90 minutes in the I.O. solution and then the experiment was repeated for another 20 cycles resulting in a total of 25 cycles being run on the sample and a total I.O. immersion time of approximately 4.5 hrs. The current draw at the potential of +0.8 V was 3.6 nA during the first cycle which increased to 78.1 nA for the fifth cycle.

During the second half of this experiment the peak current for the 6th cycle increased to 0.145 mA (145 µA). This equates to the samples being in the I.O. salt solution for a total of 120 minutes. The final cycle (25th cycle) had a peak current of 0.258 mA; this equates to 253 minute soak time in the salt solution. This is a significant increase of ~71667% in current draw over the entire experiment, which equates to a decrease in resistance from 278 MΩ to 4 KΩ at a 1.0 V potential (Figure 6.17).

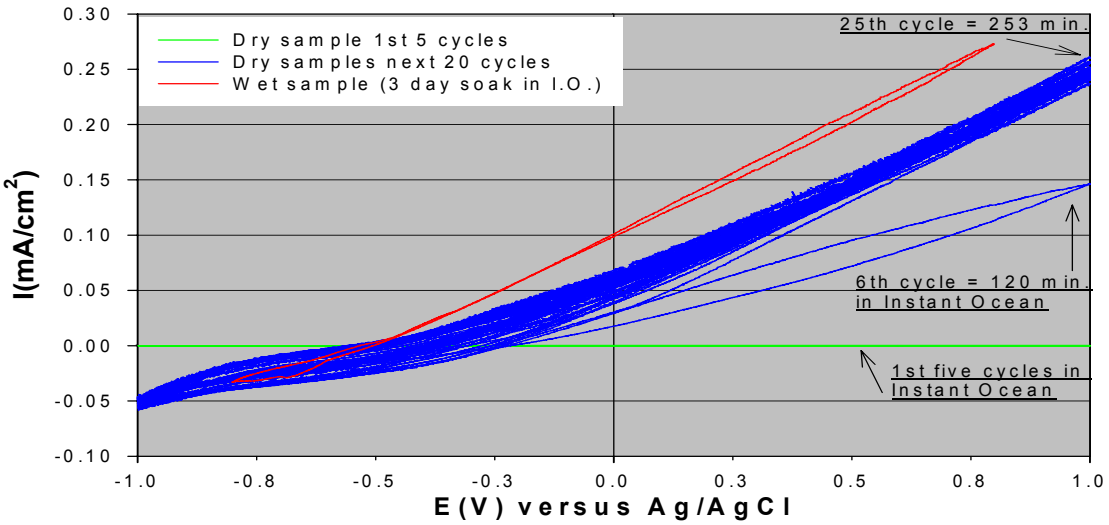

Figure 6.17 Effects of sample hydration on cyclic voltammetry for wet and dry PPy/PDMSe samples.

6.4.3.2 Effects of PDMSe surface segregation

An interesting trait noticed for all the THF prepared PPy/PDMSe composites is they exhibited bulk conductivity and swelled when soaked in I.O.. Samples prepared by other methods (EtOH, IPA, $scCO_2$ soaks) exhibited no bulk conductivity and do not swell in the I.O. solution. The samples that were conductive and swelled all have a rough flat black surface while nonconductive samples all have a flat shiny black surface. This was determined to be due to sample handling in between the oxidizer insertion and the pyrrole monomer exposure steps. Samples were non-conductive if the surface was rinsed, placed on Kimwipe® to dry, or manipulated in any way. The nonconductive surfaces were flat, shiny and black similar to the surfaces produced from the previous $scCO_2$ treatments.

Due to the fact the PDMSe rearranges its surface depending on the environment. It is believed that the formation of true PPy/PDMSe IPN systems is hindered on the PDMSe surface. This trend was discussed earlier in the studies on the $scCO_2$ systems by ATR/FTIR analysis. It is believed that the same thing happens in the THF systems. ATR-FTIR analysis of PPy/PDMSe samples prepared by EtOH, IPA, $scCO_2$, and THF treatments was conducted using a Nicolet 20SXB FTIR. There is no detectable difference in the ATR spectra of samples prepared by EtOH, IPA and $scCO_2$ methods (Figure 6.18). However THF prepared samples have a characteristic peak for PPy at ~1540 cm^{-1}.[149-152] This peak is characteristic of the pyrrole ring vibrations (C-C and C=C ring vibrations; 1500-1600 cm^{-1}). The rest of the characteristic peaks for PPy are confounded with the peaks associated with PDMSe. When the THF prepared PPy/PDMSe (same sample of previous) sample surface is cleaned with light whipping with Kimwipe® and EtOH the PPy surface layer is removed and a pure PDMSe surface is detected by ATR-FTIR.

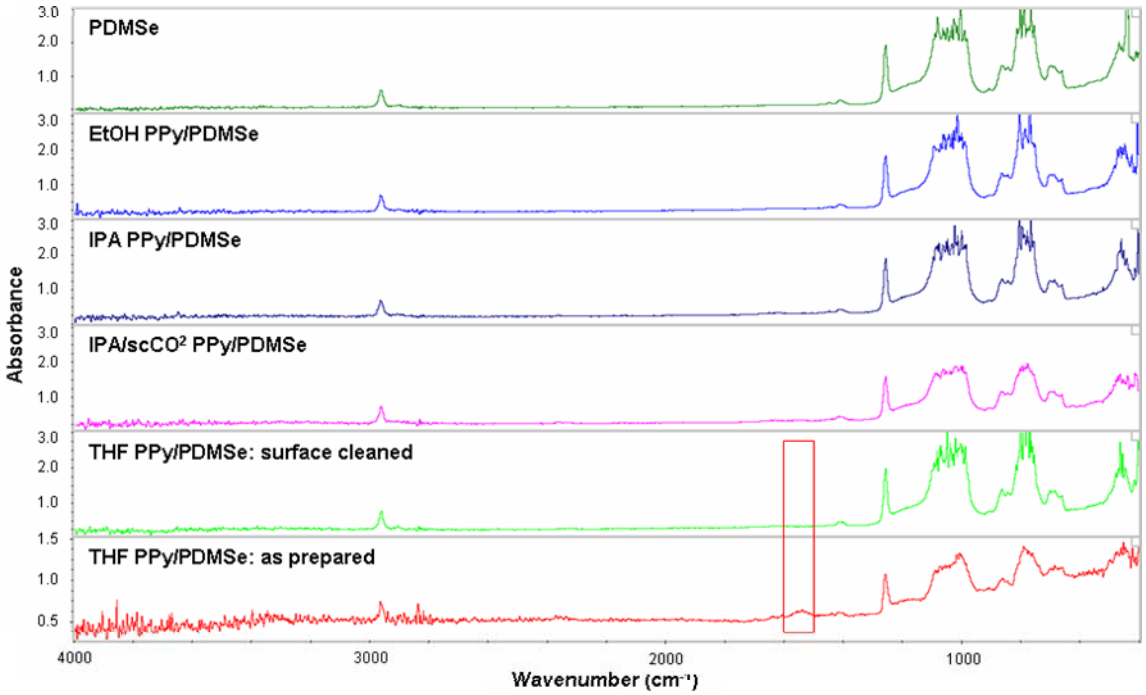

Figure 6.18 ATR-FTIR analysis of PPy/PDMSe IPN systems prepared by various solution soaking procedures. Inset box shows location of characteristic pyrrole ring vibrations (1500-1600 cm^{-1}).

This could explain batch inconsistency with respect to conductivity. Handling of the samples between the oxidizer insertion and pyrrole monomer exposure potentially removes or disrupts the deposited $FeCl_3$ layer which would heighten this effect.

It is also believed that the conductive samples have a PPy surface layer that is sitting directly on top of a predominately pure PDMSe layer that and it is not truly incorporated into the PDMSe sample. This is supported by the observation that the PPy/PDMSe samples mark easily, i.e., PPy flacks off when the sample surface is rubbed. The conductivity of the samples is easily destroyed by minor surface abrasion. Removing or disrupting the $FeCl_3$ deposited on or near the PDMSe sample surface prevents formation of a uniform, continuous PPy surface layer. This ultimately makes the surface nonconductive.

The effects of PDMSe surface segregation was evaluated using cross sectional EDS mapping on $FeCl_3$/THF doped PDMSe samples. The EDS spectrum for the $FeCl_3$ doped PDMSe is shown in Figure 6.19. EDS mapping was conducted for silicon, chlorine, and iron (Figure 6.20). From the EDS mapping for iron and chlorine ($FeCl_3$), it can be shown that the doped PDMSe samples have a ~60-100 µm surface layer relatively devoid of $FeCl_3$ (Figure 6.21). Chlorine was selected to illustrate the surface segregation of PDMSe due to its higher EDS signal intensity compared to iron.

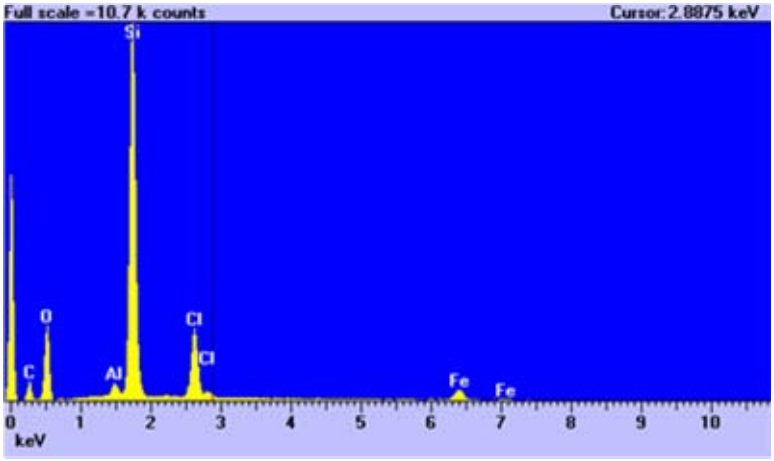

Figure 6.19 EDS spectra of cross sectioned $FeCl_3$/THF doped PDMSe.

$FeCl_3$ is still present in this surface layer however its concentration is appears ro be much lower than in the bulk of the sample. Subsequent exposure of this sample to pyrrole monomer vapor would result in the formation of a PPy/PDMSe IPN. However; the majority of the PPy would be buried in the bulk of the samples and not on the sample surface thus resulting in a non-conductive sample due to a predominantly pure PDMSe surface.

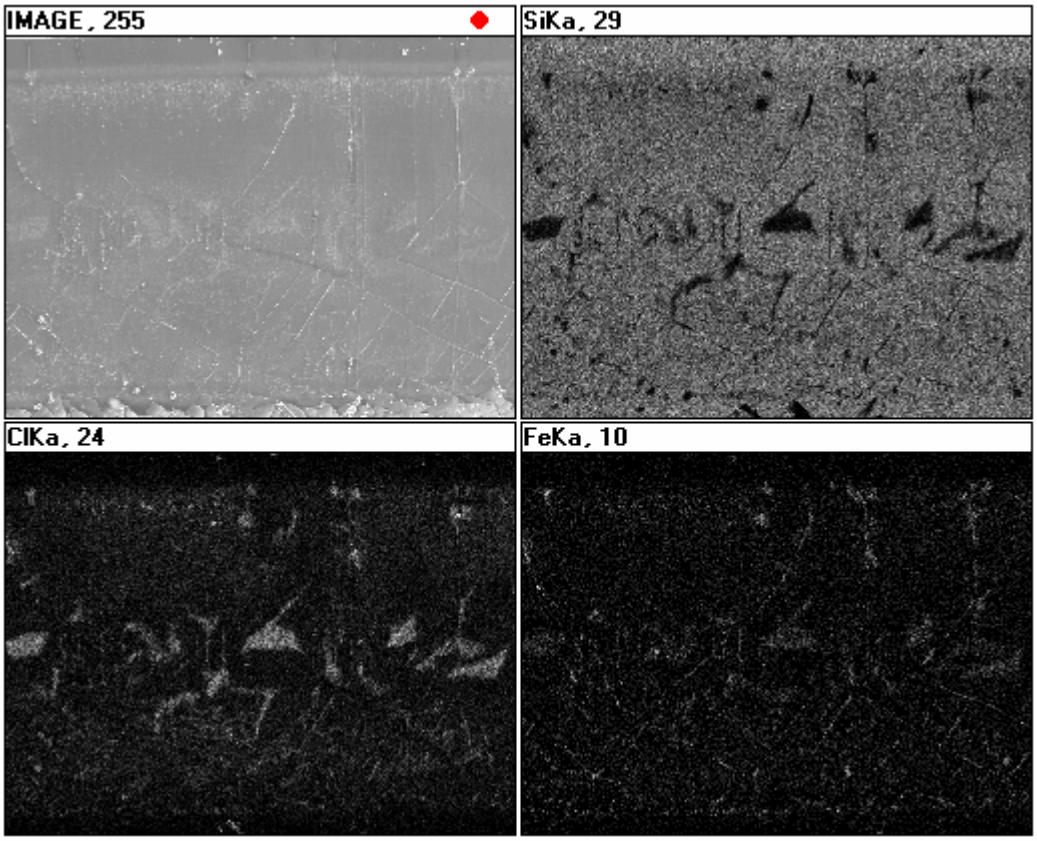

Figure 6.20 EDS mapping of cross sectioned $FeCl_3$/THF doped PDMSe (magnification = 70X).

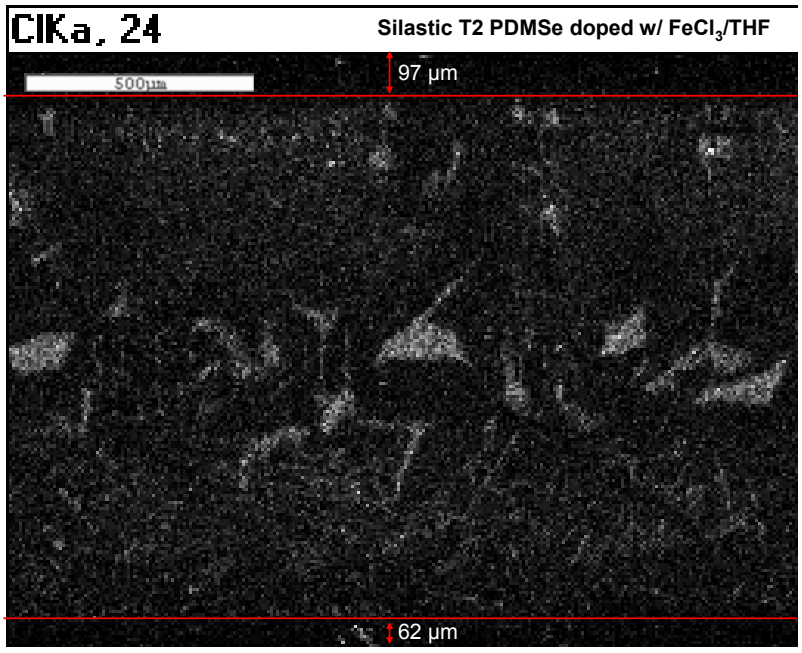

Figure 6.21 EDS chlorine mapping of cross sectioned $FeCl_3$/THF doped PDMSe showing a ~60-100 µm surface layer of predominantly pure PDMSe (mag. =70X).

6.4.3.3 Effects of $FeCl_3$/THF doping on PDMSe mechanical properties

The effects of the $FeCl_3$/THF doping process on the mechanical properties of PDMSe samples were investigated using tensile testing methods. The tensile strength, stain at break, and modulus of PDMSe dog bones samples was evaluated as a function of $FeCl_3$ solution exposure time.

As can be seen from Figure 6.22 there is an overall decrease in the strain at break and peak stress (tensile strength) as the $FeCl_3$ soak time is increased. The strain at break for untreated PDMSe is about 230% with a peak stress of 5.96 MPa. The decrease in peak stress occurs in almost a linear fashion. The values for peak stress decrease from the initial point (untreated) of 5.96 MPa to 1.44 MPa for the 20 hr soak. In contrast the decrease in the strain at break seems to occur in two different stages due to a change in the degradation rate between the 5 and 6 hr point. The strain at break rapidly decreases from 230% for the untreated sample to the about 130% for the 5 hr soak time (rate = ~20 %/hr). After this point the strain at break slowly decreases form the 156% for the 6 hr soak to about 90% for the 20 hr soak (rate = ~4 %/hr).

The modulus data, shown in Figure 6.23, shows an initial decrease in modulus from the unmodified PDMSe (1.22 MPa low strain and 3.35 MPa high strain) to the 1 and 2 hr treatment times (~0.91 MPa low, ~2.57 MPa high). After this the modulus increased and stabilizes for the 3-6 hr treatments (~1.47 MPa low, ~3.65 MPa high) after this the modulus again decreases and stabilizes for the 12, 16, and 20 hr treatments (~0.67 MPa low, ~2.09 MPa high). This trend is evident in both the low and high strain modulus values. The initial increase then stabilization in modulus up to the 6 hr mark is most likely due to the extraction to uncured oligomers, oils, and other soluble components. After this point the decrease in modulus is most likely due to the possible degradation of

the PDMSe. The extraction of unreacted oligomers, oils, and other soluble components is also evident from the weight loss data produced for the $scCO_2$, $EtOH/scCO_2$, and $IPA/scCO_2$ treatments on PDMSe.

The samples run at the 24 hr treatment times were too brittle to mount and run tensile tests on. The PDMSe samples change form a clear elastic material to an opaque yellow/orange material that tends to fracture if not handled correctly after the 24 hr exposure to the oxidizer solution. However; after exposure to the pyrrole monomer vapor for 24 hrs the samples regain their elastic nature and durability.

The decreases in mechanical properties suggest that the Silastic® T2 PDMSe used in these experiments is not a suitable choice for prolonged exposure to oxidizers due to oxidative degradation and extraction of unreacted silicone oligomers, oils, and other soluble components.

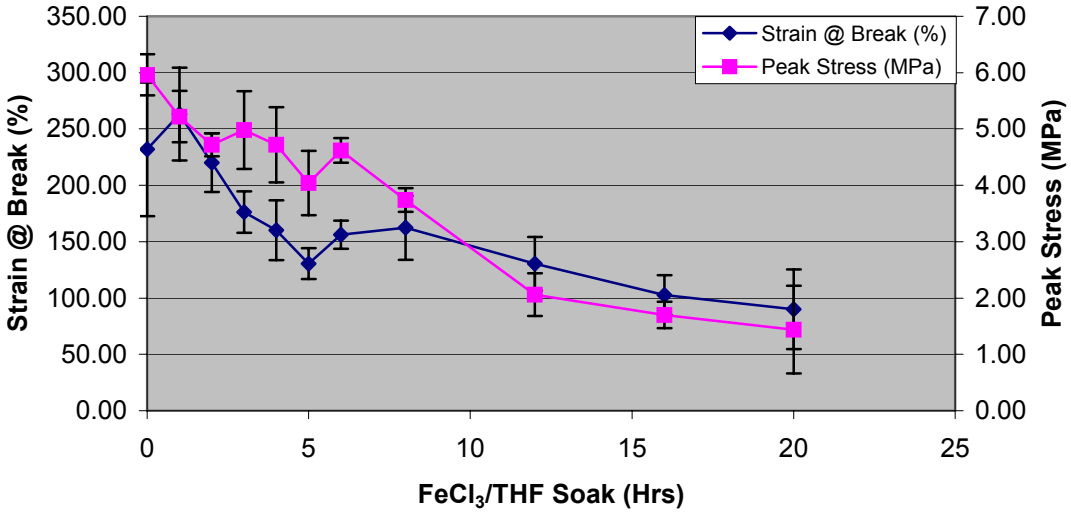

Figure 6.22 Strain at break and peak stress data for the degradation of Silastic® T2 PDMSe with prolonged exposed to a 5 wt% $FeCl_3$/THF solution.

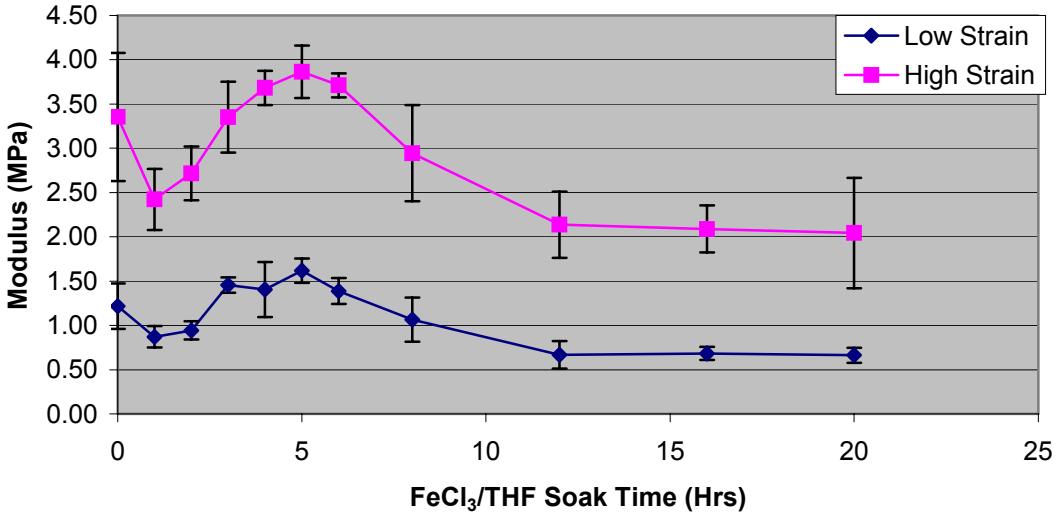

Figure 6.23 High and low strain modulus data for the degradation of Silastic® T2 PDMSe with prolonged exposed to a 5 wt% $FeCl_3$/THF solution.

6.5 Conclusions

From this set of experiments it was shown that it is possible to form dynamic PPy/PDMSe composite structures which are capable of producing a 21° change in contact angle when switched between ± 1.0 V. It was also shown that by changing the solvent system that the overall loading/formation of PPy inside PDMSe can be increased thus improving the overall properties of the system. Supercritical CO_2 cosolvent solutions were shown to be effective in doping PDMSe samples when compared to plain ethanol systems. In particular isopropyl alcohol/$scCO_2$ mixtures were shown to increase the PPy loading in PDMSe to 4-5 wt% compared to 2-3 wt% for ethanol/$scCO_2$.

It was later determined that THF was a better solvent medium for the $FeCl_3$ doping of PDMSe than either of the $scCO_2$ methods. THF was used to form conductive PPy/PDMSe composite systems with conductivities in the range of 278 MΩ to 4 KΩ depending on sample hydration. Dry samples have really low conductivities (resistivety > 300 MΩ) which could then be increased with exposure to an electrolyte solution.

However it was determined that the PPy/PDMSe surface layers are unstable due to PDMSe surface segregation. From EDS mapping and FTIR/ATR measurement techniques it was shown that the Silastic® T2 PDMSe tends to rearrange its surface prior to PPy formation forming a predominantly pure PDMSe surface layer. From the EDS mapping for the chlorine and iron atoms from the $FeCl_3$ it was shown that the PDMSe sample formed a 60-100 μm surface layer that was much lower in concentration of $FeCl_3$ than the bulk of samples. Exposure of this sample to pyrrole vapor would result in the formation of a PPy/PDMSe composite system with the majority of the PPy being buried in the bulk of the material resulting in a non-conductive sample.

The degradative effects of the $FeCl_3$/THF doping process on the mechanical properties of PDMSe were also investigated. It was found that the $FeCl_3$/THF soaking process seriously decreased the tensile strength (peak stress) and strain at break of the PDMSe samples. As the oxidizer doping process was carried out the tensile strength and strain at break decreased from 5.96 MPa and 230% to 1.44 MPa and 90%, respectively. This was also evident in both the low and high strain moduli. The untreated modulus values were 1.22 and 3.35 MPa at the low and high strain values where after the 20 hr treatment the modulus values were 0.66 and 2.04 MPa respectively. After 24 hrs the samples were too brittle to handle and could not be run.

From this; it is obvious that improved techniques for the formation of PPy/PDMSe IPN systems are needed. It is believed that by chemically binding the PPy into the PDMSe network that the surface segregation of the PDMSe can be overcome. One route that was initially investigated and needs further work is the formation and use of vinyl and/or silanol functional pyrrole monomers. By incorporating pyrrole functional groups

in the PDMSe network or by incorporating silanol or vinyl functional groups into the PPy structure further PPy/PDMSe formation would be chemically bound together thus restricting there movement and segregation.

CHAPTER 7
TP AND TPE BASED DYNAMIC, NON-TOXIC, ANTI-FOULING SURFACE COATINGS

7.1 INTRODUCTION

Polydimethylsiloxane elastomer (PDMSe) was previously studied as a base material for the formation of PPy/PDMSe IPN systems due to its low surface energy and modulus. However due to the low modulus of PDMSe the film durability becomes an issue. Due to this concern, efforts have been put forth to increase the durability of PDMSe coatings as well as investigating the use of other low modulus rubber type materials for foul release coatings.

Another alternative to PDMSe is the thermoplastic elastomer (TPE) class of materials. These materials are generally characterized as having elastomer phases dispersed in thermoplastic materials such as polypropylene. They impart a relatively low modulus with increased durability (tear strength, hardness, and modulus) due to the thermoplastic phase of the material. PPy IPNs systems have been formed in three different TPEs manufactured by Advanced Elastomer Systems.

The systems currently being studied are Santoprene® 8211-65, 8281-65, and 271-55. Santoprene® is a PP/EPDM (ethylene propylene diene monomer) based TPE material. EPDM is mechanically melt phase mixed into PP and is then lightly crosslinked to form dispersed elastomer phases in the PP matrix. Santoprene® 271-55 is a FDA approved food grade TPE with physical properties comparable to that of Silastic®

T2 PDMSe, but with a higher elongation to break (330% compared to 250% for Silastic® T2).

Santoprene® 8211-65 and 8281-65 are both from a newer series of Santoprene® TPEs that have better oxidative stability and physical properties (elongation at break, hardness, and tear and tensile strengths) than 271-55 thus allowing for a broader range of uses. Santoprene® 8211-65 is a general purpose grade thermoplastic elastomer (TPE) that is formulated to replace thermoset elastomers such as chloroprene and EPDM. 8281-65 is a FDA approved biocompatible TPE. This material is typically used in short term blood contact medical conditions such as in catheters and septum.

Both 8211-65 and 8281-65 are non-hygroscopic, shear sensitive and can be easily processed using standard extrusion, injection and blow molding equipment. The only difference between 8211-65 and 8281-65 is that more stringent control is used in the manufacturing processing of 8281-65 to comply with FDA regulations. The 8000 series materials have a higher durometer hardness (65 vs. 47), tear strength (150 psi vs. 130 psi), and elongation at break (530% vs. 250%) than Silastic® T2 PDMSe.

Other prospective choices for a substrate material are engineering thermoplastics such as Udel® polysulfone. Polysulfone is a very hard thermoplastic (TP) material with excellent oxidative stability (thermal and hydrolytic (hot water and steam) stability, inorganic acid and base resistance) and physical properties (modulus, tensile strength, and elongation at break) comparable to polycarbonate.

Udel® polysulfone is approved for use in food, water, and medical applications. Typical applications include membrane (water purification, gas separation), medical

(surgical trays, nebulizers, and humidifiers), food services (microwave cookware, etc.), and plumbing (hot water fixtures and fittings).

PPy IPNs have been formed with polysulfone resulting in an extremely hard and durable surface coating that is resistant to surface abrasion and damage. An added advantage is that it can be applied from solution, thus allowing for more conventional application techniques. Another benefit of polysulfone is that it can be functionalized with various substituents (carboxylic acid, sulfonic acid, etc.) allowing for easy manipulation of the surface and bulk properties of the material. This will in turn produce IPN systems with easily modifiable properties.

7.2 MATERIALS AND METHODS

7.2.1 Materials

7.2.1.1 General Chemicals

Pyrrole (Sigma-Aldrich) was filtered, before use, through a neutral alumina (Brockman activity 1; Fisher Scientific) column until colorless to remove impurities. Lithium perchlorate ($LiClO_4$) and sodium perchlorate ($NaClO_4$) (Sigma-Aldrich), iron (III) chloride ($FeCl_3$) (Fisher Scientific), tetrahydrofuran (Fisher Scientific), and allyltriethoxy silane (Gelest) were used as received unless otherwise stated. Deionized (ultrapure) water was produced using an 18 MΩ Millipore system. Artificial sea water was made using Instant Ocean® artificial sea salt (Fisher Scientific) and deionized water (1 ml I.O. in 30.7 ml H_2O; specific gravity = 1.020-1.023 g/cm^3, salinity = ~28-34 ppt).

7.2.1.2 PPy/Santoprene® Sample Preparation and Mounting

Advanced Elastomer Systems (AES) Santoprene® 271-55 was purchased from McMaster-Carr in the form of a 0.03” thick sheet. Samples were cut to size (18 mm x 18 mm) and then used as received.

Santoprene® 8211-65 was obtained directly from Advanced Elastomer Systems (AES) in the form of 4.38 x 4.38 x 0.06" plaques. Plaques were prepared by injection molding on a 170 Ton Vandoren injection molding machine to a thickness of 0.08". The plaques were then compression molded down to a thickness of 0.06" by heating at 204°C for 5 minutes followed by a 10 minute cool down period before removal from the mold.

7.2.1.3 Polydimethylsiloxane Elastomer Preparation

PDMSe was prepared using Silastic® T2 resin (Dow Corning). The resin and curing agent are thoroughly mixed (~10 min.) in a 10:1 weight ratio. The resin is then degassed under vacuum until most of the bubbles are removed (~10-15 min.). The resin is then applied and cured at room 50°C for 5 hrs.

7.2.1.4 ATS Coupling Agent Preparation

The general procedure for the preparation of the allyltriethoxy silane (ATS) coupling is as follows. In a 50 ml polypropylene cup, add 30 ml EtOH (95%) and 1.58 ml H_2O and stir with magnetic stir bar. Adjust pH of the solution to 4.5-5.5 by adding drop-wise glacial acetic acid (~2 drops). After the pH is adjusted add 0.17 ml ATS and let mix for 5 minutes. Apply ATS solution to cleaned glass slide and let react for 2-3 minutes. Rinse ATS treated glass slides with EtOH and place in 120°C oven for 10 minutes. After this you can apply the uncured PDMSe as usual.

7.2.2 Sample Preparation Methods

The oxidizer insertion method was used to form PPy/TPE IPN systems. The general procedure for this process is described as follows using 8281-65 samples.

Santoprene® 8281-65 film was cut into 18 mm x 18 mm squares to produce samples. Nine of these samples were placed in a 5 wt% $FeCl_2$/THF solution and allowed to soak for 24 hrs. After the 24 hr treatment the samples were placed under vacuum for 1

hr to dry (remove residual THF). The dried 8281-65 samples appeared to shrink after the drying process. They were initially swollen when removed from the THF solution; prior to drying. The samples were then placed directly in a sealed PP centrifuge tube containing 2 ml of pyrrole monomer for 24 hrs to facilitate the formation of PPy. After the pyrrole monomer treatment the samples were again dried under vacuum to remove any residual pyrrole monomer.

7.2.2.1 Sample Mounting

In order to conduct contact angle measurements samples were produced using the standard $FeCl_3$/THF method mentioned above. Samples were then mounted to glass slides using Ag epoxy and encapsulated with PDMSe.

Glass slides were cleaned with ethanol and flame treatment. After cleaning lead wires were super glued to the glass slides. Sample mounting pads and lead wire runners were painted onto the glass slide using Ag-filled epoxy. The Ag-filled epoxy was then cured for 30 minutes at 175°C. The bottom sides of the samples were then coated with a thin layer of Ag-filled epoxy and placed on top of the mounting pads. The samples were then sandwiched between two glass plates and placed in a 175°C oven for 30 minutes to cure.

The substrate surface (glass slide, Ag-filled epoxy, and lead wire) is then cleaned and oxidized prior to ATS treatment using a radio frequency discharge argon plasma treatment (Ar plasma) for 1 minute at ~50 mTorr. The sample surface is protected from the argon plasma using a layer of double sided sticky tape. This protective layer also protects the sample surface during the preceding ATS and PDMSe backfilling process.

The substrate is then treated with an ATS coupling agent to improve the adhesion of the PDMSe encapsulant to the glass substrate. A top cover plate (PET covered glass

slide) was applied to the sample and the edges of the glass slides were sealed with scotch tape (create a small mold).

Samples were then encapsulated by pumping uncured PDMSe resin in between the two glass plates with a syringe pump. A 30 cc syringe and an 18 gauge needle were used for this process. The flow rate of the syringe pump was varied throughout the backfilling process due to the increasing in viscosity of the PDMSe as it started to cure at room temperature. The PDMSe was then cured in an oven at 50°C for 5hrs.

After this the top cover plate and protective tape layer are removed and the sample is ready to use. A general schematic of this process is depicted in Figure 7.1.

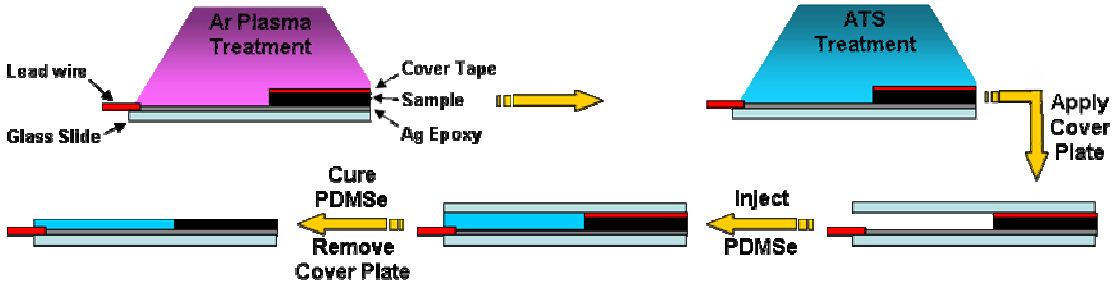

Figure 7.1 Preparation scheme for the formation of PDMSe encapsulated PPy composite samples for contact angle measurement and marine testing.

Samples were mounted this way in single and double element configurations. Single element samples were used for contact angle measurements and require the use of an external stainless steel counter electrode. However for marine testing a dual element design was developed. In the dual element design both of PPy/TPE elements alternate roles as the working and counter electrodes. Therefore the need for a separate counter electrode is eliminated. The layouts for the single and dual element designs are shown in Figure 7.2.

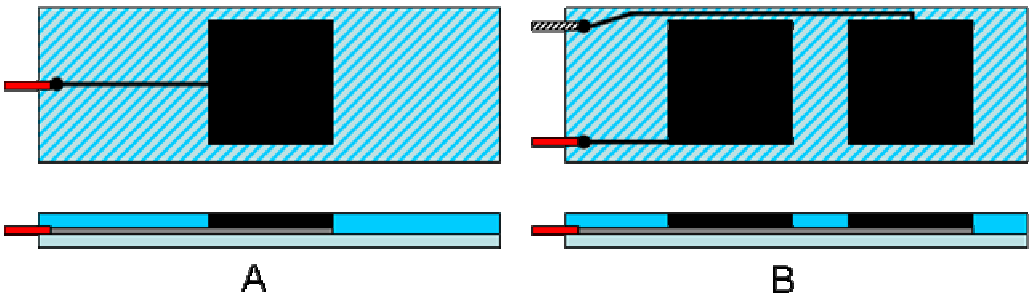

Figure 7.2 PDMSe encapsulated PPy composite samples for testing in aqueous/marine environments using a single (A) and dual (B) element designs.

7.2.2.6 Micropatterning

Hot embossing methods were employed to micropattern Santoprene® TPEs. Patterned silicon wafers, patterned with the negative of the sharklet pattern, were glued to standard glass slides (pattern side up). TPE films were then placed in between the glass slides and the patterned silicon wafers. The pieces were held together using standard binder clips to form molds. The molds were placed in an oven at 185°C and 200°C for 35 minutes.

The molds were removed from the oven and allowed to cool before extracting the elastomer. The TPE tended to stick to the patterned silicon wafer and had to be removed carefully in order to prevent damage to the pattern. This was accomplished by slowly pulling the elastomer off of the patterned silicon wafer. The patterned surface was then imaged using optical and scanning electron microscopy.

7.2.2.7 TP Film Formation by Spin Casting and Spraying

$FeCl_3$/PSU films were formed using spin casting and spraying techniques. These films where then used to form PPy/PSU composite structures.

$FeCl_3$/PSU solutions were prepared containing 1, 5, 10, and 20 wt% $FeCl_3$ and 5 wt% PSU. Both the $FeCl_3$ and PSU were pre-dissolved in separate THF solutions and then mixed to form solutions of the above concentrations. PSU/$FeCl_3$ solutions in THF

were then spin cast onto cleaned glass microscope slides for ~ 30 seconds at 1000, 1400 and 2000 rpm. The PSU/$FeCl_3$ solution was placed drop wise onto the slide surface until the surface appeared to be completely coved.

During the spin casting process the THF is rapidly evaporated from the sample therefore no vacuum drying was required after the spin casting process. The $FeCl_3$/PSU coated slides were placed in a sealed PP tube containing ~2 ml pyrrole monomer for 24 hrs. The films were then dried under vacuum for 1hr to remove any residual pyrrole monomer. The films turned opaque black rapidly upon exposure to the pyrrole monomer vapor.

7.2.2.8 Conductivity Determination

Sample conductivity was checked either by a hand held digital multimeter (Omega HHM57) or on a four point (4-pt) conductivity probe. Conductivety measurements taken by digital multimeter were taken diagonally from corner to corner on both the front and back sides of the sample. This results in a total of 4 different measurements taken for each sample.

Four point conductivity probe measurements were taken using a Keithley 181 nanovolt meter and a Keithley 224 programmable current source. The 4-pt conductivity probe applies a current between the outer two probes and the resultant voltage is measured from the inner two probes. The conductivity (δ) of the sample is then calculated from the following equation:

$$\delta = \frac{I}{V} \cdot \frac{\ln 2}{\omega \cdot \pi} \tag{7.1}$$

where I is the current applied (amps), V is the measured voltage (volts), and ω is the sample thickness (cm).

The voltage was measured at 5 different currents; 10, 20, 30, 40, and 50 μA. These measurements were taken at three different spots on the sample surface and then repeated on the opposite side of the samples (N=6). From this the conductivity of the samples was determined using equation 7.1.

7.3 POLYPYRROLE/8281-65 IPN SYSTEMS

7.3.1 PPy/Santoprene® 8281-65 Contact Angle Measurements

The dynamic character of the PPy/8281-65 samples contact angle measurements were conducted in Instant Ocean® artificial sea water. This approximates the environment within which the samples are expected to operate.

Table 7.1 Contact angle values obtain for PPy/8281-65 dual element sample in Instant Ocean® artificial sea water versus a Ag/AgCl reference electrode.

	0.0 V	+0.5 V	-0.5 V
	38	31	44
	35	33	45
	38	27	39
	36	N/A	43
	42	29	37
	37	28	38
Average	38	30	41
StDev	2	2	3

Dual element PPy/8281-65 samples were preconditioned by cyclic voltammetry prior to testing. The samples were cycled from ±0.5 V at 10 mV/sec for 10 cycles. Contact angle values (captive air bubble technique) were then collected at +0.5, 0.0, and -0.5 V from one of the element surfaces. A Ag/AgCl counter electrode was used for all electrochemical experiments. Three captive air bubbles (repeated twice) were collected at each potential. The potentials were chosen in a random order to produce 6 measurements at each potential. The average contact angle value for the reduced state (-0.5 V) was 41° ±3° (Table 7.1). This value then dropped to 38° ±2° and 30° ±2° for the

oxidized states of 0.0 V and +0.5 V, respectively. This resulted in an 11° change in contact angle for a 1 V difference in potential. This is comparable to the 21° change produced from a 2 V difference in potential for the PPy/PDMSe samples. The results of this experiment are shown if table 7.1 and Figure 7.3.

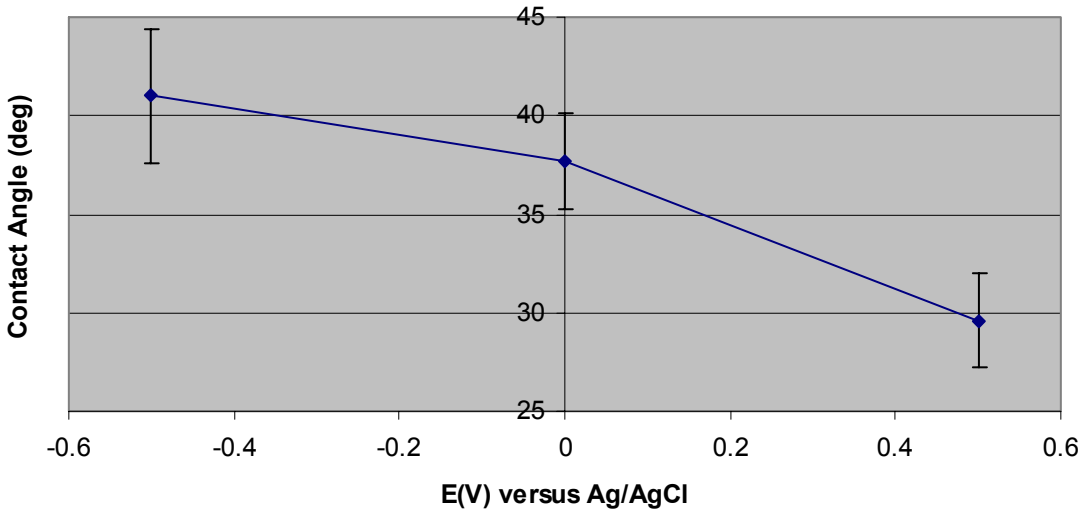

Figure 7.3 Change in contact angle for a PPy/8281-65 dual element sample in Instant Ocean® artificial sea water versus a Ag/AgCl reference electrode.

7.3.2 Determination of PPy Content in PPy/8281-65 Samples

In order to investigate the effects of the PPy formation process on 8281-65 a more detailed weight and volume change experiment was conducted. This was done to determine the amount of $FeCl_3$ and PPy deposited in the Santoprene® base material. Two samples sets (N=7) were used; one being pure THF soak (control) and the other a 5 wt% $FeCl_3$/THF soak.

The average initial sample weights and volumes were 399.6 mg, 461.94 mm^3 and 401.0 mg, 463.53 mm^3 for the THF and $FeCl_3$/THF samples respectively. After the 24 hr solution treatment the average sample weights and volumes were 224.3 mg, 262.16 mm^3 and 235.1 mg, 268.89 $mm^3$for the THF and $FeCl_3$/THF samples respectively. This

equates to a 44%, 43% and 41%, 42% change in the sample weights and volumes after the treatment process. The THF samples lost an extra 3% of weight and 1% of volume during the solvent soak process compared to the $FeCl_3$/THF samples.

After the pyrrole monomer exposure the average sample weights and volumes were 227.7 mg, 277.19 mm^3 and 240.1 mg, 284.70 mm^3 for the THF and $FeCl_3$/THF samples respectively. This equates to a 1.53%, 5.73% and 2.13%, 5.88% increase in sample weight and volume for the THF and $FeCl_3$ samples during the polymerization step.

From this set of experiments it was not possible to determine the amount of $FeCl_3$ and PPy deposited in the system. It can be said that there is not much of a difference between the control and experimental samples during the PPy formation process. This is most likely due to the samples not being thoroughly dried after the solution and monomer soak steps.

Table 7.2 Weight and volume change data for the formation of PPy/8281-65 IPN systems using the FeCl3/THF solvent soak process.

	V (THF)	V ($FeCl_3$)	ΔV		Wt (THF)	Wt ($FeCl_3$)	ΔWt	
ΔPPy=	15.03	15.81	0.78	(mm^3)	0.0034	0.0050	0.0016	(gm)
ΔPPy (%)=	5.73	5.88	0.15	(%)	1.5349	2.1328	0.5979	(%)
ΔTotal =	-184.74	-178.83	5.91	(mm^3)	-0.1718	-0.1609	0.0110	(gm)
% ΔTotal =	-39.99	-38.58	1.41	(%)	-43.0053	-40.1169	2.8884	(%)

However there is a 41-43% decrease in both the sample weight and volume from the 24 hr exposure to the THF based solutions and an overall change in sample weight and volume over the whole process of 40-43% and 38-40% respectively. This weight change is due to soluble components being extracted from the system. This is likely due to the extraction of extender oils and thus decreases the elastic properties of the system. The overall differences in the PPy formation process between the THF and $FeCl_3$/THF soaked samples is shown in table 7.2.

7.4 POLYPYRROLE/271-55 IPN SYSTEMS

PPy/271-55 samples were prepared in the same manner as previously described for PPy/8281-65 and PPy/PDMSe formation. Contact angle measurements were conducted on PPy/271-55 samples in Instant Ocean® artificial sea water.

These measurements turned out to be inconclusive resulting in very erratic values and bubble shapes. This is believed to be due random surface defects present in the 271-55 base material as obtained from the manufacturer.

The previous PDMSe and 8281-65 samples were cured against smooth glass and melt pressed against polished aluminum resulting a initially smooth sample surface. Surface defects in Santoprene® TPE materials used as received are shown later in the Hysitron and AFM analysis section.

7.4.1 Determination of PPy Content in PPy/271-55 Samples

In order to determine the amount of PPy formed during the doping and polymerization process weight and volume change experiments were conducted on 3 sets of 9 samples. The first sample set was a control set that was just exposed to THF for 24 hrs and not the $FeCl_3$/THF oxidizer solution. The other two samples sets were $FeCl_3$/THF systems and were exposed to a 5 wt% $FeCl_3$/THF solution for 24 hrs.

The initial sample weights and volumes were recorded and then the samples were placed in their appropriate solutions and allowed to soak for 24 hrs on a rotator. The average initial sample weights and volumes for all the sample sets were 248.9 mg ±9.2 and 247.8 mm^3 ± 9.2 respectively.

After the 24 hr solvent soak the control set lost 38% of the sample weight and 36% of sample volume; while the $FeCl_3$ treated samples lost about 31% of the sample weight and 33% of the sample volume.

After the pyrrole monomer vapor exposure the control set lost an additional 3% of its weight and 10% of its volume for a total weight and volume loss of 41% and 46% respectively. The $FeCl_3$ treated samples also lost an additional 3% of their weight but only lost 5% of their volume for a total weight and volume loss of 34% and 38% respectively.

Due to the continued weight and volume loss after the pyrrole monomer vapor exposure it can be said that there was still residual THF in the samples that was not completely removed during the vacuum drying process. This complicated the determination of the amount of $FeCl_3$ and PPy deposited in the samples. However for both the solvent soak and monomer soak process the $FeCl_3$ treated samples maintained about 7% more of their initial weight compared to the control set.

Even though all the sample set started out with roughly the same sample weights and volumes the $FeCl_3$ treated samples average weight and volume were 7.8% and 8.7% higher than the control set after the PPy formation. This can be attributed to either the deposition of $FeCl_3$ inside the 271-55 sample or to the formation of the PPy IPN system or to both of these processes.

It is difficult to separate the two due to the $FeCl_3$ and PPy weight and volume data being confounded with the THF solvent evaporation. The presence of PPy is evident in the systems due to the color change from off white to dark black, and all the samples were conductive. This data is shown in Figures 7.4 and 7.5.

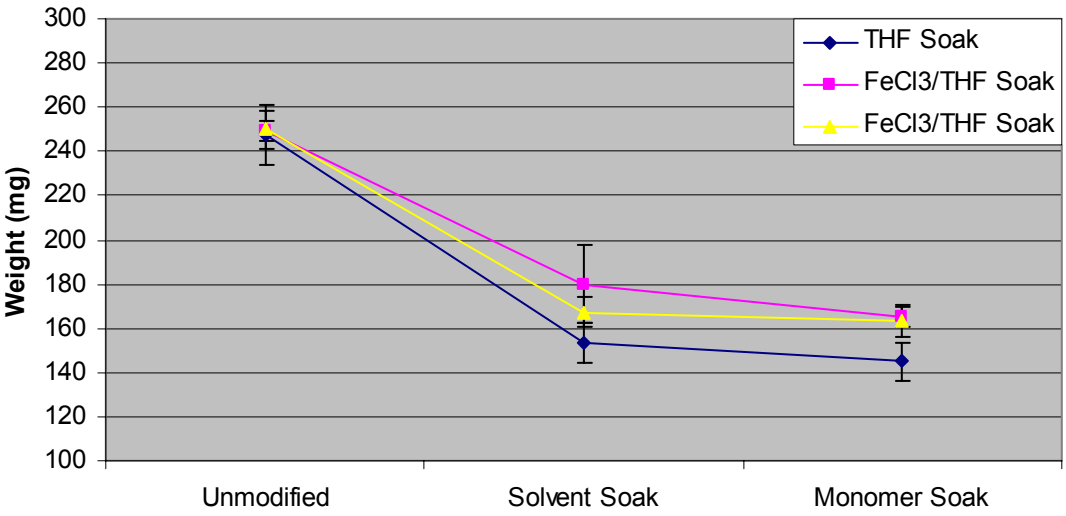

Figure 7.4 Weight loss data for the formation of PPy/271-55 IPN systems.

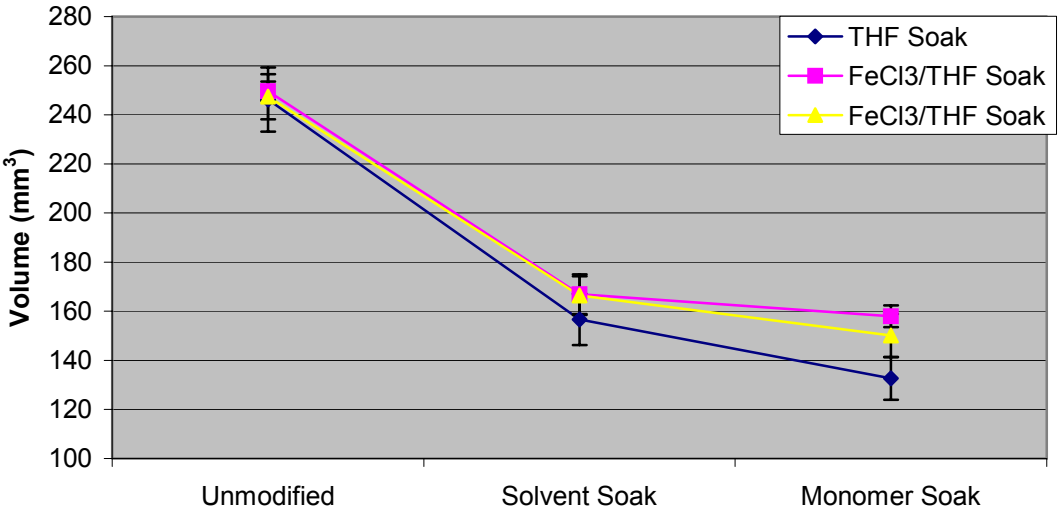

Figure 7.5 Volume loss data for the formation of PPy/271-55 IPN systems.

7.4.2 Effects of Counter Ion Exchange on PPy/271-55 Conductivity

All PPy IPN samples have been made up to this point using $FeCl_3$ as the oxidizer. This results in Cl^- being inserted into the PPy matrix as the counter ion. From the previous studies with the conducting polymer actuators we saw an improved performance of the actuators when using the ClO_4^- counter ion compared to Cl^-.

An attempt was made to make PPy using $Fe(ClO_4)_3$ instead of the typical $FeCl_3$. This would result in the perchlorate ion being used as the counter ion. However when a solution of $Fe(ClO_4)_3$ in THF was made the $Fe(ClO_4)_3$ (crystalline) sank to the bottom of the flask and started to dissolve. However after about a minute the whole solution started to turn cloudy white. After letting the mixture stir for ~30 minutes the mixture was still cloudy white in appearance and small white crystals were visible. After stopping the stirring and letting the mixture settle a large amount of white crystals precipitated out of solution and the solution turned a transparent brown color.

The amount of crystals formed during this reaction was in great excess of the amount of $Fe(ClO_4)_3$ initially added to the THF. It is believed that $Fe(ClO_4)_3$ is able to ring-open polymerize the THF and form polybutylene glycol (poly(butylene oxide)) or various oligomers.[153, 154]

In order to incorporate the ClO_4^- into the PPy structure a solvent exchange process was performed. PPy/271-55 samples (N=9) were prepared using the $FeCl_3$/THF preparation method. After the final drying process the samples were placed in a 3wt% $NaClO_4$ solution in THF for 24hrs.

The 3 wt% $NaClO_4$/THF solution was clear with no visible signs of crystal formation or other side reactions between the $NaClO_4$ and THF. After the samples were soaked for 24hrs they were dried under vacuum for 1hr and then the conductivities were tested on three random samples and compared to standard PPy/271-55 samples that were prepared at the same time.

The resistivity of the samples was measured at 16 kΩ ± 5 and 18 kΩ ± 17 for the ClO_4^- and Cl^- samples. Three more random samples were measured again 64hrs later and

were measured at 38 kΩ ± 12and 17 kΩ ± 13 respectively. There is no significant difference between these values so it appears that there is no real difference between these two sample sets.

It is unclear if there is a difference in conductivity between the counter ions used or if the counter ion exchange even took place. One way to remedy this would be to run the experiment in an aqueous $NaClO_4$ solution and apply a cyclic potential to the samples. This would force the ion exchange process.

However the same thing would happen when these systems were run under real environmental conditions. When these samples are submerged in a marine environment and cycled the counter ions associated with the film, form the PPy formation process, will be exchanged with the anion present in the highest concentration. In sea water this happens to be the Cl^- anion (sea water = ~2.72% NaCl, ~19,500 ppm Cl^- ~10,770 ppm Na^+, 67 ppm Br^-).

After this experiment the conductivity of the PPy/272-55 samples was measured on a 4-point conductivity probe at currents of 10, 20, 30, 40, and 50 μA. The PPy/271-55 sample thickness was 0.7mm (0.07 cm); which results in a bulk sample conductivity of $9.57E^{-7} \pm 9.09E^{-9}$ S/cm^2. This is comparable to values obtain for other CP/elastomer blend systems which typically range $10^{-6} – 10^{-9}$ S/cm^2.[155-158] This measurement is for the bulk conductivity of the whole film. This assumes that the sample is bulk conductive; however if the sample is not completely bulk conductive the conductivity of the conductive layer would be higher due to its thinner nature. Calculations were done assuming a conductive layer thickness (film thickness) of 700μm (0.07 cm, bulk conductive), 100 μm, 50 μm, 25 μm, and 5μm. This resulted in film conductivities of

$9.57E^{-7}$, $6.70E^{-6}$, $1.34E^{-5}$, $2.68E^{-5}$, $6.70E^{-5}$, and $1.34E^{-4}$ S/cm^2 respectively. This data is graphically shown in Figure 7.6.

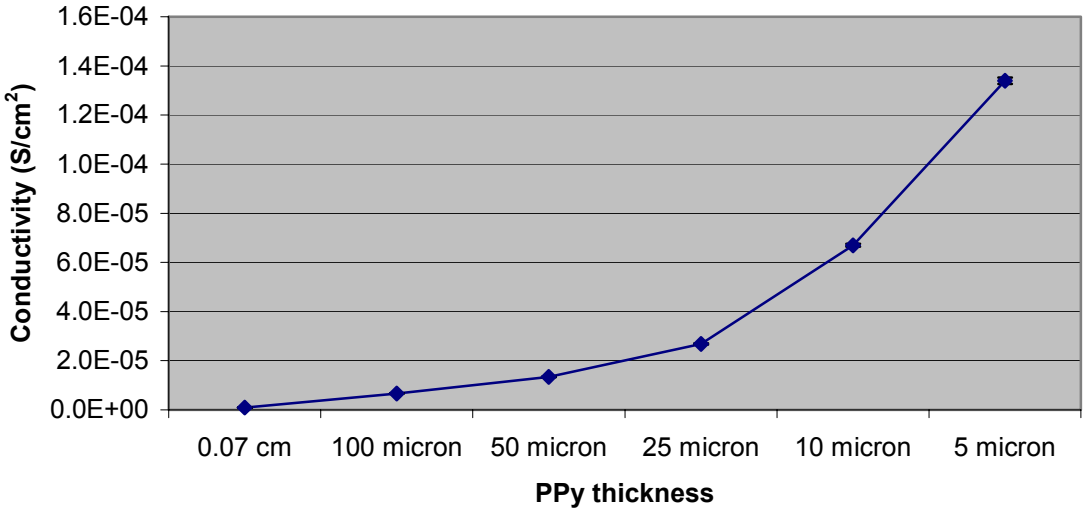

Figure 7.6 Calculated PPy/271-55 film conductivity based on conductive layer thickness. Value for 0.07 cm is actual conductivity of PPy/271-55 film assuming bulk conductive.

7.4.3 Formation of poly(3-methylthiophene)/271-55 IPN systems

Poly(3-methylthiophene) (PMeT) was also incorporated into the 271-55 material in the same manner as the PPy/271-55. By incorporating different conducting polymers, like PMeT, into base materials different surface properties can be produced. PMeT has different oxidation and reduction potentials than PPy and is capable of producing a net negative charge during reduction unlike PPy. This would result in a dynamic surface that switched between two hydrophilic states (positively and negatively charges) with a hydrophobic state in between the two.

271-55 sample films (N=18) were doped with $FeCl_3$ as previously described and then dried under vacuum for 4 hrs. The samples were split in half and placed in PP tubes containing ~3 ml of 3-methylthiophene and pyrrole monomer respectively. Samples

placed in the MeT monomer exhibited no initial color change when exposed to the monomer vapor. However the samples placed in pyrrole monomer started to turn black instantaneously upon exposure to the monomer vapor.

After 24 hrs both sets of samples were removed from the monomer vapor and dried under vacuum for 1 hr. The pyrrole exposed samples were completely black in color while the MeT exposed samples were generally greenish/brown in color ($FeCl_3$ insertion) with dispersed black regions on the sample surface. The PMeT samples were non-conductive except on the black areas. The PMeT samples appeared to have turned darker during the vacuum drying process. The PPy/271-55 and PMeT/271-55 samples were placed in separate PP tubes and sealed for storage.

After being sealed in the PP tube for 25 days the PMeT/271-55 had turned completely black in color and had a completely conductive surface. The resistively of the PMeT/271-55 and PPy/271-55 samples was 20-30 MΩ and ~15 kΩ respectively.

Methylthiophene can be chemically polymerized by $FeCl_3$ in solution at room temperature much like pyrrole. The vapor pressure of 3-methylthiophene is 42 mmHg compared to 65 mmHg for pyrrole with boiling points of 115-117°C and 129-131°C respectively so both monomers vaporize relatively easily.

It is currently unclear weather the kinetics of the vapor phase polymerization of 3-methylthiophene are lower than that of pyrrole or if the presence of oxygen inhibits the polymerization of 3-methylthiophene. From this it was determined that the use of PMeT was undesired due to the long polymerization times utilizing the current polymerization process.

Other oxidizer systems can be used in the polymerization process but the most common one is an $AlCl_3/CuCl_3$ mixture. Currently the use of copper in marine coating is under the process of being banned therefore the use of this oxidizer system would be undesirable.

7.4.4 Micropatterning of 271-55

Santoprene® 271-55 was micropatterned with a biomimetic sharklet pattern using a hot embossing method. A biomometic sharklet pattern developed by the Brennan research group at the University of Florida has been shown to greatly reduce the settlement of Ulva spore (green algae) when patterned on Silastic® T2 PDMSe compared to smooth unpatterned PDMSe (Figure 7.7).

Hot embossing methods were employed to micro pattern Santoprene® 271-55 TPE. Samples patterned at 185°C produced the best results (Figures 7.8 and 7.9). However there are obvious defects in the pattern features produced at this temperature. Samples patterned at 200°C replicated very poorly resulting in virtually no pattern transfer to the 271-55 (Figure 7.10).

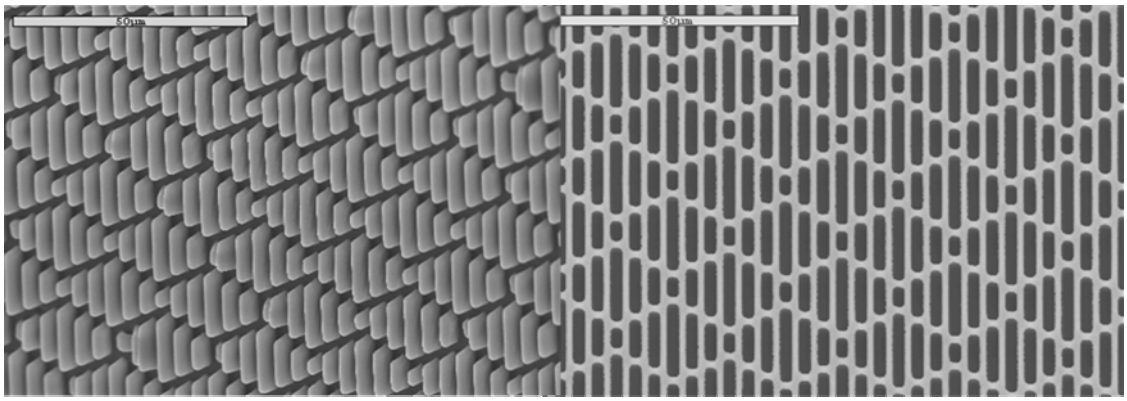

A B

Figure 7.7 Example of 5µm biomimetic sharklet pattern on PDMSe (A) and patterned silicon wafer used to create the patterned PDMSe. SEM micrographs taken at 1000X (scale bar = 50 µm; WD = 15 mm and EV = 15 KeV, and AuPd coated). Images taken by James Schumacher.

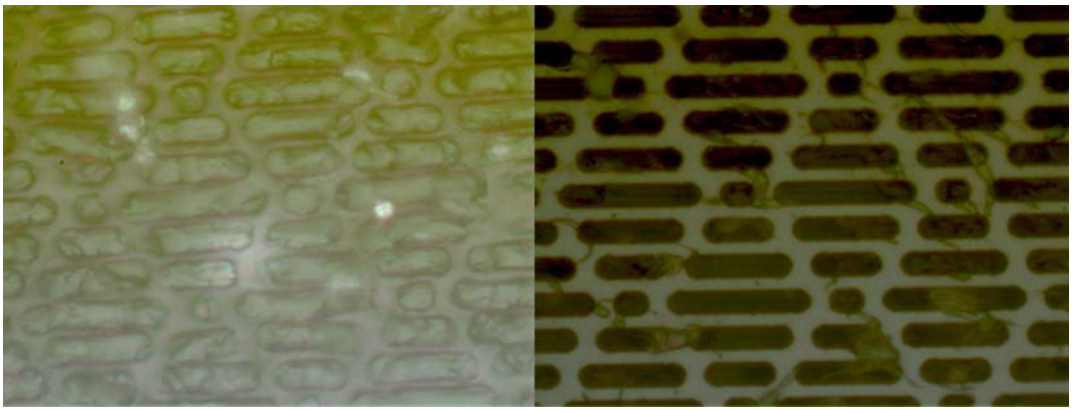

A B

Figure 7.8 Optical micrograph of 5µm biomimetic sharklet pattern on 271-55 produced at 185°C (A) and patterned silicon wafer used to create the patterned 271-55. Images taken at 1000X.

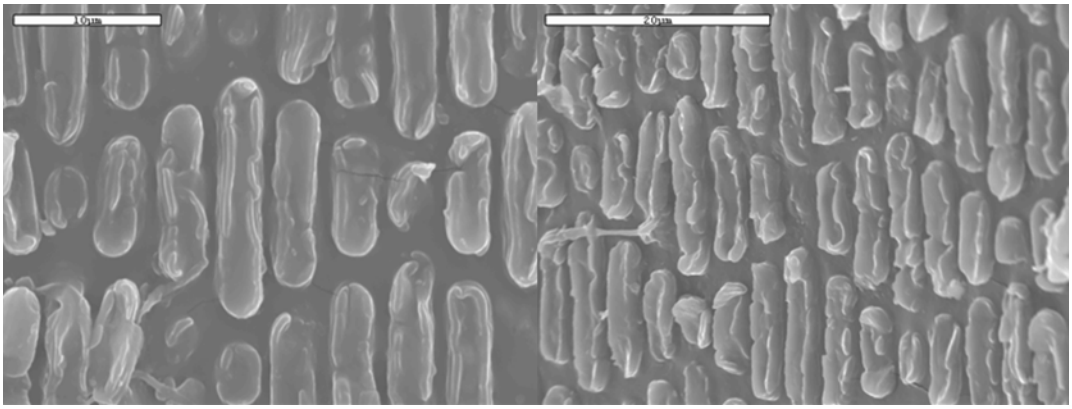

A B

Figure 7.9 SEM micrographs of sharklet patterned Santoprene® 271-55 patterned at 185°C; 3300X (A) and 2500X 40° tilt (B). Images taken at 15 KeV with a working distance of 15 mm and a AuPd surface coating. Images taken by James Schumacher.

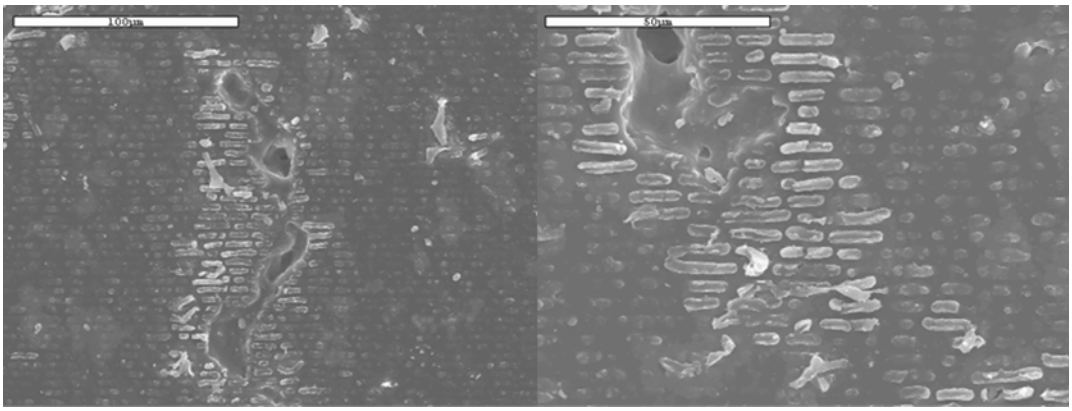

A B

Figure 7.10 SEM micrographs of sharklet patterned Santoprene® 271-55 patterned at 200°C; 500X (A) and 1000X (B). Images taken at 15 KeV with a working distance of 15 mm and a AuPd surface coating. Images taken by James Schumacher.

This initial patterning test shows that it is possible to micropattern on Santoprene® materials. However improvements in the patterning technique need to be made. The current patterning process utilizes standard office binder clips to apply the pressure for patterning. By using a more standard heated compression mold higher pressures can be applied potentially improving the replicated pattern. Also by reproducing the pattening technique under vacuum it might be possible to improve the replicated pattern by removing the air in the cavities of the negative pattern (silicon wafer).

7.5 EDS and SEM ANALYSIS of SANTOPRENE® TPE's

THF is a good solvent for EPDM but not for PP therefore the $FeCl_3$/THF should preferentially swell and deposit $FeCl_3$ in the EPDM phases of the Santoprene® TPE material. By using the EDS mapping technique it is possible to determine the location and dispersion of the Fe and Cl in the Santoprene® material. It is also possible to determined that the location and dispersion of the clay filler in the Santoprene® material due to the presence of silicon and aluminum.

Santoprene® 271-55 and 8211-65 samples were doped with $FeCl_3$ using the previously described $FeCl_3$/THF solution method. Cross section samples were prepared by cutting the samples in half with a razor blade. After this the samples were mounted onto a SEM stub and coated with carbon prior to SEM analysis. Carbon was used to coat the sample instead of Au to prevent masking/blocking of the EDS and backscatter signal from the SEM.

Due to differences in sample thickness (0.03'' vs. 0.06" for 271-55 and 8211-65) the magnification of the two mapping images are different. 271-55 and 8211-65 were mapped at 180X and 85X respectively (Figures 7.11-7.13).

From the EDS spectra (Figure 7.11) the content of alumina filler is much higher in the 8211-65 materials than the 271-55 where the silica filler content is higher in the 271-55. From the EDS map of 271-55 the $FeCl_3$ tends to have a higher concentration closer to the samples surface with the center of the material being lower in concentration. The dispersion of $FeCl_3$ is more uniform throughout the bulk of the sample for 8211-65.

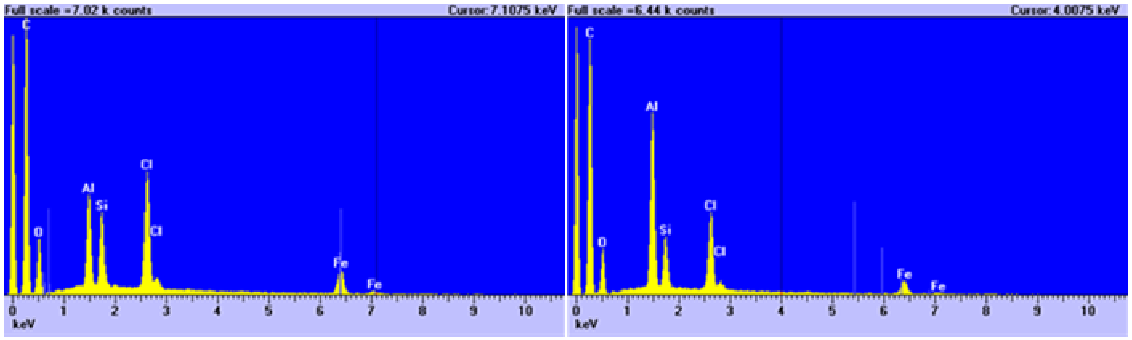

A B

Figure 7.11 Cross sectional EDS spectrum of $FeCl_3$ doped Santoprene® 271-55 (A) and 8211-65 (B) showing the presence of Fe and Cl.

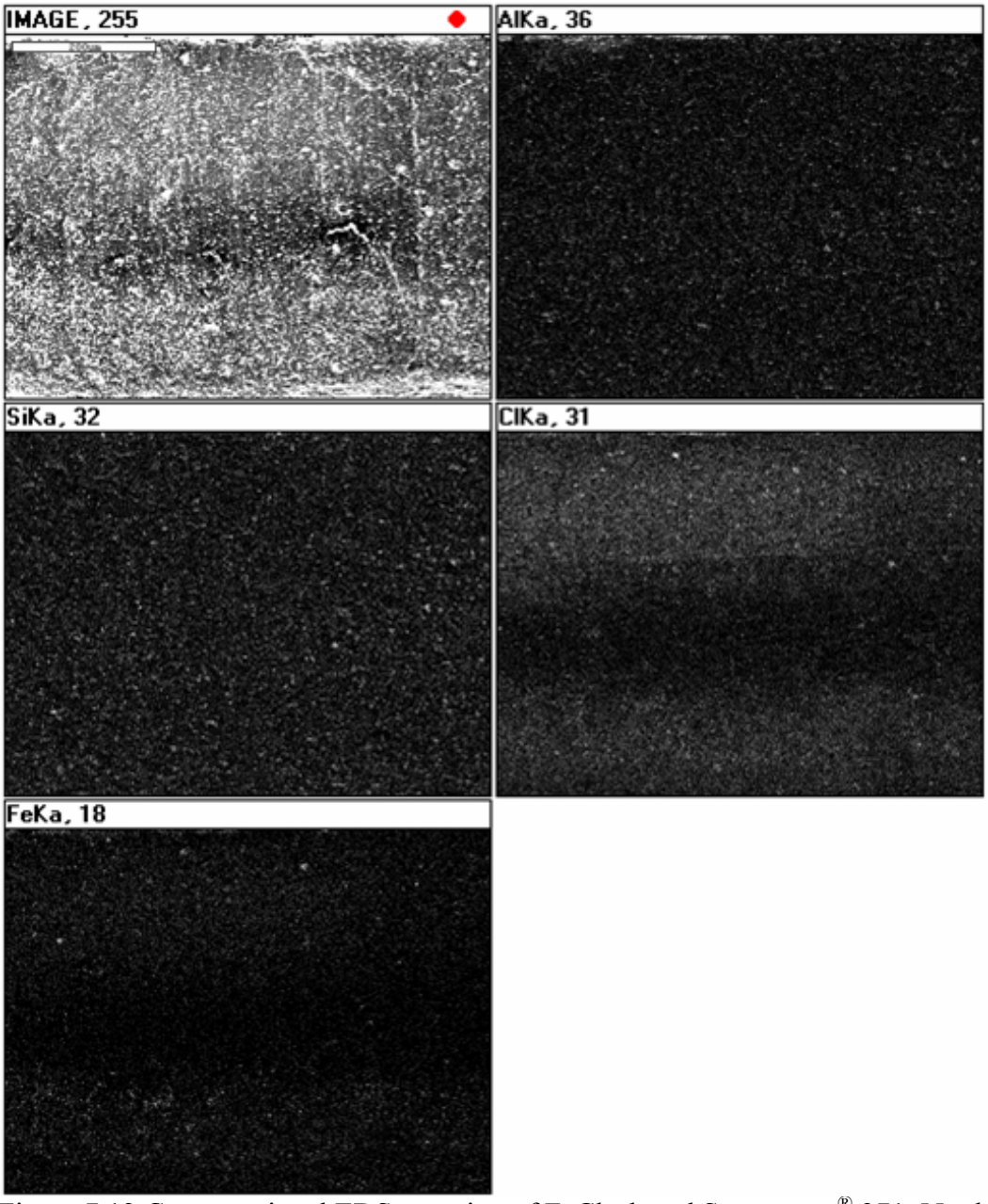

Figure 7.12 Cross sectional EDS mapping of $FeCl_3$ doped Santoprene® 271-55 taken at 180X; scale bar = 200 µm.

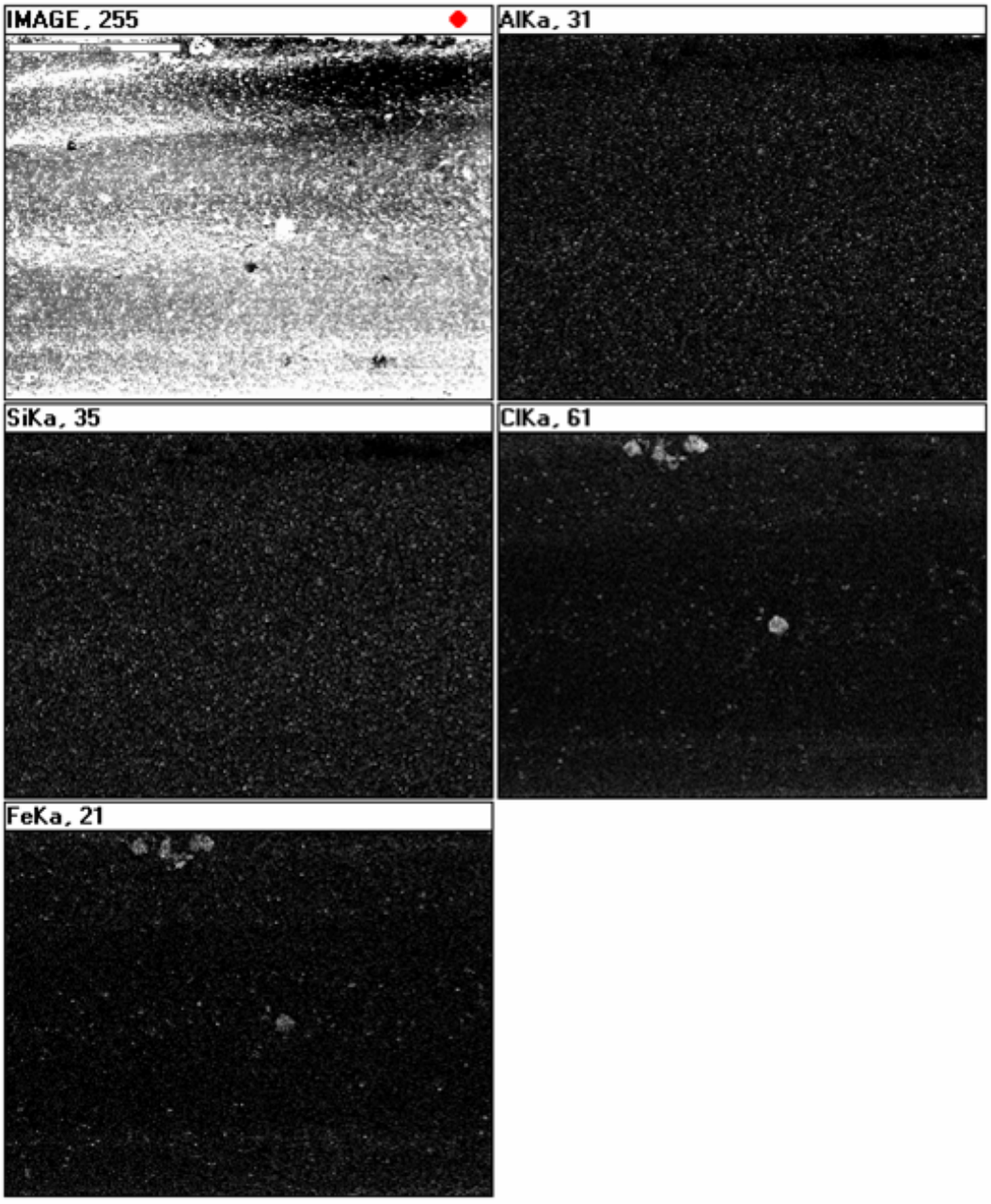

Figure 7.13 Cross sectional EDS mapping of $FeCl_3$ doped Santoprene® 8211-65 taken at 85X; scale bar = 500 µm.

Figure 7.14 shows the difference between the dispersion of the $FeCl_3$ in PDMSe, 271-55, and 8211-65 elastomers. The $FeCl_3$ tends to concentrate in the center of the

PDMSe samples (also confirmed with ATR-FTIR; Figure 6.18) while in both the Santoprene® materials the $FeCl_3$ is more uniformly dispersed. This results in a more uniform polymerization of pyrrole in the Santoprene® base materials resulting in a more bulk conductive material compared to PDMSe.

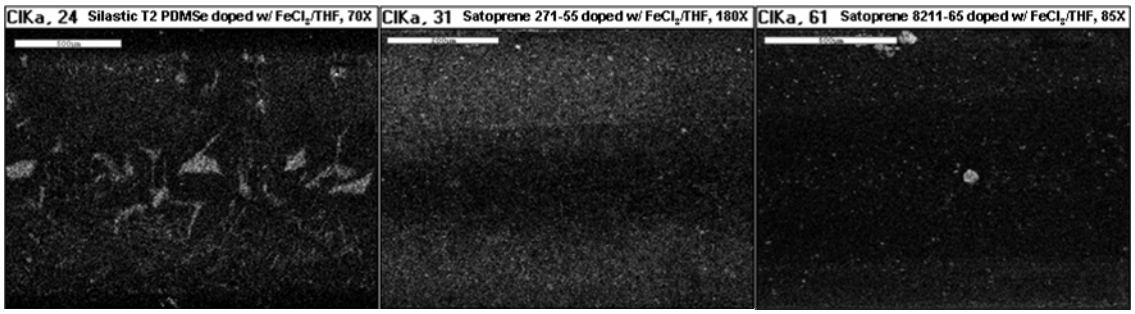

Figure 7.14 Cross sectional EDS mapping for Cl in $FeCl_3$ doped PDMSe (A), 271-55 (B), and 8211-65 (C). Magnification and scale bars equal to 70X, 180X, and 85X and 500 µm, 200 µm, and 500 µm respectively. Images taken at 15 KeV and 15 mm on carbon coated cross section samples.

This type of analysis was also conducted on PPy/271-55 and PPy/8211-65 samples (Figures 7.15 and 7.16). From this the dispersion of the clay filler (Si, Al, and O) and the PPy (Fe and Cl) can be detected. The formation of PPy should only occur where the $FeCl_3$ was deposited, therefore by mapping for Fe and Cl the location of the PPy can be determined.

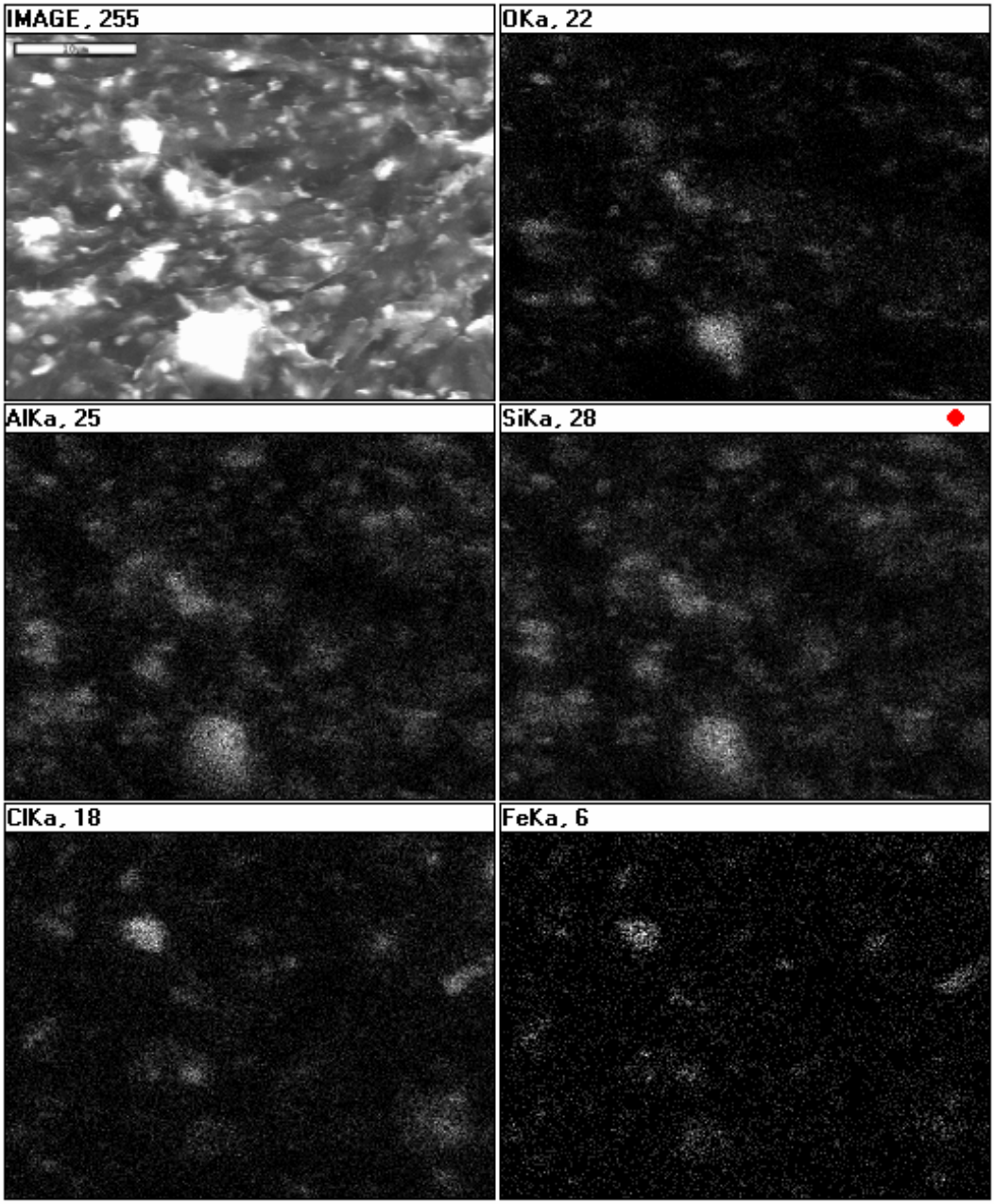

Figure 7.15 Cross sectional EDS mapping of $FeCl_3$ doped PPy/271-55 taken at 3000X; scale bar = 10 µm. Images taken at 15 KeV and 15 mm on carbon coated cross section samples.

The 271-55 and 8211-65 samples have large clusters on the order of 1-8 µm of clay filler. The dispersion of the $FeCl_3$ deposited in the 271-55 base material is in the form of large cluster as well with dimensions on the order of 2-5 µm. A finer uniform dispersion $FeCl_3$ is also present. However the dispersion of the $FeCl_3$ deposited in the 8211-65 is

almost completely uniform. There is no evidence of the large clusters of $FeCl_3$ that are evident in the 271-55 material.

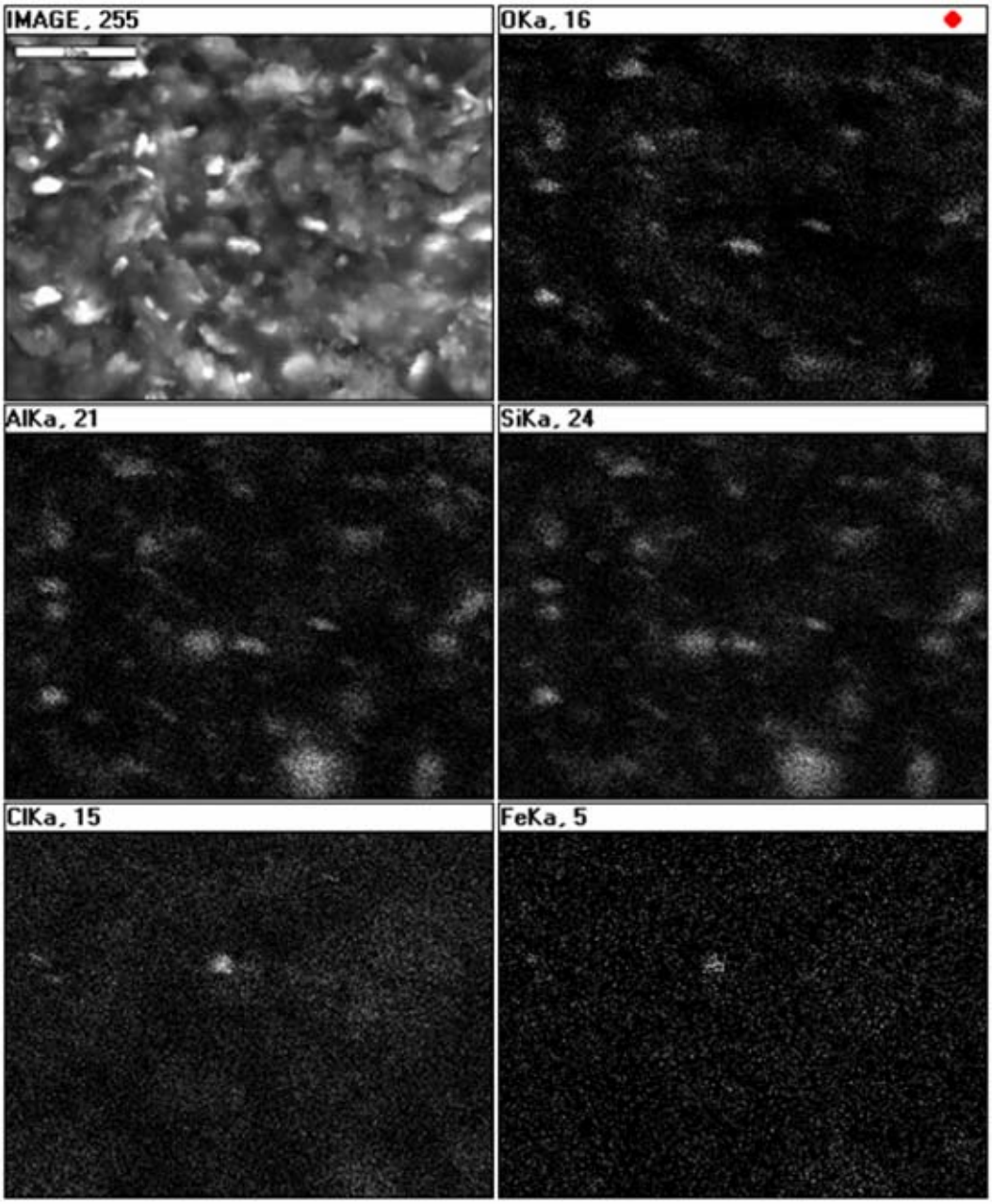

Figure 7.16 Cross sectional EDS mapping of $FeCl_3$ doped PPy/8211-65 taken at 3000X; scale bar = 10 µm. Images taken at 15 KeV and 15 mm on carbon coated cross section samples.

The distribution of higher density phases (clay filler and $FeCl_3$) in PPy/271-55 and PPy/8211-65 are also shown in the cross sectional SEM secondary and backscatter electron images, Figures 7.17 and 7.18. These images were taken at 3000X.

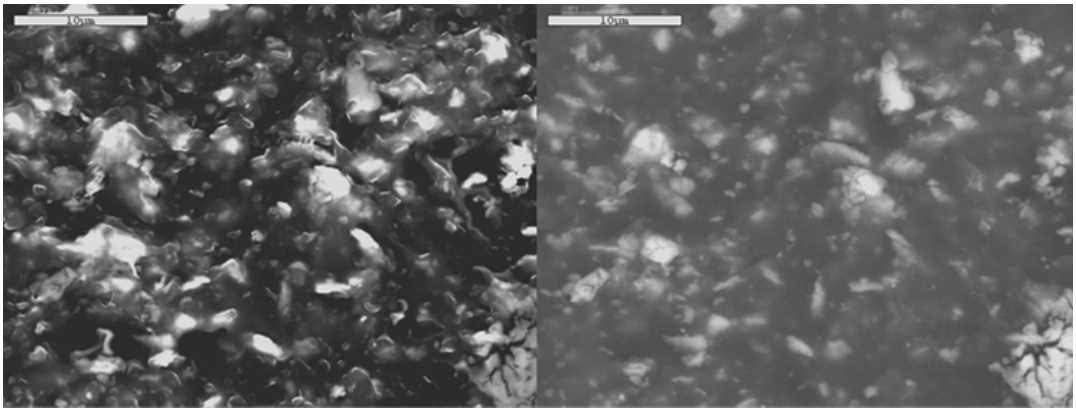

A B

Figure 7.17 Cross sectional SEM secondary (A) and backscatter (B) electron micrographs of PPy/271-55. Images taken at 3000X and scale bar equal to 10 μm. Images taken at 15 KeV and 15 mm on carbon coated cross section samples.

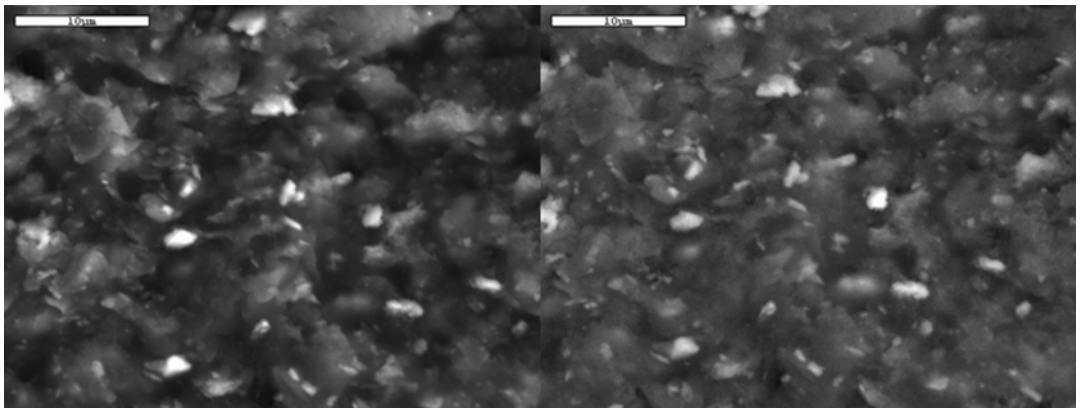

A B

Figure 7.18 Cross sectional SEM secondary (A) and backscatter (B) electron micrographs of PPy/8211-65. Images taken at 3000X and scale bar equal to 10 μm. Images taken at 15 KeV and 15 mm on carbon coated cross section samples.

7.6 PPy/POLYSULFONE SYSTEMS

PPy has also been incorporated into the thermoplastic material polysulfone (PSU). Polysulfone has excellent oxidative resistance and mechanical properties. The overall mechanical properties of this material are comparable to that of polycarbonate. By

utilizing hard thermoplastic materials such as polysulfone very hard and durable dynamic surface coatings should be able to be formed. Also these systems can be applied by conventional paint application processes.

To investigate the effects of substrate material and $FeCl_3$ concentration $FeCl_3$/PSU films were cast onto glass and PET substrates at various concentrations of $FeCl_3$. Concentrations of 1, 5, 10, and 20 wt% $FeCl_3$ were used. The 1 wt% $FeCl_3$ solution produced films of a light grey color that were non-conductive while the 5, 10, and 20 wt% films turned dark opaque black in color with an increasing level of opacity. Films cast onto the cleaned glass slides produced a non-uniform surface morphology. The samples had a blochy appearance with shiny and dull sections. However the films cast onto the PET covered slides had a uniform shiny black surface.

There was no real difference in the conductivity of the PPy/PSU films cast on glass and PET covered glass. But as the $FeCl_3$ concentration was increased the overall conductivity of the samples increased. Samples produced from the 5 wt% solution had a resistivity range of ~450-1000 kΩ, while the samples produced from the 10 wt% solution had a resistivity of 120-600 kΩ. The samples prepared from the 20 wt% solution had the highest conductivity with a resistivity range of 14-200 kΩ.

Spray application techniques were also investigated. Solution concentrations were evaluated at 5 and 10 wt% PSU. Argon was used to the spray the films at a pressure of 10 psi. A commercial blue thermoplastic dye was added to the solution to improve the contrast of the film. The films sprayed from the 5 wt% solution produced the smoothes and most uniform surface texture. While the films sprayed from the 10 wt% solution

tended to fibrous in nature. An example of this is shown in Figure 7.19 at a magnification of 7X.

The films formed a very hard and scratch resistant layer on the glass substrate. However the films easily delaminate from the glass when exposed to water. This was initially thought to be due to the $FeCl_3$ potentially degrading the PSU and making it more hydrophilic or due to the hydration and swelling of the incorporated PPy. However this does not happen for the films cast on the PET. Also pure PSU that was applied to glass slides in the same manner also delaminate from the glass substrate. It turns out that PSU does not bind well to glass and simply de-wets the glass surface when exposed to water.

PSU has also been solution cast onto the biomimetic sharklet design. The PSU replicated the sharklet pattern nicely and results in patterns with improved mechanical properties compared to PDMSe. From this it should be possible to form hard dynamic micropatterned surface coatings.

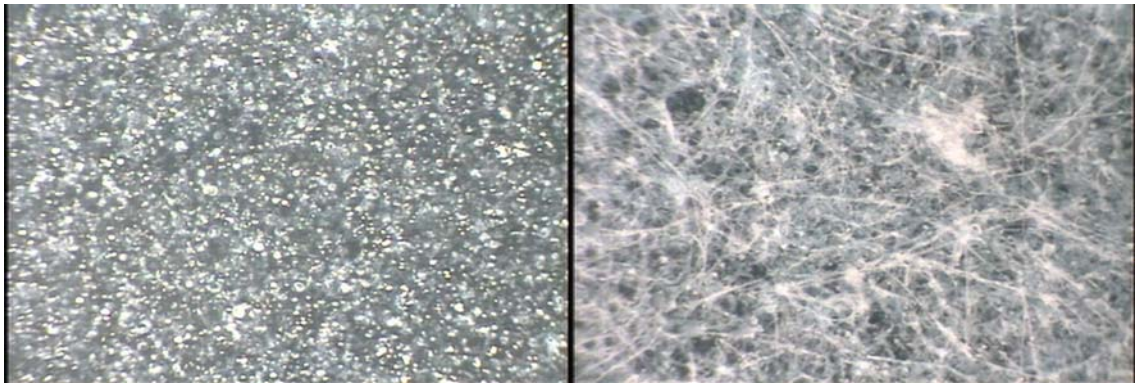

Figure 7.19 Optical micrographs of PSU films sprayed from 5 wt% (A) and 10 wt% (B) PSU/THF solutions. Magnification = 7X.

7.8 CONCLUSIONS

From this it has been shown that it is possible to form conducting polymer composite structures with dynamic surface properties such as surface energy, modulus,

and topography. PPy was incorporated into Santoprene® 8281-65 TPE and was shown to produce a dynamic contact angle change of 11° under a ±0.5 V stimulus. The contact angle was shown to change from 30±2° in its oxidized form at +0.5 V to 41±3° in its reduced form at -0.5 V. PPy/8211-65 samples were then shown to produce a dynamic surface modulus change when switched between its two redox states.

Micro contact patterning of a biomimetic sharklet pattern developed here at the University of Florida was accomplished on Santoprene® 271-55 and Udel® polysulfone. This pattern has been shown to reduce the settlement of Ulva spore on patterned PDMSe by ~85% when compared to smooth PDMSe. By incorporating the micro patterning process with the dynamic surface materials the overall performance of these systems should be greatly enhanced.

Also the distribution and morphology $FeCl_3$ deposited inside Santoprene® TPEs was investigated using EDS mapping. From this it was shown that the dispersion of $FeCl_3$ inside Santoprene® 271-55 and 8211-65 was relatively uniform when compared to PDMSe. PDMSe was previously shown to surface segregate and force the $FeCl_3$ into the center of the sample resulting in an overall non-conductive material. Where as the Santoprene® materials have a uniform $FeCl_3$ dispersion throughout the bulk of the material producing conductive samples with a very stable surface PPy layer.

CHAPTER 8
DYNAMIC MODULUS MAPPING OF PPY/SANTOPRENE® BLENDS

8.1 INTRODUCTION

In order to investigate the dynamic modulus properties of the PPy/TPE systems nano-DMA measurements were conducted using a Hysitron Triboindenter® equipped with the nano-DMA package.

Hysitron nano-DMA is performed in a similar fashion to standard DMA testing techniques. A load is applied to a sample at a given frequency and the resulting displacement and phase shift between the frequency of the displacement and applied load is measured. By monitoring the displacement and phase shift of the sample under various loads and frequencies or temperatures the viscous and elastic responses of the material can be determined. The Hysitron nano-DMA accomplishes this by applying a small force/load to the sample surface by oscillating the tip on the sample surface. As this is done the applied force and oscillation frequency are monitored and the displacement and phase lag produced in the sample is measured.

The most common technique used for nano-DMA is the ramping dynamic frequency test. In this test a constant quasistatic load and dynamic load amplitude are used while the frequency is ramped. The Triboindenter® is capable of applying and measuring frequencies from 1-300 Hz; however below 10 Hz the testing time becomes too long to be feasible and above 200 Hz the displacement signal amplitude becomes very small making it difficult to measure the phase and amplitude response of the material. Therefore the typical measurement ranges is around 10-200 Hz.

8.2 MATERIALS AND METHODS

8.2.1 Materials

Pyrrole (Sigma-Aldrich) was filtered, before use, through a neutral alumina (Brockman activity 1; Fisher Scientific) column until colorless to remove impurities. Iron (III) chloride ($FeCl_3$) (Fisher Scientific) and tetrahydrofuran (Fisher Scientific) were used as received unless otherwise stated. Deionized (ultrapure) water was produced using an 18 MΩ Millipore system. Artificial sea water was made using Instant Ocean® artificial sea salt (Fisher Scientific) and deionized water (1 ml I.O. in 30.7 ml H_2O; specific gravity = 1.020-1.023 g/cm^3, salinity = ~28-34 ppt).

8.2.2 Sample Preparation Methods

8.2.2.1 PPy/TPE (8211-65) Sample Preparation

The oxidizer insertion method was used to form PPy/TPE IPN systems as previously descrbed. Santoprene® 8211-65 films were cut into 18 mm x 18 mm squares to produce samples. Samples were then exposed to a 5 wt% $FeCl_2$/THF solution for 24 hrs and then dried for 1 hr. The samples were then placed directly in a sealed PP centrifuge tube containing 2 ml of pyrrole monomer for 24 hrs to facilitate the formation of PPy. After the pyrrole monomer treatment the samples were again dried under vacuum for 1 hr to remove any residual pyrrole monomer.

8.2.2.2 Sample Mounting

Samples were then mounted to glass slides using Ag-filled epoxy and encapsulated with PDMSe using the procedure previously described in chapter 7.

The base electrode structure (Ag-filled epoxy) was painted onto clean glass slides and then cured at 175°C for 30 minutes. Samples were then mounted onto the patterned

glass slide using Ag-filled epoxy and then sandwiched between two glass plates and cured as above.

The substrate surface (glass slide, Ag-filled epoxy, and lead wire) was then cleaned by Ar plasma treatment for 1 minute at ~50 mTorr. The sample surface was protected from the Ar plasma using a layer of double sided sticky tape. After the cleaning process the substrate was treated with an ATS coupling agent to improve the adhesion of the PDMSe encapsulant to the glass substrate.

A top cover plate (PET covered glass slide) was applied to the sample and the edges of the glass slides were sealed with scotch tape (creating a small mold). PDMSe was then backfilled in-between the two glass plates to encapsulate the sample. The PDMSe was then cured in an oven at 50°C for 5hrs. After this the top cover plate and protective tape layer are removed and the sample is ready to use.

8.2.2.3 Electrochemical Polymerization of Pyrrole

Polypyrrole was electrochemically polymerized on an EvAu coated polyimide films from a 0.1 M aqueous solution of pyrrole and $NaClO_4$ using a stainless steel counter electrode and an Ag/AgCl reference electrode.

The films were grown to a current density of 4 C/cm^2. The PPy films were then broken in by cycling the samples between ±0.8 V at 10 mV/sec ten times in I.O. artificial sea water prior to nano-DMA measurements.

8.2.3 Hysitron Nano-DMA

8.2.3.1 Hysitron Introduction

The Hysitron Triboindenter® uses a three plate capacitance transducer (Figure 8.1) to produce small tip displacements (<5μm) and to measure and apply loads to the sample

surface. The whole transducer is mounted on a stepper motor assemble to produce large scale displacements (>5µm).

The sampling tip is mounted on the center plate and its position is controlled by a DC current passed between it and the top and bottom plates. By applying a DC current between the center and top plates the center plate is electrostatically attracted to the top plate produces a negative displacement in the tip (retraction). The opposite (extension) occurs when the DC current is applied between the center and bottom plates.

The position of the center plate and therefore the tip is monitored by two separate AC currents. AC currents are passed between the center plate and the top and bottom plates and are 180° out of phase in the zero position. By monitoring the phase shift between the two AC signals the position of the center plate is determined.

The force/load exerted on the sample is determined by monitoring how much DC current is required to maintain the center plate position.

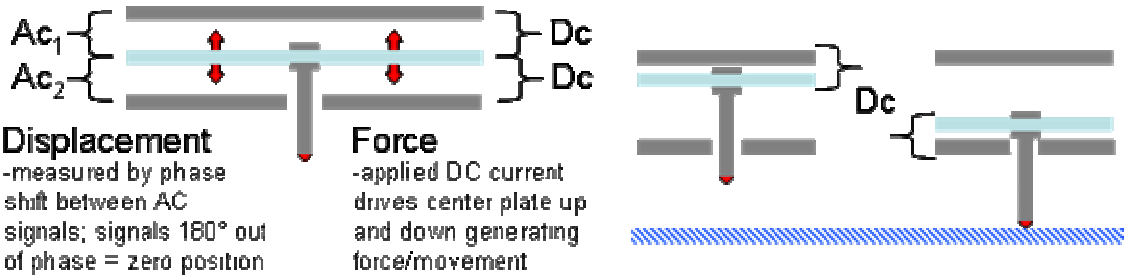

Figure 8.1 Diagram of three plate capacitor transducer used in the Hystitron Triboindenter®.

The Triboindenter® is capable of performing nano-DMA measurements between 1-300 Hz but is typically run from 10-200 Hz. At measurement speeds of less then 10 Hz the experimental time becomes exorbitant and to speed greater than 200 Hz the response signal becomes difficult to detect (response signal amplitude decreases with increased scan speed).

8.2.3.2 Experimental conditions

Nano-DMA mapping was conducted on dry 271-55 and PPy/271-55 samples using the ramping dynamic frequency test from 10 Hz-200 Hz. A quasistatic load (pre-load) of 2 μN and dynamic load of 1 μN was used. The tip used during these experiments was a diamond cono-spherical tip (Figure 8.2A) with a tip radius of 0.94 μm and a cone angle of 60°. Under these conditions this equates to a calculated contact area of about 100-200 nm if a sample surface modulus of 1-4 GPa is used (circular Herzian contact calculator with sample radius approaching infinity; http://grove.ufl.edu/~wgsawyer/Laboratory/Software/Software.html). The tip has a modulus of 1140 GPa and a Poisson's ratio of 0.07.

Dynamic fluid cell nano-DMA mapping was conducted on PPy/8211-65 and PPy samples driven by a Princeton Applied Research 263A-2 potentiostat. The fluid cell was constructed using a standard glass Petri dish (150 mm X 20 mm) with a stainless steel counter electrode and Ag/AgCl reference electrode. The stainless steel counter electrode was placed on the bottom of the fluid cell adjacent to the sample for the initial experiments. In subsequent experiments (experiments discussed here) the counter electrode was wrapped around the inside edge of the Petri dish wall. The sample was mounted in the center of the fluid cell and covered with artificial sea water. A diagram and photograph of the fluid cell setup are shown in Figure 8.3.

The detection of the sample surface during tip approach is controlled by the load measured on the tip. Once a load equal to the quasistatic load is detected the Triboindenter® assumes it has found the sample surface and starts scanning that surface. Due to the viscosity of the artificial sea water in the fluid cell the load on the transducer repeatedly exceeded 2 μN during the sample approach. This caused the Triboindenter®

to falsely engage the surface about 5-10 mm above the actual sample surface (visual observation). To overcome this problem a higher quasistatic load of 10 μN was used during the fluid cell experiments. The dynamic load was 1 μN.

Ramping dynamic frequency test were conducted from 10 Hz-200 Hz. The machine scan rate was 0.25 Hz with scan areas of 25 μm x 25 μm, 10 μm x 10 μm, or 1 μm x 1 μm. The tip velocity was 5 μm/sec. A Berkovich fluid tip (Figure 8.2B) was used for these experiments due to the fact that no other fluid tip was available.

The Berkovich tip is not ideal for polymeric materials and is typically used for indention testing of harder materials and metals. The Berkovich tip has a total included angle of 142.3° with a half angle of 65.35° making it a very flat tip with a large contact area especially in polymers. The average radius of curvature for these tips is typically between 100 and 200 nm. A more suitable choice for a fluid tip is the cono-sherical tips.

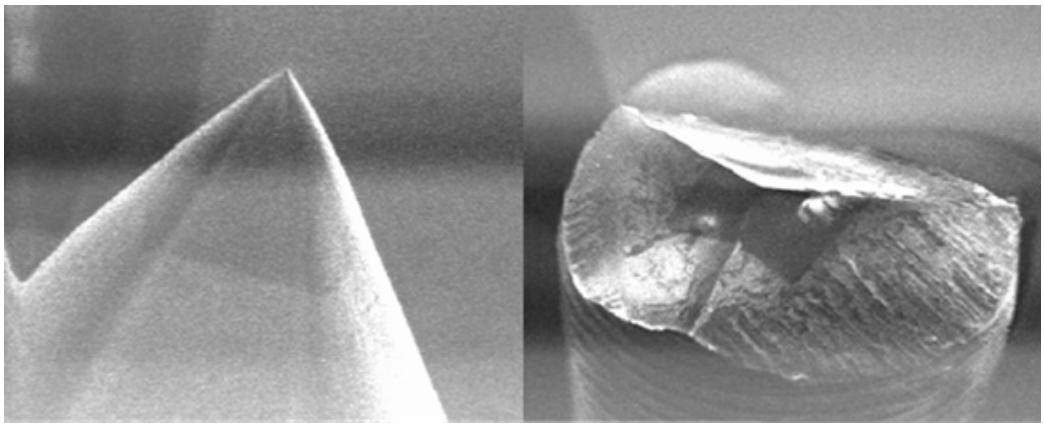

Figure 8.2 Images of cono-spherical (A) and Berkovich (B) Hysitron tips. Images obtained from www.hysitron.com (magnification unknown).

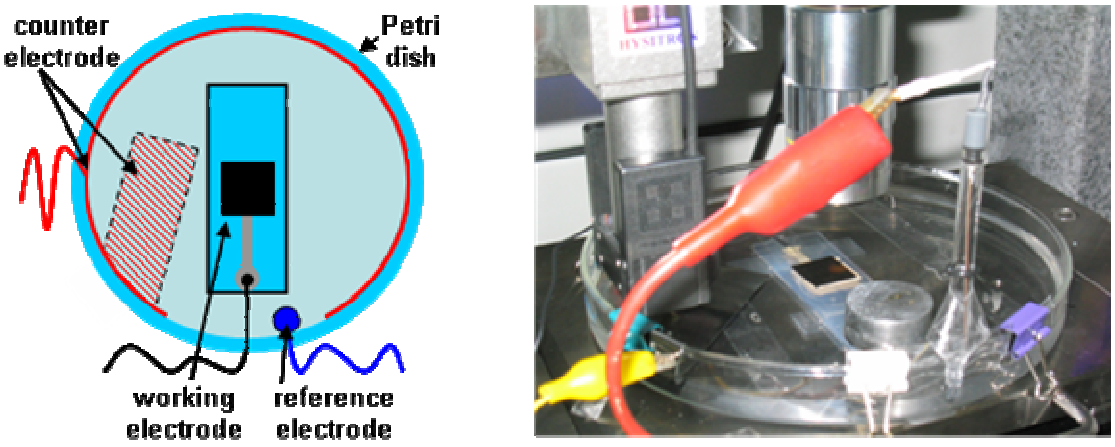

Figure 8.3 Diagram (A) and optical image (B) of fluid cell setup inside the Hysitron Triboindenter®.

8.3 HYSITRON NANO-DMA and AFM ANALYSIS

8.3.1 Nano-DMA mapping of 271-55 and PPy/271-55 samples

A 50 µm x 50 µm square area was mapped on 271-55 and PPy/271-55 samples. One of the first things noticed is the appearance of dark black phases in the sample surface after the formation of the PPy IPN system. These phases were detected using the optical camera mounted in the Triboindenter® and are shown in Figure 8.4 (magnification = 5X). These phases are either due to clustering of PPy on/in the sample surface or due to surface defects present in the material.

These features are also present in the 3D surface topography images (Figure 8.5). From this it can be seen that the PPy/271-55 sample surface is much more irregular than the untreated 271-55 sample. The cracks present in the PPy/271-55 material reach depths up to 900 nm while the change in surface height for the untreated 271-55 is on the order of 200-400 nm.

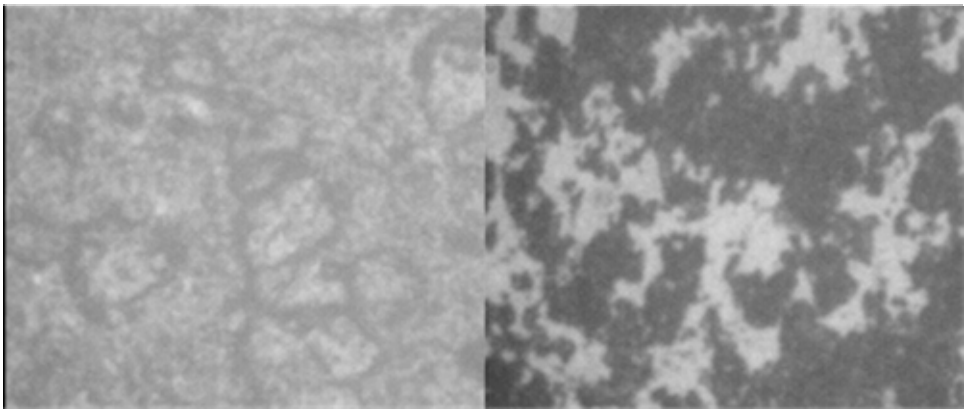

A B

Figure 8.4 Optical micographs of Santoprene® 271-55 (A) and PPy/271-55 (B) samples obtain by the onboard optical camera of the Hysitron Triboindenter® (magnification = 5X).

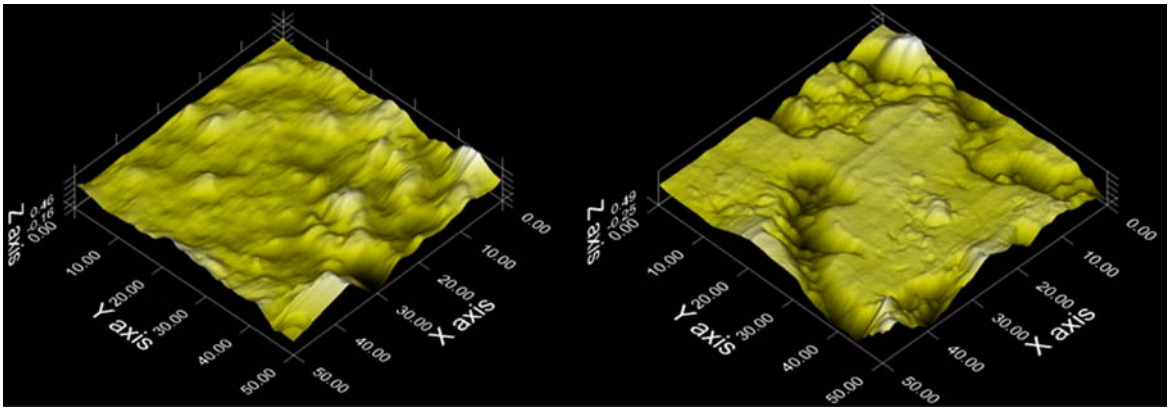

A B

Figure 8.5 3D surface plots of Santoprene® 271-55 (A) and PPy/271-55 (B) surfaces. Scan area is equal to 50 µm x 50 µm square.

However it should be noted that large surface defects have also been detected in untreated 271-55 samples using modulus mapping. In one area a hole with approximate dimensions of 50 µm long and about 40 µm wide was detected in untreated 271-55. The depth of the defect was in excess of 2 µm. The Hysitron tip lost contact with the surface in the defect so its exact depth could not be determined.

Phase and modulus mapping data of the samples surfaces reveals that there is a distinct difference between the 271-55 and PPy/271-55 samples. The phase and modulus

images for the untreated 271-55 show a relatively uniform surface morphology with a surface complex modulus in the range of 0.5-0.7 GPa (Figure 8.6). While the PPy/271-55 samples have a very erratic non-uniform surface morphology and an average surface complex modulus in the range of 0.4 GPa to 2.5-3.5 GPa (8.7).

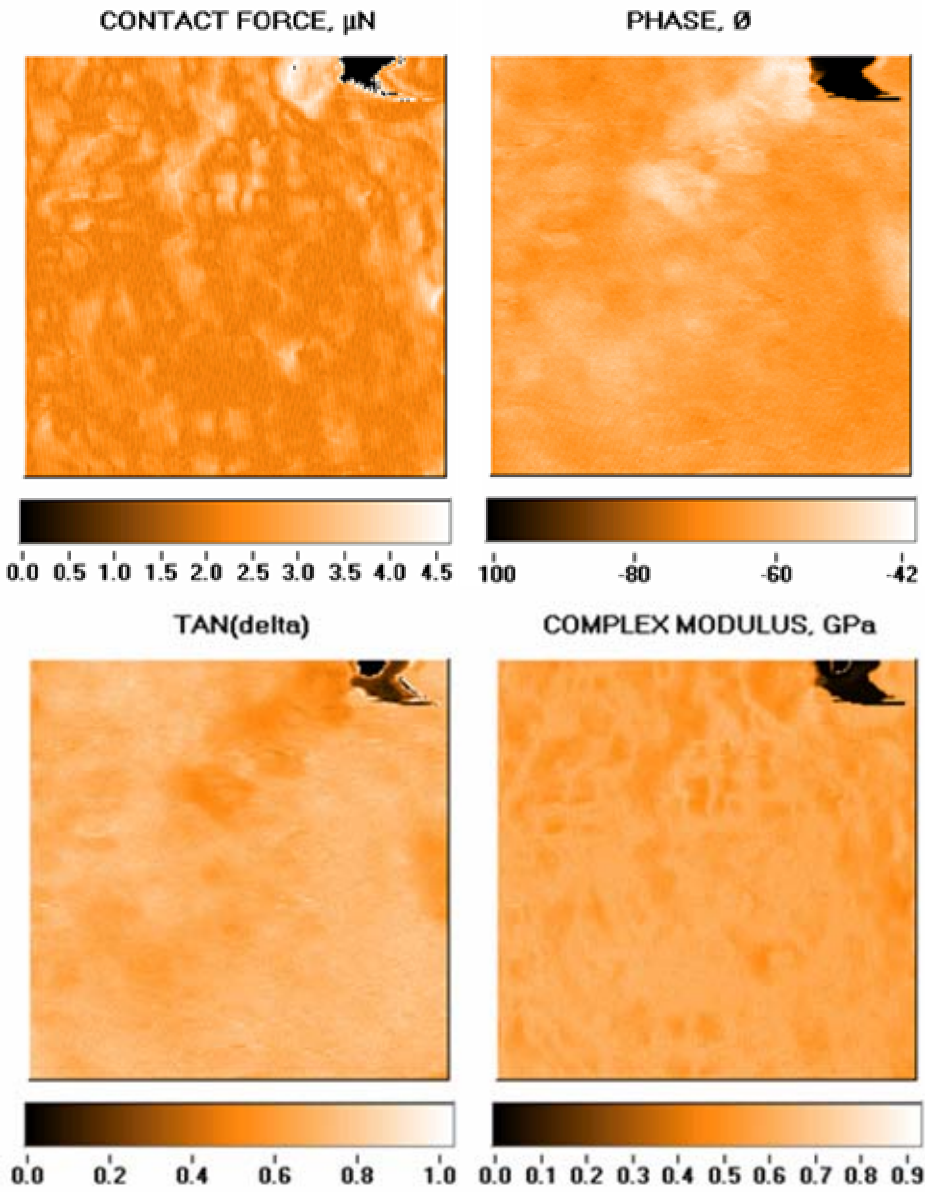

Figure 8.6 Nano-DMA mapping images of Santoprene® 271-55 showing uniform surface phase and modulus morphology. Scan area is 50 µm x 50 µm square.

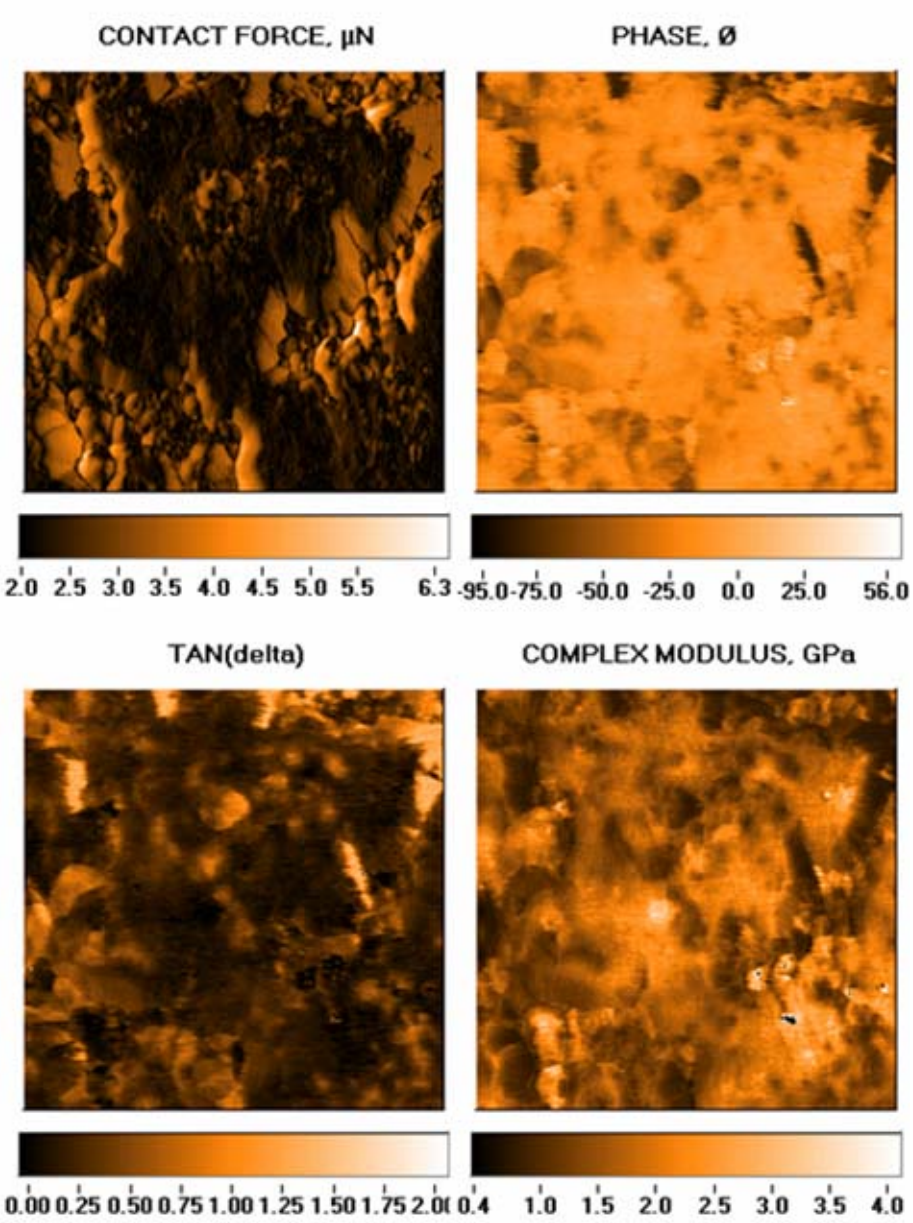

Figure 8.7 Nano-DMA mapping images of PPy/271-55 showing uniform surface phase and modulus morphology. Scan area is 50 µm x 50 µm square.

8.3.2 Dynamic fluid cell nano-DMA mapping of PPy/8211-65

Using modulus mapping and nano-DMA testing, changes in complex, storage, and loss modulus along with changes in tan delta and surface topography were measured *in situ* while switching the material between its oxidized and reduced states.

Dynamic fluid cell nano-DMA analysis of PPy/8211-65 revealed a phase separated morphology comparable to that seen for PPy/271-55 (Figure 8.7B). Initially it was believed that these darker phases were PPy rich phases. A 25 µm x 25 µm scan of the dark phase (Figure 8.8) produced images with large amounts of tip effects. A difference in the sample morphology was detected due to changes in redox states.

Tip effects are usually seen when the surface being imaged is very rough and features sizes are much smaller than the tip contact area. In this case you actually end up imaging the tip with the sample surface instead of imaging the surface with the tip.

Yet, even with the tip effects present; changes in the average surface modulus of the scanned area were detectable. The average surface modulus (complex) of the sample at the applied potentials of +0.7 V, 0.0 V, and -0.7 V were 6.47 ± 2.76, 6.83 ± 2.83, and 10.85 ± 0.68 GPa respectively. Due to the unknown tip area for the Birkovich tip the only thing that can be said is that there is about a 40% decrease in surface modulus when switched from the reduced state to the oxidized state.

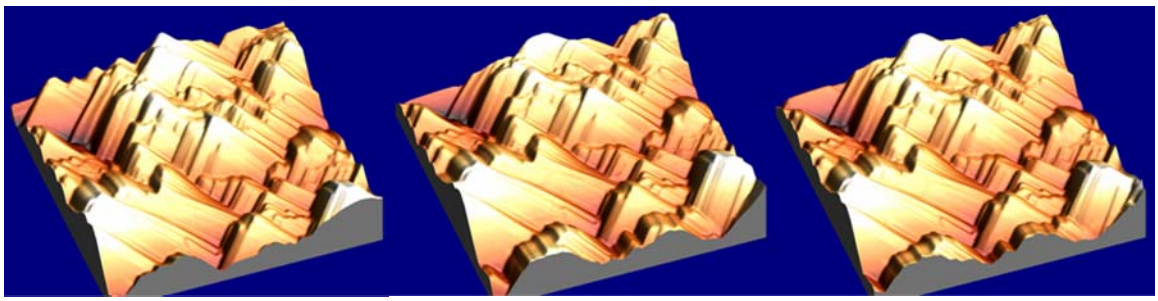

Figure 8.8 3D surface topography images of PPy/8211-65 at applied potentials of -0.7 V (A), 0.0 V (B), and +0.7 V (C). Scan area is 25 µm x 25 µm square.

An AFM analysis of the sample surface was conducted to confirm the morphology observed with the Hysitron (Figure 8.9). These measurements were conducted on a dry sample in tapping mode on a Veeco Dimension 3100 AFM. Surface imaging of 50 µm,

10 µm, 5 µm, and 1 µm square scan areas was conducted. These AFM images reveal that the phase contrast observed in the optical images is due to large surface defects and not PPy segregation. This supports the observations in the initial fluid cell nano-DMA imaging of PPy/8211-65.

The AFM topography and phase imaging of the sample surface also revealed some interesting surface morphology (Figure 8.10). Some surface features with regular angles are evident in the 10 µm and 5 µm scan area images. It is not clear at this time what these features are due to and further investigation needs to be done. These features could be the result of $FeCl_3$ salt deposition in the sample surface, the presence of clay filler particles, or the formation of PPy.

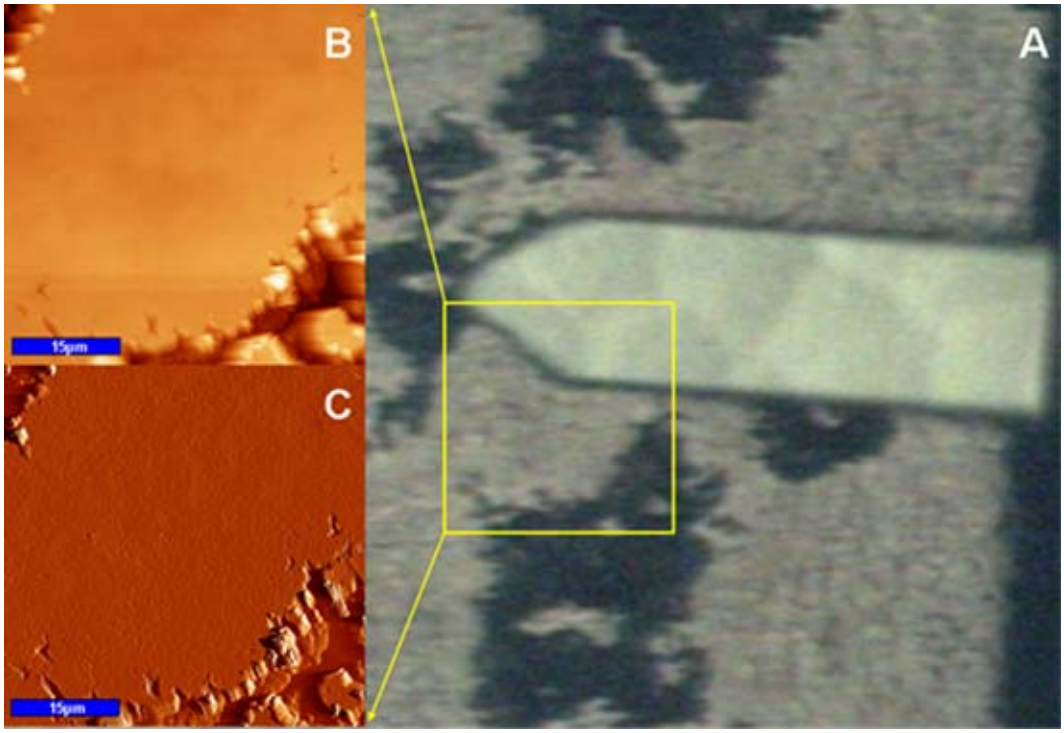

Figure 8.9 AFM optical micrograph (A) of PPy/8211-65 with corresponding surface topography (B) and phase contrast (C) images taken at a 50µm square scan area. Scale bars equal to 15µm.

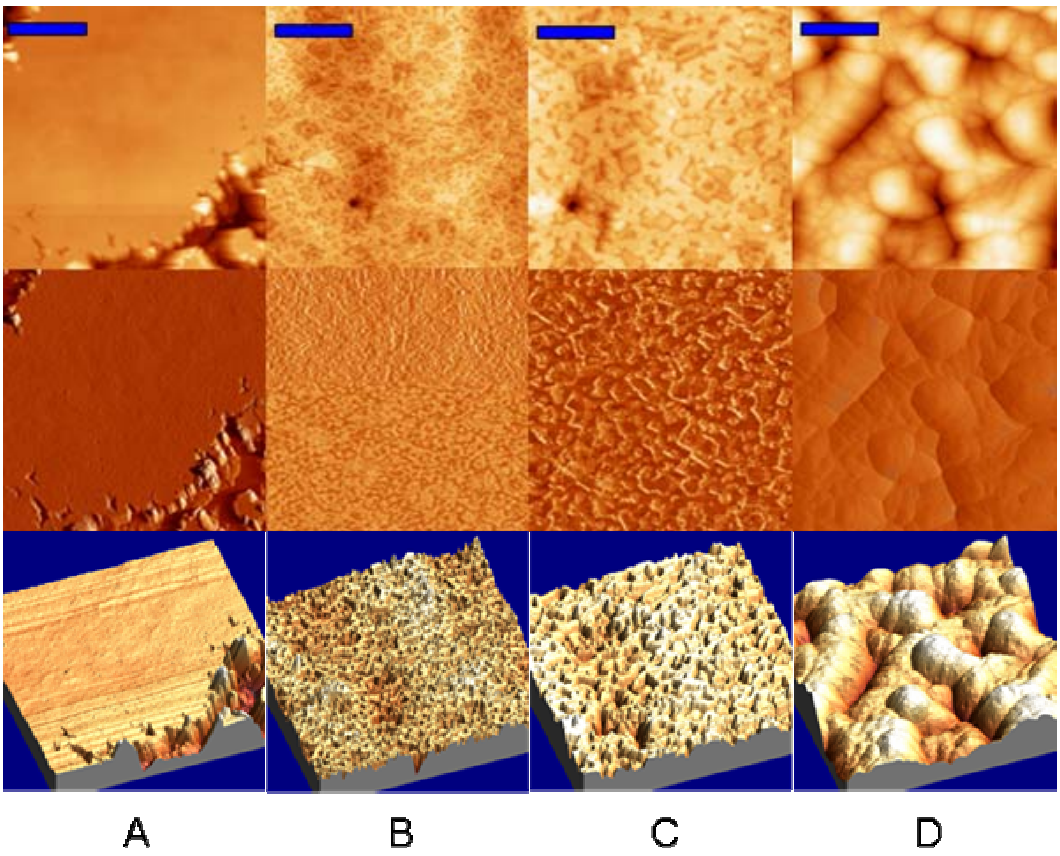

Figure 8.10 AFM surface topography, phase imaging, and 3D surface plot of PPy/8211-65 at 50 µm (A), 10 µm (B), 5 µm (C), and 1 µm (D) square scan areas. Scale bars equal to 15 µm, 3 µm, 1.5 µm, and 0.3 µm respectively.

The surface morphology of the PPy in the PPy/8211-65 material is still not evident. Future studies will include SPM (scanning probe microscopy) imaging of the PPy/TPE materials using the AFM setup. By using SPM techniques the spreading resistivity of the sample surface can be mapped. This should reveal the location and morphology of the conductive regions on the sample surface thus giving the location and morphology of the PPy phase.

After the determining the phase contrast observed in the optical images was due to surface defects; dynamic fluid cell nano-DMA experiments were conducted on the lighter phase regions. The scan area was reduced to 10 µm square for this set of measurements. The scan area was also translated 30 µm in the positive X direction from the initial tip

engagement point. This was done to insure that the sample surface being imaged was not damaged due to the initial tip engagement process.

Due to the fluid cell setup false engagements were a problem during the initial tip approach to the sample surface (tip stops about 5-10 mm above sample surface). This was overcome by increasing the quick approach set point (quasistatic load). The set point value is the static load the tip places on the sample during the nano-DMA measurements and is also used to automatically detect the surface. Once the tip experiences a force of equal or greater value than the set point the Triboindenter® algorithm converts to surface mapping. The tip engagement force (set point) is typically 2 μN but due to the false engagement problems the set point had to be increased to 10 μN. This high force could potentially damage the sample surface during the initial approach process. The dynamic load (oscillating load) used for these experiments was 1 μN.

Under these conditions there were no tip effects evident for the sampled area scanned. For this location the average surface complex modulus for the 10μ x 10μm scan area changed from 7.71 ± 0.70 GPa to 14.23 ± 2.00 GPa and 13.23 ± 1.75 GPa under the applied potentials of +0.8 V, 0.0 V, and -0.8 V respectively. This equates to a 42% decrease in surface modulus when switched from the reduced state to the oxidized state.

Line scan modulus data was also extracted from the complex modulus map. The line scan data for the positions shown in Figure 8.11 are exhibited in Figure 8.12. This data agrees with the values obtained for the average complex modulus for the whole sample surface. This data also shows the presence of a surface feature of about 1μm in diameter that does not change its modulus with the applied potential as much as the rest of the sample surface.

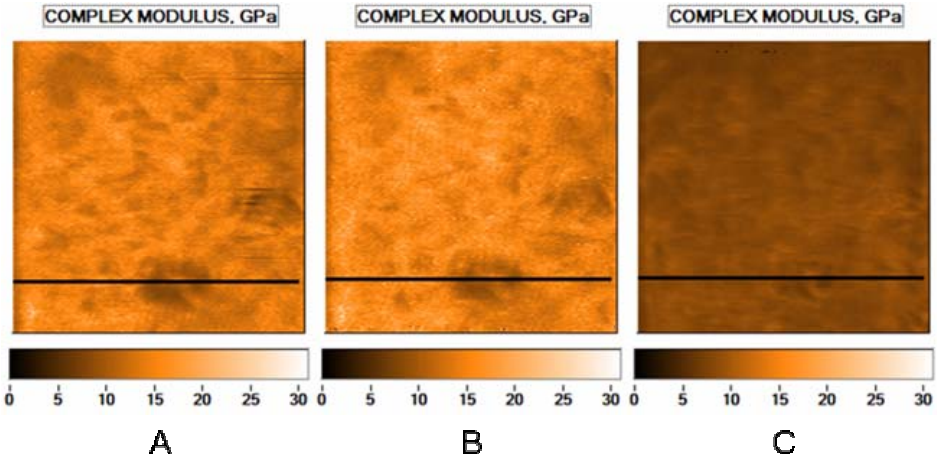

Figurer 8.11 Complex modulus maps for PPy/8211-65 at an applied potential of -0.8 V (A), 0.0 V (B), and +0.8 V (C).

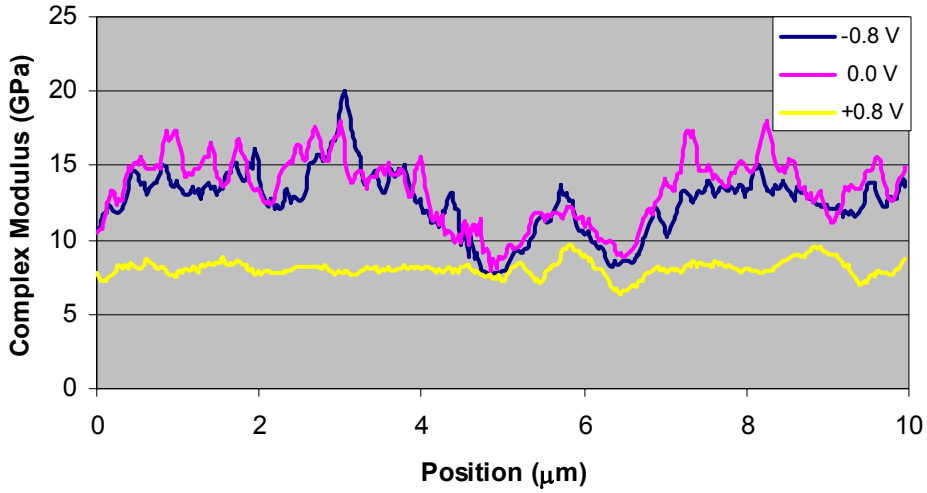

Figure 8.12 Complex modulus line scan data for PPy/8211-65 obtained from the location depicted in Figure 7.28

By looking at the 3D surface plots obtained from these measurements it can be seen that the naturally occurring surface features present on the sample surface swell and de-swell with the changes in the applied potential. The 3D surface plots show a ridge (top center of the plot) that waves up and down from the sample surface when the potential is switched between -0.8 V and +0.8 V (Figure 8.13). This demonstrates the dynamic surface topography capabilities of these types of materials. With improved processing

and patterning techniques precise engineered dynamic surface topographies should be able to be produced,

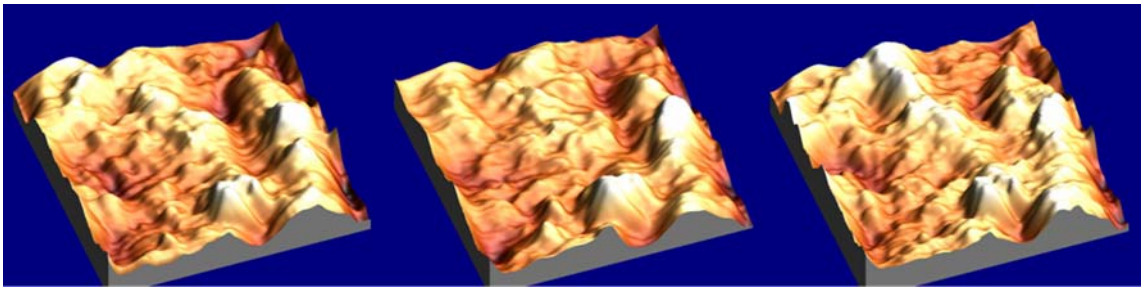

Figure 8.13 3D surface plots of PPy/8211-65 under the applied potentials of -0.8 V (A), 0.0 V (B), and +0.8 V (C).

The average surface complex modulus changed from 11.95 ± 1.64 GPa to 11.90 ± 2.02 GPa and 14.92 ± 5.76 GPa under an applied potential of +0.8 V, 0.0 V, and -0.8 V respectively over a 1 μm square area. On this scale the decrease in surface modulus was only ~20% when switched from the reduced to the oxidized state. The modulus changes measured for this area are not as significant as those produced in the previous measurements. However they are on the same order as the previous measurements and follow the same trend as before. This could be due to the smaller scan size and the sample morphology of the area being mapped.

As a comparative study dynamic fluid cell nano-DMA measurements were conducted on pure PPy. The PPy sample were electrochemically switched between -0.8 V, 0.0 V, and +0.8 V and nano-DMA measurements were conducted. The average surface complex modulus changed from 2.42 ± 1.03 GPa to 2.34 ± 0.15 GPa and 25.83 ± 7.53 GPa for potentials of +0.8 V, 0.0 V , and -0.8 V respectively. This equates to a 90% decrease in the surface modulus when switched from the reduced to oxidized state. Conducting polymers have previously been shown to change their modulus during

electrochemical redox switching.[94, 143-147] The average surface complex modulus for PPy and PPy/8211-65 are plotted against each other in Figure 8.14.

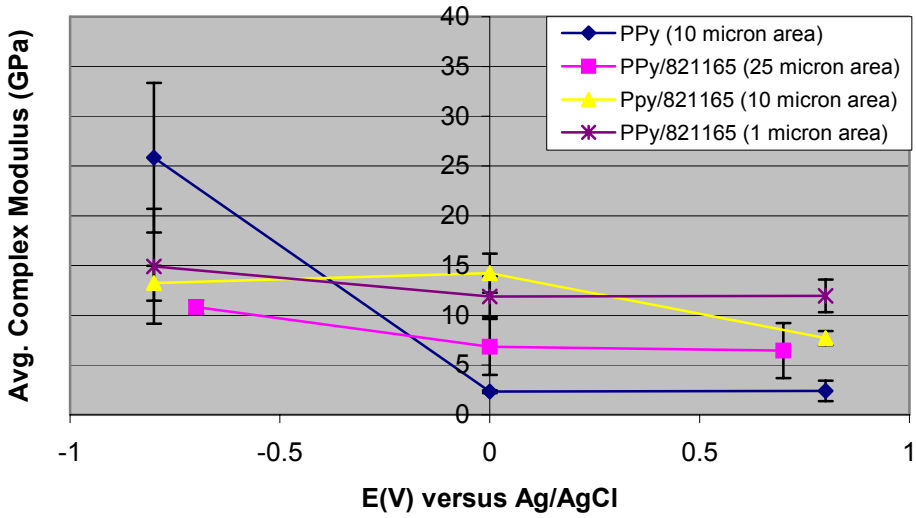

Figure 8.14 Average surface modulus for PPy and PPy/8211-65 systems as a function of the applied potential.

The modulus change produced by the PPy sample is significantly larger than recorded for the PPy/821-65 materials. This is expected since the PPy is the reactive material in this system. By incorporating it into the 8211-65 TPE as a minor component the overall change produced from this system would be reduced. The overall properties of these IPN systems are directly dependent on the amount of conducting polymer incorporated into the system.

From this it can be said that the surface of the PPy/8211-65 samples are capable of producing dynamic surface properties such as surface modulus and topography. Further tests need to be conducted on these samples with the proper fluid cell tip in order to determine the true value and magnitude for the changes in surface modulus.

8.4 CONCLUSIONS

Hysitron nano-DMA was used to conduct dynamic electrochemical fluid cell measurements on the PPy/8211-65 system. The PPy/8211-65 systems were shown to produce an average surface modulus change on the order of ~20-40% when switched between its two redox states.

Also dynamic changes in surface morphology were also shown to follow the redox switching process in these systems. Dynamic fluid cell nano-DMA measurements were also conducted on PPy. Polypyrrole was shown to undergo a dynamic surface modulus change on the order of 90% when switched.

This is the first time anybody has conducted dynamic surface modulus and topography mapping in this manner. This technique could prove to be very valuable in the characterization of these types of material.

CHAPTER 9
CONCLUSIONS AND FUTURE WORK

The initial goal of this work was to develop new and advanced high performance conducting polymer based actuator designs and evaluation techniques. After this initial work the knowledge and lessons learned were then applied to the development of conducting polymer based dynamic surface coatings. These dynamic surfaces have a potential role as dynamic non-toxic antifouling surface coatings for marine and commercial applications. A quick summery of some of the major points to this work are listed below; they will be discussed in further detail in the following paragraphs:

1. A new in situ strain gage measurement technique was developed using commercially available strain gages to monitor the *in situ* strain performance of conducting polymer (CP) based bimorph actuators. This new i*n situ* strain gage measurement technique was used to evaluate the strain performance of a commercially available CP polypyrrole (PPy) and two new CPs poly(3,4-ethylenedioxypyrrole) (PEDOP) and poly[3,6-2(2-(3,4-ethylenedioxythienyl)-carbazole] (PBEDOT-Cz). From this study it was shown that the strain performance of PPy far exceeded (~4.5 times higher) that of PEDOP and PBEDOT-Cz. Due to this PPy was chosen as the standard material for all continued work.
2. Interlayer adhesion between the CP and base electrode was determined to be a problem associated with CP based actuators. A new electrochemically deposited Au (EcAu) layer was developed that greatly

enhanced the interlayer adhesion between the CP and base electrode. As a result of this; a drastic improvements in the overall strain performance and lifetime of these devices was obtained.

3. A new rapid patterning technique was developed for the fabrication of advanced electrode designs utilizing standard office software and printer systems. This rapid patterning technique was used to design and fabricate advance linear actuator designs. It was also shown that this technique can also be used to quickly produce inexpensive photomasks for lithographic processing.

4. Utilizing techniques obtained from the previous studies conducting polymer based dynamic surface coating were developed. The dynamic surface energy of these materials was shown using contact angle measurement techniques. These films were based on the formation of a PPy IPN system inside a PDMSe base material. The effects of various solvent soak systems used in the fabrication of these materials were also evaluated.

5. Further development of CP based dynamic surface coatings was continued using Santoprene® thermoplastic elastomers (TPE). By utilizing elastomers with improved mechanical properties compared to PDMSe tougher more robust dynamic surface coating were developed. These materials were shown to have a dynamic surface energy and were also shown to have dynamic surface moduli and topographies as measure by dynamic fluid cell nano-DMA mapping.

Throughout the various studies conducted the formation and evaluation of conducting polymer based composite structures and devices was the common theme. In the initial studies conducting polymer based actuators were developed by the forming CP based laminate composite structures. Conducting polymer based actuators were formed by electrochemical polymerization of various CP monomers on EvAu coated flexible substrates. Due to the expansion and contraction of the conducting polymer layer during redox cycling a bending motion can be produced from the actuator. The determination of the performance characteristics of these devices under there intended application conditions is crucial to there continued development and use. A new in situ strain gage measurement technique was developed and utilized to evaluate the strain performance of PPy, PEDOP, and PBEDOT-Cz based actuators. PPy being a commercially available conducting polymer is widely used in various conducting polymer applications. The two new conducting polymers PEDOP and PBEDOT-Cz were thought to be potential contenders for the replacement of PPy in CP based actuator applications. In order to evaluate the strain performance of actuator system based on these materials the in situ strain gage measurements technique was used. Utilizing this technique it was shown that cyclic strain response of these materials can precisely be measured. PPy was shown to be capable of producing a significantly higher strain than PEDOT and PBEDOT-Cz. PPy produced an average overall strain response on the order of 250με while PEDOP and PBEDOT-Cz produced an average overall strain response of about 45με and 35με respectively. Also the degree of hysteresis present in the strain response of these materials was also shown. While PPy produced the largest strain response it also has the largest degree of hysteresis when compared to PEDOP and PBEDOT-Cz.

From this study it was also determined that the interlayer adhesion between the conducting polymer layer and the base electrode (EvAu) was a potential problem for the prolonged use of these devices. Due to the repeated swelling and deswelling of the CP layer and the resultant bending motion developed in these devices during electrochemical cycling a large amount of interlayer strain is produced. This initiates micro-crack formation which eventually propagates and cause the complete delamination of the CP from the base electrode. This drastically reduced the potential lifetime of these devices. Also as the interlayer cracks propagate across the electrode surface the CP contact area with the base electrode is reduced. This in turn reduces the ability of CP to generate the desired strain response.

This issue was remedied by the application of an electrochemically deposited Au (EcAu) layer on top of the base EvAu layer. The EcAu layer was found to greatly improve the interlayer adhesion of the CP layer to the base electrode layer. This was the result of the drastically increased electrode surface produced by the EcAu treatment along with the improved mechanical adhesion due the growth of the CP layer into the nooks and crannies of the EcAu layer (mechanical interlocking). The application of the EcAu layer to the base electrode layer was also found to improve the performance properties such as strain, strain rate, and frequency response of the actuator systems. This believed to be due the decreased CP layer thickness due to the increased electrode surface area. This improves the diffusion rate of counter ions and associated solvent into and out of the CP layer. By controlling the EcAu deposition time the size of the EcAu crystals can be controlled thus controlling the CP layer thickness. It was shown that by increasing the EcAu layer thickness up to a point that the overall strain production, strain rate,

frequency response, and lifetime was improved. The EcAu treatment produced an increase in the strain response of about 110% and improved the actuator strain performance after 2000 cycles by 20%.

The in situ strain gage measurement technique was also used to evaluate the effects of counter ion type, driving potentials, electrochemical polymerization charge, and electrochemical polymerization potential on the overall strain response of PPy/EcAu and PPy/EvAu based actuators. From these tests it was determined that the counter ion type greatly influenced the overall strain response of the actuator systems. Larger counter ions such as $ClO4^-$ produced about a two fold increase it the strain response than smaller counter ions such as Cl^-. An increase in the applied driving potential (oxidation potential) was shown to increase the overall strain response of the material up to a potential of 0.6V. It was also shown that as the electropolymerization charge was increased, resulting in thicker CP thickness, the overall strain response of the system also increased. However for a given increase in electropolymerization charge the resultant increase in the strain response decreases. This is believed to be due to a decrease in the diffusion rate of the counter ions and associated solvent in the CP layer as the layer thickness increases. The evaluation of the effects of electrochemical polymerization potential showed that as the electropolymerization potential is increased above 0.5V the overall strain response if the system is increased up to 0.7V. Above this potential the overall strain response of the system was found to decrease. The strain response of the system was decreased by ~20% when the electropolymerization potential was increased from 0.7V to 1.0V. As the electropolymerization potential is increase the ability of side reactions to occur such as the 3,4 polymerization in pyrrole also increases. This disrupts

the overall π conjugation of the system and increases the crosslink density of the system. This results in a decrease in conductivity and in increase in the stiffness of the material. The increased material stiffness will result in a decrease in the diffusion rate and swellability of the system decreasing the overall strain performance.

In order to further the development of CP based actuators the ability to fabricate new and diverse electrode patterns on various substrates is required. A new rapid patterning technique was developed utilizing standard office printers and standard Au coating techniques. This technique allows for the rapid development and fabrication of virtually any electrode pattern of flexible substrates such as polyimide and PET.

This technique was used in the development of advanced linear actuator designs. Initial linear actuator designs were based on a staggered placement of PPy segments on opposite sides of a conductive flexible substrate. These actuators were capable of producing linear strains of 2.5%, 12.5%, and 24% for 5, 10, and 20mm PPy segments. Advanced pattern designs were created with both the working and counter electrode being placed on the actuator surface. This eliminated the need for an external counter electrode. Both single and double sided designs were created. The double layer design was constructed using a modified backbone type configuration where CP segments are placed on opposite sides of the flexible substrate. As one side is oxidized the other is reduced resulting in a push-pull type strain production. The major issue with using this technique in the fabrication of electrode patterns is that the final fabricated electrode fidelity is only as good as that of the printer used to print it. Laser jet printers have the capability of printing on almost any substrate but they suffer from toner overspray. Random toner particles end up in the un-patterned areas of the design causing defects in

the final electrode pattern. Ink jet printers were found to greatly reduce the amount of overspray in the unpatented areas. However; ink jet printers require the use of specially treated substrates to improve the wetting and drying characteristics of the ink on the substrate. This surface treatment has been found to prevent the adhesion of the applied Au layer thus preventing the fabrication of the electrode pattern. However ink jet printing has been shown to be an effective way of rapidly producing inexpensive photomasks for use in standard photolithographic techniques.

Conducting polymer based dynamic surface coatings were developed utilizing the induced changes in physical property of CPs that occur during redox cycling. The production of strain seen in CP based actuator systems is produced from the dynamic change in charge developed in the CP system. As a positive charge is developed in the CP during the oxidation process counter ions and there associated solvent are driven into the CP to neutralize the developed charge. This results in the swelling of the CP thus producing the observed strain. The swelling of the CP also results in a decrease in the modulus of the CP compared to the reduced state. The solvent associated with the counter ions acts as a plasticizer in the CP and also increases the free volume of the system this in turn decreasing the overall modulus of the material.

The surface properties of dynamic PPy/PDMSe composite coatings were evaluated using electrochemical fluid cell contact angle measurements. These coatings produced a 21° change in contact angle when stepped between an applied potential of ±1.0V. The overall dynamic properties of these composite structures are directly proportional the weight percent of the CP phase incorporated into the system.

The loading of the CP phase in the composite structure is dependent on the solvent system used during the fabrication of these systems. By changing the solvent system used in the formation of PPy/PDMSe composite structures from ethanol/supercritical CO_2 ($scCO_2$) to isopropanol/$scCO_2$ the weight percent of PPy incorporated into the structure was increased from ~2wt% to ~5wt%. Supercritical CO_2 based solvent systems were initially chosen due the low environmental impacts and cost associated with the use of $scCO_2$. $ScCO_2$ is very effective at swelling PDMSe however the solubility of $FeCl_3$ and other inorganic oxidizers is very low in $scCO_2$. By adding alcohol based co-solvents to the solvent system the solubility of $FeCl_3$ was improved. THF was found to be a better solvent medium than $scCO_2$ based systems due to the improved solubility of $FeCl_3$ and PDMSe and was in place of the $scCO_2$ based systems.

The distribution of $FeCl_3$ in $FeCl_3$/THF doped PDMSe was found to be mainly concentrated in the bulk of the material using EDS mapping. A 60-100μm surface boundary layer in PDMSe was detected that was very low in concentration of $FeCl_3$ compared to the bulk of the material. This resulted in the formation of an unstable PPy surface layer (due to oxidizer deposited directly on the sample surface) that was not directly connected to the PPy deposited in the bulk of the material. Due to this; the PPy/PDMSe samples were found to be mainly surface conductive and not bulk conductive.

Dynamic surface coatings based on Santoprene® TPEs and Udel® polysulfone were developed in order to produce dynamic surface coating with improved mechanical properties and chemical stability compared to PDMSe based systems. Dynamic contact angle changes of 11° were produced in PPy/TPE systems when subjected to a ±0.5V

stimulus. Dynamic changes in surface modulus were measured using Hysitron nano-DMA modulus mapping conducted in an electrochemical fluid cell. This is the first time measurements of this type have been conducted. A ~40% change in the average PPy/TPE surface modulus was measured when scanned over a 10μm square area. When the scan area was reduced to one square micron the change in the average surface modulus was determined to be ~20%. It should be noted that a Berkovich fluid cell tip was used for these experiments. The Berkovich tip design is not ideal for the mapping and measurement of polymers and can distort the actual physical property values obtained during nano-DMA measurements. During the electrochemical oxidation of PPy the material expands due to the influx of counter ions and their associated solvent (H_2O). This swelling behavior increases the free volume of the system and decreased the overall density of the material due to the differences in the density of PPy (ρ = 1.05 g/ml) and H_2O (ρ = 1 g/ml).

Santoprene® TPEs and Udel® polysulfone have also been micropatterned with an engineered biomimetic sharklet pattern. This pattern has been shown to decrease the settlement of Ulva spore by 85% on patterned PDMSe compared to un-patterned PDMSe. By incorporating this type of micropatterning with the dynamic surface coatings the overall performance and capabilities of these films should be enhanced.

The future development of these systems needs to focus on improved fabrication techniques. The current solvent/oxidizer soak system is effective in the formation of conducting polymer IPN systems. However this technique is limited in its ability to form composite structures containing high volume fractions of CP due the diffusion limited process of oxidizer insertion into the base material. This process is also

impractical as a commercially utilized process. By incorporating higher amounts of CP in the composite structure the dynamic properties of these materials should be increased. More conventional processing techniques such as melt mixing/compounding and reactive extrusion would be more commercially viable as a fabrication technique. These techniques allow for precise control over the loading of the CP phase. One issue to be considered in utilizing these techniques is the morphology of the resultant CP phases. During mechanical melt mixing the CP would be added into the system as a dry filler material. This would result in the formation of particulate CP phase. While the use of reactive extrusion processes could result in the formation of a more uniform IPN type phase. During reactive extrusion separate conducting polymer monomer and oxidizer feeds would be pumped into the melt and would then polymerize as a secondary phase. By controlling the processing conditions the morphology of this secondary phase should be able to be changed between particulate and IPN type morphologies. Also by utilizing these techniques a variety of base materials and conducting polymers could be used allowing for the creation of various systems each with its own unique properties. This would allow for the tailoring of these coating systems to there particular applications and environments.

The effects of these dynamic surfaces on the settlement and adhesion of marine organisms needs to be evaluated in order to evaluate the potential use of these materials as dynamic non-toxic antifouling coatings. The wave form, magnitude, and timing of the electrical stimuli used operate these materials needs to be thoroughly evaluated. Square and sinusoidal/cyclic wave forms can be used to drive these systems. Under a square wave stimulus the system can be instantaneously switched or incrementally stepped

between its maximum oxidation and reduction potentials. A random walk approach could also be used to switch the applied potential as well. The length of each of these steps can also be varied. Under a sinusoidal or cyclic stimulus the applied potential is continuously ramped between the oxidation and reduction set points. The magnitude of these set points and the scan/ramp rate of the applied potential can be varied. All of these variables will affect the ability of these coating to deter the settlement and adhesion of marine organisms on these surfaces. An example of the problem being faced is for the settlement of the Ulva spore. These spores have been shown to probe a given substrate surfaces prior to settling on that surface. Once a suitable surface has been found the spore will settle. If the dynamic surface is being driven by a square wave potential the switching time would potentially be a critical factor influencing the settlement of the spore. If the switch time is sufficiently long that the spore has time to probe and then settle on the surface before the potential is switched then the spore will probably settle and adhere to the surface. However if the switching time is shorter than the time required for the spore to probe and settle on the surface then the properties of that surface would change during the probing process. This would most likely deter the spore from settling on the sample surface. If a cyclic wave form was used then the sample surface would constantly be in flux. This would make it difficult for the spore to determine if it liked the surface and it would probably not settle on the surface. The scan/cycle rate applied to the surface would affect how much change in the sample surface the spore would detect for a given amount of time. All of these variables need to be thoroughly evaluated in order to optimize these systems for the prevention of marine organism settlement and adhesion.

APPENDIX A
ABBREVIATIONS

271-55:	Santoprene® 271-55 thermoplastic elastomer
8211-65:	Santoprene® 8211-65 thermoplastic elastomer
8281-65:	Santoprene® 8281-65 thermoplastic elastomer
AFM:	atomic force microscopy
Ag:	silver
Ag/AgCl:	silver-silver chloride reference electrode
ATR:	attenuated total reflectance
ATR-FTIR:	attenuated total reflectance Fourier transform infrared spectrometry
ATS:	allyltriethoxy silane
CO_2	carbon dioxide
Au:	gold
CP:	conducting polymer
DI:	distilled water
DMA:	dynamic mechanical analysis
EAP:	electroactive polymer
EcAu:	electrochemical gold
EDS:	energy dispersive x-ray spectroscopy
EPDM:	ethylene propylene diene monomer
EtOH:	ethanol
EvAu:	evaporated gold

FTIR: Fourier transform infrared spectrometry

I.O.: Instant Ocean® artificial sea water

IPA: isopropanol

IPN: interpenetrating polymer network

PBEDOT-Cz: poly(3,6-bis(2-(3,4-ethylenedioxy)thienyl)-N-carbazole)

PDMSe: polydimethylsiloxane elastomer (Dow Corning Silastic® T2)

PEDOP: poly(3,4-ethylenedioxypyrrole)

PET: polyethylene terephthalate

PMeT: poly(3-methylthiophene)

PP: polypropylene

PPP: poly(p-phenylene)

PPy: polypyrrole

PSU: polysulfone

$scCO_2$: supercritical carbon dioxide

SEM: scanning electron microscopy

SPM: scanning probe microscopy

THF: tetrahydrofuran

TP: thermoplastic

TPE: thermoplastic elastomer

V: volts

LIST OF REFERENCES

1. Irvin, D. J.; Goods, S. H.; Whinnery, L. L., Direct measurement of extension and force in conductive polymer gel actuators. *Chemistry of Materials* **2001,** 13, (4), 1143-1145.

2. Tuijthof, G. J. M.; Herder, J. L., Design, actuation and control of an anthropomorphic robot arm. *Mechanism and Machine Theory* **2000,** 35, (7), 945-962.

3. Low, L. M.; Seetharaman, S.; He, K. Q.; Madou, M. J., Microactuators toward microwaves for responsive controlled drug delivery. *Sensors and Actuators B-Chemical* **2000,** 67, (1-2), 149-160.

4. Otero, T. F.; Grande, H.; Rodriguez, J., An electromechanical model for the electrochemical oxidation of conducting polymers. *Synthetic Metals* **1996,** 76, (1-3), 293-295.

5. Chen, X. W.; Xing, K. Z.; Inganas, O., Electrochemically induced volume changes in poly(3,4- ethylenedioxythiophene). *Chemistry of Materials* **1996,** 8, (10), 2439-2443.

6. Kaneto, K.; Kaneko, M.; Min, Y.; MacDiarmid, A. G., "Aritificial muscle": Electromechanical actuators using polyaniline films. *Synthetic Metals* **1995,** 71, 2211-2212.

7. Otero, T. F.; Grande, H.; Rodriguez, J., A New Model for Electrochemical Oxidation of Polypyrrole under Conformational Relaxation Control. *Journal of Electroanalytical Chemistry* **1995,** 394, (1-2), 211-216.

8. Baughman, R. H.; Shacklette, L. W.; Elsenbaumer, R. L.; Plichta, E. J.; Becht, C., Micro electromechanical actuators based on conducting polymers. In *Molecular Electronics*, Lazarev, P. I., Ed. Kluwer Academic Publishers: Dordrecht, 1991; pp 267-289.

9. Baughman, R. H., Conducting polymer artificial muscles. *Synthetic Metals* **1996,** 78, 339-353.

10. Della Santa, A.; De Rossi, D.; Mazzoldi, A.; Tiberi, M. In *Conducting polymer actuating structures for steerable microcatheters*, Proceedings of the International Symposium on Microsystems, Intelligent Materials and Robots, Sendai, Japan, Sept. 27-29, 1995; Sendai, Japan, 1995; p 275.

11. Pei, Q.; Inganas, O., Electrochemical muscles: Bending strips built from conjugated polymers. *Synthetic metals* **1993,** 55-57, 3718-3723.

12. Naoi, K.; Lien, M.; Smyrl, W. H., Quartz Crystal Microbalance Study - Ionic Motion across Conducting Polymers. *Journal of the Electrochemical Society* **1991,** 138, (2), 440-445.

13. Gandhi, M. R.; Murray, P.; Spinks, G. M.; Wallace, G. G., Mechanism of electromechanical actuation in polypyrrole. *Synthetic metals* **1995,** 73, 247-256.

14. Chiarelli, P.; Dellasanta, A.; Derossi, D.; Mazzoldi, A., Actuation Properties of Electrochemically Driven Polypyrrole Freestanding Films. *Journal of Intelligent Material Systems and Structures* **1995,** 6, (1), 32-37.

15. Torresi, R. M.; Detorresi, S. I. C.; Matencio, T.; Depaoli, M. A., Ionic Exchanges in Dodecylbenzenesulfonate-Doped Polypyrrole .2. Electrochemical Quartz-Crystal Microbalance Study. *Synthetic Metals* **1995,** 72, (3), 283-287.

16. Yang, H.; Kwak, J., Mass transport investigated with the electrochemical and electrogravimetric impedance techniques .2. Anion and water transport in PMPy and PPy films. *Journal of Physical Chemistry B* **1997,** 101, (23), 4656-4661.

17. Yang, H.; Kwak, J., Mass transport investigated with the electrochemical and electrogravimetric impedance techniques .1. Water transport in PPy/CuPTS films. *Journal of Physical Chemistry B* **1997,** 101, (5), 774-781.

18. Yang, H.; Kwak, J., Mass transport investigated with the electrochemical and electrogravimetric impedance techniques. 3. Complex charge transport in PPy/PSS films. *Journal of Physical Chemistry B* **1998,** 102, (11), 1982-1988.

19. Peres, R. C. D.; Depaoli, M. A.; Torresi, R. M., The Role of Ion-Exchange in the Redox Processes of Polypyrrole Dodecyl-Sulfate Films as Studied by Electrogravimetry Using a Quartz Crystal Microbalance. *Synthetic Metals* **1992,** 48, (3), 259-270.

20. Maia, G.; Torresi, R. M.; Ticianelli, E. A.; Nart, F. C., Charge compensation dynamics in the redox processes of polypyrrole-modified electrodes. *Journal of Physical Chemistry* **1996,** 100, (39), 15910-15916.

21. Slama, M.; Tanguy, J., Electrogravimetrical Study of Polypyrrole. *Synthetic Metals* **1989,** 28, (1-2), C171-C176.

22. Song, M. K.; Gong, M. S.; Rhee, H. W., Anion movement in polypyrrole films prepared in lithium dodecylsulfate aqueous solutions. *Molecular Crystals and Liquid Crystals Science and Technology Section a-Molecular Crystals and Liquid Crystals* **1996,** 280, 145-150.

23. Bay, L.; Jacobsen, T.; Skaarup, S.; West, K., Mechanism of actuation in conducting polymers: osmotic expansion. *Journal of Physical Chemistry B* **2001,** 105, (36), 8492-8497.

24. Otero, T. F.; Grande, H.-J., Electrochemomechanical Devices: Artificial Muscles Based on Conducting Polymers. In *Handbook of Conducting Polymers*, second ed.; Skotheim, T. A.; Elsenbaumer, R. L.; Reynolds, J. R., Eds. Marcel Dekker: 1998; pp 1015-1028.

25. Jager, E. W. H.; Smela, E.; Inganas, O., Microfabricating conjugated polymer actuators. *Science* **2000,** 290, (5496), 1540-1545.

26. Kaneko, M.; Kaneto, K., Electrochemomechanical deformation of polyaniline films doped with self-existent and giant anions. *Reactive & Functional Polymers* **1998,** 37, (1-3), 155-161.

27. Lee, A. P.; Hong, K. C.; Trevino, J.; Northrup, M. A. In *Thin film conductive polymer for microactuator and micromuscle applications*, Micro-Mechanical Systems Symposium of the International Mechanical Engineering Congress and Exposition, Chicago, IL, 6-11 November, 1994; Proceedings of the Dynamics, Systems, and Controls Division: Chicago, IL, 1994; pp 725-732.

28. Lewis, T. W.; Spinks, G. M.; Wallace, G. G.; De Rossi, D.; Pachetti, M., Development of an all polymer electromechanical actuator. *Polym. Prep.* **1997,** 38, 520.

29. Madden, J. D.; Cush, R. A.; Kanigan, T. S.; Hunter, I. W., Fast contracting polypyrrole actuators. *Synthetic Metals* **2000,** 113, (1-2), 185-192.

30. Min, Y.; MacDiarmid, A. G.; Kaneto, K., Electromechanical actuators using polyaniline-polyaniline films. *Polym. Mater. Sci. Eng.* **1994,** 71, 713.

31. Onoda, M.; Okamoto, T.; Tada, K.; Nakayama, H., Polypyrrole films with anisotropy for artificial muscles and examination of bending behavior. *Japanese Journal of Applied Physics Part 2-Letters* **1999,** 38, (9AB), L1070-L1072.

32. Otero, T. F.; Angulo, E.; Rodriguez, J.; Santamaria, C., Electrochemomechanical Properties from a Bilayer - Polypyrrole Nonconducting and Flexible Material Artificial Muscle. *Journal of Electroanalytical Chemistry* **1992,** 341, (1-2), 369-375.

33. Otero, T. F., Artificial muscles, electrodissolution and redox processes in conducting polymers. In *Vol. 4. Conductive Polymers: Transport, Photophysics, and Applications*, Nalwa, H. S., Ed. John Wiley & Sons: New York, 1997; pp 517-594.

34. Pei, Q. B.; Inganas, O., Electrochemical Applications of the Bending Beam Method .1. Mass-Transport and Volume Changes in Polypyrrole During Redox. *Journal of Physical Chemistry* **1992,** 96, (25), 10507-10514.

35. Smela, E.; Inganas, O.; Lundstrom, I., Controlled Folding of Micrometer-Size Structures. *Science* **1995,** 268, (5218), 1735-1738.

36. Pei, Q. B.; Inganas, O., Electrochemical Applications of the Bending Beam Method .2. Electroshrinking and Slow Relaxation in Polypyrrole. *Journal of Physical Chemistry* **1993,** 97, (22), 6034-6041.

37. Pei, Q.; Inganas, O., Conjugated Polymers as Smart Materials, Gas Sensors and Actuators Using Bending Beams. *Synthetic Metals* **1993,** 55-57, 3730-3735.

38. Szabo, D.; Szeghy, G.; Zrinyi, M., Shape Transition of Magnetic Field Sensitive Polymer Gels. *Macromolecules* **1998,** 31, 6541-6548.

39. Chen, X.; Inganas, O., Doping-induced volume changes in poly(3-octylthiophene) solids and gels. *Synthetic Metals* **1995,** 74, 159-164.

40. Takashima, W.; Kaneko, M.; Kaneto, K.; MacDiarmid, A. G., The electrochemical actuator using electrochemically-deposited poly-aniline film. *Synthetic Metals* **1995,** 71, 2265-2266.

41. Baughman, R. H.; Cui, C.; Zakhidov, A. A.; Iqbal, Z.; Barisci, J. N.; Spinks, G. M.; Wallace, G. G.; Mazzoldi, A.; De Rossi, D.; Rinzler, A. G.; Jaschinski, O.; Roth, S.; Kertesz, M., Carbon Nanotube Actuators. *Science* **1999,** 284, 1340-1344.

42. Della Santa, A.; Mazzoldi, A.; Tonci, C.; De Rossi, D., Passive mechanical properties of polypyrrole films: a continuum poroelastic model. *Materials Science and Engineering C* **1997,** 5, (2), 101-109.

43. Ouyang, J.; Li, Y., Preperation and characterization of flexible polypyrole nitrate films. *synthetic metals* **1996,** 79, 121-125.

44. Della Santa, A.; De Rossi, D.; Mazzoldi, A., Performance and work capacity of a polypyrrole conducting polymer linear actuator. *Synthetic Metals* **1997,** 90, 93-100.

45. Lewis, T. W.; Moulton, S. E.; Spinks, G. M.; Wallace, G. G., Optimisation of a polypyrrole based actuator. *Synthetic metals* **1997,** 85, 1419-1420.

46. Mazzoldi, A.; Degl'Innocenti, C.; Michelucci, M.; De Rossi, D., Actuative properties of polyaniline fibers under electrochemical stimulation. *Materials Science and Engineering C* **1998,** 6, 65-72.

47. Murray, P.; Spinks, G. M.; Wallace, G. G.; Burford, R. P., Electrochemical induced ductile-brittle transition in tosylate-doped (pTS) polypyrrole. *Synthetic metals* **1998,** 97, 117-121.

48. Hutchison, A. S.; Lewis, T. W.; Moulton, S. E.; Spinks, G. M.; Wallace, G. G., Development of polypyrrole-based electromechanical actuators. *Synthetic Metals* **2000,** 113, (1-2), 121-127.

49. Smela, E.; Gadegaard, N., Surprising volume change in PPy(DBS): An atomic force microscopy study. *Advanced Materials* **1999,** 11, (11), 953-+.

50. Callow, M. E.; Callow, J. E., Marine biofouling: a sticky problem. *Biologist* **2002,** 49, 1-5.

51. Phillippi, A. L.; O'Conner, N. J.; Lewis, A. F.; Kim, Y. K., Surface flocking as a possible anti-biofoulant. *Aquaculture* **2001,** 195, (3-4), 225-238.

52. Brady, R. F.; Singer, I. L., Mechanical Factors Favoring Release from Fouling Release Coatings. *Biofouling* **2000,** 15, 7-81.

53. Wang, X.-H.; Li, J.; Zhang, J.-Y.; Sun, Z.-C.; Yu, L.; Jing, X.-B.; Wang, F.-S.; Sun, Z.-X.; Ye, Z.-J., Polyaniline as marine antifouling and corrosion-prevention agent. *Synthetic Metals* **1999,** 102, (1-3), 1377-1380.

54. Bar-Cohen, Y., *Electroactive polymer (EAP) actuators as artificial muscles : reality, potential, and challenges*. SPIE Press: Bellingham, Wash., 2001; p xiv, 671.

55. Reddinger, J. L.; Reynolds, J. R., Molecular engineering of pi-conjugated polymers. In *Radical Polymerisation Polyeletrolytes*, SPRINGER-VERLAG BERLIN: Berlin, 1999; Vol. 145, pp 57-122.

56. Bohn, C. C.; Sadki, S.; Brennan, A. B.; Reynolds, J. R., In-Situ Electrochemical Strain Gage Monitoring of Actuation In Conducting Polymers. *Journal of the Electrochemical Society* **2002,** 149, (8), E281-E285.

57. Baughman, R. H.; Shacklette, L. W., Application of dopant-induced structure-property changes of conducting polymer. *Science & Applications of conducting polymers* **1990,** May, 47-61.

58. Baughman, R. H., Conducting Polymers in Redox Devices and Intelligent Materials Systems. *Makromolekulare Chemie-Macromolecular Symposia* **1991,** 51, 193-215.

59. Bar-Cohen, Y., *Electroactive Polymer (EAP) Actuators as Artificial Muscles*. Yoseph Bar-Cohen ed.; SPIE Press: Bellingham, Washington USA, 2001.

60. DellaSanta, A.; DeRossi, D.; Mazzoldi, A., Characterization and modelling of a conducting polymer muscle- like linear actuator. *Smart Materials & Structures* **1997,** 6, (1), 23-34.

61. Diaz, A. F.; Hall, B., Mechanical-Properties of Electrochemically Prepared Polypyrrole Films. *Ibm Journal of Research and Development* **1983,** 27, (4), 342-347.

62. Kaneko, M.; Fukui, M.; Takashima, W.; Kaneto, K., Electrolyte and strain dependences of chemomechanical deformation of polyaniline film. *Synth. Met.* **1997,** 84, 795-6.

63. Chandrasekhar, P., *Conducting polymers, fundamentals and applications : a practical approach*. Kluwer Academic: Boston, 1999; p xxxvi, 718.

64. Sadki, S.; Schottland, P.; Brodie, N.; Sabouraud, G., The mechanisms of pyrrole electropolymerization. *Chemical Society Reviews* **2000,** 29, (5), 283-293.

65. Otero, T. F.; Rodriguez, J.; Angulo, E.; Santamaria, C., Artificial Muscles from Bilayer Structures. *Synthetic Metals* **1993,** 57, (1), 3713-3717.

66. Otero, T. F.; Sansinena, J. M., Artificial Muscles Based on Conducting Polymers. *Bioelectrochemistry and Bioenergetics* **1995,** 38, (2), 411-414.

67. Baughman, R. H.; Shacklette, L. W.; Elsenbaumer, R. L.; Plichta, E. J.; Becht, C., Micro electromechanical actuators based on conducting polymers. *P. I. Lazarev* **1991,** Molecular Electronics.

68. Kaneto, K.; Kaneko, M.; Takashima, W., Response of chemomechanical deformation in polyaniline film on variety of anions. *Japanese Journal of Applied Physics, Part 2 (Letters)* **1995,** 34, (7A), L837-L840.

69. Otero, T. F.; Sansiñena, J. M., Bilayer dimensions and movement in artificial muscles. *Bioelectrochem. Bioenerg.* **1997,** 42, 117.

70. Otero, T. F.; Sansinena, J. M., Soft and wet conducting polymers for artificial muscles. *Advanced Materials* **1998,** 10, (6), 491-+.

71. Madden, J. D.; Cush, R. A.; Kanigan, T. S.; Brenan, C. J.; Hunter, I. W., Encapsulated polypyrrole actuators. *Synthetic Metals* **1999,** 105, (1), 61-64.

72. Bohn, C. C.; Pyo, M. H.; Smela, E.; Reynolds, J. R.; Brennan, A. B., In-situ measurement of conducting polymers on evaportated and electrochemically deposited Au surfaces. *Proc. SPIE* **2002,** 4695, 245-252.

73. Pyo, M.; Bohn, C. C.; Smela, E.; Reynolds, J. R.; Brennan, A. B., Direct strain measurement of polypyrrole actuators controlled by the polymer/gold interface. *Chemistry of Materials* **2003,** 15, (4), 916-922.

74. Dally, J. W.; Riley, W. F., *Experimental Stress Analysis*. 3rd ed.; College House Enterprises: 2001; p 639.

75. Lennox, J. A Biofilm Primer. http://www.biofilmsonline.com/cgi-bin/biofilmsonline/ed_how_primer.html. Last accessed 7/15/04.

76. Pasmore, M.; Todd, P.; Pfiefer, B.; Rhodes, M.; Bowman, C. N., Effect of polymer surface properties on the reversibility of attachment of Pseudomonas aeruginosa in the early stages of biofilm development. *Biofouling* **2002,** 18, (1), 65-71.

77. Melo, L. F.; Bott, T. R., Biofouling in water systems. *Experimental Thermal and Fluid Science* **1997,** 14, (4), 375-381.

78. Gray, N. L.; Banta, W. C.; Loeb, G. I., Aquatic biofouling larvae respond to differences in the mechanical properties of the surface on which they settle. *Biofouling* **2002,** 18, (4), 269-273.

79. Yamamoto, H.; Nishida, A.; Ohkawa, K., Wettability and adhesion of marine and related adhesive proteins. *Colloids and Surfaces a-Physicochemical and Engineering Aspects* **1999,** 149, (1-3), 553-559.

80. Callow, M. E.; Jennings, A. R.; Brennan, A. B.; Seegert, C. E.; Gibson, A.; Wilson, L.; Feinberg, A.; Baney, R.; Callow, J. A., Microtopographic cues for settlement of zoospores of the green fouling alga Enteromorpha. *Biofouling* **2002,** 18, (3), 237-245.

81. Wilkerson, W. R.; Seegert, C. A.; Feinberg, A. W.; Zhao, L. C.; Callow, M. E.; Baney, R.; Brennan, A. B., Bioadhesion studies on microtextured siloxane elastomers. *Abstracts of Papers of the American Chemical Society* **2001,** 221, 253-POLY.

82. de Nys, R.; Steinberg, P. D., Linking marine biology and biotechnology. *Current Opinion in Biotechnology* **2002,** 13, (3), 244-248.

83. Kim, J.; Shen, W.; Latorre, L.; Kim, C.-J., A micromechanical switch with electrostatically driven liquid-metal droplet. *Sensors and Actuators A: Physical* **2002,** 97-98, 672-679.

84. Chou, T., Geometry-dependent electrostatics near contact lines. *Physical Review Letters* **2001,** 8710, (10), art. no.-106101.

85. Digilov, R., Charge-induced modification of contact angle: The secondary electrocapillary effect. *Langmuir* **2000,** 16, (16), 6719-6723.

86. Moon, H.; Cho, S. K.; Garrell, R. L.; Kim, C. J., Low voltage electrowetting-on-dielectric. *Journal of Applied Physics* **2002,** 92, (7), 4080-4087.

87. Lee, J.; Moon, H.; Fowler, J.; Schoellhammer, T.; Kim, C. J., Electrowetting and electrowetting-on-dielectric for microscale liquid handling. *Sensors and Actuators a-Physical* **2002,** 95, (2-3), 259-268.

88. Vallet, M.; Berge, B.; Vovelle, L., Electrowetting of water and aqueous solutions on poly(ethylene terephthalate) insulating films. *Polymer* **1996,** 37, (12), 2465-2470.

89. Peykov, V.; Quinn, A.; Ralston, J., Electrowetting: a model for contact-angle saturation. *Colloid and Polymer Science* **2000,** 278, (8), 789-793.

90. Clarisse, C.; Fadda, E., Characterization of the surface modifications of conducting poly(3-octylthiophene) films by contact angle measurements. *Synthetic Metals* **1995,** 72, (1), 99-103.

91. Liu, M. J.; Tzou, K.; Gregory, R. V., Influence of the Doping Conditions on the Surface Energies of Conducting Polymers. *Synthetic Metals* **1994,** 63, (1), 67-71.

92. Lee, M.-H.; Kim, S. S.; Kang, Y., Potential of zero charge for polypyrrole. *Synthetic Metals* **1999,** 101, (1-3), 442-443.

93. Habib, M. A., Electrogravimetric Characterization of the Electrochromic Polyaniline Film Surface. *Langmuir* **1988,** 4, (6), 1302-1304.

94. Bartlett, P. N.; Grossel, M. C.; Millan Barrios, E., Electrochemistry and contact angle measurements on polymer films of [omega]-(3-pyrrolyl)-alkanoic acids in aqueous solution. *Journal of Electroanalytical Chemistry* **2000,** 487, (2), 142-148.

95. Tourillon, G.; Garnier, F., Stability of Conducting Polythiophene and Derivatives. *Journal of the Electrochemical Society* **1983,** 130, (10), 2042-2044.

96. Skotheim, T. A., *Handbook of Conducting Polymers*. 1st edition ed.; Dekker: 1986.

97. Shenoy, S. L.; Kaya, I.; Erkey, C.; Weiss, R. A., Synthesis of conductive elastomeric foams by an in situ polymerization of pyrrole using supercritical carbon dioxide and ethanol cosolvents. *Synthetic Metals* **2001,** 123, (3), 509-514.

98. Song, K. T.; Lee, J. Y.; Kim, H. D.; Kim, D. Y.; Kim, S. Y.; Kim, C. Y., Solvent effects on the characteristics of soluble polypyrrole. *Synthetic Metals* **2000,** 110, (1), 57-63.

99. Lee, Y. H.; Lee, J. Y.; Lee, D. S., A novel conducting soluble polypyrrole composite with a polymeric co-dopant. *Synthetic Metals* **2000,** 114, (3), 347-353.

100. Lee, J. Y.; Song, K. T.; Kim, S. Y.; Kim, Y. C.; Kim, D. Y.; Kim, C. Y., Synthesis and characterization of soluble polypyrrole. *Synthetic Metals* **1997,** 84, (1-3), 137-140.

101. Lee, C. H.; Lee, J. Y.; Lee, H., Solutions and solution-cast films of conducting polymers. *Synthetic Metals* **1997,** 84, (1-3), 149-150.

102. McCullough, R. D., The Chemistry of Conducting Polythiophenes. *Advanced Materials* **1998,** 10, (2), 93-116.

103. Otero, T. F.; Rodriguez, J., Polypyrrole Electrogeneration at Different Potentials in Acetonitrile and Acetonitrile Water Solutions. *Synthetic Metals* **1993,** 55, (2-3), 1418-1423.

104. Pfluger, P.; Street, G. B., Chemical, electronic, and structural properties of conducting heterocyclic polymers: a view by XPS. *Journal of Chemical Physics* **1984,** 80, (1), 544-553.

105. Sapp, S. A.; Sotzing, G. A.; Reynolds, J. R., High Contrast Ratio and Fast-Switching Dual Polymer Electrochromic Devices. *Chemical Materials* **1998,** 10, 2101-2108.

106. Somanathan, N.; Wegner, G., Mechanical properties of conducting poly(3-cyclohexyl thiophene) films. *Polymer* **1996,** 37, (10), 1891-1895.

107. Sotzing, G. A.; Reddinger, J. L.; Katritzky, A. R.; Soloducho, J.; Musgrave, R.; Reynolds, J. R., Multiply colored electrochromic carbazole-based polymers. *Chemistry of Materials* **1997,** 9, (7), 1578-1587.

108. Yamato, H.; Kai, K.; Ohwa, M.; Wernet, W.; Matsumura, M., Mechanical, electrochemical and optical properties of poly(3,4- ethylenedioxythiophene) sulfated poly(beta-hydroxyethers) composite films. *Electrochimica Acta* **1997,** 42, (16), 2517-2523.

109. Kovacic, P.; Jones, M. B., Dehydro Coupling of Aromatic Nuclei by Catalyst Oxidant Systems - Poly(Para-Phenylene). *Chemical Reviews* **1987,** 87, (2), 357-379.

110. Durham, J. E.; McFarland, K. N.; Kovacic, P., Polymerization of Aromatic Nuclei .18. Polymerization of Benzene to Poly-Para-Phenylene by Aluminum Chloride Air-Water. *Journal of Polymer Science Part a-Polymer Chemistry* **1978,** 16, (5), 1147-1157.

111. Engstrom, G. G.; Kovacic, P., Polymerization of Aromatic Nuclei .16. Mechanism of Chain Propagation in Polymerization of Benzene by Aluminum Chloride Cupric Chloride. *Journal of Polymer Science Part a-Polymer Chemistry* **1977,** 15, (10), 2453-2468.

112. Durham, J. E.; Kovacic, P., Polymerization of Benzene by Aluminum-Chloride. *Journal of Polymer Science Part C-Polymer Letters* **1976,** 14, (6), 347-349.

113. Kovacic, P.; Koch, F. W., Polymerization of Benzene to P-Polyphenyl by Ferric Chloride. *Journal of Organic Chemistry* **1963,** 28, (7), 1864-&.

114. Kovacic, P.; Wu, C., Reaction of Ferric Chloride with Benzene. *Journal of Polymer Science* **1960,** 47, (0149), 45-54.

115. Gaupp, C. L.; Zong, K. W.; Schottland, P.; Thompson, B. C.; Thomas, C. A.; Reynolds, J. R., Poly(3,4-ethylenedioxypyrrole): Organic electrochemistry of a highly stable electrochromic polymer. *Macromolecules* **2000,** 33, (4), 1132-1133.

116. Thomas, C. A.; Zong, K.; Schottland, P.; Reynolds, J. R., Poly(3,4-alkylenedioxypyrrole)s as highly stable aqueous-compatible conducting polymers with biomedical implications. *Adv. Mater* **2000,** 12, (3), 222-225.

117. Li, Y. F.; Yang, J., Effect of electrolyte concentration on the properties of the electropolymerized polypyrrole films. *Journal of Applied Polymer Science* **1997,** 65, (13), 2739-2744.

118. Thomas, C. A.; Zong, K.; Schottland, P.; Reynolds, J. R., Poly(3,4-alkylenedioxypyrrole)s as highly stable aqueous- compatible conducting polymers,vith biomedical implications. *Advanced Materials* **2000,** 12, (3), 222-+.

119. Kang, M. S.; Martin, C. R., Investigations of potential-dependent fluxes of ionic permeates in gold nanotubule membranes prepared via the template method. *Langmuir* **2001,** 17, (9), 2753-2759.

120. Gileadi, E.; Eisner, K. E.; Penciner, J., *Interfacial Electrochemistry. An Experimental Approach*. Addison-Wesley Reading: MA, 1975.

121. Zalewska, T.; Lisowska-Oleksiak, A.; Biallozor, S.; Jasulaitiene, V., Polypyrrole films polymerised on a nickel substrate. *Electrochimica Acta* **2000,** 45, (24), 4031-4040.

122. Finot, M. O.; Braybrook, G. D.; McDermott, M. T., Characterization of electrochemically deposited gold nanocrystals on glassy carbon electrodes. *Journal of Electroanalytical Chemistry* **1999,** 466, (2), 234-241.

123. Martin, H.; Carro, P.; Creus, A. H.; Gonzalez, S.; Salvarezza, R. C.; Arvia, A. J., Growth mode transition involving a potential-dependent isotropic to anisotropic surface atom diffusion change. Gold electrodeposition on HOPG followed by STM. *Langmuir* **1997,** 13, (1), 100-110.

124. Schmidt, U.; Donten, M.; Osteryoung, J. G., Gold electrocrystallization on carbon and highly oriented pyrolytic graphite from concentrated solutions of LiCl. *Journal of the Electrochemical Society* **1997,** 144, (6), 2013-2021.

125. Li, Y. G.; Chrzanowski, W.; Lasia, A., Nucleation and crystal growth in gold electrodeposition from acid solution .1. Soft gold. *Journal of Applied Electrochemistry* **1996,** 26, (8), 843-852.

126. Holmbom, G.; Jacobson, B. E., Nucleation and Initial Growth of Pulse-Plated Gold on Crystalline and Amorphous Substrates. *Journal of the Electrochemical Society* **1988,** 135, (11), 2720-2725.

127. Hou, Z. Z.; Abbott, N. L.; Stroeve, P., Electroless gold as a substrate for self-assembled monolayers. *Langmuir* **1998,** 14, (12), 3287-3297.

128. Hou, Z. Z.; Dante, S.; Abbott, N. L.; Stroeve, P., Self-assembled monolayers on (111) textured electroless gold. *Langmuir* **1999,** 15, (8), 3011-3014.

129. Skaarup, S.; West, K.; Gunaratne, L.; Vidanapathirana, K. P.; Careem, M. A., Determination of ionic carriers in polypyrrole. *Solid State Ionics* **2000,** 136, 577-582.

130. Reynolds, J. R.; Pyo, M.; Qiu, Y. J., Cation and Anion Dominated Ion-Transport During Electrochemical Switching of Polypyrrole Controlled by Polymer-Ion Interactions. *Synthetic Metals* **1993,** 55, (2-3), 1388-1395.

131. Sonoda, Y.; Takashima, W.; Kaneto, K., Characteristics of soft actuators based on polypyrrole films. *Synthetic Metals* **2001,** 119, (1-3), 267-268.

132. Maw, S.; Smela, E.; Yoshida, K.; Sommer-Larsen, P.; Stein, R. B., The effects of varying deposition current density on bending behaviour in PPy(DBS)-actuated bending beams. *Sensors and Actuators a-Physical* **2001,** 89, (3), 175-184.

133. Hohnholz, D.; MacDiarmid, A. G., Line patterning of conducting polymers: New horizons for inexpensive, disposable electronic devices. *Synthetic Metals* **2001,** 121, (1-3), 1327-1328.

134. MacDiarmid, A. G., "Synthetic metals": a novel role for organic polymers. *Current Applied Physics* **2001,** 1, (4-5), 269-279.

135. MacDiarmid, A. G., Synthetic metals: a novel role for organic polymers. *Synthetic Metals* **2001,** 125, (1), 11-22.

136. Okuzaki, H.; Ishihara, M.; Ashizawa, S., Characteristics of conducting polymer transistors prepared by line patterning. *Synthetic Metals* **2003,** 137, (1-3), 947-948.

137. Hara, S.; Zama, T.; Sewa, S.; Takashima, W.; Kaneto, K., Highly stretchable and powerful polypyrrole linear actuators. *Chemistry Letters* **2003,** 32, (7), 576-577.

138. Bay, L.; West, K.; Sommer-Larsen, P.; Skaarup, S.; Benslimane, M., A conducting polymer artificial muscle with 12% linear strain. *Advanced Materials (Weinheim, Germany)* **2003,** 15, (4), 310-313.

139. Qi, B.; Lu, W.; Mattes, B. R., Strain and Energy Efficiency of Polyaniline Fiber Electrochemical Actuators in Aqueous Electrolytes. *Journal of Physical Chemistry B* **2004,** 108, (20), 6222-6227.

140. Lu, W.; Smela, E.; Adams, P.; Zuccarello, G.; Mattes, B. R., Development of Solid-in-Hollow Electrochemical Linear Actuators Using Highly Conductive Polyaniline. *Chemistry of Materials* **2004,** 16, (9), 1615-1621.

141. Rittschof, D.; Costlow, J. D., Surface determination of macroinvertibrate larval settlement. *Proceedings of the 21st Conference on Engineering in Medicine and Biology* **1989**.

142. Holm, E. R.; Cannon, G.; Roberts, D.; Schmidt, A. R.; Sutherland, J. P.; Rittschof, D., The influence of initial surface chemistry on development of the fouling community at Beaufort, North Carolina. *Journal of Experimental Marine Biology and Ecology* **1997,** 215, (2), 189-203.

143. Hillman, A. R.; Efimov, I.; Skompska, M., Dynamics of regioregular conducting polymer electrodes in response to electrochemical stimuli. *Faraday Discussions* **2002,** 121, 423-439.

144. Skompska, M.; Jackson, A.; Hillman, A. R., Evolution from gravimetric to viscoelastic response of poly(3-methylthiophene)-loaded acoustic wave resonators. *Physical Chemistry Chemical Physics* **2000,** 2, (20), 4748-4757.

145. Murray, P.; Wallace, G. G.; Spinks, G. M.; Burford, R. P., In-situ mechanical properties of tosylate doped (pTS) polypyrrole. *Synthetic Metals* **1997,** 84, (1-3), 847-848.

146. Duvail, J. L.; Retho, P.; Godon, C.; Marhic, C.; Louarn, G.; Chauvet, O.; Cuenot, S.; Pra, N.; Demoustier-Champagne, S., Physical properties of conducting polymer nanofibers. *Synthetic Metals* **2003,** 135, (1-3), 329-330.

147. Li, P. C. H.; Thompson, M., Water-instigated changes in elastic modulus of polypyrrole studied by thin rod acoustic wave sensor. *Analytica Chimica Acta* **1997,** 353, (2-3), 255-262.

148. Zoppi, R. A.; De Paoli, M.-A., Chemical preparation of conductive elastomeric blends: polypyrrole/EPDM III. Electrochemical characterization. *Journal of Electroanalytical Chemistry* **1997,** 437, (1-2), 175-182.

149. Xie, H.; Yan, M.; Jiang, Z., Transition of polypyrrole from electroactive to electroinactive state investigated by use of in situ FTIR spectroscopy. *Electrochimica Acta* **1997,** 42, (15), 2361-2367.

150. Turcu, R.; Brie, M.; Leising, G.; Niko, A., Reflection and absorption studies on polypyrrole films electrochemically prepared with different electrolyte types. *Synthetic Metals* **1999,** 100, (2), 217-221.

151. He, C.; Yang, C.; Li, Y., Chemical synthesis of coral-like nanowires and nanowire networks of conducting polypyrrole. *Synthetic Metals* **2003,** 139, (2), 539-545.

152. Song, M.-K.; Kim, Y.-T.; Kim, B.-S.; Kim, J.; Char, K.; Rhee, H.-W., Synthesis and characterization of soluble polypyrrole doped with alkylbenzenesulfonic acids. *Synthetic Metals* **2004,** 141, (3), 315-319.

153. Cataldo, F., Iodine: A ring opening polymerization catalyst for tetrahydrofuran. *European Polymer Journal* **1996,** 32, (11), 1297-1302.

154. Avgousti, C.; Georgolios, N.; Kyriacou, G.; Ritzoulis, G., The electrochemical oxidation of tetrahydrofuran in sulphuric acid solution. *Electrochimica Acta* **1999,** 44, (19), 3295-3301.

155. Tsotra, P.; Friedrich, K., Thermal, mechanical, and electrical properties of epoxy resin/polyaniline-dodecylbenzenesulfonic acid blends. *Synthetic Metals* **2004,** 143, (2), 237-242.

156. Faez, R.; Schuster, R. H.; De Paoli, M. A., A conductive elastomer based on EPDM and polyaniline. II. Effect of the crosslinking method. *European Polymer Journal* **2002,** 38, (12), 2459-2463.

157. Faez, R.; De Paoli, M. A., A conductive rubber based on EPDM and polyaniline - I. Doping method effect. *European Polymer Journal* **2001,** 37, (6), 1139-1143.

158. Faez, R.; Gazotti, W. A.; De Paoli, M. A., An elastomeric conductor based on polyaniline prepared by mechanical mixing. *Polymer* **1999,** 40, (20), 5497-5503.

BIOGRAPHICAL SKETCH

Clayton Bohn was born in Metairie, Louisiana, on June 6, 1974. He lived in the Metairie – New Orleans area until he was 5 and then moved to the Mississippi gulf coast where he grew up.

After high school he completed a Bachelor of Science in polymer pcience at the University of Southern Mississippi with a minor in chemistry in May 1998. Following graduation, he attended the University of Florida where he earned his Master of Science degree in materials science and engineering in August 2003.

The author enjoys Gator football, mountain bike riding, hiking/backpacking, scuba diving, and other outdoor activities. He also enjoys disassembling just about anything he can get his hands on and then trying to put them back together. His mother's favorite day was when he first figured out how to reassemble the things he had taken apart.